BULGARIAN CHEMICAL COMMUNICATIONS

2012 Volume 44 / Special Issue

Proceedings of the III[rd] National Crystallographic Symposium

Journal of the Chemical Institutes
of the Bulgarian Academy of Sciences
and of the Union of Chemists in Bulgaria

Preface

Dear reader,

This special issue of the "Bulgarian Chemical Communication" puts together the best studies, represented during the 3rd National Crystallographic Symposium (**NCS'11)**, which took place on October 3–5, 2011 at the grounds of the "Earth and Man National Museum" in Sofia. For a second consecutive year, the organizers of this event gratefully take the chance to reach the audience, through the pages of this journal.

The National Crystallographic Symposium (NCS) is the annual meeting of the active and rapidly growing Bulgarian crystallographic community as well as the most important activity of the recently re-established Bulgarian Crystallographic Society (**BCS)**. During the last years it won recognition as the leading scientific event, not only for the Bulgarian crystallographers, but also welcoming participants from different European countries. Along with the invited distinguished lecturers in key fields of crystallography, the reputation of the event is based on the participation of Bulgarian scientists, working abroad and using the experience of approved crystallographic schools. A testimony for the growing interest to the National Crystallographic Symposium is the fact that the second and third symposiums were both attended by over 100 participants.

With up to 14 hours of continuous face-to-face communication each symposium day, attendees find out about the latest developments from research and industry, participate in workshops, improve their skills at hands-on demonstrations or join other sessions, which feed their minds in creative and fun ways.

The participants of the last NCS'11 now have the chance to refresh their memories about the ideas, represented at the symposium and get acquainted about all the details that couldn't find place during the presentations; Those who didn't have the chance to be there – to find a reason to attend the next meeting in the fall of 2012.

Wishing you thrilling reading,

Guest editors of the special issue:
D. Kovacheva
T. Kerestedjian

Bulgarian Chemical Communications, Volume 44, Proceedings of the III[rd] National Crystallographic Symposium (pp. 7–16) 2012

Crystallographic, chemical and structural characteristics of harmotome from Zlatolist, Eastern Rhodopes, Bulgaria

R. Atanassova[1]*, R. D. Vassileva[1], M. Kadiyski[2], Z. Zlatev[3]

[1] *Geological Institute, Bulgarian Academy of Sciences, 1113 Sofia;*
[2] *Institute of Mineralogy and Crystallography, Bulgarian Academy of Sciences, 1113 Sofia;*
[3] *Bulgarian Mineralogical Society, Sofia*

Received February 15, 2012; Revised March 15, 2012

Large volumes of intermediate and acid volcaniclastic rocks were formed during the Paleogene in the Eastern Rhodopes, South Bulgaria. Most of them were deposited in a shallow marine environment, lately transformed into clays, adularia, opal-CT and zeolites. Rare mineralization was observed in voids and cavities of basaltic rocks near the Zlatolist village. The voids, now amygdales are filled by calcite, quartz and several zeolites (harmotome, analcime, mordenite, heulandite etc.). Among these harmotome occurs as remarkably well-defined crystals up to 3.5 cm in size.

Harmotome has been characterized using optical microscopy, X-ray, SEM/EDS, EPMA, LA-ICP-MS and DTA. The investigated crystals invariably consist of complex penetration twins and twinning simulates pseudo-orthorhombic forms according to the morvenite law. Crystals are elongated along the a-axis, and flattened on the {010}. Such complex twinning results in an optical heterogeneity and characteristic uneven extinction.

The average chemical formula is: $Ba_{2.46}Ca_{0.17}K_{0.26}[Al_{5.89}Si_{10.19}O_{32}]\bullet 12H_2O$. Registered are 35 trace elements, up to 1.3 wt.% Na, 330 ppm Sr, and 26 ppm Ti. The thermal behavior of harmotome represents water loss in three steps: at 125, 210, and 280 °C, and complete dehydration at 400 °C.

A crystal fragment of harmotome was used also for single crystal X-ray diffraction study. Reliable structure model with satisfactory R-values (R1 = 0.0403; R*all* = 0.0473) was obtained using the P2/m space group and it was chosen for the structure refinement. The obtained unit cell dimensions are: a = 9.8903(5), b = 14.1394(3), c = 8.6713(4) Å, β = 124.628(7)° and V = 997.81(8) Å^3. The final refinement included all atomic coordinates and anisotropic thermal displacement parameters.

Key words: zeolites, phillipsite series, harmotome, crystal structure refinement, crystal morphology.

INTRODUCTION

Zeolites are crystalline hydrated aluminosilicates of the alkali and alkaline elements. They have a framework structure characterized by the presence of interconnected channels or cages, occupied by relatively large cations and water molecules [1]. Depending on their structure and composition, zeolites are widely used as sorbents, detergents, ion-exchangers, and especially as materials for heterogeneous catalysis [2]. Large zeolite crystals provide an ideal possibility for crystal structure determinations [3], studies of the crystal growth mechanism [4], adsorption and diffusion measurements, and more recently spatially resolved probing of catalytic events [5].

Harmotome $Ba_2(Ca_{0.5},Na)_4[A1_5Si_{11}O_{32}]\cdot 12H_2O$ and phillipsite $K_2(Ca_{0.5},Na)_4[A1_6Si_{10}O_{32}]\cdot 12H_2O$ are members of a continuous series with exchangeable cations from barium to potassium. Considerable calcium and sodium content is commonly present. Barium is the most abundant extra-framework cation in harmotome. The name harmotome (after Haüy, 1801, in Combs *et al.* [6]) predates phillipsite; on grounds of history and usage, both are retained in spite of the rules of the report of the CNMMN [6]. Named from Greek words for a "joint" and "to cut", in allusion to a tendency to split along junctions (twin planes). It is well known that crystal individuals invariably consist of complex twins, and Deer *et al.* [7] suggest that the twinning may simulate single crystal forms (mimetic twins), such as tetragonal and rhombic dodecahedra. Sahama and Lehtinen [8] described sectorial twinning in harmotome from Finland. Akizuki [9, 10] has interpreted sector twinning in some minerals in terms of atomic order-

* To whom all correspondence should be sent:
E-mail: radi@geology.bas.bg

ing of such cations as Al/Si and Fe^{3+}/Al, produced during growth. The surface and internal textures of harmotome suggest that the sectorial twinning may originate by the same mechanism. Untwinned crystals have not been found so far. A transparent, spindle-shaped variety of harmotome that was originally described from the Strontian mines north of Morven (now Morvern), Argyllshire, Scotland, UK [11], later was used to describe a type of twinning also observed for phillipsite. The complex interpenetration twinning of phillipsite was classified by Lacroix (1897, 1923 in: Tschernich [12]) to include the Morvenite twin, Marburg twin, Perier twin and Stempel twin according to the dominant habits.

Harmotome is typically monoclinic, although its actual space group is debatable due to acentricity, which is lowering the symmetry [13]. Harmotome and phillipsite have the same (structural code, PHI) framework topology with double "crankschafts" parallel to the *a*-axis.

Until now harmotome was known from one occurrence in Bulgaria. It was described from fissures of latitic lavas North of Iskra, Haskovo district with laumontite and heulandite [14]. In this study, we present the crystallographic, mineralogical and chemical data on harmotome from Zlatolist, Eastern Rhodopes. In addition, the values of the cell parameters are obtained by single-crystal X-ray diffractometry.

GEOLOGICAL OVERVIEW

Intense collision-related volcanism took place in the East Rhodopes, South Bulgaria during the Paleogene. Eruptive products, both lava and volcaniclastic rocks, are assigned to four intermediate (to basic) phases alternating in time with five acidic ones [15]. The first two phases (intermediate and acidic) are Priabonian while all following are of Rupelian age. Large volumes of pyroclastic rocks were erupted during the first three acidic volcanic phases and deposited in a shallow marine environment. They were subsequently transformed into zeolites, clay minerals, adularia and opal-CT [15].

Rare zeolite mineralization was observed in voids and in some microdruses and cavities of basaltic andesits near the Zlatolist village, Eastern Rhodopes (Fig. 1). The voids, now amygdales are filled predominantly by calcite, quartz, chalcedony and several zeolites (mainly represented by harmotome, analcime, chabasite, mordenite and heulandite). Among these zeolites, harmotome occurs as remarkably well-defined large crystals.

Fig. 1. Photographs of: a) outcrop of basaltic rocks near Zlatolist, b-d) handspecimens representing large harmotome crystals in amygdales

EXPERIMENTAL AND ANALYTICAL PROCEDURES

Harmotome has been characterized using optical microscopy, X-ray diffraction, SEM/EDS, EPMA, LA-ICP-MS and DTA.

Detailed morphological studies on separate crystals and aggregates were carried with a binocular optical and scanning electron microscopes JEOL JSM 6390 with EDS Oxford INCA system (SEM). Electron probe microanalyses (EPMA) were performed with a JEOL JSM CF with Tracor Northern – 2000 analyzing system at an accelerating voltage of 25 kV and a beam diameter of 1 μm. Electron microprobe analyses are performed on the same samples used for the structure determination. In each crystal, several spots were analyzed to check for sample homogeneity.

LA-ICP-MS analytical system consists of a 193 nm ArF excimer laser and an ELAN DRC-e ICP quadrupole mass spectrometer. For controlled ablation, an energy density of above 10 J/cm^2 on the sample and a laser pulse frequency of 10 Hz were used. Analyses were performed with 50 or 75 μm beam diameters and external standardization on NIST glass standard SRM-610.

TG-DTA-DTG measurements were performed in air with heating rate 10 °C/min.

The powder diffraction patterns of harmotome were measured on a D2 Phaser Bruker AXS at room temperature with Ni-filtered Cu-Kα radiation (λ = 1.5406 Å). Data was collected in step-scan mode from 4 to 70 °2θ with 0.05 °2θ step and 1s exposure time.

CRYSTAL STRUCTURE

A single crystal of harmotome from Zlatolist with dimensions 0.25 × 0.22 × 0.20 mm was mounted on a glass fibre and measured on an Oxford diffraction Supernova diffractometer equipped with Atlas CCD detector. X-ray data collection was carried out at room temperature with monochromatic Mo-Kα radiation (λ = 0.71073 Å). After the initial matrix procedure, a C-centred unit cell (Laue class *mmm*) with parameters a = 9.9034(5), b = 14.2979(9), c = 14.1612(7) Å, and V = 2005.2(2) Å^3 was selected. Data collection strategy was chosen for 100% completeness and redundancy of 3.9. Data reduction and analysis were carried out with the CrysAlisPro program [16]. Lorentz and polarization corrections were applied to intensity data using WinGX [17]. Reliable model with satisfactory R-values was obtained using the *P*2/*m* space group and it was chosen for the refinement. For the framework atoms, starting coordinates were taken from [18], and the extra-framework cations and water molecules were then assigned from the difference Fourier list. Structure refinements were performed using the program SHELXTL [17], employing neutral atomic scattering factors. Due to the Si, Al disorder, tetrahedral positions were later refined with Si scattering factors. Extraframework cations and water molecules were first refined using isotropic temperature factors. Each occupancy parameter was refined by fixing the occupancies of the remaining atoms. At the final stage of refinement, anisotropic temperature factors were introduced. Unit cell dimensions and experimental details are given in Table 1.

Table 1. Experimental details for harmotome from Zlatolist

Parameter \ Sample	Harmotome (this study) P121/m1
a [Å]	9.8903(5)
b [Å]	14.1394(3)
c [Å]	8.6713(4)
β [°]	124.628(7)
V [Å^3]	997.81(8)
№ of reflections	8642
R_{int}	0.0266
R_{sigma}	0.0344
h min	–12
h max	13
k min	–20
k max	18
l min	–9
l max	13
theta min [°]	2.85
theta max [°]	32.82
unique reflections	3516
Ref. $F_o > 4sigF_o$	3099
№ of parameters	156
R_1	0.0403
$R_{(all)}$	0.0473
GooF	1.064

The analysis of measured intensity peaks and diffraction patterns confirmed that the sample is harmotome (Fig. 2, PDF Card 00-053-1175) [19]. Atomic coordinates, thermal displacement parameters, T–O–T angles, and T–O bond lengths, acquired from the X-ray single crystal measurement are listed in Tables 2-4.

The structure of harmotome from Zlatolist has a phillipsite-type framework with chains of four-membered rings, parallel to the *a*-axis (Fig. 3). The arrangement of Si, Al tetrahedra leads to the formation of three types of eight-membered rings, running along the three axes. Barium cations occupy the centre of the channels, parallel to the **c**-axis.

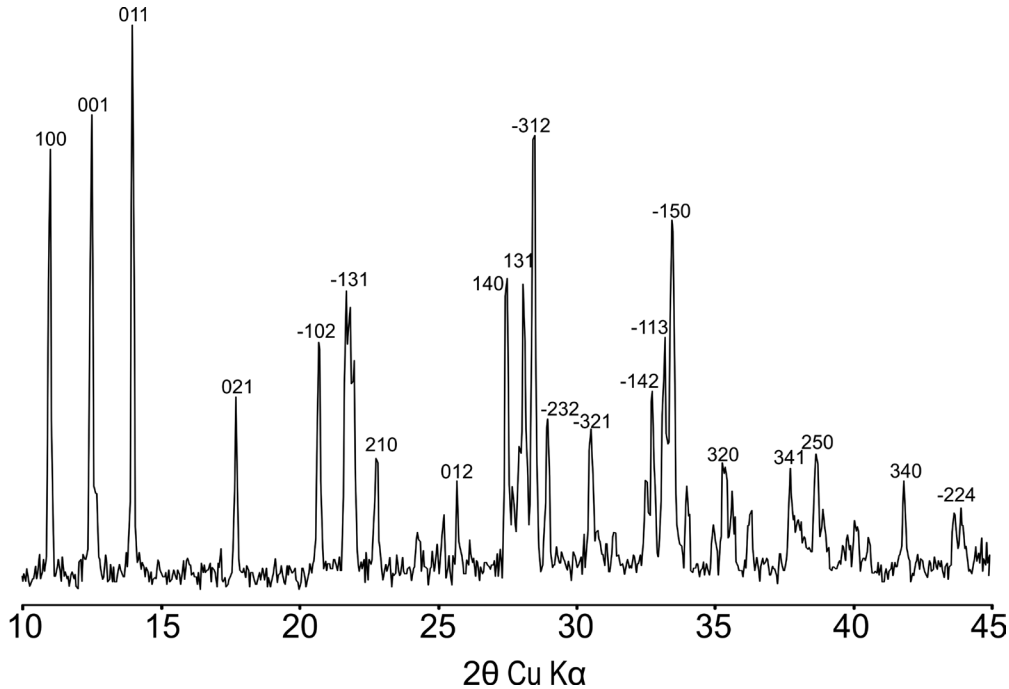

Fig. 2. Powder pattern of harmotome from Zlatolist. All intensity peaks correspond to the diffraction pattern of harmotome (PDF Card 00-053-1175)

Barium is coordinated by seven O atoms from the framework (2 × O1, 2 × O3, 2 × O5, and O9) and by four water molecules (W1, W2, and 2 × W3). Two of the five refined water molecules (W4 and W5) are disordered and are not bonded to barium, similar to [18].

MORPHOLOGICAL PROPERTIES

Harmotome from Zlatolist is transparent with vitreous luster, and though crystals are typically colourless, some fragments may be yellow-brownish or pale beige. Crystal size ranging from several mm to

Table 2. Atomic coordinates, $U_{iso}(U_{eq})$ parameters and occupancies for harmotome

Label	x	y	z	U_{iso} or U_{eq}	Occ.
T1	–0.05692(10)	–0.00826(6)	0.73246(10)	0.01031(16)	1
T2	0.12075(10)	0.13889(6)	0.58390(10)	0.0110(6)	1
T3	0.42053(10)	0.14073(6)	0.90646(10)	0.00990(16)	1
T4	0.26340(10)	–0.02459(6)	1.04746(11)	0.0105(6)	1
Ba	0.86210(5)	¼	0.16707(4)	0.02476(11)	0.93
O1	0.6148(3)	0.11714(19)	0.9344(3)	0.0207(5)	1
O2	0.0960(3)	–0.05218(18)	0.8903(3)	0.0192(5)	1
O3	0.2190(3)	–0.0137(2)	1.2151(3)	0.0225(5)	1
O4	0.4111(5)	¼	0.9672(5)	0.0230(7)	1
O5	0.3516(3)	0.07257(19)	1.0193(3)	0.0232(5)	1
O6	–0.0049(3)	0.0915(2)	0.6651(4)	0.0269(6)	1
O7	0.3119(3)	0.1291(2)	0.7102(3)	0.0234(5)	1
O8	0.0666(5)	¼	0.5432(5)	0.0261(8)	1
O9	0.1035(4)	0.0921(2)	0.4077(4)	0.0318(6)	1
W1	0.8845(10)	¼	0.8450(9)	0.0621(19)	1
W2	1.1986(10)	¼	0.1881(10)	0.071(2)	1
W3	0.6983(7)	0.1375(4)	0.3277(6)	0.0702(14)	1
W4	0.532(3)	¼	0.548(3)	0.124(12)	0.38
W5	0.508(2)	0.048(3)	0.4793(19)	0.21(2)	0.42

Table 3. Anisotropic displacement parameters for harmotome

Label	U_{11}	U_{22}	U_{33}	U_{23}	U_{13}	U_{12}
T1	0.0102(3)	0.0119(4)	0.0090(3)	–0.0007(3)	0.0035(3)	–0.0004(3)
T2	0.0137(7)	0.0087(7)	0.0096(7)	–0.0009(3)	0.0030(3)	–0.0013(3)
T3	0.0081(3)	0.0076(3)	0.0132(4)	0.0010(3)	0.0028(3)	0.0002(3)
T4	0.0087(7)	0.0115(7)	0.0119(7)	0.0016(3)	0.0044(4)	0.0008(3)
Ba	0.0331(2)	0.01613(16)	0.02686(19)	0.000	0.01274(14)	0.000
O1	0.0136(10)	0.0204(11)	0.0284(13)	0.0037(10)	0.0077(9)	0.0037(9)
O2	0.0157(10)	0.0199(11)	0.0189(11)	0.0009(9)	0.0022(9)	0.0015(9)
O3	0.0166(10)	0.0338(14)	0.0168(11)	–0.0005(10)	0.0055(9)	0.0034(10)
O4	0.0327(19)	0.0117(14)	0.0265(18)	0.000	0.0129(15)	0.000
O5	0.0241(12)	0.0191(11)	0.0290(13)	0.0032(10)	0.0126(10)	–0.0049(9)
O6	0.0253(12)	0.0248(13)	0.0350(15)	0.0115(11)	0.0161(11)	–0.0009(10)
O7	0.0185(11)	0.0310(13)	0.0168(11)	–0.0001(10)	0.0012(9)	0.0015(10)
O8	0.0246(18)	0.0143(15)	0.036(2)	0.000	0.0063(16)	0.000
O9	0.0386(16)	0.0336(15)	0.0237(13)	–0.0127(12)	0.0117(12)	–0.0067(13)
W1	0.103(5)	0.033(3)	0.078(5)	0.000	0.066(4)	0.000
W2	0.079(5)	0.078(5)	0.076(5)	0.000	0.053(4)	0.000
W3	0.070(3)	0.092(4)	0.056(3)	0.013(3)	0.031(2)	–0.006(3)
W4	0.104(18)	0.23(4)	0.086(16)	0.000	0.089(16)	0.000
W5	0.039(6)	0.33(7)	0.044(8)	–0.012(17)	0.016(6)	–0.058(17)

Table 4. T–O bond lengths [Å] and T–O–T angles [°] for tetrahedra of harmotome

T–O bond	Distance [Å]	T–O bond	Distance [Å]	T–O–T angle	Angle [°]
T1 – O9	1.646(3)	T3 – O5	1.631(3)	T3–O1–T4	139.36(18)
T1 – O6	1.650(3)	T3 – O5	1.642(3)	T4–O2–T1	144.14(17)
T1 – O3	1.652(3)	T3 – O4	1.6440(16)	T4–O3–T1	138.65(17)
T1 – O2	1.658(2)	T3 – O1	1.650(2)	T3–O4–T3	140.0(3)
mean	1.652(3)	mean	1.642(3)	T3–O5–T4	151.3(2)
T2 – O9	1.626(3)	T4 – O5	1.632(3)	T2–O6–T1	144.1(2)
T2 – O6	1.635(3)	T4 – O3	1.640(3)	T2–O7–T3	139.69(19)
T2 – O7	1.642(3)	T4 – O2	1.653(2)	T2–O8–T2	146.1(3)
T2 – O8	1.642(1)	T4 – O1	1.654(3)	T2–O9–T1	155.2(2)
mean	1.636(3)	mean	1.645(3)		

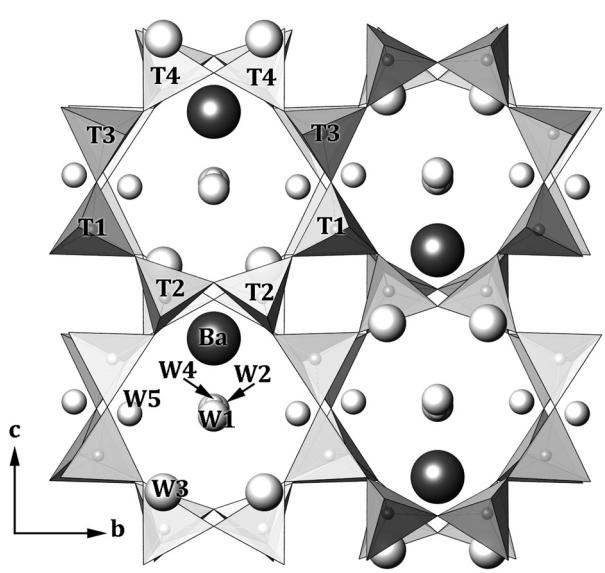

Fig. 3. The atomic structure of harmotome from Zlatolist, projected along the *a*-axis. Size of spheres corresponds to site occupancies, larger spheres have higher occupancies. T stands for tetrahedral site, W – water molecule

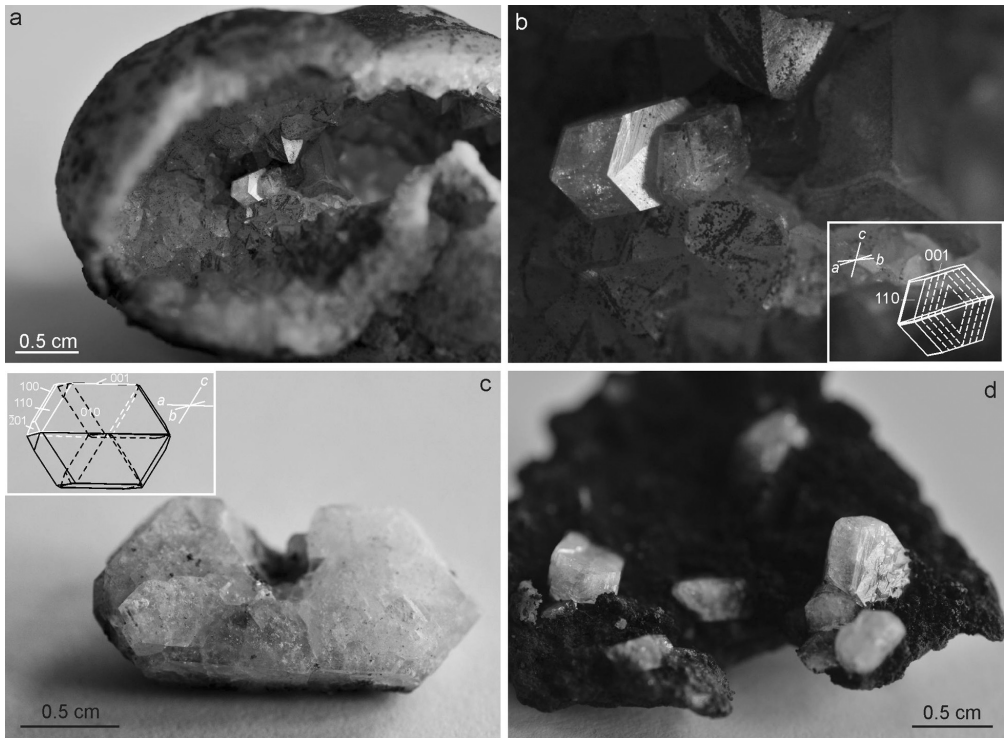

Fig. 4. Morphology of harmotome crystals: a) small amygdale partially filled by quartz, analcime and harmotome; b) twin variety after so-called morvenite law according to the characteristic striae parallel to the edge between {010} and {110} and twin suture running parallel to {001}; c) pseudo-orthorhombic twin, composed by four individuals; d) transparent crystals with oriented, stepped hillocks on {010} faces

1.5 cm (Figs 4, 6). Large crystals up to ~3.5 cm have been collected rarely.

Optical and SEM observations indicate that the mineral prevalently forms penetration twins without re-entrant angels. The crystal habit is characterized by short prismatic pseudo-orthorhombic forms. Equant crystals and radiating aggregates are common. The crystals are always pseudo-orthorhombic penetration twins. Twinning suture and combination striations can be detected on each crystal (Fig. 4b-d). Judging from the values of interfacial angles, the presence of characteristic striae parallel to the edge between {010} and {110} and twin suture running parallel to {001} the twin variety form pseudo-orthorhombic

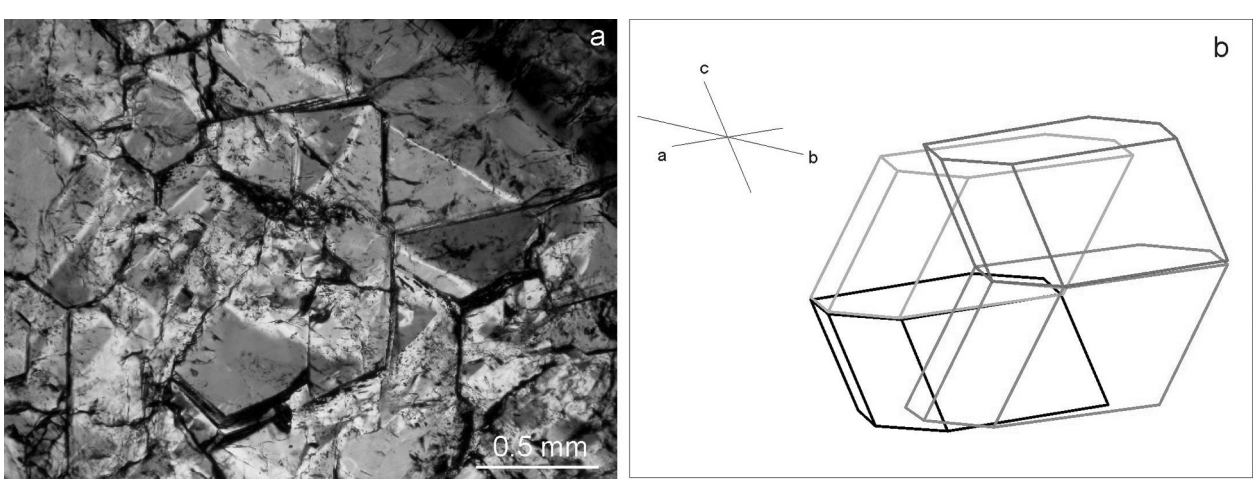

Fig. 5. Crystallographic characteristics: a) microphotograph with characteristic uneven extinction, thin section under crossed polars; b) habit of a simple penetration twin

penetration twins after the so-called morvenite law. Complex twinning results in an optical heterogeneity and shows characteristic uneven extinction under crossed polars (Fig. 5a).

The morvenite twin is a fourling twin, present in all investigated crystals and without re-entrant angles. It is composed of four individuals (Fig. 5b), arranged across the twin planes (001) and ($20\bar{1}$), displaying the {100}, {010}, {001}, {110}, and small {$\bar{2}$01} forms. The four sets of intersecting striations, which indicate the presence of the four individuals, are seen only on the (010) faces. Morvenite twins are commonly elongated along the *a*-axis, and flattened on the {010}.

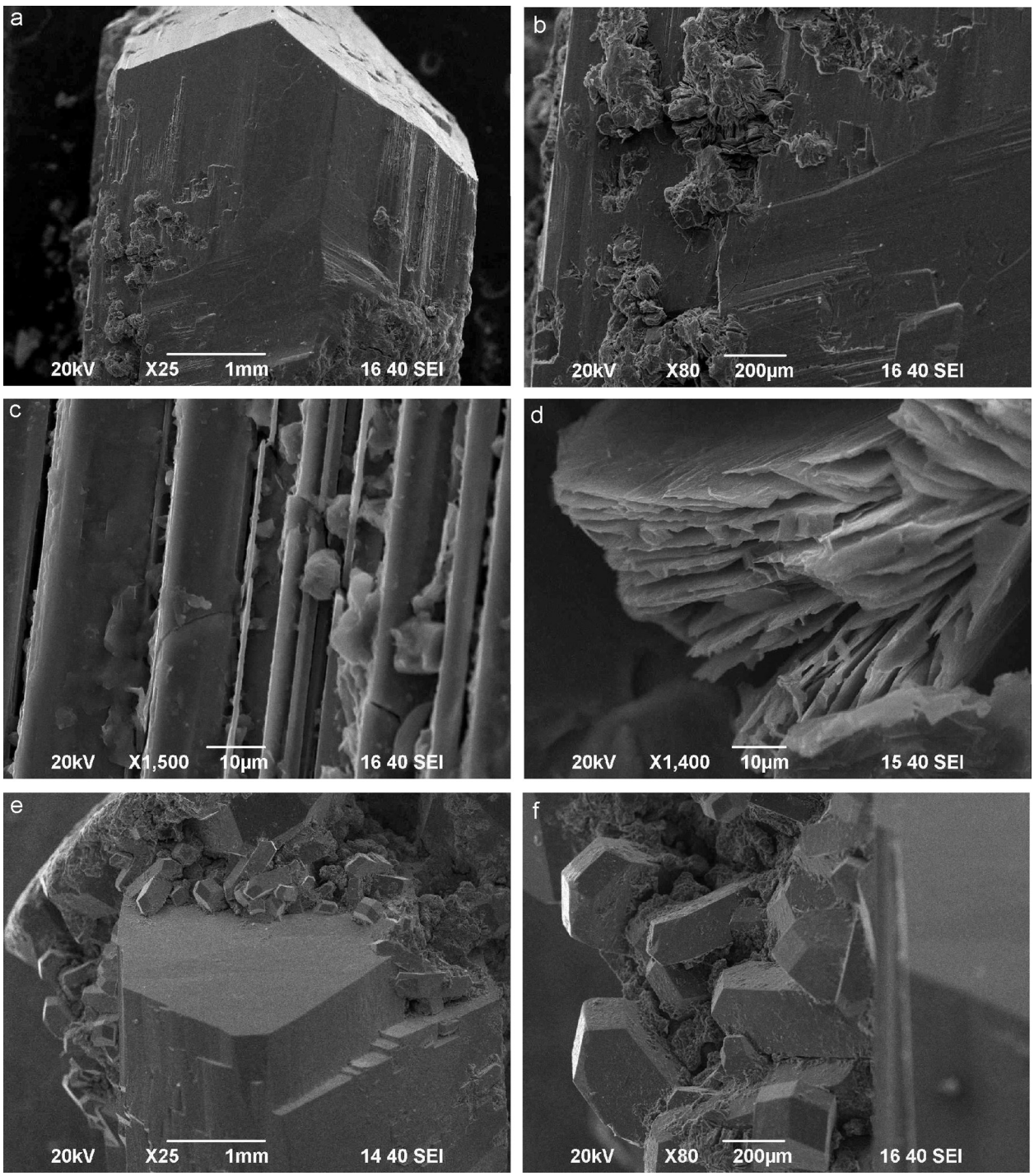

Fig. 6. SEM images of: a-c) harmotome crystal surface; d) a detail showing partial replacement by chlorite; e-f) groups of small twinned individuals on large pseudo-orthorhombic crystal from one amygdale

Under SEM it is revealed that mineral surfaces of some crystals are decorated by spherulitic aggregates (Fig. 6b–d), probably after partial replacement by chlorite (?).

CHEMICAL COMPOSITION

The average chemical formula based on EPMA is as follows: $Ba_{2.46}Ca_{0.17}K_{0.26}[Al_{5.89}Si_{10.19}O_{32}]\cdot 12H_2O$. Calcium and potassium are both conspicuous in the chemical composition of the harmotome studied (Table 5). Sodium, magnesium and iron often reported in harmotome [20, 21] was not found using EPMA. Additionally, the mineral analysed is characterized by distinctly higher amounts of aluminium and barium than those cited in the literature. Si/(Si+Al) ratio shows an average value of 0.71 in Zlatolist, and ranges from 0.68 in crystals from trachyandesite of Iskra, Bulgaria [14], to 0.76 in crystals from basalts of Weitendorf, Austria [22]. According to the average ratio (Ra) after Passaglia and Sheppard [23] and experimentally determined in this study Ra=0.63 harmotome can be classified as intermediate zeolite.

Data are "reliable", i.e. with the content of tetrahedral cations (Si+Al) close to half of the oxygen atoms and the balance error $E = [(Al–Al_{theor.})/Al_{theor.}]\times 100$ lower than 10% [24].

Chemical analyses were performed by electron microprobe and the water content is the result of normalization of data to 100%. The number of water molecules is known to be related to both structural and chemical parameters because it increases with Si/Al and divalent/monovalent cation ratios. Contents of H_2O tend to decrease with increasing number and size of extra-framework cations, as well as with increasing temperature and decreasing $P(H_2O)$. Such variations can be vital to petrological, geochemical, environmental, and experimental considerations [6].

Minor and trace elements in harmotome are registered also by LA-ICP-MS. Determined are up to 1.3 wt.% Na, 1.2 wt.% K, and 0.6 wt.% Ca. Traces of: Sr (330), V (100), Rb (65), Ti (26), Zn (20), Mn (16), Cu (15), P (15), Fe (14) in ppm are found.

Table. 5. Chemical analyses and formulae on the basis of 32 oxygens

wt.%	Bar1 p.1	Bar1 p.2	Bar1 p.3	Bar2 p.1	Bar2 p.2	Bar2 p.3	Bar3 p.1	Bar3 p.2
Al_2O_3	18.42	18.68	22.18	18.29	18.11	21.72	18.57	18.65
SiO_2	39.53	40.55	38.3	39.04	40.81	37.99	39.91	39.23
K_2O	0.34	0.51	0.6	0.95	0.82	1.58	0.85	0.58
CaO	0.63	1.68	0.25	0.42	0.46	0.71	0.15	0.56
BaO	25.68	23.42	23.41	25.87	25.64	21.72	25.28	25.37
MnO	–	0.19	0.16	–	0.15	0.25	0.08	0.15
Total	84.6	85.03	84.9	84.57	85.99	83.97	84.84	84.54
H_2O*	15.4	14.97	15.1	15.43	14.01	16.03	15.16	15.46
*–H_2O by difference to approx. 100 wt.% total								
Weight % – analyses computed to 100% without H_2O								
Al_2O_3	21.77	21.97	26.12	21.63	21.06	25.87	21.89	22.06
SiO_2	46.73	47.69	45.11	46.16	47.46	45.24	47.04	46.40
K_2O	0.40	0.60	0.71	1.12	0.95	1.88	1.00	0.69
CaO	0.74	1.98	0.29	0.50	0.53	0.85	0.18	0.66
BaO	30.35	27.54	27.57	30.59	29.82	25.87	29.80	30.01
MnO	0.00	0.22	0.19	0.00	0.17	0.30	0.09	0.18
Total	100.00	100.00	100.00	100.00	100.00	100.00	100.00	100.00
Number of cations on the bases of 32 oxygen equivalents, ignoring H_2O								
Al	5.67	5.65	6.65	5.67	5.47	6.56	5.68	5.74
Si	10.32	10.42	9.75	10.27	10.46	9.73	10.36	10.25
K	0.11	0.17	0.20	0.32	0.27	0.52	0.28	0.19
Ca	0.18	0.46	0.07	0.12	0.13	0.20	0.04	0.16
Ba	2.63	2.10	2.33	2.67	2.58	2.18	2.57	2.60
Mn	0.00	0.04	0.03	0.00	0.03	0.05	0.02	0.03
Si/(Si+Al)	0.65	0.65	0.59	0.64	0.66	0.60	0.65	0.64
K/(K+Ba)	0.04	0.07	0.08	0.11	0.09	0.19	0.10	0.07
E%	–5.56	–5.76	10.84	–5.45	–8.81	9.34	–5.35	–4.28

The thermal behavior of harmotome, from TG-DTA-DTG measurements, with five different water sites in the structure, represents water loss in three steps: at 125, 210, and 280 °C, and complete dehydration at 400 °C.

GENETIC AND CONCLUDING REMARKS

Zeolites can originate from a variety of precursor materials including volcanic and impact glasses, aluminosilicate minerals including other zeolites, smectite, feldspars and feldspathoids [25]. Most of the famous zeolite specimens known from the mineral collections are incrustations on the walls of geodes and vugs of basic lavas (basalts sensu lato). The genesis of these crystals could be considered, as those occurring in non-volcanic rocks, due to hydrothermal deposition [26]. Harmotome is known to have both sedimentary and hydrothermal origin; the second one being by far the most common [1, 25, 27]. However, zeolitic rocks, widespread in Eastern Rhodopes, are known as product of volcanic glass and pyroclastics transformation. Zeolites form more rapidly from glass than from crystalline materials, and the reaction rate of glass varies inversely with its silica content [28]. Most of the features of Zlatolist zeolites differ compared to microcrystalline zeolites formed in sediments. Well-developed large crystals, number of zeolite species and average chemical composition are indicative for hydrothermal origin, according to the criteria suggested by Gottardi [26].

The source of barium, the element necessary in the formation of harmotome, could be barite concretions in adjacent pyroclastic rocks. Also, in some basic to intermediate rock varieties from the volcanic complex Ba-content up to 1970 ppm was determined [29]. Barium could have been derived from feldspars, common in the volcanic varieties of the area, as well. Moreover, Ba-sanidine with up to 8.9 wt.% BaO was recently described by Yanev and Ivanova [30] from the acid volcanic varieties from the adjacent region in the Eastern Rhodopes.

Finally, the co-existence of the Zlatolist harmotome with chalcedony, quartz and calcite crystals and its occurrence in geodes indicates the hydrothermal, probably low temperature, origin of the mineral with a transport of the substance at some distance.

Acknowledgements*: The authors would like to express thanks to Stela Atanasova (Institute of Physical Chemistry, BAS) for SEM/EDS analyses and Vilma Petkova (Institute of Mineralogy and Crystallography, BAS) for DTA measurements.*

REFERENCES

1. G. Gotardi, E. Galli, in: Natural zeolites, Springer-Verlag, 1985, p. 135.
2. A. Corma, *Chem. Rev*., **95**, 559 (1995).
3. Z. A. D. Lethbridge, J. J. Williams, R. I. Walton, K. E. Evans, C. W. Smith, *Micropor. Mesopor. Mater*., **79**, 339 (2005).
4. R. Brent, M.W. Anderson, *Angew. Chem. Int. Ed*., **47**, 5327 (2008).
5. M. H. F. Kox, E. Stavitski, B. M. Weckhuysen, *Angew. Chem. Int. Ed*., **46**, 3652 (2007).
6. D. Coombs, A. Alberti, T. Armbruster, G. Artioli, C. Colella, E. Galli, J. D. Grice, F. Liebau, J. A. Mandarino, H. Minato, E. H. Nickel, E. Passagila, D. R. Peacor, S. Quartieri, R. Rinaldi, M. Ross, R. A. Sheppard. E. Tllmanns, G. Vezzalini, *Canadian Mineralogist*, **35**, 1571 (1997).
7. W. A. Deer, R. A. Howie, J. Zussman, Rock-forming minerals, vol. 4, Framework silicates, Longman, London, 1963.
8. Th. G. Sahama, M. Lehtinen, *Mineralogical Magazine*, **36**, 444 (1967).
9. M. Akizuki, *American Mineralogist*, **66**, 403 (1981).
10. M. Akizuki, *American Mineralogist*, **70**, 822 (1985).
11. T. Thomson, Outlines of Mineralogy, geology and mineral analysis, vols. I and II, London, 1836.
12. R. Tschernich, Zeolites of the World, Geoscience Pres., Arizona, 1992.
13. T. Armbruster, M. Gunter, in: Natural Zeolites: Occurrence, Properties, Applications, D. L. Bish, D. W. Ming (eds.), vol 45, Mineralogical Society of America, Virginia, 2001, p. 217.
14. I. Kostov, *Annu. Univ. Sofia, Fac. Biol. Geol. Geogr*. livre 2, Geol., **55**, 159 (1962).
15. Y. Yanev, J.-J. Cochemé, R. Ivanova, O. Grauby, E. Burlet, R. Pravchanska, *N. Jb. Miner. Abh*., **182**(3), 265 (2006).
16. Oxford Diffraction. CrysAlis PRO, Oxford Diffraction Ltd, Yarnton, England, 2010.
17. G. M. Sheldrick, *Acta Crystallographica A*, **64**, 112 (2008).
18. E. Stuckenschmidt, H. Fuess, A. Kvick, *European Journal of Mineralogy*, **2**, 861 (1990).
19. J. Faber, T. Fawcett, *Acta Crystallographica B*, **58**, 325 (2002).
20. R. Rinaldi, J. J. Pluth, J. V. Smith, *Acta Crystallographica B*, 2426 (1974).
21. P. Cherny, R. Rinaldi, R.C. Surdam, *Neues Jahrb. Miner. Abh*., **128(**3), 312 (1977).
22. T. Armbruster, M. Wenger, T. Kohler, *Mitt. Abt. Mineral. Landesmus.*, **59**, 13 (1991).
23. E. Passaglia, R. A. Sheppard, in: Natural Zeolites: Occurrence, Properties, Applications, D. L. Bish, D. W. Ming (eds.), vol 45, Mineralogical Society of America, Virginia, 2001, p. 69.
24. E. Passaglia, *American Mineralogist*, **55**, 1278 (1970).
25. R. L. Hay, R. A. Sheppard, in: Natural Zeolites: Occurrence, Properties, Applications, D. L. Bish, D. W. Ming (eds.), vol 45, Mineralogical Society of America, Virginia, 2001, p. 217.

26. G. Gottardi, *European Journal of Mineralogy*, **4**, 479 (1989).
27. T. Wieser, *Mineralogia Polonica*, **16**, 3 (1985).
28. R. A. Sheppard, R. L. Hay, in: Natural Zeolites: Occurrence, Properties, Applications, D.L. Bish, D.W Ming (eds.), vol 45, Mineralogical Society of America, Virginia, 2001, p. 261.
29. Y. Yanev, R. Ivanova, *Geochemistry, Mineralogy and Petrology*, **48**, 39 (2010).
30. B. Yardonov, S. Sarov, S. Georgiev, V. Valkov, E. Balkanska, V. Grozdev, R. Marinova, N. Markov, *Explanatory note to the Geological Map of the Republic of Bulgaria Scale 1:50 000*, 2008, p. 124.

КРИСТАЛОГРАФСКИ, ХИМИЧНИ И СТРУКТУРНИ ХАРАКТЕРИСТИКИ НА ХАРМОТОМ ОТ ЗЛАТОЛИСТ, ИЗТОЧНИ РОДОПИ, БЪЛГАРИЯ

Р. Атанасова[1]*, Р. Д. Василева[1], М. Кадийски[2], З. Златев[3]

[1]Геологически институт, Българска академия на науките, 1113 София;
[2] Институт по минералогия и кристалография , Българска академия на науките, 1113 София;
[3] Българско минералогическо дружество, София

Постъпила на 15 февруари, 2012 г.; приета на 15 март, 2012 г.

(Резюме)

През палеогена големи количества от средни и кисели вулканокластични скали са отложени в Източните Родопи, Южна България. Повечето от тях са образувани в плиткоморски условия и в последствие са трансформирани в глини, адулар, опал-CT и зеолити. Интересна минерализация беше установена в празнини и кухини на базалтови андезити в района на с. Златолист. Празнините, сега миндали са запълнени с калцит, кварц и разнообразни зеолити (хармотом, аналцим, морденит, хейландит и др.). Сред тях хармотомът се отличава със забележителни добре оформени кристали с размер достигащ до 3,5 cm.

Хармотомът е характеризиран с оптична микроскопия, прахова и монокристална рентгенография, SEM/EDS, микросондови анализи, LA-ICP-MS и DTA. Изследваните кристали неизменно са изградени от комплексни проникващи двойници. Двойникуването симулира псевдоромбични форми съгласно морвенитов закон на сращване. Кристалите са удължени по *a*-оста и с плочесто развитие по {010}. Това комплексно двойникуване се отразява на оптичната хетерогенност и анизотропия.

Средната кристалохимична формула е: $Ba_{2.46}Ca_{0.17}K_{0.26}[Al_{5.89}Si_{10.19}O_{32}]\cdot 12H_2O$. Определени са и 35 елементи-примеси и следи: до 1.3 тегл.% Na, 330 ppm Sr, and 26 ppm Ti. Термичното поведение на хармотома се изразява в загуба на вода на три стъпки: при 125, 210, и 280 °C. Окончателна дехидратация се достига при 400 °C.

Кристален фрагмент от хармотом е характеризиран и с монокристална рентгенова дифрактометрия. Добър модел с удовлетворителни стойности на R (R1 = 0.0403; R(all) = 0.0473) е достигнат с използване на пространствената група P2/m, която е избрана за структурни уточнения. Получените параметри на елементарна клетка са: a = 9.8903(5), b = 14.1394(3), c = 8.6713(4) Å, β = 124.628(7)° и V = 997.81(8) Å^3. Финалните уточнения включват всички атомни координати и анизотропни термични параметри.

Bulgarian Chemical Communications, Volume 44, Proceedings of the III[rd] National Crystallographic Symposium (pp. 17–23) 2012

X-Ray, DTA and TGA analysis of zinc sulfide concentrates and study of their charging for roasting in fluidized bed furnace

B. S. Boyanov*, A. B. Peltekov

Paisii Hilendarski University of Plovdiv, Department of Chemical Technology
24 Tsar Asen St., Plovdiv, Bulgaria

Received March 20, 2012; Revised April 17, 2012

Bulgaria is a major producer of zinc in Central and Eastern Europe (about 100 000 tons per year). The two zinc metallurgical plants in KCM S.A., Plovdiv and LZC S.A., Kardjali deliver the necessary raw materials from Bulgaria and abroad.

In this connection, 7 Bulgarian and imported zinc concentrates have been investigated with the use of chemical analysis, X-ray phase analysis, DTA and TGA. The following phases were established: β-ZnS; nZnS.mFeS; $CuFeS_2$; PbS; SiO_2 (α-quartz). The phase β-ZnS is present in all concentrates and the other established phases are represented differently in the studied concentrates.

The results obtained are interpreted from the standpoint of receipt by roasting of an appropriate zinc calcine on the basis of its chemical and phase content. For this purpose a Web-based software system, developed by mathematicians and technologists from the Paisii Hilendarski University of Plovdiv, for calculating the charges of zinc concentrates at a fixed optimizing criterion was used. This enables appropriate mixture of materials to be processed during roasting of concentrates in fluidized bed furnace. This promotes obtaining of zinc calcine with minimum insoluble zinc ferrite and content of admixtures below certain technology requests.

Key words: ZnS, zinc concentrates, X-ray analysis, DTA and TGA, roasting.

INTRODUCTION

The synthesis and properties of pure ZnS [1–4] and ZnS doped with different impurities (P, Cu, Mn, Ag, Se, Te, etc.) [5–7] have been of interest for many years. This is due to the use of this sulfide in electronics, semiconductor equipment, optics, as a pigment, etc. [8–10]. Furthermore, iron ions are introduced into the crystal lattice of ZnS to obtain ZnS single-phase thin films showing ferromagnetism [11–13].

Zinc sulfide is essential zinc mineral in zinc ores [14]. Its two polymorphs are β-ZnS (Sphalerite) and α-ZnS (Wurtzite). Sphalerite is a typical hydrothermal mineral with cubic structure $F\bar{4}\,3m$, and tetrahedrally coordinated zinc and sulfur atoms. Wurtzite has hexagonal ($C6_3mc$) symmetry, usually stabilized by some Cd. It is a rare species.

Sphalerite is the common mineral in zinc ores. It almost always contains iron. Varieties with more than 6% Fe are named marmatite. Since marmatite has a brilliant black color like the black sphalerite, it very often goes unrecognized.

In addition to Fe, sphalerite in high-temperature deposits often contains Co, Cu, In, Sn and Se. Its impurities in low-temperature deposits are mainly Cd, Ga, Ge, Hg and Tl [14]. During the flotation of zinc ores, other mineral phases contribute Pb, SiO_2, Al_2O_3, CaO, MgO, Ni, As, Sb, Cl, F to the chemical composition of zinc concentrates.

Currently, during the incoming control of zinc concentrates in processing plants, about 20 components are analyzed to determine whether a raw material is suitable for the used technology [15].

Very often it turns out that chemical analysis alone is not sufficient to choose the most suitable conditions for the successive implementation of the process chain "roasting of zinc concentrates – calcine leaching – electrowinning of zinc". The main problem is the presence of increased contents of Fe, Pb and SiO_2. Iron in the zinc concentrates can be connected as FeS_2, $CuFeS_2$ or incorporated in the crystal lattice of ZnS [16–18]. During the oxidation of zinc concentrates in the temperature

* To whom all correspondence should be sent:
E-mail: boyanb@uni-plovdiv.bg

range 920–950 °C iron-containing sulfides oxidize and Fe_2O_3 is obtained. The iron (III) oxide forms ferrites with various metal oxides (mainly ZnO, obtained from the oxidation of ZnS). The formation of $ZnFe_2O_4$ [19–21] decreases the rate of leaching of zinc and necessitates further processing of the zinc-containing cake [22–24]. To reduce this unfavorable phenomenon, complete preliminary characterization of zinc concentrates is necessary.

Usually in practice various zinc raw materials are used simultaneously – often 5–6 zinc concentrates having different origins and chemical, phase and granulometric compositions. It is necessary to conduct a preliminary assessment of the possibilities for optimization of the technological process, by calculating and using appropriate charges from zinc-containing materials.

The aim of this study is to characterize most completely the Bulgarian and imported zinc sulfide concentrates by chemical, X-ray, differential thermal and thermogravimetric analysis and to use the obtained results for their optimal processing. This can be done using the Web-based expert system for calculating zinc concentrate charges [15, 25].

EXPERIMENTAL

Seven zinc sulfide concentrates from Bulgaria, Turkey, Greece, Morocco and Peru are studied.

The X-ray phase analysis of the concentrates was carried out with an apparatus "TUR-M62" (Dresden, Germany) equipped with a computer-controlled HZG-4 goniometer with Co-K_α radiation and Bragg-Brentano geometry. Data base (Powder Diffraction Files, Joint Committee on Powder Diffraction Standards, Philadelphia PA, USA, 1997) was used for the phase identification.

DTA and TGA (Q Derivatograph, Hungary) were carried out under the following conditions: sensitivity of DTA, 0.5 mV; DTG, 1 mV; TG, 100 mg; heating rate, 10° min^{-1}; sample mass 100 mg. A ceramic crucible was used. All the studies were performed in air medium.

A Web-based information system for calculation and prognosis of the chemical and phase composition of the mix proportions of concentrates is used [15, 25]. It is built on a modular principle using server programming language PHP. Its main modules provide opportunities for construction, management and use of Web-based database of zinc concentrates [15, 25] in the management control system relational database MySQL.

The used Web-based information system gives the following opportunities:

1. Input of the chemical composition of the used (available or in the process of being contracted to be purchased) zinc concentrates, each of which is allotted a name and a number. Thus the *main database* of the system is created. At present there are data entered for 67 concentrates with different origin (Bulgarian, Turkish, etc.).

2. From the data in the main database up to 15 concentrates can be used, with which a *working database* is created that serves for calculations.

3. With concentrates from the working database the following calculations can be made:

A) In *user mode* calculations are made at user-selected ratio of the concentrates in the working database. For that purpose the percentage share of each separate concentrate is specified, and the system calculates the composition of the charge from zinc concentrates of 18 components.

B) In *automatic mode* the system calculates charges that meet restrictive conditions with regard to 11 components that are selected together with experts in the field of zinc hydrometallurgy.

- In this specific case work was performed satisfying the following input restrictions (in mass %): Zn > 50; S – 31 ± 1%; Pb < 2.5; Fe < 9.0; SiO_2 < 2.5; Sb < 0.008; As < 0.12; MgO < 0.3; CaO < 0.5; F < 0.02; Ge < 30 g/t.
- Various step changes in iterations of the concentrates can be selected – from 1 to 15%.
- The content is calculated of each charge that meets the restrictive conditions and is presented under an appointed number.
- During oxidized roasting in a fluidized bed of the charge made out of zinc concentrates a zinc calcine is obtained that is extracted using solutions of sulfuric acid.
- On the basis of data from literature, own studies and experience from practice coefficients are offered with which, based on the chemical composition of the charge, calculations are made for the prognostic chemical and phase composition of the calcine.
- When more than one charge is obtained an optimization criterion is used according to which the charges are ranked in descending or ascending order.
- For the optimization criterion in this study "Zinc soluble in 7% solution of sulfuric acid" is used.
- The aim is to select a charge with maximum soluble zinc in a 7% solution of sulfuric acid so that the extraction of the calcine can be carried out at the best technical and economical indices. All calculated charges are arranged in descending order according to this technical index.
- The system also allows the use of other optimization criteria – minimal quantity of obtained zinc ferrite, maximum percentage of zinc in the charge, minimal prime cost of the charge, etc.

RESULTS AND DISCUSSION

Chemical composition

The chemical composition of the studied zinc concentrates is presented in Table 1.

Most concentrates show high content of Pb and SiO_2. Improper mixing of such concentrates can lead to partial aggregation of calcine and increase of the sulfide sulfur in it. Iron is particularly undesirable in terms of ferrite formation. Its harmful effects may be limited by appropriate selection of a charge, well balanced in its chemical composition. Especially unfavorable in terms of As and Sb are the concentrates with numbers 5 and 6. The strong harmful influence of these components in zinc electrowinning from zinc sulfate solutions is well known, as well as all the negative consequences [26].

X-ray phase analisis

Sphalerite (β-ZnS) is the main phase in sulfide zinc concentrates. This shows that in terms of the process of oxidative roasting the majority of zinc will form oxide, which is favorable for the calcine leaching.

At the same time it can be argued with some probability that in all concentrates the phase marmatite (nZnS.mFeS) is observed. The crystal lattice of ZnS can include different amounts of iron [27–29]. Co-oxidation of zinc and iron sulfide at 920–950 °C leads to the formation of zinc ferrite that goes directly into the cake after zinc leaching. The Zn content in the cake is in the range of 15–17% the major part of which is due to the ferrite.

The studied zinc concentrates were subjected to X-ray analysis to determine their phase composition. The resulting X-ray diffraction patterns are presented in Figure 1 and summarized in Table 2.

DTA and TGA study

The obtained DTA and TGA curves are combined into general graphs (Figs. 2 and 3). The observed exothermic effects in the temperature range of 450–500 °C are due to oxidation of iron and copper sulfides ($CuFeS_2$, FeS_2). These effects are best

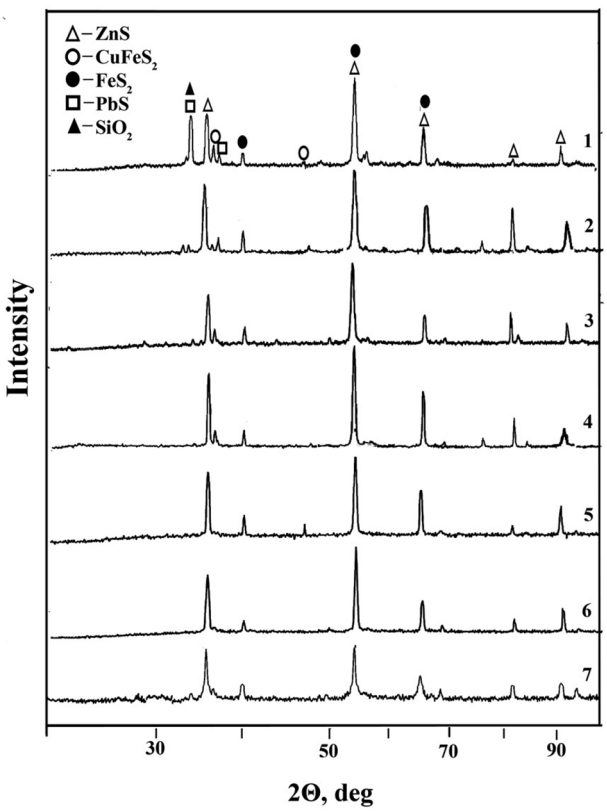

Fig. 1. X-ray diffraction patterns of studied zinc sulfide concentrates: Bulgaria (1, 2), Turkey (3, 4), Greece (5), Morocco (6), Peru (7)

Table 1. Chemical composition of sulfide zinc concentrates from Bulgaria (1, 2), Turkey (3, 4), Greece (5), Morocco (6), Peru (7)

Component	Content (mass %)						
	1	2	3	4	5	6	7
Zn	51.10	54.60	47.45	53.65	53.57	51.19	54.60
S	31.60	30.30	34.50	31.50	32.50	33.20	32.40
Fe	8.20	6.45	9.75	3.58	8.85	11.90	8.95
Pb	2.85	1.60	0.65	4.28	1.06	0.67	0.61
SiO_2	2.25	4.30	3.30	3.58	0.95	0.66	1.75
Cu	1.96	1.02	2.06	0.63	0.27	0.68	0.38
Cd	0.29	0.28	0.23	0.25	0.30	0.10	0.09
As	0.002	0.005	0.05	0.029	1.02	0.099	0.028
Sb	0.001	0.001	0.002	0.003	0.02	0.002	0.001
Co	0.006	0.027	0.006	0.012	0.001	0.006	0.006
Ni	0.002	0.002	0.002	0.002	0.002	0.001	0.002
CaO	0.38	0.54	0.43	0.19	0.30	0.42	0.41

Table 2. Results from X-ray phase analysis of zinc concentrates

№	Phases						
	1	2	3	4	5	6	7
1.	β – ZnS	β – ZnS	β – ZnS	β – ZnS	β – ZnS	β – ZnS	β – ZnS
2.	(nZnS.mFeS)	(nZnS.mFeS)	(nZnS.mFeS)	(nZnS.mFeS)	(nZnS.mFeS)	(nZnS.mFeS)	(nZnS.mFeS)
3.	FeS_2		FeS_2		FeS_2		
4.	$CuFeS_2$	$CuFeS_2$	$CuFeS_2$	$CuFeS_2$		$CuFeS_2$	
5.	SiO_2 (α-кварц	SiO_2 (α-кварц)		SiO_2 (α-кварц)			SiO_2 (α-кварц)
6.	PbS	PbS	PbS	PbS		PbS	

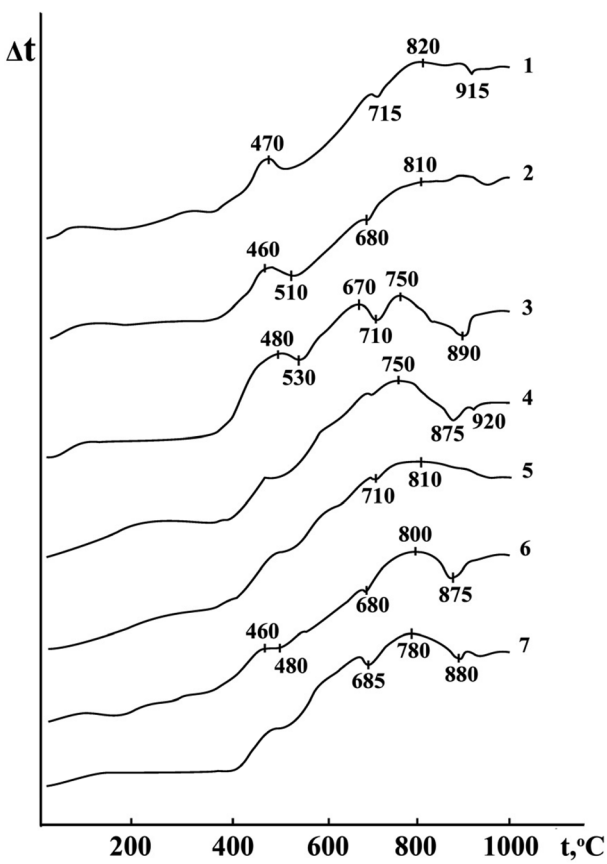

Fig. 2. DTA curves of the studied zinc concentrates

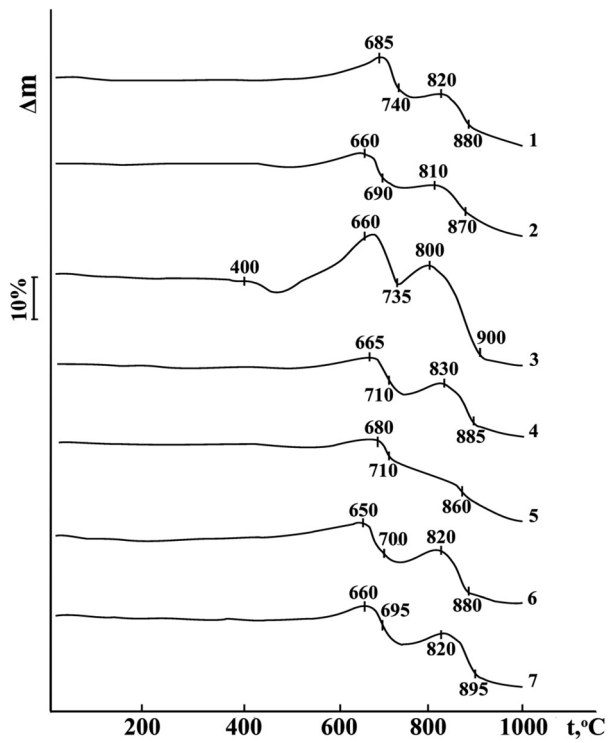

Fig. 3. TGA curves of the studied zinc concentrates

observed and are relatively intense in concentrates 1, 2 and 3, which is an indirect confirmation that they have separate phases of iron and copper. The X-ray study of concentrate 5 shows the presence of a FeS_2 line, but in the DTA curve 5 has no clear exothermic effect, which indicates that the content of pyrite in the concentrate is low.

In the other concentrates, well-expressed exothermic effects, corresponding to the oxidation of the shown copper and iron sulfides were not observed. The shown weak endothermic effects at 670–700 °C are due to dissociation of the obtained in small quantities $FeSO_4$ and $CuSO_4$. The most intensive exothermic effect is the one caused by the intensive oxidation of ZnS at 750–820 °C.

The differences observed in the zinc solubility from calcines, obtained under different conditions of roasting can be explained using the terminology introduced by us: "primary" $ZnFe_2O_4$, obtained by oxidation of marmatite and "secondary" $ZnFe_2O_4$, formed as a result of solid state interaction of ZnO (from oxidation of β-ZnS) and Fe_2O_3 (by oxidation of FeS_2). Roasting conditions influence

Table 3. Results from the calculation of zinc concentrate charges and chemical and phase composition of the best charge and prognostic calcine

Charge composition from concentrate N and % of it								
Conc.1	Conc.2	Conc.3	Conc.4	Conc.5	Conc.6	Conc.7		
20	10	5	20	5	20	20		
Calculated chemical composition of charge, mass %								
Zn	S	Fe	SiO_2	Pb	Cu	Cd	As	Sb
52.61	32.12	8.36	2.29	1.93	0.95	0.20	0.086	0.003
Co	Ni	CaO	MgO	Al_2O_3	Cl	F	Ge	Tl
0.011	0.002	0.37	0.20	0.34	0.008	0.009	8 g/t	7 g/t
Prognostic chemical composition of zinc calcine, mass %								
Zn	S	Fe	SiO2	Pb	Cu	Cd	As	Sb
60.47	2.95	9.61	2.63	2.22	1.09	0.23	0.098	0.003
Co	Ni	CaO	MgO	Al2O3	Cl	F	Ge	Tl
0.012	0.002	0.43	0.23	0.39	0.009	0.011	9 g/t	8 g/t

Prognostic phase composition of zinc calcine, mass %			
Zn (oxide + silicate)	52.34	Zn_{H2O}	2.72
Zn (ferrite)	4.80	Fe (ferrite)	9.41
Zn (sulphate)	2.72	Fe (oxide + silicate)	0.19
Zn (sulphide)	0.60	Pb (sulphate)	1.77
$Zn_{H_2SO_4}$	55.06	Pb (sulphide)	0.44

mainly the formation of "secondary" $ZnFe_2O_4$, while being a negligible factor in the formation of "primary" $ZnFe_2O_4$.

Calculation of charges

The abovementioned Web-based expert system [15, 25] was used for calculating the optimal charges of the studied zinc concentrates. The Bulgarian 2 and Peruvian 7 concentrates were considered to be the principal ones in the charge calculation, based on available and contractual quantities of zinc concentrates for a long time period.

Best charge was obtained at the ratio of concentrates given in Table 3. Zinc, dissolved in 7% H_2SO_4 solution (Zn as oxide, sulphate and silicate) makes up 91.06% of the total zinc in it. This is a very high percentage and the indexes of neutral and acid leaching will be very high if the technological parameters are obeyed.

The calculated charges of zinc concentrates that meet the specified requirements are 36. They have zinc, soluble in 7% solution of sulfuric acid, in the range 90.40–91.06%. This allows to vary the choice of charge depending on the quantities of concentrates.

The results show that the use of the Web-based expert system gives very good results concerning composition of the charge and quality of the obtained calcine. The system also allows optimization on economic criteria, when the concentrate prices are known.

CONCLUSIONS

1. X-ray, differential thermal and thermogravimetric analysis of 7 Bulgarian and imported zinc sulphide concentrate are made.

2. The relationship between the phase composition and type of the obtained DTA and TG curves is shown, highlighting the influence of FeS_2 and $CuFeS_2$ phases on the mass change of samples and allowing the opportunity to establish the presence of these phases in concentrates on the basis of the TG curves obtained.

3. Calculations based on the Web-based information system allow optimization of the composition of zinc concentrate charges. From all studied concentrates a charge is recommended in which zinc, soluble in 7% H_2SO_4 solution constitutes 91.06% of the total zinc in accordance with 11 restrictive conditions for obtaining high quality calcine in terms of its hydrometallurgical processing.

Acknowledgments: *This study was conducted with financial help through the project NI11-CD-007 of Paisii Hilendarski Plovdiv University.*

REFERENCES

1. R. Vacassy, S. M. Scholz, J. Dutta, C. J. G. Plummer, R. Houriet, H. Hofmann, *Journal of the American Ceramic Society*, **81**, 2699 (1998).
2. M. Bouroushian, Electrochemistry of Metal Chalcogenides, Springer-Verlag Berlin Heidelberg, 2010.
3. T. Kanniainen, Studies of Zinc and Lead Chalcogenide Thin Films Grown by SILAR (Successive Ionic Layer Adsorption and Reaction) Technique, University of Helsinki, 2001, ISBN 952-91-3895-4 (Print), ISBN 952-10-0155-0 (PDF)
4. Y. Ding, X. D. Wang, Z. L. Wang, *Chemical Physics Letters*, **398**, 32 (2004).
5. C. F. Wang, H. Bo, H. H. Yi, W. B. Li, *Optics & Laser Technology*, **43**, 1453 (2011).
6. J. Liu, C. Zhao, Z. Li, J. Chen, H. Zhou, S. Gu, Y. Zeng, Y. Li, Y. Huang, *Journal of Alloys and Compounds,* **509**, 9428 (2011).
7. P. Yang, M. Lu, D. Xu, D. Yuan, G. Zhou, *Chemical Physics Letters*, **336**, 78 (2001).
8. Z. Zhao, F. Geng, H. Cong, J. Bai, H.M. Cheng, *Nanotechnology*, **17**, 4731 (2006).
9. W. Q. Peng, G. W. Cong, S. C. Qu, Z. G. Wang, *Optical Materials*, **29**, 313 (2006).
10. Y. F. Nicolau, M. Duouy, M. Brunel, *Journal of the Electrochemical Society*, **137**, 2915 (1990).
11. P. P. Chin, J. Ding, J. B. Yi, B. H. Liu, *Journal of Alloys and Compounds*, **390**, 255 (2005).
12. O. Khani, H. R. Rajabi, M. H. Yousefi, A. A. Khosravi, M. Jannesari, M. Shamsipur, *Spectrochimica Acta – Part A: Molecular and Biomolecular Spectroscopy*, **79**, 361 (2011).
13. F. Zhu, S. Dong, G.Yang, *Optoelectronics and Advanced Materials – Rapid Communications*, **4**, 2072 (2010).
14. I. Kostov, Mineralogy, Nauka i Izkustvo, Sofia, 1973 (in Bulgarian).
15. B. S. Boyanov, M. P. Sandalski, K. I. Ivanov, *World Academy of Science, Engineering and Technology*, **73**, 420 (2011).
16. B. S. Boyanov, R. I. Dimitrov, Z. D. Zivkovic, *Thermochimica Acta*, **269**, 123 (1997).
17. R. I. Dimitrov, N. Moldovanska, I. K. Bonev, Z. Zivcovic, *Thermochimica Acta*, **362**, 145 (2000).
18. Z. D. Zivkovic, D. Zivkovic, D. Grujicic, N. Strbac, V. Savovic, *Journal of Thermal Analysis*, **54**, 35 (1998).
19. T. T. Chen, J. E. Dutrizac, *JOM*, **56**, 46 (2004).
20. R. Hansson, P.C. Hayes, E. Jak, *Metal. Meter. Trans. B, Process Metallurgy and Materials Processing Science*, **36**, 179 (2005).
21. B. S. Boyanov, R. I. Dimitrov, *Journal of Mining and Metallurgy*, **33** (1B) 95 (1997).
22. V. N. Ramachandra Sarma, K. Deo, A. K. Biswas, *Hydrometallurgy*, **2**, 171 (1976).
23. H. Takala, *Erzmetall: Journal for Exploration, Mining and Metallurgy*, **52**, 37 (1999).
24. J. Krueger, R. Puellenberg, *Erzmetall: Journal for Exploration, Mining and Metallurgy*, **34**, 380 (1981).
25. M. P. Sandalski, B. S. Boyanov, P. G. Georgiev, A. K. Sotirov, Proceedings of 42nd International October Conference of Mining and Metallurgy, S. Ivanov, D. Zivkovic (eds.), University of Belgrade – Technical Faculty in Bor, 2010, p. 569.
26. J. C. Balarni, L. d. O. Poli, T. L. S. Miranda, R. M. Z. d. Castro, A. Salum, *Minerals Engineering*, **21**, 100 (2008).
27. K. Wright, J. D. Gale, *Geochimica et Cosmochimica Acta*, **74**, 3514 (2010).
28. E. G. Osadchii, Y. E. Gorbaty, *Geochimica et Cosmochimica Acta*, **74**, 568 (2010).
29. S. Kharbish, *Physics and Chemistry of Minerals*, **34**, 551 (2007).

РЕНТГЕНОФАЗОВ, DTA И TG АНАЛИЗ НА СУЛФИДНИ ЦИНКОВИ КОНЦЕНТРАТИ И ИЗСЛЕДВАНЕ ТЯХНОТО ПЪРЖЕНЕ В ПЕЩ С КИПЯЩ СЛОЙ

Б. С. Боянов, А. Б. Пелтеков

Пловдивски университет „Паисий Хилендарски“, катедра „Химична технология“, ул. „Цар Асен“ № 24, Пловдив, България

Постъпила на 20 март, 2012 г.; приета на 17 април, 2012 г.

(Резюме)

България е основен производител на цинк в Централна и Източна Европа (около 100 000 тона годишно). Двата цинкови завода в КЦМ АД, Пловдив и ОЦК ЕООД, Кърджали доставят необходимите суровини от България и чужбина.

В тази връзка, 7 български и вносни цинкови концентрати бяха изследвани с използване на химичен, рентгенофазов анализ, ДТА и ТГА. В тях са установени следните фази: β-ZnS; nZnS.mFeS; $CuFeS_2$; PbS; SiO_2 (α-кварц). Фазата β-ZnS присъства във всички концентрати, а другите фази са представени в различна степен в изследваните концентрати.

Получените резултати са интерпретирани от гледна точка на получаване на подходяща цинкова угарка при пърженето съгласно нейния химичен и фазов състав. За тази цел е използвана Web-базирана програмна система, разработена от математици и технолози от Пловдивския университет „Паисий Хилендарски“ за изчисляване на шихти от цинкови концентрати при използване на определен оптимизиращ критерий. Това позволява по време на пърженето на концентратите в пещ с кипящ слой да се преработват подходящи по състав шихти. Това допринася за получаване на цинкова угарка с минимално количество неразтворим цинков ферит и съдържание на примесни компоненти съгласно определени технологични изисквания.

Bulgarian Chemical Communications, Volume 44, Proceedings of the III[rd] National Crystallographic Symposium (pp. 24–29) 2012

Preparation and investigation of nanodimensional nickel ferrite

Z. P. Cherkezova-Zheleva[1]*, K. L. Zaharieva[1], V. S. Petkova[2],
B. N. Kunev[1], I. G. Mitov[1]

[1] *Institute of Catalysis, Bulgarian Academy of Sciences, "Acad. G. Bonchev" St., Bl. 11, 1113 Sofia, Bulgaria*
[2] *Institute of Mineralogy and Crystallography, Bulgarian Academy of Sciences, Acad. G. Bonchev St., Block 107, 1113 Sofia, Bulgaria*

Received April 27, 2012; Revised May 4, 2012

Nickel ferrites with different Ni content – $Ni_xFe_{3-x}O_4$, $0 \leq x \leq 1$ are technologically important materials for microwave, electronic and magnetic storage devices. These materials are members of solid solution series of spinel-type materials (Fe_3O_4–$NiFe_2O_4$) having specific magnetic properties and different degree of electron delocalization. They demonstrate good gas sensing properties and catalytic activity in various catalytic processes, such as complete oxidation of waste gases, oxidative dehydrogenation of hydrocarbons, decomposition of alcohols etc. Up today, much attention has been paid to the preparation of such nanocrystalline materials, because of difficulty of their synthesis procedures and special techniques used. However the problem is still topical. The nickel contained ferrite materials $Ni_xFe_{3-x}O_4$ (x=0.25, 0.5, 1) were prepared by co-precipitation method using $FeCl_3 \cdot 6H_2O$, $FeCl_2 \cdot 4H_2O$ and $NiCl_2 \cdot 6H_2O$ as precursors in our previous investigations. But small quantities of intermediate phase – FeOOH was obtained in synthesized material. So the aim of the study is to find cheap and easy way for preparation of nano-sized magnetite-type materials. In order to prepare single phase spinel material thermogravimetric, differential thermogravimetric and differential thermal analysis (TG, DTG and DTA), as well as different chemical and structural studies such as X-ray diffraction (XRD), Moessbauer spectroscopy, were done. As a result of investigation the appropriate preparation conditions are obtained. The synthesis procedure includes combination of co-precipitation combined with low temperature thermal treatment of materials.

Key words: nickel ferrites, nano-sized powders, low temperature theatment, thermal analysis, Moessbauer spectroscopy, X-ray diffraction analysis.

INTRODUCTION

Preparation of high-quality magnetic nanoparticles with a narrow size distribution, reproducible physical properties and production with short processing times is one of the key issues in nanoparticle research today. Recent studies have also focused on the development of novel synthesis techniques for the production of uniform magnetic oxide materials [1]. Nanoparticles with controlled sizes and properties can be synthesized by wet chemical techniques [2]. It is known that the crystal size is related to the relative interdependence between the nucleation and growth steps, which in turn can strongly be affected by the solution chemistry and precipitation conditions [3].

Nanosized $NiFe_2O_4$ is one type of ferrite that has been studied intensively. It shows peculiar structural and magnetic properties. Small particle size promotes a mixed spinel structure whereas the bulk form is an inverse spinel. As far as the magnetic properties of these materials are concerned, spin glass like behavior can be considered as the most interesting property that leads to high field irreversibility, shift of the hysteresis loops, and anomalous relaxation dynamics [4]. The properties of ferrite particles are influenced by the composition and microstructure, which are sensitive to the preparation methodology used in their synthesis [5]. The magnetic and the electrical properties of ferrites are reported to be highly sensitive to the cation distribution, which in turn depend on the material of synthesis and sintering conditions [1]. The catalytic properties of spinels containing transition metal ions are dependent on the redox properties of substituting ions and on their distribution among the octahedral and tetrahedral coordination sites. The surface of

* To whom all correspondence should be sent:
E-mail: zzhel@ic.bas.bg

spinel oxide powders contains mainly octahedral sites and, consequently, its catalytic activity is crucially related to the octahedral cations [6].

The main direction of our present research is to obtain a single phase nano-sized nickel ferrites $Ni_xFe_{3-x}O_4$ (x=0.25, 0.5, 1) promising as catalyst and magnetic material. In order to obtain this ferrite material will be made low temperature treatment at different temperatures of nickel contained ferrite sample produced by chemical co-precipitation procedure. The structural properties of samples at each stage of the synthesis are studied using the following methods as Thermal analysis, X-ray diffraction analysis, Moessbauer spectroscopy.

EXPERIMENTAL

The nickel contained ferrite samples: *Sample A* – $Ni_xFe_{3-x}O_4$ (x=0.25) *Sample B* – $Ni_xFe_{3-x}O_4$ (x=0.5) and *Sample C* – $Ni_xFe_{3-x}O_4$ (x=1) were produced using chemical co-precipitation method described in details previously [7]. Dried brown ferrite powders were investigated by using several methods for characterization.

The thermal analysis as TG, DTG and DTA are obtained with a "Stanton Redcroft" (England) installation equipped with a PC. The 10.00 mg prepared nickel contained ferrite samples are heating in the temperature range 20–1000 °C at 10 °C/min heating rate in stabilized corundum crucible and air medium with flow – 1l/h.

Moessbauer measurements were carried out with apparatus Wissenschaftliche Elektronik GmbH, working with a constant acceleration mode, $^{57}Co/Cr$ source, α-Fe standard. The computer fitting was used to determine the parameters of hyperfine interactions of Moessbauer spectral components: isomer shift (IS), quadrupole splitting (QS), hyperfine effective magnetic field in the site of iron nuclei (H_{eff}), line widths (FW) and component relative weights (G).

X-ray diffraction (XRD) patterns of the nanostructured nickel ferrite samples during the synthesis were performed with a TUR M62 apparatus with computer management and data collection, working with HZG-4 goniometer and CoKα radiation. The presence of the phases was determined with JCPDS database (Powder Diffraction Files, Joint Committee on Powder Diffraction Standards, Philadelphia PA, USA, 1997). Scherrer equation was used to made calculation of the average crystallite size, lattice microstrain parameter and unit cell parameter of the ferrite samples [8].

The effect of thermal treatment of the nickel contained ferrites is investigated for different times and at different temperatures in argon medium in the furnace "Eurotherm", England.

RESULTS AND DISCUSSION

Series of nickel contained ferrite samples with different stoihiometry $Ni_xFe_{3-x}O_4$ (x=0.25, 0.5 and 1) were produced using co-precipitation procedure [7]. These materials are members of solid solution series of spinel materials Fe_3O_4–$NiFe_2O_4$ and different degree of incorporation of Ni metal ion in the magnetite host matrix is expected. Physicochemical characterization of materials shows their ultradisperse character. However small quantities of intermediate oxihydroxide phase (FeOOH) was also obtained in

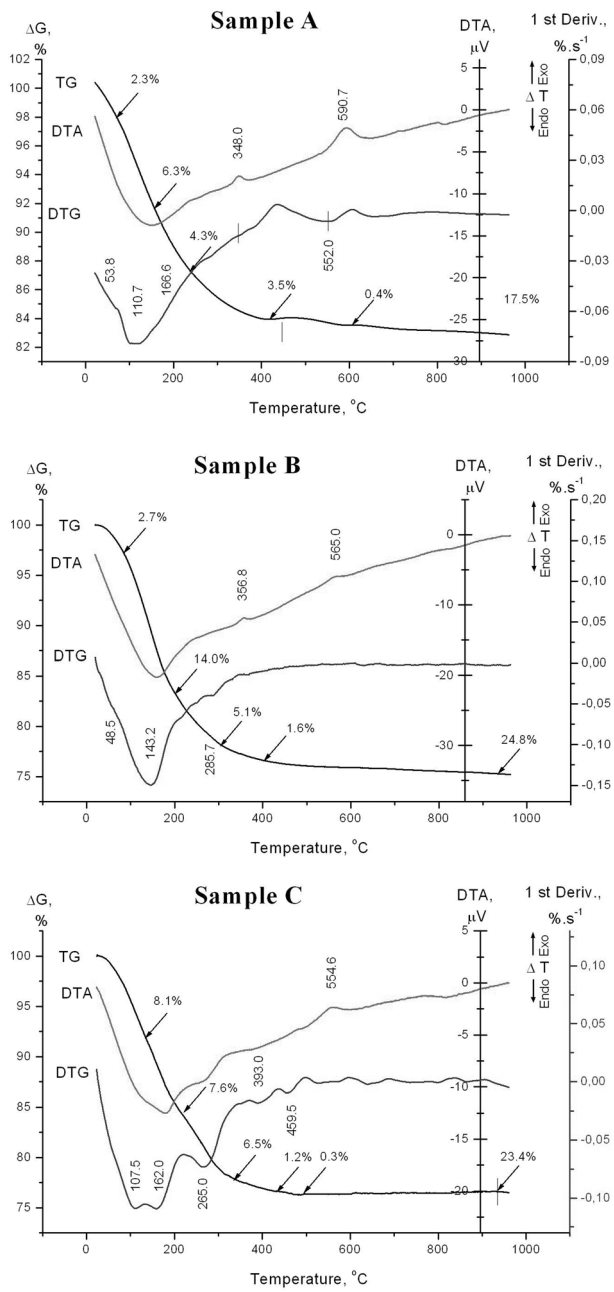

Fig. 1. TG, DTG and DTA curves of synthesized nickel contained ferrite samples

all samples, due to incompletely realized synthesis process. In order to prepare single phase material number of initial analysis are carried out. The behaviour of synthesized ferrite materials during the thermal treatment gives results concerning the further investigations about effect of calcinations as the dehydration and dehydrogenation temperatures and crystallisation processes (see Fig. 1).

Moessbauer spectra of the studied samples after thermal treatment are presented on Figure 2. In all three cases the spectra represent superposition of sextet-type lines only. The spectra are fitted by the CONFIT program using several models for the fitting procedures. The best spectra fit show the presence of two or three sextuplet components in all registered spectra. The calculated Moessbauer parameters are shown in Table 1. The obtained hyperfine parameter values of these components show presence of tetrahedrally coordinated Fe^{3+} ions in a spinel phase – Sxt1 and octahedrally coordinated Fe^{3+} ions in a spinel phase – Sxt2. The calculated hyperfine parameter values of the third sextet component (Sxt 3) show the presence of octahedrally coordinated iron ions in third oxidation degree, which are included in the α-Fe_2O_3 (Hematite) phase [9]. With an increase of Ni content, the relative weight of hematite phase decreases and in the case of *Sample C* only octahedrally and tetrahedrally coordinated iron ions in spinel structure are detected [10].

Figure 3 shows the XRD patterns of nickel contained ferrite materials after thermal analysis. The formation of the non-stoichiometric spinel ferrite phase $Ni_xFe_{3-x}O_4$ (PDF-10-0325; 75-0449) and different amount of hematite α-Fe_2O_3 phase (PDF-73-2234) are observed in the *Sample A* – $Ni_{0.25}Fe_{2.75}O_4$ and *Sample B* – $Ni_{0.5}Fe_{2.5}O_4$ respectively. Diffraction peaks due to single phase cubic spinel ferrite $NiFe_2O_4$ (PDF-10-0325) are indexed in the *Sample C* – $NiFe_2O_4$. The sharp and broad lines in the three XRD patterns indicate the presence of highly dispersed particles and high crystallinity of the synthesized ferrite materials. The average particle size, lattice microstrain parameter and unit cell parameter of studied spinel phase was calculated by

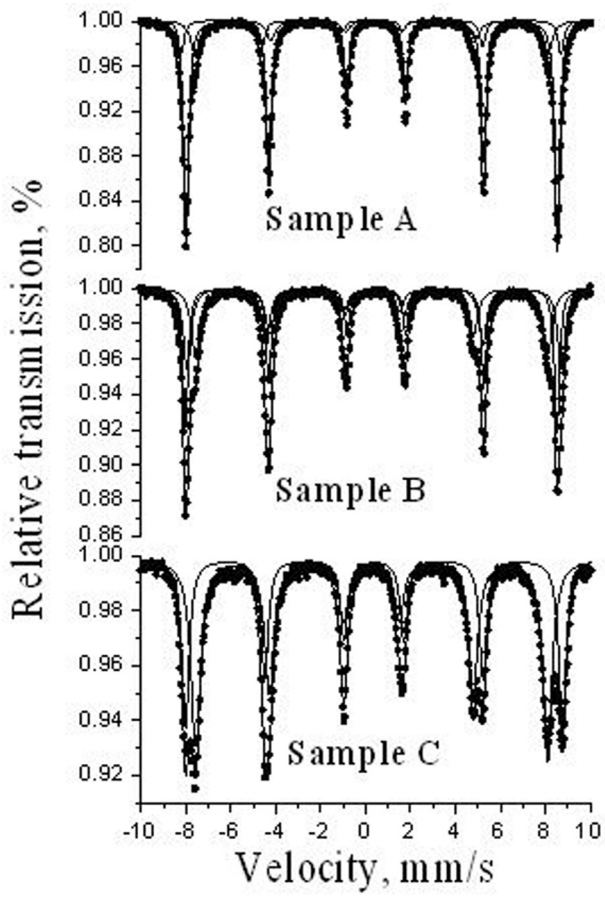

Fig. 2. Moessbauer spectra of synthesized nickel contained ferrite materials after thermal analysis

Scherrer equation [8]. The obtained values can be seen in Table 2. It can be seen that the mean crystallite size of spinel ferrite particles is about 20–35 nm. The obtained results for the presented phases and their relative weights in studied samples are in very good agreement with Moessbauer data.

On the base of the obtained results, thermal behavior of investigated materials is resolved. Three stages of weight loss in the TG curves are established (Fig. 1). The main mass losses – 8.6%, 15.7%

Table 1. Moessbauer parameters of samples after DTA

Sample	Components	IS, mm/s	QS, mm/s	H_{eff}, T	FMHW, mm/s	G, %
Sample A – after DTA	Sxt 1 – Fe^{3+}_{tetra}	0.34	–0.03	48.2	0.47	20
	Sxt 2 – Fe^{3+}_{octa}	0.20	–0.02	51.6	0.32	17
	Sxt 3 – Hematite Fe^{3+}	0.37	–0.20	51.4	0.28	63
Sample B – after DTA	Sxt 1 – Fe^{3+}_{tetra}	0.37	–0.01	48.5	0.41	35
	Sxt 2 – Fe^{3+}_{octa}	0.26	–0.01	51.8	0.47	33
	Sxt 3 – Hematite Fe^{3+}	0.37	–0.19	51.3	0.28	32
Sample C – after DTA	Sxt 1 – Fe^{3+}_{tetra}	0.37	0	48.7	0.37	49
	Sxt 2 – Fe^{3+}_{octa}	0.25	0.01	52.2	0.43	51

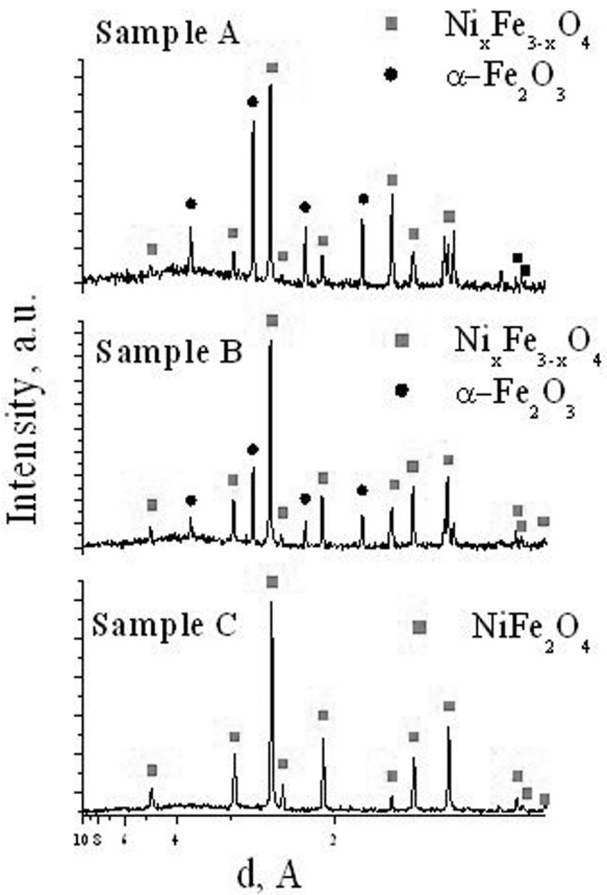

Fig. 3. XRD patterns of synthesized nickel contained ferrite materials after thermal analysis

and 16.7% results from dehydration process. The presence of endothermic peak in the temperature region 20–200 °C is related to remove of water molecules coordinated in crystal lattice. The exothermic effects at 348.0°C, 356.8°C of the ferrite materials *Sample A* – $Ni_{0.25}Fe_{2.75}O_4$ and *Sample B* – $Ni_{0.5}Fe_{2.5}O_4$ in the DTA curves and weight losses 7.8%, 5.1% and 6.5% are assigned to the thermal transformation of intermediate phase β-FeOOH and formation of hematite phase α-Fe_2O_3 respectively [11–14]. A high presence of hematite due to a low content of nickel in spinel ferrite $Ni_{0.25}Fe_{2.75}O_4$ explains the more intensive exothermic peak at 348.0 °C compared with this one at 356.8 °C for $Ni_{0.5}Fe_{2.5}O_4$. The absence of exothermic effect around this temperature in the thermal behavior of ferrite material *Sample C* – $NiFe_2O_4$ is connected with the presence of single spinel ferrite phase only. The registered DTA thermograms of all studied samples show the second exothermic peak at 590.7 °C, 565.0 °C and 554.6 °C, respectively. It can be attributed to formation and crystallization of nickel ferrite phase in all prepared ferrite samples.

In order to prepare single phase materials the co-precipitated samples have to be heated in inert atmosphere to avoid oxidation. The interpretation of the above presented thermal analysis data gives as a result the appropriate temperature of heating 300 °C. The crystal water from the materials is dehydrated at temperatures lower than 300 °C and therefore the synthesis of ferrites below this temperature can be done. The lowest temperature to start the synthesis in isothermal conditions is 300 °C. A fresh reaction surface is formed, during the process of dehydration. Getting a fresh reactive surface and the heating in the inert atmosphere, are a basics for the synthesis of ferrite compounds. Figure 4 presents the X-ray diffraction pattern of *Sample B* – $Ni_{0.5}Fe_{2.5}O_4$

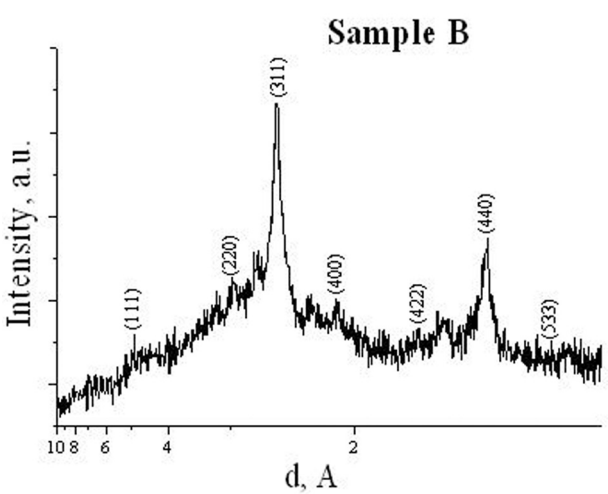

Fig. 4. XRD pattern of *Sample B* – $Ni_{0.5}Fe_{2.5}O_4$ after heating at 300 °C in argon media

Table 2. Calculated values of mean crystallite size (D), lattice strain (e) and unite cell parameter (a) of spinel ferrite phase

Sample	D, nm	e, a.u	a, A
$Ni_{0.25}Fe_{2.75}O_4$	21	$3{,}5.10^{-3}$	8.34
$Ni_{0.5}Fe_{2.5}O_4$	28	$2{,}4.10^{-3}$	8.33
$NiFe_2O_4$	34	$0{,}7.10^{-3}$	8.31

after heating at 300 °C in inert atmosphere (Ar media) as an example. It clearly shows the preparation of ultra dispersed single phase spinel material. The exact composition of sample will be established by chemical analysis, but all studied materials are members of solid solution series Fe_3O_4 (PDF-75-0449) – $NiFe_2O_4$ (PDF-10-0325). The presence of single phase composition shows the incorporation of Ni^{2+} ions in the magnetite host matrix.

CONCLUSIONS

Physicochemical characterization of prepared by co-precipitation procedure series of ferrite materials with different stoichiometry $Ni_xFe_{3-x}O_4$ (x = 0.25, 0.5, 1) are carried out using different techniques. The DTA-TG study and the obtained analysis results show the dehydration and dehydrogenation temperatures and crystallisation processes, as well as the appropriate conditions for preparation of single phase materials. High dispersion and nano-size particles is registered in all studied samples. The studied materials are members of solid solution series of magnetite-type materials (Fe_3O_4). With increasing of Ni-content in materials increasing of particle size is obtained. The low temperature thermal treatment at 300 °C in argon media leads to production of single phase spinel nickel ferrite material.

Acknowledgements: *The financial support by the Bulgarian National Science Fund at the Ministry of Education and Science – Project DO 02-295/2008 is gratefully appreciated.*

REFERENCES

1. C. Venkataraju, G. Sathishkumar, K .Sivakumar, *Journal of Magnetism and Magnetic Materials*, **322**, 230 (2010).
2. J. C. Aphesteguy, S. E. Jacobo, N. N. Schegoleva, G. V. Kurlyandskaya, *Journal of Alloys and Compounds*, **495**, 509 (2010).
3. Y. Cedeño-Mattei, O. Perales-Pérez, *Microelectronics Journal*, **40**, 673 (2009).
4. A. Ceylan, S. Ozcan, C. Ni, S. I. Shah, *Journal of Magnetism and Magnetic Materials,* **320**, 857 (2008).
5. J. Jiang, Y.-M. Yang, *Materials Letters*, **61**, 4276 (2007).
6. A. S. Albuquerque, M. V. C. Tolentino, J. D. Ardisson, F. C. C. Moura, R. de Mendonça, W. A. A. Macedo, *Ceramics International*, **38** (9), 2225 (2012).
7. Z. Cherkezova-Zheleva, K. Zaharieva, B. Kunev, M. Shopska, I. Mitov, in: Nanoscience & Nanotechnology, E. Balabanova and I. Dragieva (eds.), vol. 12, Prof. Marin Drinov Academic Publishing House, Sofia, 2012, in press.
8. U. Schwertmann, R. Cornell, Iron Oxides in the Laboratory, Weinheim, New York-Basel-Cambridge, 1991.
9. V. Rusanov, R. G. Gilson, A. Lougear, A. X. Trautwein, *Hyperfine Interactions*, **128**, 353 (2000).
10. Y. Sui, W.-H. Su, F.-L. Zheng, D.-P. Xu, *Materials Science and Engineering*, **A286**, 115 (2000).
11. D. Thickett, M. Odlyha, *Journal of Thermal Analysis and Calorimetry*, **80**, 565 (2005).
12. S. A. Kahani, M. Jafari, *Journal of Magnetism and Magnetic Materials*, **321**, 1951 (2009).
13. S. Musić, S. Krehula, S. Popović, *Materials Letters,* **58**, 444 (2004).
14. M. D. Meroño, J. Morales, J. L. Tirado, *Thermochimica Acta*, **92**, 525 (1985).

СИНТЕЗ И ИЗСЛЕДВАНЕ НА НАНОРАЗМЕРЕН НИКЕЛОВ ФЕРИТ

З. П. Черкезова-Желева[1]*, К. Л. Захариева[1], В. Петкова[2],
Б. Н. Кунев[1], И. Г. Митов[1]

[1] Институт по катализ, Българска академия на науките, ул. „Акад. Г. Бончев“, бл.11, 1113 София, България
[2] Институт по минералогия и кристалография, Българска академия на науките, ул. „Акад. Г. Бончев“, бл. 107, 1113 София, България

Постъпила на 27 април, 2012 г.; приета на 4 май, 2012 г.

(Резюме)

Никеловите ферити с различно съдържание на никел – $Ni_xFe_{3-x}O_4$, $0 \leq x \leq 1$ са технологично важни материали за микровълнови, електронни и магнитни запомнящи устройства. Тези материали са представители на серия от твърди разтвори на шпинелов тип материали (Fe_3O_4–$NiFe_2O_4$), имащи специфични магнитни свойства и различна степен на електронна делокализация. Те показват добри газ-детекторни свойства и висока каталитична активност в различни процеси като пълно окисление на отпадъчни газове и летливи органични съединения, окислително дехидрогениране на въглеводороди, разлагане на алкохоли и др. Понастоящем голямо внимание се отделя на получаването на такива нанокристални материали. Проблемът все е още актуален поради редица трудности при техния синтез и използването на специални техники. Никел-съдържащи феритни материали $Ni_xFe_{3-x}O_4$ (x=0.25, 0.5, 1) са получени по метода на утаяване с използване на $FeCl_3 \cdot 6H_2O$, $FeCl_2 \cdot 4H_2O$ и $NiCl_2 \cdot 6H_2O$ като прекурсори в наши предишни изследвания. Но в синтезираните материали са регистрирани малки количества междинна фаза – FeOOH. Цел на изследването е да се намери евтин и лесен начин за получаването на наноразмерни материали от магнетитов тип. С цел да се получат еднофазни шпинелни материали са проведени термогравиметричен, диференциален термогравиметричен и диференциален термичен анализ, както и различни химични и структурни изследвания като рентгенова дифракция и Мьосбауерова спектроскопия. В резултат на изследването са намерени подходящите условия на получаване. Синтезът включва процес на утаяване, комбинирано с ниско температурна термична обработка на материалите.

Bulgarian Chemical Communications, Volume 44, Proceedings of the III[rd] National Crystallographic Symposium (pp. 30–36) 2012

Adsorption capacity of modified metallurgical slag

S. V. Dimitrova[1], I. K. Mihailova[2]*, V. S. Nikolov[3], D. R. Mehandjiev[4]

[1] Department of Water Supply, Sewerage and Water Treatment, University of Architecture, Civil Engineering and Geodesy, 1 Christo Smirnenski blvd., 1046 Sofia, Bulgaria
[2] Department of Silicate Technology, University of Chemical Technology and Metallurgy, 8 St. Kliment Ohridski blvd., 1756 Sofia, Bulgaria
[3] Institute of General and Inorganic Chemistry, Bulgarian Academy of Sciences, Acad. Georgi Bonchev str., bld. 11, Sofia 1113, Bulgaria
[4] Institute of Catalysis, Bulgarian Academy of Sciences, Acad. Georgi. Bonchev str., bld. 11, Sofia 1113, Bulgaria

Received March 12, 2012; Revised April 24, 2012

A study was conducted of the adsorption capacity of slag samples obtained by crystallization of granulated blast furnace slag with and without Al_2O_3 and MgO additions in aqueous solutions of Cu (II), and a comparison was made between the original amorphous slag and the synthesized samples with main phases gehlenite and åkermanite. The purpose of the study was to make evaluation of the adsorption of heavy metal ions by the main phases (crystalline and amorphous) of blast furnace slag. The comparative analysis of adsorption and XRD data showed that the formation in slag of melililite crystal phases (gehlenite and åkermanite) and merwinite results in an almost double increase of Cu (II) adsorption, compared to amorphous slag. The addition of Al_2O_3 alone and in combination with MgO leads to crystallization of a sorption inactive spinel phase.

Key words: blast furnace slag, Cu (II) adsorption, crystallization, merwinite, melilite.

INTRODUCTION

The disposal of a large volume of metallurgical slags as by-products in iron and steel industry is an important environmental and economic problem. Its solution should be sought in three directions: 1) use in construction (production of cement, concrete, railroad ballast, roof coverings, mineral wool, glass, etc.); 2) extraction of useful components 3) water treatment reagents (neutralization and precipitation systems for purification of industrial water contaminated by heavy metals, adsorbents).

The good adsorption capacity of blast-furnace slag (BFS) for heavy metals, phosphates, arsenic (V and III) and organic pollutants [1-6] provides good opportunity for the use of slag in locally based processes of waste water treatment. Slag low price and large quantities are a prerequisite for the economic efficiency of such treatment processes. The BFS chemical composition and structure play a key role in the adsorption activity. Previous research on sorption-active phase/phases in BFS [7, 8] has shown the positive effect of the thermal treatment of granulated blast furnace slag (GBFS) due to the crystallization of melilite – a crystal phase typical for BFS. The term melilite is used to denote the representatives of isomorphic series gehlenite ($Ca_2Al_2SiO_7$) – åkermanite ($Ca_2MgSi_2O_7$). However, in its broad sense the term also encompasses other crystalline phases of a melilite-type structure. The melilite structure tolerates isomorphic substitutions; therefore, the formation of a melilite phase with a complex composition is highly probable, given the complex composition of Kremikovtsi BFS (presence of Mn, Fe, Ba, Na, etc.). In addition to components such as gehlenite ($Ca_2Al_2SiO_7$) and åkermanite ($Ca_2MgSi_2O_7$), amounts of $Ca_2MnSi_2O_7$, $Ca_2Fe^{2+}Si_2O_7$, $Ca_2Fe^{3+}{}_2SiO_7$ as well as partial substitutions in the structural positions of Ca by Ba and Na should also be expected. Similar-type melilites containing barium and manganese have been found in Kremikovtsi BFS crystal samples [9]. Furthermore, synthetic melilites with a higher Ca content have been reported to exhibit large stoichiometric deviations [10]. For these reasons, the quantity of the formed melilite phase often exceeds the expected quantity based on preliminary calculations.

* To whom all correspondence should be sent:
E-mail: irena@uctm.edu

The formation of melilites in Kremikovtsi BFS is limited by its low Al_2O_3 and MgO content. It could be assumed that an appropriate ratio modification of the major oxides CaO, MgO Al_2O_3 and SiO_2 would enhance the crystallization of adsorption-active phases with a melilite structure. Therefore, the goal of the study was to add Al_2O_3 and MgO in amounts that promote melilite crystallization. The amounts to be added in slag were calculated based on the chemical composition of the original slag. The effect of these additions on the adsorption capacity of BFS was evaluated in terms of adsorption capacity to remove copper ions from aqueous solutions.

EXPERIMENTAL

Synthesis of samples

The samples were synthesized using GBFS with the following composition (in $\%_{mass}$): SiO_2 – 34.0; CaO – 44.0; Al_2O_3 – 6.40; MnO – 2.33; MgO – 2.45; BaO – 3.2. In the present study the original granulated slag sample is denoted as sample GBFS.

The following samples were synthesized:

– Sample GBFS/1050 – the sample of granulated blast furnace slag was crushed with a mortar and then heated at 1050 °C for 6 hours in air.

– Sample GBFS/1400 – using the same procedure, heated at 1400 °C.

– Sample GBFS+Al_2O_3 – mixture of 2 g slag and 0.72 g of aluminum oxide crushed and heated for 6 hours at 1400 °C.

– Sample GBFS+MgO – mixture of 2 g slag and 0.3 g magnesium oxide heated at 1400 °C for 6 hours.

– Sample GBFS+Al_2O_3+MgO was obtained by using the above procedure plus additions of 0.24 g aluminum oxide and 0.15 g magnesium oxide to amount of 2 g of the original slag.

The synthetic gehlenite ($2CaO.Al_2O_3.SiO_2$) was obtained through solid-state synthesis using the following high purity (over 98.5%) reagents: $CaCO_3$, Al_2O_3 and SiO_2. A stoichiometric mixture of 1.56 g $CaCO_3$, 1.02 g Al_2O_3 and 0.60 g SiO_2, crushed in an agate mortar and placed in a corundum crucible, was heated successively at 1000, 1200 and 1400 °C for 6 hours with intermediate grinding of the product. The same procedure was used to synthesize synthetic åkermanite ($2CaO.MgO.2SiO_2$), by mixturing 1.56 g $CaCO_3$, 0.403 g MgO and 1.20 g SiO_2. The synthesis of samples was preformed in a high-temperature *Kanthal Super* furnace with Temperature Controller/Programmer. The XRD analysis showed that the synthesis of both minerals occurred at temperatures above 1200 °C. The synthesis was conducted at the maximum temperature (1400 °C) at which they are treated slag samples. Under these conditions, the main phases in the samples are, respectively, gehlenite and åkermanite.

Experimental methods

Structural characterization was performed by powder X-ray diffraction (XRD) using a Bruker D8 Advance Powder Diffractometer with CuKα radiation and a SolX detector. XRD spectra were recorded at room temperature. Data were collected in the 2θ range from 10 to 80 degree with a step 0.04 degree and 1s/step counting time. The crystalline phases were identified using the powder diffraction files PDF 35-0755, PDF 35-0592, PDF 79-2422, PDF 79-2423, PDF 79-2424, PDF 74-0874, PDF 35-591, PDF 33-0302, PDF 70-2144, PDF 34-1350 and PDF 82-2424 from database JCPDS - International Centre for Diffraction Data PCPDFWIN v.2.2. (2001) [11]

Adsorption evaluation of Cu (II) cations by the synthesized samples was conducted through an adsorption test under the following static conditions: 9 samples of 0.1 g of each sample and 100 ml of $CuSO_4$ solution; Cu (II) concentration of 25.45 mg/L; pH 5.40, placed for 48 hours in an oven thermostat at 25 °C to establish equilibrium.

Then samples were filtered and the values of the pH of the filtrate and Cu (II) concentration were measured. The concentration of Cu (II) was determined photometrically at λ = 560 nm using DR 2800 Spectrophotometer.

The adsorption capacity was calculated as:

$$A = \frac{(C_0 - C) \times V}{m},$$

Where: A – adsorption capacity (mg/g); C_0 – original Cu(II) concentration in the solution (mg/L); C - Cu(II) concentration in solution after 48 h. (mg/L); V – Cu (II) solution volume (L); m – mass of the sample (g).

RESULTS AND DISCUSSION

Figures 1 and 2 represent the X-ray diffraction patterns of the studied samples. In Fig. 1 (Sample GBFS XRD pattern) a halo is observed between 20 and 40° 2θ, which points to the predomination of an amorphous phase in the sample, i.e. slag glass. The diffraction peaks are related to the early stages of melilite crystallization. Heat treatment of blast furnace slag at 1050 °C (sample GBFS/1050) leads to melilite (PDF 79-2423) crystallization, accompanied by crystallization of calcium silicate $CaSiO_3$ pseudowollastonite (PDF 74-0874). The increase

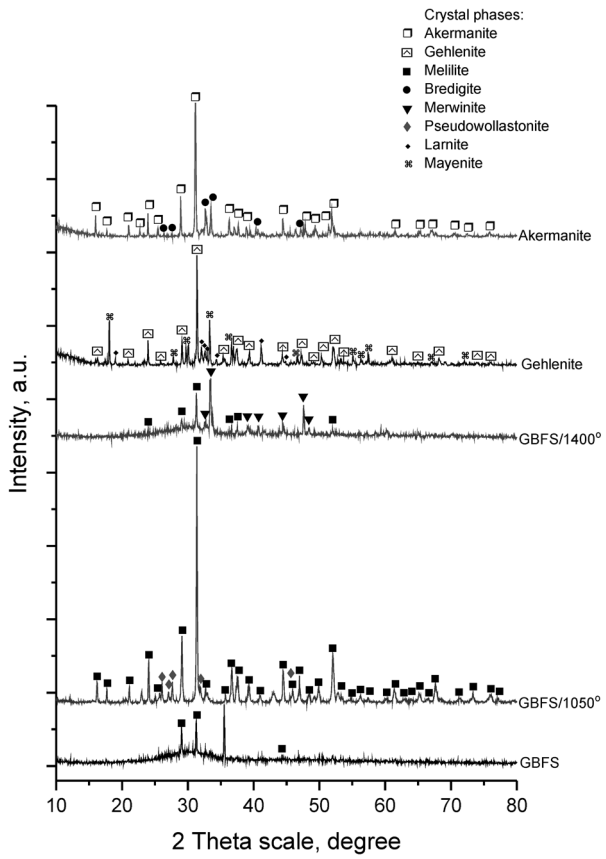

Fig. 1. XRD patterns of thermal treated slag samples and synthesized samples with main phases åkermanite ($Ca_2MgSi_2O_7$) and gehlenite (Ca_2AlSiO_7)

of treatment temperature up to 1400 °C (sample GBFS/1400) resulted in melt crystallization of merwinite $Ca_3Mg[SiO_4]_2$ (PDF 35-591) and melilite (79-2424). The separate or simultaneous addition of MgO and Al_2O_3 affected differently the phase formation. The X-ray diffractogramms of sample GBFS+Al_2O_3 (with added Al_2O_3) and GBFS/1050 sample are similar in the predomination of melilite (PDF 79-2423 and PDF 79 -2422) in both samples. Differences are found in the other crystal phases. The addition of Al_2O_3 leads to crystallization of some amounts of spinel (PDF 82-2424) in sample GBFS+Al_2O_3. Melilite (PDF 79-2423) is also the main phase in sample GBFS+Al_2O_3+MgO and the amount of the accompanying spinel is higher. The X-ray diffraction pattern of sample GBFS+MgO shows increased amounts of merwinite (PDF 35-591, compared to sample GBFS/1400 (without additions), both samples treated at the same temperature.

Figure 1 shows the X-ray diffraction patterns of the synthesized minerals gehlenite and åkermanite. The XRD patterns show successful synthesis of the specified minerals, but intermediate phases are also found. In Gehlenite sample these are gehlenite $Ca_2Al_2SiO_7$ (PDF 35-0755), larnite Ca_2SiO_4 (PDF 33-0302), and mayenite $Ca_{12}Al_{14}O_{33}$ (PDF 70-2144). In Åkermanite sample åkermanite $Ca_2MgSi_2O_7$ (PDF 35-0592) is the predominant crystal phase, but bredigite $Ca_7Mg[SiO_4]_4$ (PDF 34-1350) is also present.

Adsorption-capacity (AC) data is given in Tables 1 and 2. It can clearly be seen that slag AC is determined by the level of crystallization and the type of the crystalline phases. The lowest capacity is shown by the original sample, which is (according to XRD data) amorphous for the most part and contains small amount of melilite. The sample (sample GBFS/1050) heat treatment up to 1050 °C for 6 hours induces a higher level of crystallization. Melilite and pseudowollastonite are formed and the adsorption capacity (AC) is raised by 9%, compared to the original sample (GBFS). Heat treatment at 1400°C results in a sharp 83% increase in the retained Cu (II) compared with the original sample. Apart from melilite, in sample (GBFS/1400) merwinite is also present. The amount of melilite in sample GBFS/1400 is significantly smaller than in

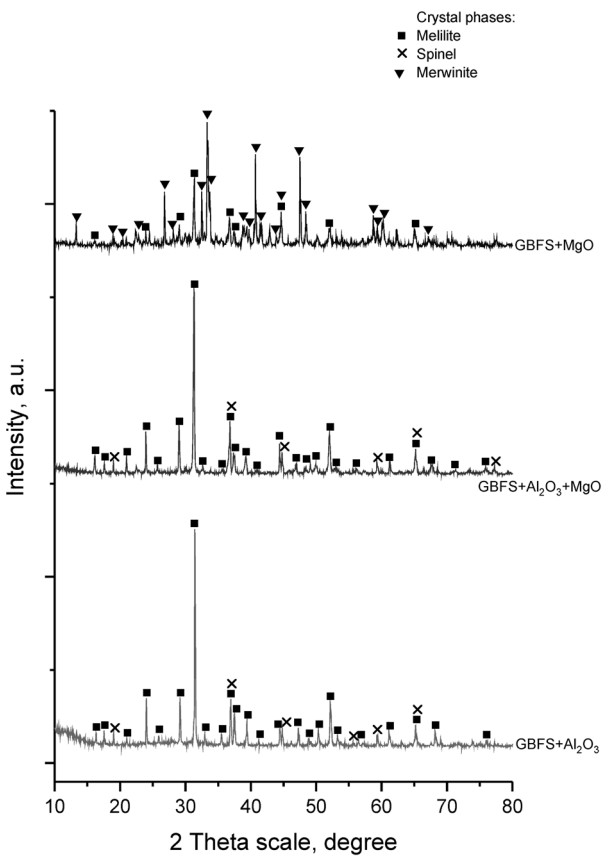

Fig. 2. XRD patterns of thermal treated slag samples with Al_2O_3 and MgO additions

Table 1.

Sample	A, mg/L	Phases
GBFS	13.3	amorphous phase + melilite
GBFS/1050	14.5	melilite + pseudowollastonite
GBFS/1400	24.4	amorphous phase +merwinite + melilite
Gehlenite	23.4	gehlenite + mayenite + larnite
Åkermanite	21.6	åkermanite + bredigite

sample GBFS/1050. Therefore, the higher AC of the slag sample treated at higher temperature can be related to the formation of a merwinite crystal phase and/or a residual glass phase.

The AC of slag samples with Al_2O_3 and MgO additions is generally lower when compared to the sample GBFS/1400 without additions, treated at the same temperature (Table 2). One exception is sample GBFS+MgO, which shows the maximum AC increase of 88 %, compared to the original slag material. The phase composition of this sample also differs, merwinite being its main phase. This leads to a conclusion that the presence of merwinite improves the adsorption properties of slag materials. AC data for the remaining slag samples with Al_2O_3 and MgO additions is similar and corresponds to their close phase composition. It is evident that additions in slag do not lead to an increase of the amount of melilite. The amount of the melilite phase in pure slag treated at 1050 °C is higher. In most of the samples, the additions react with other components in slag and new adsorption-inactive phases are formed: spinels. The synthetic samples with gehlenite and åkermanite as predominant phases also have a high AC. The obtained results are in complete accordance with previous findings [7, 8] reporting that increase of the level of crystallization and the presence of melilite phases (such as gehlenite and åkermanite) result in significant increase of slag AC. On the other hand, one should bear in mind the presence of other crystal phases in the samples that also affect the AC. Therefore, we can not make firm conclusions about the roles played by åkermanite and gehlenite.

Table 2.

Sample	A, mg/L	Crystal phases
GBFS+Al_2O_3	15.2	melilite + spinel
GBFS+Al_2O_3+MgO	15.3	melilite + spinel
GBFS+MgO	25.0	merwinite + melilite

According to the XRD data (Fig. 1 and 2), many slag samples contain identical amounts of åkermanite and gehlenite in the melilite crystal phase of the synthesized samples. However, slag samples with a predominant melilite crystal phase exhibit lower AC compared to the synthesized samples. This means that besides the phase composition and respectively quantity of the melilite phase, other factors have a significant impact on the adsorption properties, most probably the structural characteristics of the samples and the chemical composition of formed melilite. The obtained experimental data does not permit to establish clear dependency between the amounts of melilite in samples and the AC value, but it is indisputable that a 9-15 % higher AC is observed in slag samples with a predominant melilite, compared to the original slag.

The presented experimental data allows finding a correlation between the phase composition and the adsorption properties of BFS. The presence of merwinite and melilite induces a higher AC of the slag samples. The results allow us to make a new and interesting conclusion – merwinite also exhibits a high AC, apart from the minerals gehlenite and åkermanite. This is proved by the fact that samples containing this mineral showed the highest AC. The addition of Al_2O_3 and Al_2O_3+MgO did not considerably influence the adsorption properties of slag samples. Only MgO addition positively affected the promotion of the merwinite crystallization. As already known [1, 7], the AC of metallurgical slag take place primarily by a cation exchange process. The adsorption is based on exchange reactions represented by the following scheme:

$$[Al,Si,O]Ca^{2+} + Cu^{2+} \rightarrow [Al,Si,O]Cu^{2+} + Ca^{2+} \quad (1)$$

$$[Al,Si,O,Ca]Mg^{2+} + Cu^{2+} \rightarrow [Al,Si,O,Ca]Cu^{2+} + Mg^{2+} \quad (2)$$

The possibility of exchange depends on the structure of slag and accordingly of the crystal structure of the formed minerals. Schematic diagrams of åkermanite and merwinite crystal structures are shown in Figs. 3 and 4. We have chosen åkermanite instead of gehlenite for its Mg^{2+} content. Both minerals belong to different structural types and the coordination of Mg^{2+} and Ca^{2+} cations differs. As shown earlier, [12, 13] åkermanite and gehlenite are tetragonal. The crystal cell data are: space group $P\bar{4}2_1m$, a = 7.8288(8) Å, c = 5.0052(2) Å for åkermanite and. space group $P\bar{4}2_1m$, a = 7.6850(4) Å, c = 5.0636(3) Å for gehlenite [13]. Åkermanite is part of the silicates with diorthogroups of silicon-oxygen tetrahedra. These structural units are linked with each other through the so-called "particular type" of tetrahedra [MgO_4]. The tetrahedral lay-

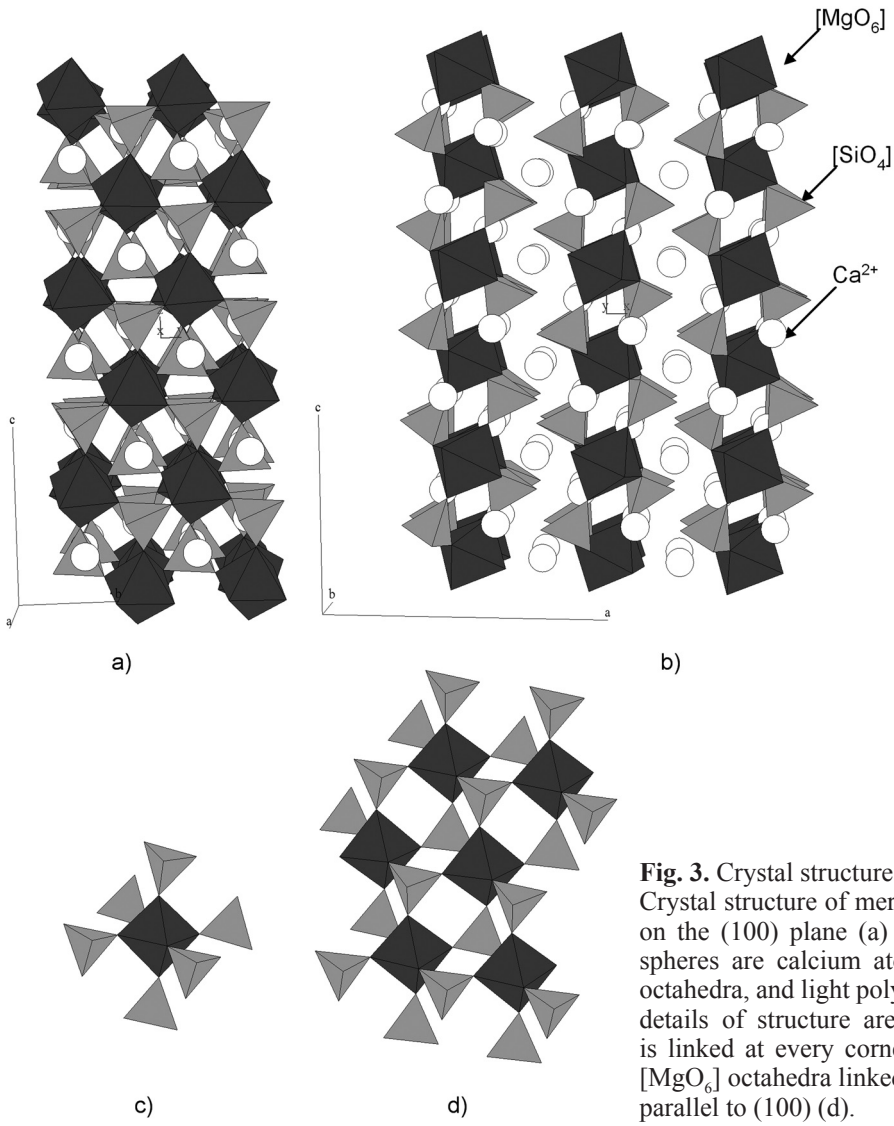

Fig. 3. Crystal structure of merwinite
Crystal structure of merwinite ($Ca_3Mg[SiO_4]_2$) projected on the (100) plane (a) and the (010) plane (b). White spheres are calcium atoms, dark polyhedra are MgO_6 octahedra, and light polyhedra are SiO_4 tetrahedra. Some details of structure are presented. [MgO_6] octahedron is linked at every corner by [SiO_4] tetrahedra (c). The [MgO_6] octahedra linked by [SiO_4] tetrahedra form slabs parallel to (100) (d).

ers alternate along c-axis with layers of calcium polyhedrons. The coordination number of Ca^{2+} is 8. Merwinite crystallizes in the orthorhombic space group $P2_1/a$ and the cell parameters are a = 13.254(21) Å, b = 5.293(9) Å, c = 9.328(17) Å, β = 91.90(15)° The structure of merwinite is an extreme example of dense packing where both O^{2-} and Ca^2 ions make up the dense-packed layers. The [MgO_6] octahedra are linked at every corner by [SiO_4] tetrahedra. The [MgO_6] octahedra are linked by [SiO_4] tetrahedra and form slabs parallel to (100). The Ca^{2+} ions have three structural positions with coordination numbers between 8 and 9 [15]. Despite the obvious differences, a common feature of both structures is the location of Ca^{2+} cations in layers between slabs of linked silicon and magnesium polyhedrons. Probably this structural feature permits the easy exchange of Mg^{2+} and Ca^{2+} cations, which increases the AC of slag containing these minerals.

The experimental results show that besides the melilite group, merwinite has certain adsorption capacity towards heavy metals, too. This finding extends the possible application of slag and slag based products in the purification of water contaminated by heavy metals.

CONCLUSIONS

The experimental results demonstrate the possibility to increase the AC of granulated blast furnace slag for heavy metals (CuII) with over 80% through crystallization.

The crystallization of granulated slag or a mixture of granulated blast-furnace slag with 13% addition of MgO leads to the formation of crystal phases – melilite and merwinite. The presence of both minerals in slag leads to an almost double increase in

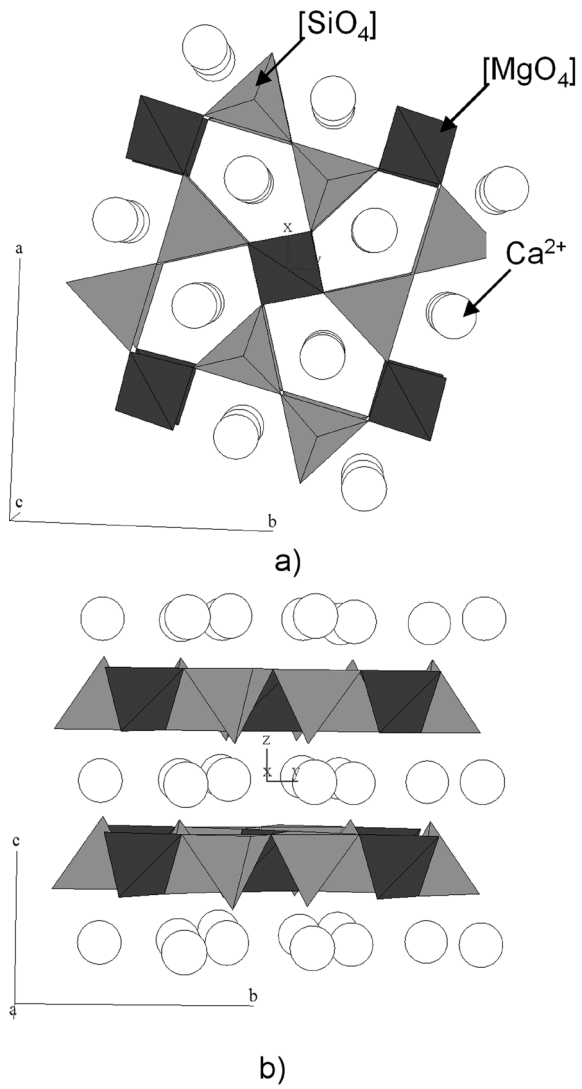

Fig. 4. Crystal structure of åkermanite
Crystal structure of åkermanite ($Ca_2MgSi_2O_7$) projected on the (001) plane (a) and the (100) plane (b). White spheres are calcium atoms, dark polyhedra are MgO_4 tetrahedra, and light polyhedra are SiO_4 tetrahedra

adsorption activity compared to the original amorphous product.

The crystallization of a mixture containing granulated blast-furnace slag with addition of Al_2O_3 (alone and in combination with MgO) does not lead to an increase of the adsorption activity.

The minerals merwinite, gehlenite and åkermanite are adsorption-active phases determinative for the very high levels of adsorption of heavy metal ions by blast furnace metallurgical slag.

Slag samples with a main crystal phase merwinite exhibit the highest adsorption capacity. The promotion of merwinite crystallization would allow synthesizing materials with high adsorption capacity towards CuII.

Acknowledgements: *The authors kindly acknowledge Dr. Daniela Kovacheva from Institute of General and Inorganic Chemistry, Bulgarian Academy of Sciences for her assistance in obtaining XRD data.*

REFERENSES

1. S. V. Dimitrova, *Water Res.*, **30**, 228 (1996).
2. S. V. Dimitrova, *Water Res.*, **36**, 4001 (2002).
3. L. J. Westholm, *Water*, 2, 826 (2010).
4. E. Oguz, *J. Hazard. Mater.,* **114**, 131 (2004).
5. S. R. Kanel, H. Choi, J. Y. Kim, S. Vigneswaran, W. G. Shim, *Water Qual .Res. J. Canada*, **41**, 130 (2006).
6. A. K. Jain, V. K.Gupta, A. S Bhatnagar, *J. Hazard. Mater.,* **101**, 31 (2003).
7. S. Dimitrova, V. Nikolov, D. Mehandjiev, *J. Mater. Sci.*, **36**, 2639 (2001).
8. S. Dimitrova, V. Nikolov, D. Mehandjiev, *C.R. Acad. Bulg. Sci.,* **62***,* 335 (2009).
9. И. Т. Иванов, *Годишник на Висшия Химико-технологически институт – София*, **20** (2) 345 (1972).
10. D. Stavrakeva, I. Georgieva, *C.R. Acad. Bulg. Sci.*, **48**, 91 (2005).
11. JCPDS - International Centre for Diffraction Data PCPDFWIN v.2.2. (2001)
12. M. Kimata, N. Ii, The crystal structure of synthetic akermanite, $Ca_2MgSi_20_7$. *N. Jb. Miner. Monat.,* **1**, 10 (1981).
13. I. P. Swainson, M. T. Dove, W. W. Schmahl, A. Putnis, *Phys. Chem. Miner.,* **19** 185 (1992).
14. S. V. Dimitrova, , D. R. Mehandjiev, *Water Res.*, **34**, 1957 (2000).
15. P. B. Moore and T. Araki, *Am. Mineral.* **57**, 1355 (1972).

АДСОРБЦИОННА СПОСОБНОСТ НА МОДИФИЦИРАНА МЕТАЛУРГИЧНА ШЛАКА

С. В. Димитрова[1]*, И. К. Михайлова[2], В. С. Николов[3], Д. Р. Механджиев[4]

[1] Катедра „Водоснабдяване, канализация и пречистване на води“, Университет по архитектура, строителство и геодезия, бул. „Хр. Смирненски” №1, София 1036, България
[2] Катедра „Технология на силикатите“, Химикотехнологичен и металургичен университет, бул. „Кл. Охридски“ № 8, София 1756, България
[3] Институт по обща и неорганична химия, Българска академия на науките, бул. „Акад. Г. Бончев“, бл. 11, София 1113, България
[4] Институт по катализа, Българска академия на науките, бул. „Акад. Г. Бончев“, бл. 11, София 1113, България

Постъпила на 12 март, 2012 г.; приета на 24 април, 2012 г.

(Резюме)

Адсорбционният капацитет на шлакови образци, получени чрез кристализация на гранулирана доменна шлака без и с добавки на Al_2O_3 и MgO, беше изследван във водни разтвори на Cu(II) и сравнен с този на изходна аморфна шлака и на синтезирани образци с основни фази геленит и акерманит. Целта на изследването беше: оценка на адсорбционната активност на основните фази в доменната шлака (кристални и аморфни) към тежки метални йони. Сравнителният анализ на адсорбционните данни и XRD показа, че формирането на кристалните фази мервинит и мелилит (геленит и акерманит) в шлаката предизвиква почти двойно увеличение на адсорбционният капацитет по отношение на Cu(II) в сравнение с аморфната шлака. Добавката на Al_2O_3 самостоятелно, както и в комбинация с MgO води до кристаллизация на сорбционно неактивна фаза шпинел.

Bulgarian Chemical Communications, Volume 44, Proceedings of the III[rd] National Crystallographic Symposium (pp. 37–46) 2012

Synthesis and structural details of perovskites within the series $PrCo_{1-x}Cr_xO_3$ (x = 0, 0.33, 0.5, 0.67 and 1)

S. Dimitrovska-Lazova[1]*, D. Kovacheva[2], S. Aleksovska[1], M. Marinšek[3], P. Tzvetkov[2]

[1] *University "St. Cyril and Methodius", Faculty of Natural Sciences and Mathematics, Arhimedova 5, Skopje, R. Macedonia*
[2] *Institute of General and Inorganic Chemistry, Bulgarian Academy of Science, "Acad. Georgi Bonchev" bl. 11, 1113 Sofia, Bulgaria*
[3] *University of Ljubljana, Faculty of Chemistry and Chemical Technology, Aškerčeva c. 5, 1000 Ljubljana, R. Slovenia*

Received March 21, 2012; Revised May 2, 2012

Results on synthesis, structural investigations and the morphology of complex perovskites of general formula $PrCo_{1-x}Cr_xO_3$ (with x = 0, 0.33, 0.5, 0.67 and 1) are presented. The synthesis of the perovskites within this series was performed by solution combustion method using two different fuels: urea and glycine. The annealed samples were identified using X-ray powder diffraction. The purity of the compounds obtained using glycine as a fuel was better and for further investigations perovskites obtained with this fuel were used. The crystal structure was refined by the Rietveld method, and the morphology of the particles was investigated using SEM. All compounds within the series crystallize in *Pnma* space group (Z = 4). The effect of the substitution of Co^{3+} ion with Cr^{3+} was investigated by analyzing different crystallochemical parameters (bond-lengths and tilt angels of the coordination octahedra, global instability index etc). A very interesting trend in changes of the structural distortion and global stability of the compounds in respect to x e.g. substitution of Co^{3+} with Cr^{3+} was found.

Key words: complex perovskites, XRD, SEM, crystallochemical calculations.

INTRODUCTION

Within the field of material science one of the most interesting groups of compounds belongs to perovskite structural type. Perovskite structure encompasses compounds with general formula ABX_3, where A and B are cations and X is an anion. In the ideal perovskite structure the B-cation is coordinated by six anions in almost regular octahedron. The BX_6 octahedra are sharing same corners thus forming three-dimensional network of octahedral chains. The cavities formed by the octahedra are filled by A-cations which are cubooctahedrally coordinated by the anions. This kind of arrangement leads to cubic (*Pm*3*m*) structure [1, 2]. An important feature of perovskite structure is possible rotation (for small angle) of the BX_6 octahedra, while still retaining the chain-like connectivity. As a result, the symmetry of the structure is lowered to orthorhombic, monoclinic, hexagonal, etc. This structural flexibility enables including almost all elements from the periodic table in the perovskite structure. So, there is great number of possible combinations of different cations in A and B positions, but also different anions in the X-position may be found, such as oxygen, halogen ions, cyanide group etc. Among these anions the most common are perovskites with oxide anion. Another important feature of the perovskite structure is the possibility for multiple substitutions in the positions of the cations, thus forming so-called complex perovskites. This possibility drastically enlarges the number of compounds with perovskite structure.

Depending on the nature of A and B cations and particular crystal structure, the physical and chemical properties of perovskites may vary in a wide range. Namely, in this group of compounds different physical and chemical properties emerge, namely: pyroelectricity, piezoelectricity, colossal magnetoresistance, catalytic activity, ferromagnetism, superconductivity etc. [1, 3]. From this point of view the perovskites containing cobalt ion in the B-position are intensively studied. Namely, cobalt-perovskites ($RCoO_3$) exhibit interesting properties

* To whom all correspondence should be sent:
E-mail: sandra@pmf.ukim.mk

such as high electronic conductivity [4], metal to insulator transition with increasing temperature [5], significant catalytic activity [3], specific magnetic properties [6−8], etc. Properties of cobaltates are tightly connected with some characteristics of cobalt ions such as the possibility to change the oxidation state (Co^{4+}, Co^{3+}, Co^{2+}) and also the possibility of altering the spin state of the Co^{3+} ion [7, 9, 10]. The change of the oxidation state of cobalt ion is usually triggered by substitutions in A or B positions (as in $R_{1-x}Sr_xCoO_3$) [11]. The spin state of the cobalt ion in compounds with rare earth metal in A-position has been a subject of investigation in a large number of studies [7, 9, 10, 12−16]. The spin state of Co^{3+} ion may change from low spin (LS) with t_{2g}^6 electron configuration, intermediate spin state (IS) with one electron in e_g-orbital ($t_{2g}^5e_g^1$) or high spin state (HS) with configuration $t_{2g}^4e_g^2$. It is expected that compounds with IS and HS state of the Co^{3+} ion to encounter Jahn-Teller distortion of the CoO_6 octahedra. At room temperature in most of the $RCoO_3$ perovskites (R is rare earth) Co^{3+} is in LS state. It is found that at room temperature the amount of IS Co^{3+} ions is the highest in $LaCoO_3$, while it is smaller in $PrCoO_3$ [10] Actually, with decreasing of the ionic radii of R^{3+} in the $RCoO_3$ series, the amount of the LS state of Co^{3+} ions is increasing [10, 16].

Continuing our investigation on different perovskites with cobalt ion [17, 18], in this work we present the synthesis of the perovskite series of general formula $PrCo_{1-x}Cr_xO_3$ (with x = 0, 0.33, 0.5, 0.67 and 1), the investigations of their crystal structure and some important crystallographic characteristics connected with the substitution of the cations in B position.

Although there is literature data [19−30] for the end members of the series ($PrCoO_3$ and $PrCrO_3$), any data about the solid solution between these two compounds have not been found yet. The literature data shows that $PrCoO_3$ and $PrCrO_3$ may be synthesized by different methods such as: solid stated synthesis [7, 19, 20], decomposition of citrate precursor [21−24, 8, 11], synthesis based on complex precursors [25−29], self-propagating high temperature synthesis [30] and hydrothermal synthesis [30]. In this work the synthesis of Pr-perovskites by solution combustion method using two fuels – glycine and urea is presented.

It should be pointed out that the crystal structures of the end members of the series presented in this paper are already known. According to some literature data $PrCoO_3$ is cubic [19, 21, 24], but according to some others, it is orthorhombic [7, 8, 10, 11, 20, 22]. Some more detailed structural analysis of $PrCoO_3$ by XRD and neutron diffraction [11, 22] point out also that this compound crystallizes in the orthorhombic system (space group *Pnma*). The crystal structure of $PrCrO_3$ was also reported [20, 26, 30, 31] as orthorhombic, space group *Pnma*. Taking these findings into consideration, it is expected that the new-synthesized complex perovskites of cobalt and chromium should crystallize in the orthorhombic system. Also, it is expected that the substitution of Co^{3+} ($r(Co^{3+})$ = 0.545 Å, LS) with chromium Cr^{3+} ion, which has slightly bigger ionic radii ($r(Cr^{3+})$ = 0.615 Å), would increase the lattice parameters and, consequently, the volume of the unit cell. In order to analyze the influence of substitution of Co^{3+} with Cr^{3+} on the crystal structure, the synthesized compounds were characterized by XRD and their crystal structure and several crystallographic parameters were calculated and compared. The morphology of the studied samples was also investigated by scanning electron microscopy (SEM).

EXPERIMENTAL

Synthesis

The synthesis of the $PrCo_{1-x}Cr_xO_3$ perovskites was performed by solution combustion method. For this purpose, nitrates of the constituting metals were used as starting materials. Calculated amounts of metal nitrates ($Pr(NO_3)_3{\cdot}6H_2O$, $Co(NO_3)_2{\cdot}6H_2O$ and $Cr(NO_3)_3{\cdot}9H_2O$) were dissolved in small amount of distilled water. The obtained solutions were thoroughly mixed on a stirrer. These solutions were used as starting mixtures in the combustion synthesis. The combustion syntheses were performed using two fuels: urea ($CO(NH_2)_2$) or glycine (NH_2CH_2COOH). The amounts of the fuels were calculated on the basis of propellant chemistry and were set to 1 [32]. The composition of the solutions varied according to the formula of the synthesized perovskite.

The synthesis of the perovskites using urea as a fuel was performed in the following manner: appropriate quantity of urea was dissolved in small amount of diluted nitric acid (1:1) and this solution was added to the particular mixture containing metal nitrates. After the homogenization of the solution it was transferred in muffle furnace. The mixture was slowly heated to temperature of ~500 °C. After the evaporation of water a vigorous combustion reaction started. In a very short time spongy powders were formed. Resulting materials were hand milled, transferred to ceramic dish and subjected to additional heating for 6 hours at 800 °C.

The procedure using glycine as a fuel was just a little bit different. Glycine was dissolved in small amount of distilled water and this solution was added to pre-prepared mixture of metal nitrates solutions. The obtained mixture was heated at 80 °C under constant stirring. After the evaporation of

the water and gelatinization of the solution the vessel was transferred on a hot plate preheated above 300 °C. The gel boiled and after the evaporation of remaining water an initialization and combustion of the mixtures started. As a result, black (only in case of $PrCrO_3$ the product was green) spongy powders were formed. As-prepared samples were hand milled and calcined at 800 °C for 6 hours (2h and additional 4h).

XRD

The resulting powders were analyzed by X-ray diffraction. The XRD patterns were recorded on *Bruker D8 Advance* with $Cu_{K\alpha}$ radiation and SolX detector within the range 10–120° 2θ at room temperature with step-scanning of 0.02°. The crystal structures were refined by the method of Rietveld using the Fullprof program [33].

SEM

The microstructure of the obtained compounds was investigated by SEM. Field-Emission FE-SEM Zeiss ULTRA PLUS microscope using accelerating voltage of 2kV was used. The samples were put onto graphite tape and were not gold sputtered prior to the microscopy. Images were taken using In-lens and/or standard Evernhart-Thornley secondary electron (SE) detectors.

RESULTS AND DISCUSSION

As was mentioned in the experimental part, the solid solutions $PrCo_{1-x}Cr_xO_3$ (x = 0, 0.33, 0.5, 0.67 and 1) were synthesized using both urea and glycine as a fuel. The recorded XRD patterns of the samples showed that in both cases perovskite compounds with same structure were obtained but the samples prepared using glycine as a fuel, were of better purity. This is illustrated by the XRD patterns (Fig. 1) for one of the members of the series ($PrCo_{0.5}Cr_{0.5}O_3$).

The XRD pattern on Figure 1a corresponds to $PrCo_{0.5}Cr_{0.5}O_3$ synthesized using urea and the others (Figs. 1b-d) using glycine as a fuel. Some impurities of Co_3O_4 could be detected in the compound obtained via urea (Fig. 1a), which are not present in the compound obtained at same temperature but via glycine (Fig. 1d). It should be mentioned that in the case of $PrCo_{0.5}Cr_{0.5}O_3$ the formation of the perovskite phase began right after the combustion of the initial mixture (as-synthesized sample, Fig. 1b) but by further heating on 800 °C a better crystallinity was obtained (Fig. 1b–d). Since the purity of the samples obtained using glycine was better than that using urea, the further investigations and discussion of the results were carried out on the samples synthesized by glycine.

The XRD patterns of the perovskite series $PrCo_{1-x}Cr_xO_3$ (x = 0, 0.33, 0.5, 0.67 and 1) obtained by the same synthetic route (heated 4 h on 800 °C) are presented on Figure 2.

As expected, the obtained compounds are isostructural and with perovskite structure. Namely, the obtained XRD patterns of the end members of the series, $PrCoO_3$ and $PrCrO_3$, are in accordance with the literature data [8, 22, 34]. Complex perovskites within the series show gradual shifting

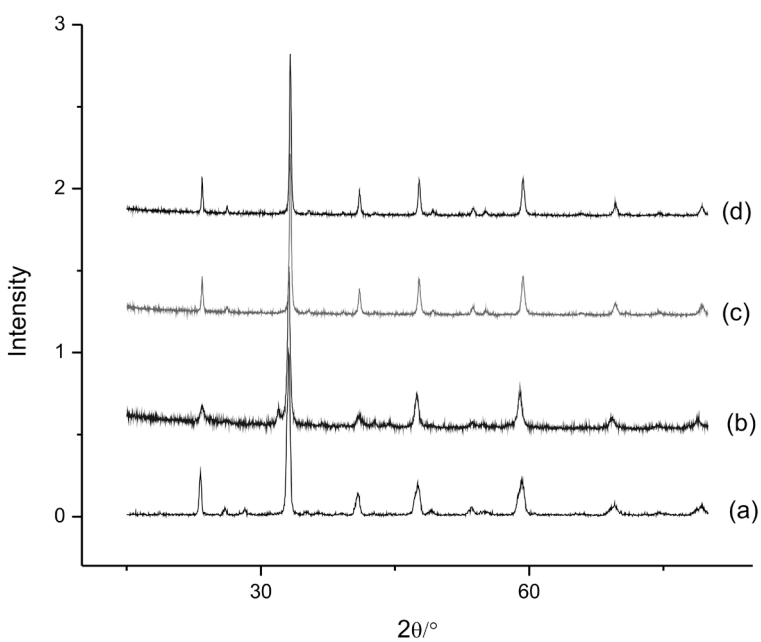

Fig. 1. XRD patterns of $PrCo_{0.5}Cr_{0.5}O_3$ obtained using (a) urea (heat treated for 6h at 800 °C), (b) glycine (as-synthesized) (c) glycine (after heat treatment for 2h at 800 °C), (d) glycine (after additional heat treatment for 4h at 800 °C)

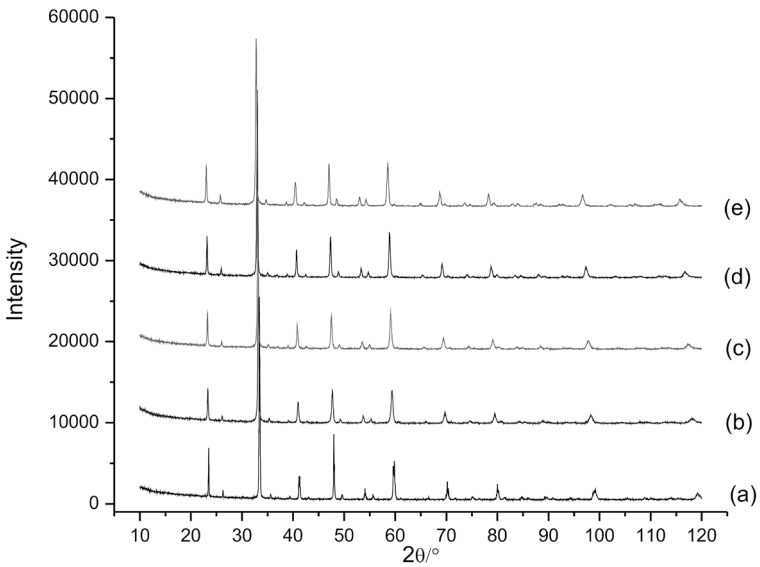

Fig. 2. XRD patterns of (a) $PrCoO_3$, (b) $PrCo_{0.67}Cr_{0.33}O_3$, (c) $PrCo_{0.5}Cr_{0.5}O_3$, (d) $PrCo_{0.67}Cr_{0.33}O_3$, (e) $PrCrO_3$

Table 1. Unit cell parameters, b/√2, pseudo-cubic parameter a_p calculated using the equation $a_p = (V/Z)^{1/3}$ where Z is number of atoms in assymetric unit and volume (V) of the unit cell

	a/Å	b/Å	c/Å	$(b/\sqrt{2})$/Å	a_p/Å	V/Å^3	ratio
$PrCoO_3$	5.34355(8)	7.57728(10)	5.37634(8)	5.3580	3.7896	217.6857	$c > b/\sqrt{2} > a$
$PrCo_{0.67}Cr_{0.33}O_3$	5.3834(3)	7.6139(4)	5.4027(4)	5.3838	3.8113	221.4495	$c > b/\sqrt{2} \approx a$
$PrCo_{0.5}Cr_{0.5}O_3$	5.4141(3)	7.6502(7)	5.4145(6)	5.4095	3.8274	224.2630	$a \approx c > b/\sqrt{2}$
$PrCo_{0.33}Cr_{0.67}O_3$	5.43702(20)	7.6750(3)	5.4292(2)	5.4270	3.8404	226.5558	$a > b/\sqrt{2} > c$
$PrCrO_3$	5.47897(10)	7.71528(16)	5.45127(11)	5.4555	3.8622	230.4349	$a > b/\sqrt{2} > c$

of the diffraction peaks towards smaller 2θ values with increasing of the value of x (Fig. 2), suggesting gradual increase of the substitution of cobalt ion. These results are in accordance with the expected changes in the XRD pattern in a case when smaller cation (Co^{3+}) is substituted with bigger one (Cr^{3+}).

As previously mentioned, the end members of the series, $PrCoO_3$ and $PrCrO_3$, have $GdFeO_3$-orthorhombic structure [8, 22, 34] and, accordingly, it was expected that all members of the series would be orthorhombic. The refinement of the crystal structures showed that all compounds crystallize in the orthorhombic space group *Pnma*, with four formula units per unit cell. The unit cell parameters, cell volumes, as well as, the pseudo-cubic parameter are presented in Table 1.

In aim to present the complete crystal structure of the newly synthesized members of the series, the Rietveld refinement approach was undertaken. The refinements were carried out using the structural model for $PrCoO_3$ as a starting model. For the intermediate structures it was assumed that the Co(III) and Cr(III) cations are randomly distributed in same crystallographic positions. The calculated and observed patterns obtained by Rietveld refimenent for one of the compounds ($PrCo_{0.5}Cr_{0.5}O_3$) is presented on Fig. 3 just as an example.

The fractional atomic coordinates and the discrepancy factors are presented in Table 2, and Table 3 presents selected distances and angles as well as the distortions of the coordination polyhedrons.

The values of the unit cell parameters of the end members of this series are in good agreement with the literature data [8, 22, 34]. Analyzing the changes of the unit cell parameters throughout the series and the relations between them, some interesting facts have arisen. Namely, as expected, the substitution of smaller Co^{3+} with slightly bigger Cr^{3+} increases the unit cell parameters, cell volumes, and the pseudo-cubic parameter a_p (Table 1). However, it is interesting to note the changes in the relationship between a and c parameters. As may be noticed from Figure 4, this relationship changes from $c > a$ ($PrCoO_3$ and $PrCo_{0.67}Cr_{0.33}O_3$) through $c \approx a$ ($PrCo_{0.5}Cr_{0.5}O_3$) to $c < a$ ($PrCo_{0.33}Cr_{0.67}O_3$ and $PrCrO_3$).

Obviously, in $PrCo_{1-x}Cr_xO_3$ series the decrease of the ionic radii of B-cation (from $r(Cr^{3+}) = 0.615$ Å to $r(Co^{3+}) = 0.545$ Å) leads toward change in the

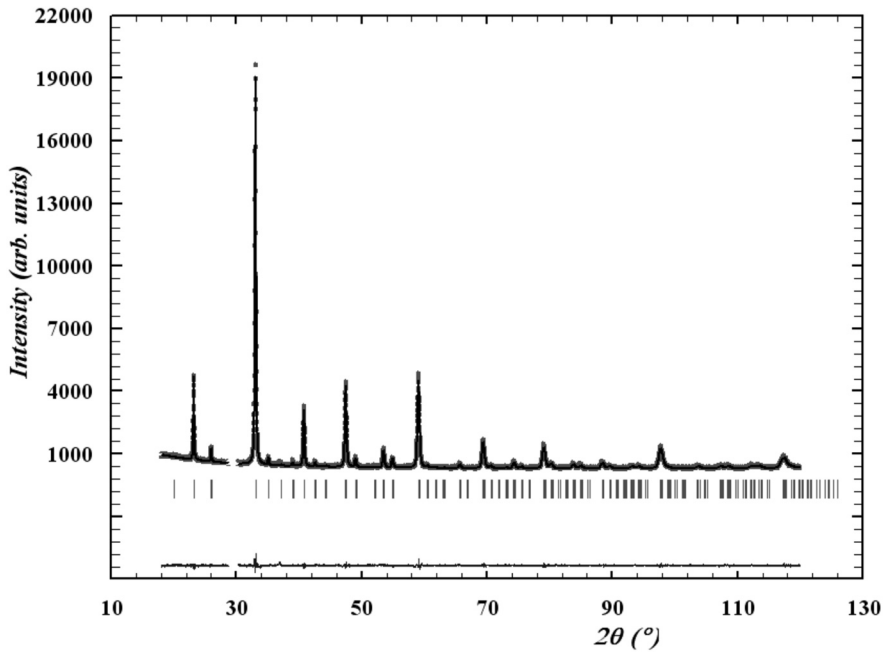

Fig. 3. Observed and calculated XRD patterns for $PrCo_{0.5}Cr_{0.5}O_3$ as well as their difference plot obtained by Rietveld refinement

Table 2. Fractional atomic coordinates and discrepancy factors for $PrCo_{1-x}Cr_xO_3$ solid solution

Atoms	Param.	$PrCoO_3$	$PrCo_{0.67}Cr_{0.33}O_3$	$PrCo_{0.5}Cr_{0.5}O_3$	$PrCo_{0.33}Cr_{0.67}O_3$	$PrCrO_3$
Pr	*x*	0.02913(13)	0.02964(15)	0.03142(13)	0.03306(10)	0.03545(8)
	y	0.25	0.25	0.25	0.25	0.25
	z	0.9954(5)	0.9955(6)	0.9940(5)	0.9947(4)	0.9927(2)
	B	0.33(2)	0.29(3)	0.25(2)	0.292(19)	0.390(14)
Co/Cr	*B*	0.06(3)	0.18(4)	0.06(3)	0.12(3)	0.22(2)
O1	*x*	0.4947(15)	0.4893(16)	0.4864(15)	0.4897(14)	0.4869(10)
	y	0.25	0.25	0.25	0.25	0.25
	z	0.060(2)	0.054(3)	0.060(3)	0.072(4)	0.0643(18)
	B	1.9(4)	0.2(6)	0.6(7)	0.9(6)	0.9(3)
O2	*x*	0.274(2)	0.282(3)	0.288(3)	0.294(2)	0.2905(13)
	y	0.0388(14)	0.0420(17)	0.0353(16)	0.0364(14)	0.0428(10)
	z	0.7138(19)	0.700(3)	0.701(3)	0.7086(19)	0.7101(13)
	B	0.9(3)	1.8(3)	0.9(3)	0.9(3)	1.04(16)
R_I	R_p/%	14.6	13.8	11.3	10.3	7.74
	R_{wp}/%	10.7	11.9	10.4	9.86	8.66
	R_{exp}/%	9.45	9.50	8.98	8.50	7.72
	χ^2	1.28	1.56	1.34	1.35	1.26
	R_B/%	3.09	2.33	1.88	2.14	1.68

relationship of the unit cell parameters from $a < c$ to $c > a$. This *a/c* relationship points out to the reasons for distortion of perovskite structure. Namely, it is known that the transition from cubic to orthorhombic structure (*Pnma*) due to the tilting of the octahedra leads to unit cell with $c < a$. The inverse relationship, $a < c$ is characteristic for perovskites in which additional distortion of the BO_6 octahedrons appears [10]. It this series, the additional distortion appears in cases when the content of Co^{3+} prevails that of Cr^{3+}, such as in $PrCo_{0.67}Cr_{0.33}O_3$. This additional octahedral distortion may also be noticed from the comparison of *a*, $b\sqrt{2}$ and *c* (Table 1). It is interesting to point out that only in $PrCrO_3$ and $PrCo_{0.33}Cr_{0.67}O_3$ the relation between these parameters is $a > b\sqrt{2} > c$ as in the O-type perovskites. In this type of perovskites the octahedral tilting is primarily the only distortional mechanism and the lattice distortion is small. In $PrCo_{0.5}Cr_{0.5}O_3$ *a* and *c* parameters are almost identical, $a \approx c > b/\sqrt{2}$ and this perovskite

Table 3. Values of Pr-O and B-O distances, average <Pr-O> distances in twelve coordinated praseodymium and average distance in BO_6 octahedra, Δ_{12}, Δ_{10} and Δ_6, B-O1-B and B-O2-B angles

	$PrCoO_3$	$PrCo_{0.67}Cr_{0.33}O_3$	$PrCo_{0.5}Cr_{0.5}O_3$	$PrCo_{0.33}Cr_{0.67}O_3$	$PrCrO_3$
Pr-O1	2.877(8)	2.926(9)	2.972(8)	2.984(8)	3.031(6)
	2.512(8)	2.495(9)	2.489(8)	2.518(8)	2.504(6)
	2.992(11)	2.977(16)	3.010(16)	3.09(2)	3.048(10)
	2.397(11)	2.444(16)	2.427(16)	2.36(2)	2.430(10)
Pr-O2 x 2	2.562(11)	2.627(15)	2.673(15)	2.667(11)	2.623(7)
	2.384(11)	2.324(15)	2.356(14)	2.365(11)	2.362(7)
	3.140(11)	3.235(15)	3.238(15)	3.254(11)	3.304(7)
	2.697(11)	2.682(14)	2.641(14)	2.658(11)	2.723(8)
$<Pr\text{-}O>_{12}$	2.6953	2.7148	2.7262	2.7367	2.7531
Δ_{12}	9.9624	12.429	12.39	13.46	14.06
Δ_{10}	5.7991	6.5998	6.917	8.18	7.885
B-O1 x 1	1.9218(18)	1.927(2)	1.941(3)	1.959(4)	1.9617(18)
B-O2 x2	1.885(11)	1.891(16)	1.921(16)	1.979(11)	1.988(7)
	1.978(10)	2.026(16)	2.003(16)	1.958(11)	1.981(7)
<B-O>	1.9283	1.948	1.955	1.9653	1.9769
Δ_6	0.3933	0.8586	0.3189	0.0242	0.0316
B-O1-B	160.6	162.24	160.24	156.74	158.98
B-O2-B	157.8	153.6	154.7	154.7	153.6

is orthorhombic with pseudo-tetragonal unit cell. In the last two members ($PrCoO_3$ and $PrCo_{0.67}Cr_{0.33}O_3$) the ratio between the unit cell parameters changes to $c > b/\sqrt{2} > a$, which also highlights some additional distortion of the octahedra. It is interesting to compare these results with structural changes in $RCoO_3$ (R = lantanide) series [7, 22], where the change in the mutual relationship between *a* and *c* parameters (from $a > c$ to $c > a$) is driven by the increasing of the ionic radii of A-cation. This change ends with change in symmetry from orthorhombic to rombohedral (at $LaCoO_3$).

Taking into consideration these changes in the unit cell parameters relationship due to the Co^{3+}/Cr^{3+} substitution an additional crystallochemical calculations were done. Also, it seemed interesting to examine the possibility of changes in morphology and dimensions of the crystals obtained by Co^{3+}/Cr^{3+} substitution in the perovskite structure.

The distortion of the octahedra may be parameterized by the bond-length distortion of the octahedra, Δ_6, calculated using the equation: $\Delta = \Sigma[(r_i - r)/r]/n \cdot 10^3$ (Table 3). As was pointed out previously, the calculated Δ_6 values for $PrCoO_3$ and $PrCo_{0.67}Cr_{0.33}O_3$ are higher and are emphasizing an increased distortion of the octahedra. The maximal Δ_6 is found in $PrCo_{0.67}Cr_{0.33}O_3$ and throughout the complex perovskites in the series,

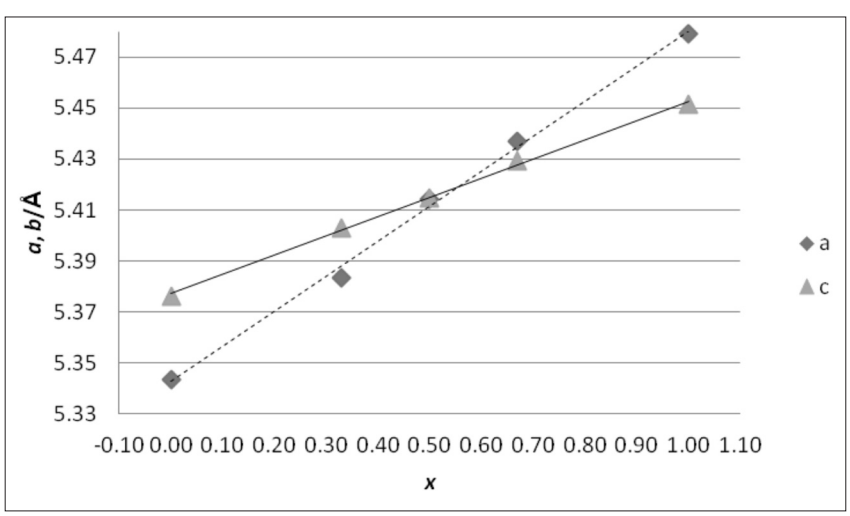

Fig. 4. The change of the relation between the unit cell parameters *a* and *c* in $PrCo_{1-x}Cr_xO_3$ with increasing of x (x = 0, 0.33, 0.5, 0.67 and 1)

the Δ_6 is decreasing. Analyzing the values of the particular B-O distances, two facts may be noticed. Firstly, the distances between the B cation and the O1 anions are increasing from $PrCoO_3$ to $PrCrO_3$. This trend is the same for B-O2 distances, although not so regular. More careful examination of the values of these distances shows that at the beginning of the series the first from the two B-O2 distances is longer, while at the end of the series (at $PrCrO_3$) the second one is shorter than the first one. Bearing in mind that the B-O2 distances are along *a* and *c* axes the interchange of these distances is in accordance with the change of the *a/c* relationship.

Contrary to the direction of the changes in bond-length distortion of the BO_6 polyhedra, the distortion of the coordination polyhedra of the A cation is increasing with increasing of the amount of chromium ion e.g. with increasing of *x* (Table 3). The average $<Pr\text{-}O>_{12}$ distances for twelve coordinated Pr are increasing from 2.6953 Å in $PrCoO_3$ to 2.7531 Å at $PrCrO_3$. This change influences the coordination around Pr-cation. Namely, starting from $PrCo_{0.67}Cr_{0.33}O_3$ two of the Pr-O2 distances are too long to be encountered as a part of the coordination of Pr^{3+}, and probably the coordination number of praseodymium changes to 10. This change in the coordination of praseodymium is expressed in high values of the distortion parameters Δ_{12}. More precisely, these values are significantly higher than the values for Δ_{10} in all compounds except in $PrCoO_3$, suggesting change in coordination sphere from 12 to 10.

The deviation from the ideal cubic perovskite structure may be also described by the observed so called tolerance factor, t_o [35]. This factor represents the ratio between the average $<Pr\text{-}O>_{12}$ and $<B\text{-}O>_6$ distances and is calculated by the equation: $t_o = <Pr\text{-}O>_{12}/\sqrt{2}\ <B\text{-}O>_6$. The observed tolerance factor is related with the degree of the octahedral tilting. The values close or equal to 1 corresponds to the structures without tilting of the octahedra [36]. In order to check the trend of changes of the observed tolerance factors in relation with tilting within this perovskite series, the tilt angles θ, φ and Φ were calculated (Table 4).

These tilt angles represents the rotation of the octahedra around $[110]_p$, $[001]_p$ and $[111]_p$ pseudo-cubic axes and are calculated using the fractional atomic coordinates [2]. It may be noticed that in the structure of $PrCoO_3$ the value of t_o (calculated assuming coordination number 12 for A cation, $t_{o(12)}$, and 10 $t_{o(10)}$) is closer to 1 and this compound has the smallest tilt angles. The values of t_o are increasing throughout the series, with increasing of *x*, and also the tilting of the octahedra is more pronounced (θ, φ and Φ, Table 4). These results are also in accordance with the values of the tilt angles calculated on the bases of the experimental B-O1-B and B-O2-B angles, using the formula $\varphi^* = (180 - <B\text{-}O1,2\text{-}B>)/2$, where $<B\text{-}O1,2\text{-}B>$ is the average value of B-O1,2-B angles (Table 4). Obviously, in complex perovskites, the tilt angles of the octahedra are increasing with increasing of *x*, e.g. of the substitution of Co^{3+} with Cr^{3+}. These values suggest that the overlap of the oxygen orbitals with the orbitals of the B cation is smaller. Namely, as this angle deviates more from 180° smaller orbital overlap is achieved [11].

In order to evaluate the overall distortion of the perovskite structure in the series, additional distortion parameters were also calculated: orthorhombic distortion, spontaneous strain (s), d-cell distortion (Table 4). These parameters are calculated using the unit cell parameters and they pointed out to the change in the type of the distortion. It may be concluded that these values are diminishing from $PrCoO_3$ to $PrCo_{0.5}Cr_{0.5}O_3$, (the smallest value) and then they start rising again.

According to the previous discussion it may be concluded that there are two types of distortions in the structures of the members of this perovskite series. In $PrCoO_3$ and $PrCo_{0.67}Cr_{0.33}O_3$, in which the content of Co^{3+} prevails the content of Cr^{3+}, the octahedra are more distorted in respect to the bond

Table 4. Change of values of several crystallographic parameters throughout the series. Calculated parameters are: orthorhombic distortion [35], spontaneous strain (s) [2], d-cell distortion [7], Global Instability index (GII) [2], observed tolerance factors $t_{o(12)}$ and $t_{o(10)}$ [2], tilt angles calculated using fractional atomic coordinates [2] and tilt angle obtained from B-O1,2-B angles

	Orthorhombic distortion	Spontaneous strain (*s*)	d-cell distortion	GII	$t_{o(12)}$	$t_{o(10)}$	Tilt angles			
							θ	φ	Φ	φ^*
$PrCoO_3$	0.0171	–0.0061	0.0626	0.2112	0.9884	0.9558	9.700	7.012	11.950	10.4
$PrCo_{0.67}Cr_{0.33}O_3$	0.0112	–0.0036	0.0279	0.2225	0.9855	0.9477	8.879	9.538	13.004	11.04
$PrCo_{0.5}Cr_{0.5}O_3$	0.0072	$-7.4 \cdot 10^{-5}$	0.0018	0.1967	0.9860	0.9490	9.880	9.948	13.985	11.265
$PrCo_{0.33}Cr_{0.67}O_3$	0.0963	0.0014	0.0062	0.1812	0.9846	0.9474	11.630	9.697	15.099	12.14
$PrCrO_3$	0.2341	0.0051	0.0497	0.0762	0.9847	0.9453	10.509	9.136	13.891	11.855

lengths. This leads to bigger instability and stress in the structure, which are expressed in the high values of GII (global instability index, Table 4). These high values (> 0.2 valence units) of GII, point out to big strain in these structures. This type of distortion may be connected with possible existence of Co^{3+} ion in intermediate spin (IS) state. Namely, the IS would increase the deformation of the octahedra as a result of appearance of Jahn-Teller distortion.

In $PrCo_{0.33}Cr_{0.57}O_3$ and $PrCrO_3$, in which the content of Cr^{3+} prevails the content of Co^{3+} the distortion is mainly due to the rotation of the octahedra, while the bond-lengths distortion of the octahedra is significantly smaller. The most stable structure is that of $PrCo_{0.5}Cr_{0.5}O_3$. It seems that the effects of the bond-lengths distortion and tilting of the octahedral act in opposite directions in this perovskite series, leading to stabilization of the structure.

In aim to check the influence of these structural changes due to partial substitution of the cations in B-position, on their morphology, SEM images of the perovskites of this series were recorded. Figure 5 shows the SEM micrographs of $PrCo_{1-x}Cr_xO_3$ powders obtained by heat treatment at 800 °C for 4 hours.

The images show single perovskite phases with appropriate nanosize crystallinity. The porous structure implies the outflow of gases produced by decomposition of nitrates and combustion of glycine. As can be seen, the morphology of the compounds within the series is very similar.

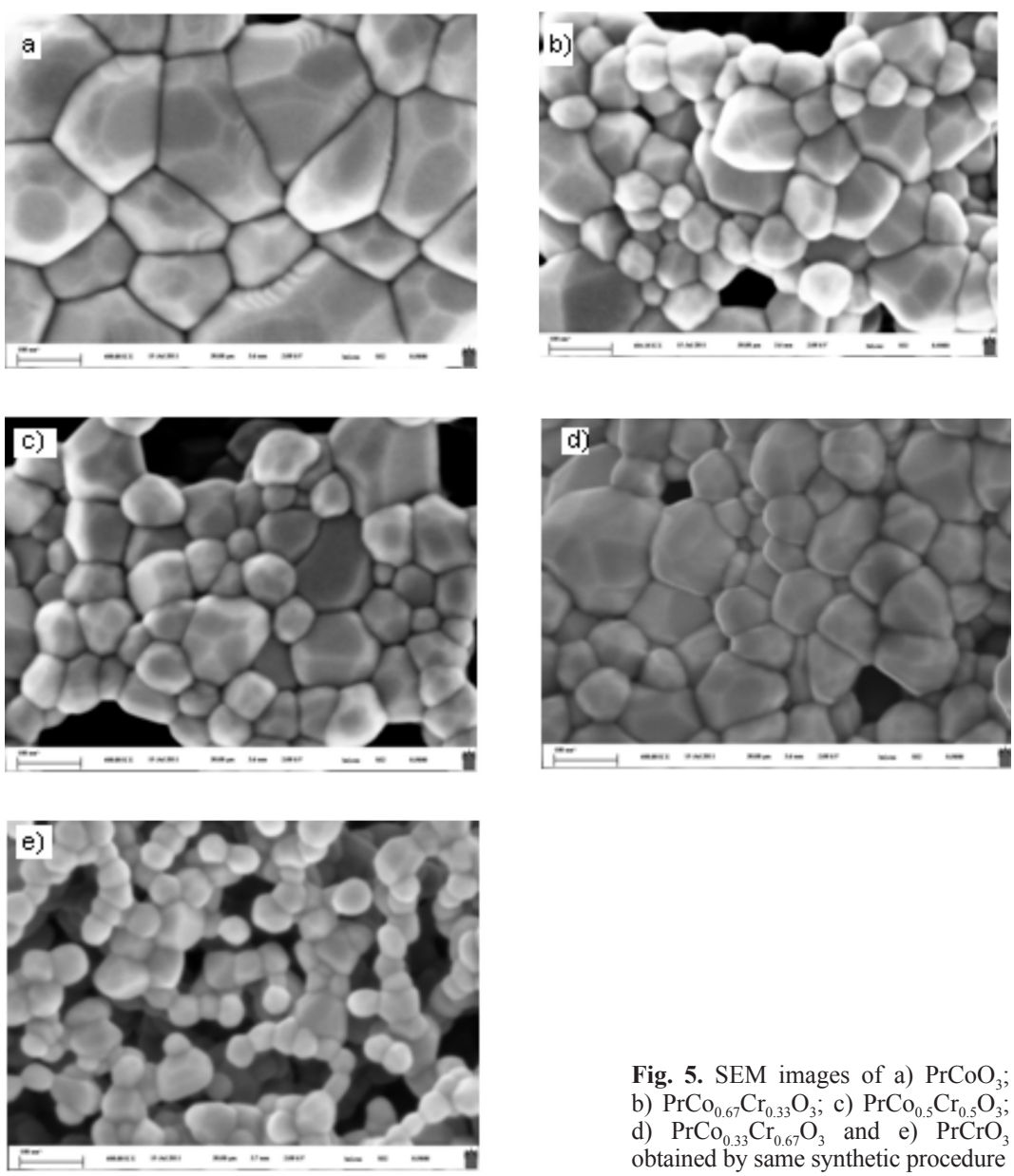

Fig. 5. SEM images of a) $PrCoO_3$; b) $PrCo_{0.67}Cr_{0.33}O_3$; c) $PrCo_{0.5}Cr_{0.5}O_3$; d) $PrCo_{0.33}Cr_{0.67}O_3$ and e) $PrCrO_3$ obtained by same synthetic procedure

CONCLUSION

The perovskites within the series $PrCo_{1-x}Cr_xO_3$ were obtained by solution combustion method using urea or glycine as a fuel. The purity of the samples obtained using glycine was better than that using urea, so the further investigations were carried out on the samples synthesized by glycine. The Rietveld refinement of the crystal structures showed that all compounds within this series crystallize in the orthorhombic space group *Pnma* with four formula units per unit cell.

In aim to study the influence of Co^{3+}/Cr^{3+} substitution on the perovskite structure, several crystallochemical parameters were calculated. The detailed analysis of structural changes due to substitution of Co^{3+} with Cr^{3+} revealed some interesting features. Thus, it was concluded that in perovskites where the content of Co^{3+} prevails that of Cr^{3+} ($PrCoO_3$ and $PrCo_{0.67}Cr_{0.33}O_3$), except the distortion due to octahedral tilting the octahedral distortion in respect to the bond lengths is also significant. This leads to bigger instability and stress in the structure, which are expressed in the high values of GII. In $PrCo_{0.33}Cr_{0.57}O_3$ and $PrCrO_3$, in which the content of Cr^{3+} prevails the content of Co^{3+} the distortion is mainly due to the octahedral tilting. The most stable structure is that of $PrCo_{0.5}Cr_{0.5}O_3$.

Acknowledgement: *The authors thank the National Science Fund of Bulgaria and the Ministry of Education and Science of Republic of Macedonia for the financial support under contract DNTS/ Macedonia 01/7/08.12.2011.*

REFERENCES

1. F. S. Galasso, Perovskites and High Tc Superconductors, Gordon and Breach Science Publishers, 1990.
2. R. H. Mitchell, Perovskites: Modern and Ancient, Almaz press – Thunder Bay, 2002.
3. M. A. Peña, J. L. G. Fierro, *Chem. Rev.*, **101**, 1981 (2001).
4. T. Ishihara (Ed), Perovskite Oxide for Solid Oxide Fuel Cells (Fuel Cells and Hydrogen Energy), Springer, Dordrecht, 2009.
5. S. Yamaguchi, Y. Okimoto, Y. Tokura, *Phys. Rev. B*, **54**, R11022 (1996).
6. A. Fondado, J. Mira, J. Rivas, C. Rey, M. P. Breijo, and M. A. Señarís-Rodríguez, *J. App. Phys.*, **87**(9), 5612 (2000).
7. K. Knížek, Z. Jirák, J. Hejtmánek, M. Veverka, M. Maryљko, G. Maris, T. T. M. Palstra, *Eur. Phys. J. B*, **47**, 213 (2005).
8. H. W. Brinks, H. Fjellvåg, A. Kjekshus, B. C. Hauback, *J. Solid State Chem.,* **147**, 464 (1999).
9. J.-Q. Yan, J.-S. Zhou, J. B. Goodenough, *Phys. Rev. B,* **69**, 134409 (2004).
10. J.-S. Zhou, J.-Q. Yan, J. B. Goodenough, *Phys. Rev. B,* **71**, 220103R (2005).
11. G.Ch. Kostogloudis, N. Vasilakos, Ch. Ftikos, *Solid State Ionics,* **106**, 207 (1998).
12. A. P. Sazonov, I. O. Troyanchuk, V. V. Sikolenko, *Crystallogr. Rep.,* **51**, 11 (2006).
13. T. Fujita, T. Miyashita, Y. Yasui, Y. Kobayashi, M. Sato, E. Nishibori, M. Sakata, Y. Shimojo, N. Igawa, Y. Ishii, K. Kakurai, T. Adachi, Y. Ohishi, M. Takata *J. Phys. Soc. Jpn.*, **73**, 1987 (2004).
14. X. G. Luo, X. Li, G. Y. Wang, G. Wu, X. H. Chen, *J. Solid State Chem.*, **179**, 2175 (2006).
15. R. Caciuffo, D. Rinaldi, and G. Barucca, J. Mira, J. Rivas, M. A. Señarís-Rodríguez, P. G. Radaelli, D. Fiorani, J. B. Goodenough, *Phys. Rev. B,* **59**, 1068 (1999).
16. G. Thornton, F. C. Morrison, S. Partingtont, B. C. Tofield, D. E. Williams, *J. Phys. C: Solid State Phys.*, **21**, 2871 (1988).
17. S. Dimitrovska-Lazova, D. Kovacheva, S. Aleksovska, V. Mirceski, *Proceedings of 45th Meeting of Serbian Chemical Society*, Novi Sad, 2007.
18. S. Dimitrovska-Lazova, V. Mirceski, D. Kovacheva, S. Aleksovska, *J. Solid State Electrochemistry*, **16**, 219 (2012).
19. V. V. Kharton, E. N. Naumovich, A. A. Vecher, A. V. Nikolaev, *J. Solid State Chem*., **120**, 128 (1995).
20. S. Pal, S. H´ebert, C. Yaicle, C. Martin, A. Maignan, *Eur. Phys. J. B*, **53**, 5 (2006).
21. J. L. G. Fierro, M. A. Pena, L. Gonzalez Tejuca, *J. Mater. Sci*., **23**, 1018 (1988).
22. J. A. Alonso, M. J. Martínez-Lope, C. de la Calle, V. Pomjakushin, *J. Mater. Chem.*, **16**, 1555 (2006).
23. J.-W. Moon, Y. Masuda, W.-S. Seo, K. Koumoto, *Mater. Sci. Eng.*, **B85**, 70 (2001).
24. Y. Ren, B. Li, J. Wang, X. Xu, *J. Solid State Chem.*, **177**, 3977 (2004).
25. P S. Devi, M. S. Rao, *J. Therm. Anal.*, **48**, 909 (1997).
26. P. S. Devi, *J. Mater. Chem.*, **3**, 373 (1993).
27. P. A. Brayshaw, A. K. Hall, W. T. A. Harrison, J. M. Harrowfield, D. Pearce, T. M. Shand, B. W. Skelton, C. R. Whitaker, A. H. White, *Eur. J. Inorg. Chem*., 1127 (2005).
28. Y. Sadaoka, E. Traversa, M. Sakamoto, *J. Mater. Chem.*, **6**, 1355 (1996).
29. Y. Seto, K. Umemoto, T. Arii, Y. Masuda, *J. Therm. Anal. Calorim.*, **76**, 165 (2004).
30. M. V. Kuznetsov, Ivan P. Parkin, *Polyhedron*, **17**, 4443 (1998).
31. K. Sardar, M. R. Lees, R. J. Kashtiban, J. Sloan, R. I. Walton, *Chem. Mater.*, **23**, 48 (2011).
32. M. M. A. Sekar, K. C. Patil, *J. Mater. Chem.*, **2**, 739 (1992).
33. J. Rodriguez-Carvajal, *Physica B*, **192**, 55 (1993).
34. S. Geller, *Acta Crystallogr.*, **10**, 243 (1957).
35. G. Huo, D. Song, Q. Yang, F. Dong, *Ceram. Int.*, **34**, 497 (2008).
36. Sasaki, C. T. Prewitt, J. D. Bass, W. A. Schulze, *Acta Crystallogr.*, **C43**, 1668 (1987).
37. C. L. Bull, P. F. McMillan, *J. Solid State Chem.*, **177**, 2323 (2004).

СИНТЕЗ И СТРУКТУРНИ ДЕТАЙЛИ НА ПЕРОВСКИТИ ОТ СЕРИЯТА $PrCo_{1-x}Cr_xO_3$ (x = 0, 0.33, 0.5, 0.67 и 1)

С. Димитровска-Лазова[1]*, Д. Ковачева[2], С. Алексовска[1], М. Маринчек[3], П. Цветков[2]

[1] *Университет „Св. Кирил и Методии“, Факултет по Естествени науки и Математика, Архимедова 2, Скопие, Македония*

[2] *Институт по обща и неорганична химия, Българска академия на науките, „Акад. Г. Бончев“ бл.11, София, България*

[3] *Университет на Любляна, Факултет по химия и химични технологии, Aškerčeva c. 5, 1000 Любляна, Словения*

Постъпила на 21 март, 2012 г.; приета на 2 май, 2012 г.

(Резюме)

Предствен е синтез, структурно изследване и морфология на комплексни перовскити с обща формула $PrCo_{1-x}Cr_xO_3$ (with x = 0, 0.33, 0.5, 0.67 и 1). Получените перовскити са синтезирани по метода на комбустия през разтвор с използване на два вида гориво: урея и глицин. Накалените образци са идентифицирани с прахова рентгенова дифракция. Получените съединения с глицин като гориво са с по-голяма чистота и за изследване бяха използвани образци синтезирани с това гориво. Кристалната структура беше уточнена по метода на Ритвелд, а морфологията на частиците характеризирана със SEM. Всички съединения от серията кристализират в пространствена група *Pnma* (Z = 4). Ефекта от заместване на Co^{3+} с Cr^{3+} е изследван с анализ на различни кристалохимични параметри (дължина на връзки и ъгли на накланяне на координационните октаедри, глобален индекс на нестабилност и др.). Беше установена интересна промяна в дисторзията на структурата и глобалният индекс на стабилност в зависимост от степента на заместване на Co^{3+} с Cr^{3+}.

Bulgarian Chemical Communications, Volume 44, Proceedings of the III[rd] National Crystallographic Symposium (pp. 47–54) 2012

Structural characteristics of $GdCo_{1-x}Cr_xO_3$ (x = 0, 0.33, 0.5, 0.67, 1) perovskites

S. Dimitrovska-Lazova[1]*, D. Kovacheva[2], P. Tzvetkov[2]

[1] *University "St. Cyril and Methodius", Faculty of Natural Sciences and Mathematics, Arhimedova 5, Skopje, R. Macedonia*
[2] *Institute of General and Inorganic Chemistry, Bulgarian Academy of Science, "Acad. Georgi Bonchev" bl. 11, 1113 Sofia, Bulgaria*

Received March 21, 2012; Revised May 2, 2012

In this paper the synthesis, crystal structure determination and calculation of structural parameters within the $GdCo_{1-x}Cr_xO_3$ (x = 0, 0.33, 0.5, 0.67 and 1) are presented. The compounds were synthesized by solution combustion method starting with the nitrates of the constituent metals and urea as a fuel. The perovskites within the series crystallize in *Pnma* with Z=4. The lattice parameters and distances and angles were used to calculate several crystallographic parameters such as, cell distortion, orthorhombic distortion, bond and angle deformation, the tilting angles, bond valences, and global instability index. These were used to obtain a clearer picture of the influence of substitution of Co^{3+} with Cr^{3+} in these complex perovskites on the distortion and stability of the perovskite structure.

Key words: complex perovskites, X-ray diffraction, crystal structure, crystallographic parameters.

INTRODUCTION

The role of the perovskites in science and technology is constantly increasing. This is a result of numerous possibilities for application of these materials due to their interesting physical and chemical properties. For example these compounds exhibit wide spread of conducting properties from insulators to conductors, superconductivity, colossal magnetoresistance, giant magneto resistance, catalytic activity toward different catalytic reactions, etc [1−3]. These properties are connected to specific structural characteristics of perovskites as well as with characteristic properties of constituting elements.

Perovskites are usually designated with the formula ABX_3, where A and B are cations and X is the anion. The positions of the cations may be occupied by different metals from the periodic table, while as an anion most frequently oxygen can be found but there are compounds with halogenides, OH^-, CN^-, or H^- anion. The diversity in perovskite structure is a result of possible multiple substitutions in the positions of the cations, leading to a great number of so-called complex perovskites.

The ideal perovskite structure is fairly simple. Namely, in cubic unit cell B-cations are surrounded by six anions arranged in octahedral geometry sharing the same vertex. This arrangement forms cubooctahedral cavity in which the A-cation is placed. This structure is very flexible. Namely, the BO_6 octahedra may be rotated to small angle leading to structural distortions and lowering of the cubic symmetry. As a result, large number of distorted (orthorhombic, tetragonal, hexagonal etc.) perovskites are known.

In the present study the structural investigation of complex perovskites with cobalt and chromium (3+) cations in B-position is presented. Our focus is on structural changes driven by mutual substitution of these ions in $GdCo_{1-x}Cr_xO_3$ (x = 0, 0.33, 0.5, 0.67 and 1) solid solution. The role of cobalt ion in perovskites on their properties is thoroughly studied [4−8] and it is evident that this cation is responsible for a number of interesting properties found in cobalt-containing perovskites. Thus, as a result of possible temperature driven spin state change of Co^{3+} and of its oxidation state, Co-containing perovskites exhibit interesting electrical and magnetic properties, as well as, pronounced catalytic activity [3, 9]. The change in oxidation state of Co^{3+} ion (to Co^{2+} or

* To whom all correspondence should be sent:
E-mail: sandra@pmf.ukim.mk

Co^{4+} state) is accompanied with appearance of vacancies or change of oxidation state of other cations in the compound, while the spin state directly influences the deformation of the structure as a result of the fact that from the three possible spin states of the cobalt ion (low, intermediate and high spin state) the intermediate and high spin state of Co^{3+} exhibit Jahn-Teller effect.

On the other hand, rare earth chromites are interesting because of their electrical conductivity, resistance to oxidation and high melting points [10].

The literature data for the end members of the series $GdCo_{1-x}Cr_xO_3$ (x = 0, 0.33, 0.5, 0.67 and 1), $GdCoO_3$ and $GdCrO_3$, showed that these compounds may be synthesized using different methods such as: solid state reaction [11, 12−16], sol-gel method [17−19], synthesis using complex precursors [20−22], hydrothermal method [23, 24], self-propagating high-temperature synthesis [10], decomposition or combustion synthesis using citric acid [9, 25] and by decomposition of nitrate salts [7, 26]. In this study, the solution combustion method was used for the synthesis of investigated compounds. Namely, in recent years the combustion synthesis is becoming one of the most popular methods for obtaining wide variety of oxide materials. Combustion synthesis is fast and inexpensive that enables producing homogeneous, very fine, crystalline, multicomponent oxide powders, without intermediate decomposition steps [27, 28]. It involves highly exothermic reaction between oxidant (usually nitrate salts of metal ions) and an organic fuel. The aim to use this fuel is to be a source of C and H, which are reducing elements in the combustion reaction. The most often used compounds as fuels are: urea, glycine, sucrose, alanine, citric acid, etc. The pathway of the reaction and the temperature of the synthesis are highly dependent on the ratio between fuel and oxidizer (metal nitrates) [29]. This ratio is usually set to 1, but it may be smaller (to 0.7) or bigger than 1. In this study nitrates of the consisting metals were used as oxidizers and the fuel was urea. The ratio between them was set to 1.

The formation of the perovskite phase was examined by X-ray diffraction. The crystalographic characteristics of the end members of the series, $GdCoO_3$ and $GdCrO_3$, are known from the literature [10, 13, 14, 16, 17, 23, 24]. These compounds are orthorhombic and they belong to $GdFeO_3$-type perovskites (space group *Pnma*). To the best of our knowledge, the intermediate members of the solid solution are synthesized for the first time and we expected that they have the same crystallographic characteristics as the end members. The refinement of the crystal structure confirmed that Co^{3+} and Cr^{3+} ions are completely interchangeable and may be substituted in the whole region of x (from 0 to 1).

EXPERIMENTAL

The starting materials for the synthesis were nitrates of the consisting metals: $Gd(NO_3)_3 \cdot 6H_2O$, $Co(NO_3)_2 \cdot 6H_2O$ and/or $Cr(NO_3)_3 \cdot 9H_2O$. The nitrates were dissolved in small amount of deionised water. The obtained solutions were thoroughly mixed together. As previously mentioned the fuel (F) to oxidizer (O) ratio was set to 1 and according to the stoichiometry, the quantity of the fuel was calculated separately for each compound. The calculated amount of urea was dissolved in 1:1 solution of nitric acid and was added to the solution of metal ions. The final solution was transferred to muffle furnace and heated up to ~500 °C. After the evaporation of the water the combustion reaction started and was followed by large emission of gasses CO_2, N_2 and H_2O. The resulting products were substances, which showed voids, pores, and were highly friable. All powders were black except $GdCrO_3$ that has pale green color.

The combustion reaction for one of the systems may be presented as follows:

$$2Gd(NO_3)_3 + Co(NO_3)_2 + Cr(NO_3)_3 + 9(NH_2)_2CO + 4.5O_2 \longrightarrow 2GdCo_{0.5}Cr_{0.5}O_3 + 9CO_2 + 9N_2 + 9H_2O$$

The obtained powders were hand grinded and subjected to additional heating at 800 °C for 4h.

The resulting powders were analyzed by X-ray diffraction. The XRD patterns were recorded on *Bruker D8 Advance* with $Cu_{K\alpha}$ radiation and SolX detector within the range 10–120° 2θ at room temperature with step scanning rate of 0.02°. The crystal structures were refined by the method of Rietveld (program Fullprof).

RESULTS AND DISCUSION

The XRD analysis of the powders obtained after the combustion reaction showed that perovskite phase was formed only in the case of $GdCrO_3$, right after the combustion of the initial solution. This as-prepared phase contains small quantity of impurity identified as $GdCrO_4$. The impurities were removed by additional heating of the obtained $GdCrO_3$ perovskite at 800 °C (Fig. 1).

In the case of the other samples the perovskite phase was not formed directly after the combustion reaction, but by further heating at 800 °C for 4 hours. The perovskite structure of the resulting powders was confirmed according to the XRD patterns (Fig. 2).

The analysis of the XRD patterns of the synthesized compounds showed continuous shift of the positions of the diffraction peaks towards lower values with increasing x (Fig. 2). As expected, this shift

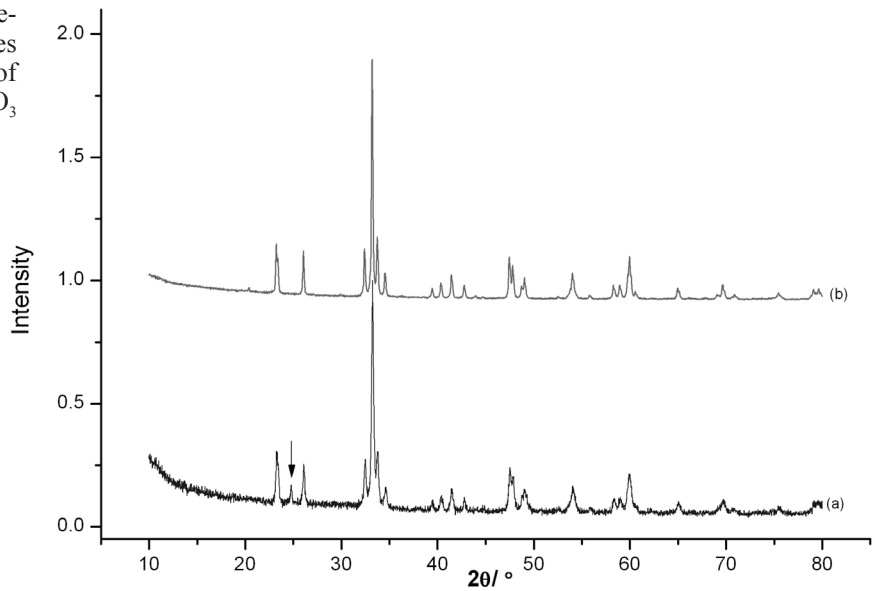

Fig. 1. XRD patterns of a) as-prepared $GdCrO_3$ (the arrow indicates the peak suggesting presence of $GdCrO_4$ as impurity) and b) $GdCrO_3$ heated for 2h at 800 °C

is a result of the continuous substitution of smaller Co^{3+} ion ($r(Co^{3+})$ = 0.545 Å) with the larger Cr^{3+} one ($r(Cr^{3+})$ = 0.65 Å) , leading to increasing of the lattice parameters from $GdCoO_3$ to $GdCrO_3$. These results showed that these two ions may be substituted in the whole range of x (form x = 0 to x = 1) and continuous solid solution may be formed.

The crystal structures of the perovskites within the $GdCo_{1-x}Cr_xO_3$ (x = 0, 0.33, 0.5, 0.67 and 1) series were refined using the Rietveld method (program Fullprof) and starting with the structural model of $GdCrO_3$ [30]. All perovskites within this series crystallize in *Pnma* space group (Z = 4) (Table 1). The selected distances and angles are given in Table 2.

The structural data for $GdCoO_3$ and $GdCrO_3$ are already reported in the literature, and the crystallographic data for mixed Co^{3+}, Cr^{3+} perovskites are given in this paper. The refined values of the unit cell parameters for $GdCoO_3$, a = 5.39074(12), b = 7.45514(17) and c = 5.22527(12) are close to the literature values [14, 16] and the obtained values for $GdCrO_3$, a = 5.52447(12), b = 7.60552(16) and

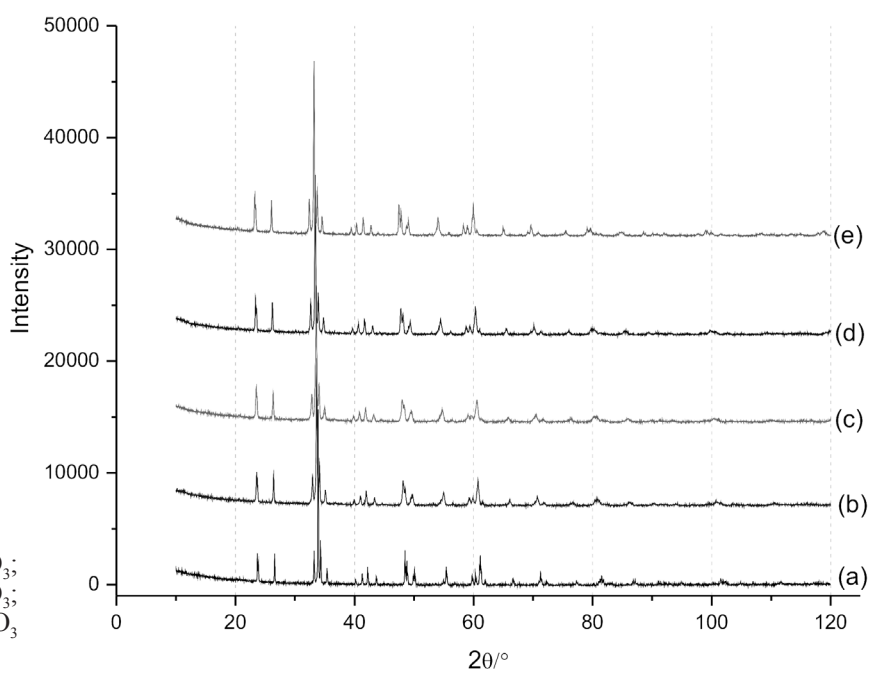

Fig. 2. XRD patterns of a) $GdCoO_3$; b) $GdCo_{0.67}Cr_{0.33}O_3$ c) $GdCo_{0.5}Cr_{0.5}O_3$; d) $GdCo_{0.33}Cr_{0.67}O_3$ and e) $GdCrO_3$ heated 4h at 800 °C

Table 1. Structural data from X-ray powder diffraction studies of $GdCo_{1-x}Cr_xO_3$ perovskites

Atoms	Parameters	$GdCoO_3$	$GdCo_{0.67}Cr_{0.33}O_3$	$GdCo_{0.5}Cr_{0.5}O_3$	$GdCo_{0.33}Cr_{0.67}O_3$	$GdCrO_3$
	a (Å)	5.39074(12)	5.4357(3)	5.4573(3)	5.4832(2)	5.52447(12)
	b (Å)	7.45514(17)	7.5046(4)	7.5280(4)	7.5572(3)	7.60552(16)
	c (Å)	5.22527(12)	5.2541(3)	5.2685(3)	5.28499(20)	5.31310(11)
Gd	*x*	0.05792(19)	0.05740(18)	0.05808(16)	0.05827(14)	0.05890(12)
	z	0.9870(5)	0.9858(4)	0.9850(3)	0.9860(3)	0.9852(2)
	B	0.06(4)	0.07(4)	0.17(3)	0.08(3)	0.25(2)
Co/Cr	*B*	0.08(7)	0.19(6)	0.12(5)	0.19(5)	0.01(4)
O1	*x*	0.4816(17)	0.4750(16)	0.4734(14)	0.4744(14)	0.4701(12)
	z	0.085(2)	0.0861(19)	0.0855(17)	0.0940(15)	0.0942(13)
	B	1.5(3)	1.8(3)	1.7(3)	1.4(3)	1.8(2)
O2	*x*	0.2958(17)	0.2949(15)	0.2969(14)	0.2960(12)	0.2968(10)
	y	0.0461(11)	0.0496(10)	0.0483(10)	0.0479(8)	0.0497(7)
	z	0.7085(18)	0.7091(17)	0.7056(15)	0.7022(13)	0.7035(10)
	B	0.5(3)	0.3(3)	0.5(2)	0.42(19)	0.87(16)
R_I	R_p:	22.9	17.6	16.6	15.4	12.1
	R_{wp}:	13.9	13.2	12.9	12.2	10.6
	R_{exp}:	12.57	10.92	11.16	10.87	9.82
	χ^2:	1.22	1.45	1.35	1.25	1.16
	R_B:	5.78	4.43	3.17	3.07	2.45

c = 5.31310(11), are also in good agreement to the literature values [13, 23].

In a series of solid solutions like this one it is important to investigate the structural distortions and the stability of the compounds resulting from the substitution of one cation with another. So, below is given the thorough structural study of the perovskites within this series. In order to quantify the structural distortion of the perovskite structure, usually the first step is to calculate the well known Goldshmidt tolerance factor, *t* [31]. It is calculated according to the equation $t = (r(A) + r(O))/\sqrt{2}(r(B) + r(O)$, taking into account the ionic radii of the constitutent metals regarding the A-cation as twelve coordinated, and B-cation and O as six coordinated. The boundaries of *t* for perovskite structure are from 0.78–1.05 [32], and it is expected that in compounds with increasing distortion from ideal perovskite structure the tolerance factor will shift to lower values. The obtained *t*-values for the investigated compounds are at the lower limit for perovskite structure and are suggesting distorted structures. The values of

Table 2. Selected distances and angles in $GdCo_{1-x}Cr_xO_3$ perovskites

	$GdCoO_3$	$GdCo_{0.67}Cr_{0.33}O_3$	$GdCo_{0.5}Cr_{0.5}O_3$	$GdCo_{0.33}Cr_{0.67}O_3$	$GdCrO_3$
Gd – O1	3.149	3.209	3.234	3.252	3.304
Gd – O1	2.341	2.33	2.328	2.352	2.344
Gd – O1	3.017	3.038	3.041	3.1	3.117
Gd – O1	2.274	2.293	2.31	2.267	2.288
Gd – O2 x 2	2.464	2.458	2.484	2.506	2.508
Gd – O2 x 2	2.313	2.312	2.312	2.322	2.329
Gd – O2 x 2	3.323	3.36	3.384	3.4	3.434
Gd – O2 x 2	2.614	2.66	2.65	2.648	2.679
$<Gd – O>_9$	2.490	2.502	2.508	2.519	2.531
Co – O1 x 2	1.919	1.935	1.941	1.959	1.9731
Co – O2 x 2	1.962	1.979	1.983	1.977	2
Co – O2 x 2	1.91	1.928	1.941	1.965	1.971
$<Co – O>_6$	1.930	1.947	1.955	1.967	1.981
B – O1 – B	152.56	151.74	151.77	149.43	149.01
B – O2 – B	151.6	150.7	150.3	150.1	149.6

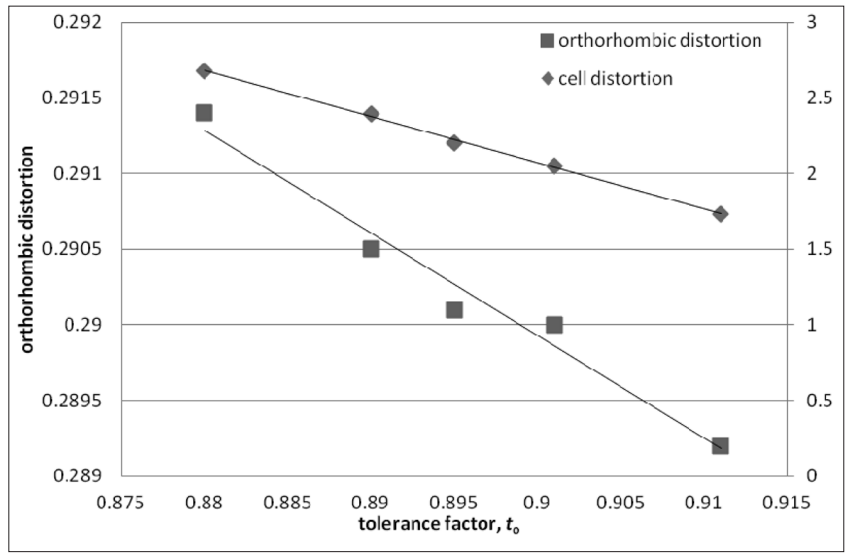

Fig. 3. Relationship between the tolerance factor and the orthorhombic distortion and distortion of the unit cell in the analyzed series $GdCo_{1-x}Cr_xO_3$

t for the investigated series are decreasing from 0.911 for $GdCoO_3$ to 0.880 for $GdCrO_3$ (Table 3).

Both end members of the series $GdCoO_3$ and $GdCrO_3$ are orthorhombicaly distorted perovskites [13, 14, 16, 23]. As expected, the middle members of the series are also distorted orthorhombic perovskites and the values of the unit cell parameters are increasing from $GdCo_{0.67}Cr_{0.33}O_3$ to $GdCrO_3$ (Table 1). The relationship between the unit cell parameters in these compounds is $b > c/\sqrt{2} > a$ as in O-type perovskites, where the tilting of the octahedra is the primary source of deformation (Fig. 3). This trend is maintained throughout the entire series. Using the values of the unit cell parameters two crystallographic parameters were calculated – cell distortion [33] and orthorhombic distortion [6] (Table 3). The obtained values point out that the distortion of the unit cell (from ideal cubic) increases with Cr con-

Table 3. Crystallographyc parameters of $GdCo_{1-x}Cr_xO_3$ perovskites

	$GdCoO_3$	$GdCo_{0.67}Cr_{0.33}O_3$	$GdCo_{0.5}Cr_{0.5}O_3$	$GdCo_{0.33}Cr_{0.67}O_3$	$GdCrO_3$
t	0.911	0.901	0.895	0.89	0.88
cell distortion	1.731	2.048	2.199	2.395	2.677
orthorhom. distortion	0.2892	0.2900	0.2901	0.2905	0.2914
Δ_9	7.906	8.634	8.374	9.459	9.779
Δ_{10}	12.727	14.138	14.244	15.234	16.186
Δ_6	0.138	0.134	0.103	0.014	0.044
θ/°	13.722	14.131	14.116	15.283	15.493
φ/°	9.931	9.763	10.362	10.62	10.571
Φ/°	16.882	17.119	17.448	18.538	18.683
BV-A	3.276	3.219	3.16	3.12	3.04
BV-Co	2.721	2.598	2.544	2.46	/
BV-Cr	/	3.287	3.218	3.112	2.995
GII	0.199	0.189	0.183	0.161	0.054

Note: For the calculation of cell distortion first the value of a_p (pseudocubic a parameter) was found according the equation: ap = (a/√2 + *b*/√2 + c/2)/3 and then it was used to obtain the cell distortion as: $[(a/\sqrt{2} - a_p)^2 + (b/\sqrt{2} - a_p)^2 + (c/2 - a_p)^2]/3a_p$ [33]. The orthorhombic distortion was calculated using the equation: $\{[\Sigma(a_i - a)^2]^{1/2}\}/a$, where $a_i = a$, b, $c/\sqrt{2}$ and a is an average of a_i [6]. The calculation of the polyhedron bond length distortion parameters Δ_9, Δ_{10} and Δ_6 was performed using the equation: $\Delta = \Sigma[(r_i - r)/r]/n \times 10^3$, where r_i is individual bond length (A − O or B − O), r is the average bond length and n is a number of bonds [34]. The tilt angles are calculated using the fractional atomic coordinates of oxygen atoms [1]. For the calculation of bond valence the used equations are: $s_i = \exp(r_o - r_{i,j})/B$ and $BV = \Sigma s_i$, where r_o is empirical parameter, $r_{i,j}$ is the bond distance and $B = 0.37$ [35]. The global instability index was calculated using the equation $GII = [(\Sigma d_i^2)/N]^{1/2}$, where d_i is the discrepancy between calculated BV and theoretical oxidation number [36].

tent. These results are in accordance with expected increase in the deformation of the structure obtained from the values of the tolerance factor.

The refined values of the fractional atomic coordinates (Table 1) were used to calculate different structural parameters. These parameters were also used to analyze the contribution of the particular cation in the compound to the structural distortions within the series. Firstly, the change in the surrounding of the gadolinium ion was considered. In the ideal cubic perovskites the coordination of the A-cation is 12 but in orthorhombic perovskites the coordination number is usually lowered to 10, 9 or 8. In this series of perovskites the coordination of Gd^{3+} is becoming more distorted as the content of Cr^{3+} is increasing. This may be noticed from the values of the Gd−O distances, which are increasing with enhancement of the substitution of Co^{3+} ion. As a consequence, the coordination number of Gd^{3+} changes and it is lowered from 10 in $GdCoO_3$ to 9 in $GdCrO_3$. This effect is also obvious from the values of the polyhedron bond length distortion Δ_9 and Δ_{10}. Namely, these parameters are reflecting the deformation of the distances in the coordination polyhedron. It may be noticed that the highest values are obtained for $GdCrO_3$.

Contrary to the trend in deformation of the coordination of gadolinium ion the deformation of the B-cations (Co^{3+} and/or Cr^{3+}) octahedra is decreasing from $GdCoO_3$ to $GdCrO_3$ (Table 3). Although the Co/Cr−O bond lengths (Table 2) are increasing the polyhedron bond length distortion parameter, Δ_6, is decreasing (Table 3) in the same direction. This parameter shows that the distortion of the bonds in the octahedra is decreasing and the octahedron is becoming more regular. The obtained values for the first members of the series are relatively high, especially if we compare them to the values of Δ_6 in ferrites ($GdFeO_3$, $\Delta_6 = 0.032$) [1], but they remain still smaller than the values found in manganites, where Mn^{3+} is a Jahn-Teller ion ($GdMnO_3$, $\Delta_6 = 6.701$) [37]. It is interesting to note that as the octahedron becomes more regular across the series, the tilt angles are increasing. Namely, if the values of the tilt angles (φ, θ, and Φ), calculated using the atomic coordinates of oxygen atoms [1] are compared, it could be stated that these values are increasing with increasing of x. From these results it may be concluded that importation of chromium ion in place of Co^{3+} makes the octahedron more regular in respect to its bond lengths but in the same time it is more tilted.

The increase in the tilting angle of the octahedra is reflected in lowering of the B−O1−B and B−O2−B angles. From Table 2 it is evident that these angles are substantially different from 180° – the value characteristic for ideal cubic perovskites. These low values are suggesting smaller Co/Cr-3d and oxygen-2p orbital overlap. Namely, as the angle is increased and approaches 180°, a greater overlap is achieved. This overlap directly controls the interaction integral β, which is proportional to the width of the Co/Cr–O bands [38].

The bond length and the valence of the bond are related in the bond valence model given by I. D. Brown [35]. The calculated values of the bond valence of cations are also presented in Table 3. It is obvious that there are positive and negative deviations from the theoretical values of the oxidation states of the cations. The values for the Gd^{3+} and Cr^{3+} ions are larger than the theoretical ones, which suggests that the average Gd−O and Cr−O distances in these compounds are shorter than the average bond distances in other oxides containing Gd or Cr compounds. It is also obvious that the values for the bond valence of cobalt ion are becoming smaller throughout the series (Table 3) with pronounced differences from the theoretical value. The values for the bond valence are used to calculate the global instability index,

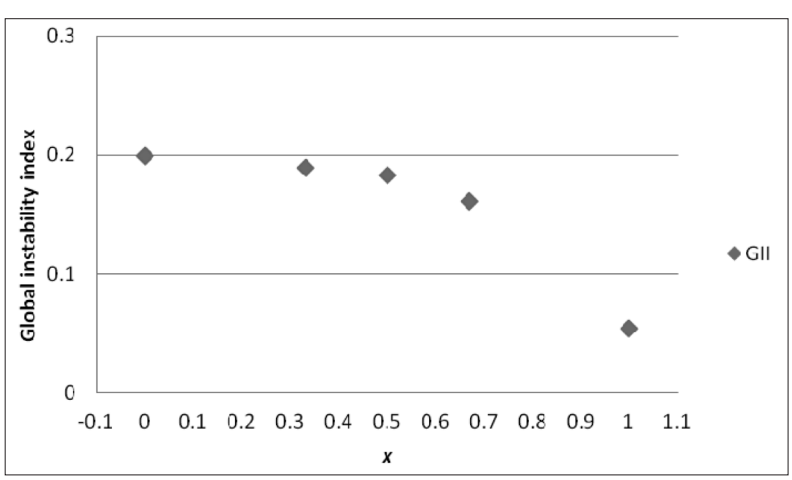

Fig. 4. Change of the global instability index with increasing x in the series $GdCo_{1-x}Cr_xO_3$

GII. This index reflects the overall stress in the structure. The values of GII are usually smaller than 0.1 in structures without internal stress, the values between 0.1 and 0.2 are characteristic for compounds with lattice-induced strains, and higher than 0.2 - for unstable structures [36]. From the calculated values of GII it may be pointed that $GdCrO_3$ (GII = 0.054) meets the requirement for structure without internal stress (Fig. 4) and GII for cobalt containing compounds within the series (of values between 0.1 and 0.2) indicate existence of lattice-induced strains.

CONCLUSION

The complex perovskites of general formula $GdCo_{1-x}Cr_xO_3$ (x = 0, 0.33, 0.5, 0.67 and 1) were obtained by solution combustion method using urea as a fuel. The Rietveld refinement of the crystal structures showed that they crystallize in *Pnma* with Z = 4. According to the lattice parameters and the distances and angles in the compounds, several important parameters were calculated indicating the influence of the mutual substitution of Co^{3+} with Cr^{3+} to the distortion and stability of the perovskite structure. Thus, it was concluded that by increasing of the content of Cr^{3+} ions in the perovskite structure the BO_6 octahedron becomes more regular but the tilting of octahedron is more pronounced. Also the deformation of Gd-O polyhedron increases with increasing of the Cr^{3+} content. The calculated bond valences and global instability indices indicate for existence of lattice-induced strains in the structure of the cobalt containing compounds.

***Acknowledgements**: The authors thank the National Science Fund of Bulgaria and the Ministry of Education and Science of Republic of Macedonia for the financial support under contract DNTS/ Macedonia 01/7/08.12.2011.*

REFERENCES

1. R. H. Mitchell, Perovskites: Modern and Ancient, Almaz press – Thunder Bay, 2002.
2. F. S. Galasso, Perovskites and High Tc Superconductors, Gordon and Breach Science Publishers, 1990.
3. M. A. Peña, J. L. G. Fierro, *Chem. Rev*., **101**, 1981 (2001).
4. T. Ishihara (Ed), Perovskite Oxide for Solid Oxide Fuel Cells (Fuel Cells and Hydrogen Energy), Springer, Dordrecht, 2009.
5. S. Yamaguchi, Y. Okimoto, Y. Tokura, *Phys. Rev. B*, **54**, R11022 (1996).
6. K. Knížek, Z. Jirák, J. Hejtmánek, M. Veverka, M. Maryško, G. Maris, T. T. M. Palstra, *Eur. Phys. J. B*, **47**, 213 (2005).
7. A. Fondado, J. Mira, J. Rivas, C. Rey, M. P. Breijo, and M. A. Señarís-Rodríguez, *J. App. Phys*., **87**(9), 5612 (2000).
8. H. W. Brinks, H. Fjellvåg, A. Kjekshus, B. C. Hauback, *J. Solid State Chem*., **147**, 464 (1999).
9. J.-W. Moon, Y. Masuda, W.-S. Seo, K. Koumoto, *Mater. Sci. Eng. B*, **85**, 70 (2001).
10. M. V. Kuznetsov, I. P. Parkin, *Polyhedron*, **17**, 4443 (1998).
11. A. K. Tripathi, H. B. Lal, *J. Mater. Sci.,* **17**, 1595 (1982).
12. B. Rajeswaran, D. I. Khomskii, A. Sundaresan, C. N. R. Rao, *Phys. Rew. B*, in press.
13. K. Yoshii, *J. Solid State Chem.*, **159**, 204 (2001).
14. S. V. Kurgan, G. S. Petrov, L. A. Bashkirov, A. I. Klyndyuk, *Inorg. Mater*., **40**, 1224 (2004).
15. H. B. Lal, R. D. Dwivedi, K. Gaur, *J. Mater. Sci.: Mater. Electron*., **1**, 204 (1990).
16. W. Wei-Ran, X. Da-Peng, S. Wen-Hui, D. Zhan-Hui, X. Yan-Feng, S. Geng-Xin, Chin. *Phys. Lett*., **22**, 2400 (2005).
17. P. S. Devi, *J. Mater. Chem*., **3**, 373 (1993).
18. R. A. da Silva, R. N. Saxena, A. W. Carbonari, G. A. Cabrera-Pasca, *Hyperfine Interact*., **197**, 53 (2010).
19. N. B. Ivanova, N. V. Kazak, C. R. Michel, A. D. Balaev, S. G. Ovchinnikov, A. D. Vasil'ev, N. V. Bulina, E. B. Panchenko, *Phys. Solid State*, **49**, 1498 (2007).
20. P. A. Brayshaw, A. K. Hall, W. T. A. Harrison, J. M. Harrowfield, D. Pearce, T. M. Shand, B. W. Skelton, C. R. Whitaker, A. H. White, *Eur. J. Inorg. Chem*., 1127 (2005).
21. Y. Seto, K. Umemoto, T. Arii, Y. Masuda, *J. Therm. Anal. Calorim*., **76**, 165 (2004).
22. R. Sawano, Y. Masuda, *J. Therm. Anal. Calorim*., **92**, 413 (2008).
23. K. Sardar, M. R. Lees, R. J. Kashtiban, J. Sloan, R. I. Walton, *Chem. Mater*., **23**, 48 (2011).
24. A. Jaiswal, R. Das, S. Adyanthaya, P. Poddar, *J. Nanopart. Res.*, **13**, 1019 (2011).
25. A. Patil, S. C. Parida, S. Dash, V. Venugopal, *Thermochimica Acta*, **465**, 25 (2007).
26. F. H. M. Cavalcante, A. W. Carbonari, R. F. L. Malavasi, G. A. Cabrera-Pasca, R. N. Saxena, J. Mestnik-Filho, J. Magn. Magn. Mater., 320, 32 (2008).
27. A. L. A. da Silva, G. G. G. Castro, M. M. V. M. Souza, *J. Therm. Anal. Calorim*., 1000 (2011).
28. K. C. Patil, M. S. Hegde, T. Rattan, S. T. Aruna, Chemistry of nanocrystalline oxide , World Scientific Publishing, Singapore, 2008.
29. A. S. Mukasyan, C. Costello, K. P. Sherlock, D. Lafarga, A. Varma, *Sep. Purif. Technol*., **25**, 117 (2001).
30. JCPDS International Center for Diffraction Data, Power Diffraction File (entry 00-025-1056), Swarthmore, PA, 1995.
31. V. M. Goldschmidt, *Naturwiss*., **14**, 477485 (1926).
32. P. M. Woodward, *Acta Cryst*., **B53**, 44 (1997).
33. G. Huo, D. Song, Q. Yang, F. Dong, *Ceram. Int*., **34**, 497 (2008).
34. R. D. Shannon, *Acta Crystallogr.*, **A32**, 751 (1976).

35. I. D. Brown, D. Altermatt, *Acta Crystallogr*., **B41**, 244 (1985).
36. M. W. Lufaso, P. M. Woodward, *Acta Crystallogr*., **B57**, 725 (2001).
37. Y. Chen, H. Yuan, G. Li, G. Tian, S. Feng, *J. Cryst. Growth*, **305**, 242 (2007).
38. G. Ch. Kostogloudis, N. Vasilakos, Ch. Ftikos, *Solid State Ionics*, **106**, 207 (1998).

СТРУКТУРНО ХАРАКТЕРИЗИРАНЕ НА $GdCo_{1-x}Cr_xO_3$ (x = 0, 0.33, 0.5, 0.67, 1) ПЕРОВСКИТИ

С. Димитровска-Лазова[1]*, Д. Ковачева[2], П. Цветков[2]

[1] Университет „Св. Кирил и Методии“, Факултет по Естествени науки и Математика, Архимедова 2, Скопие, Македония
[2] Институт по обща и неорганична химия, Българска академия на науките, „Акад. Г. Бончев“ бл.11, София, България

Постъпила на 21 март, 2012 г.; приета на 2 май, 2012 г.

(Резюме)

В статията са представени синтез, определяне на кристалната структура и калкулирани структурни параметри за серията $GdCo_{1-x}Cr_xO_3$ (x = 0, 0.33, 0.5, 0.67 и 1). Съединенията са получени по метода на комбустия през разтвор, като са използвани нитрати на съответните метали и урея за гориво. Серията получени перовскити кристализират в пространствена група *Pnma*, Z = 4. Определените параметри на елементарната клетка, разстояния и ъгли са използани за пресмятане на някои кристалографски параметри, като дисторзия на елементарната клетка, орторомбична дисторзия, деформация на разстояния и ъгли, ъгли на накланяне, сума на валентните връзки и глобален индекс на нестабилност. Тези параметри са използвани да се изясни по-добре влиянието на заместването на Co^{3+} с Cr^{3+} върху степента на деформация и стабилност на перовскитовата структура.

Bulgarian Chemical Communications, Volume 44, Proceedings of the III[rd] National Crystallographic Symposium (pp. 55–62) 2012

Molten Zn-exchanged clinoptilolite – structural behaviour and properties at high temperature

L. T. Dimowa[1]*, S. L. Petrov[2], B. L. Shivachev[1]

[1] *Institute of Mineralogy and Crystallography, Bulgarian Academy of Sciences, "Acad. Georgi Bonchev" str. building 107, Sofia 1113, Bulgaria*
[2] *Department of Chemistry, University of Toronto, 80 St. George Street, Toronto, ON, M5S 3H6 (Canada)*

Received March 20, 2012; Revised May 5, 2012

A molten exchange of $ZnCl_2$ in clinoptilolite is reported for the first time. The molten exchange occurs under solid state conditions and decreases significantly the time that is necessary for reaching a full exchange. This provides a potential alternative to the classical ion-exchange in liquids. The mechanism of the incorporation of Zn^{+2} cations in the channels of CPT-framework (their positions, Zn-content and movements along the channels) was evaluated at different temperatures by *in situ* high temperature (HT) X-ray diffraction. It is shown that molten exchanged Zn-CPT possesses a firm framework, which is thermally more resistant than natural CPT, due to the locations of Zn^{+2} cations in the eight-member channel.

Key words: clinoptilolite, zeolite, molten exchange, X-ray diffraction.

INTRODUCTION

The ion-exchange technique has been considered as an important method for improving technological properties of various natural zeolites by changing their cation content. In the ion-exchange process the cations easily exchange each other and the new ones integrate and adjust themselves in various positions into the system of pores and channels. The cation-exchanged zeolites commonly preserve their micro-porous structures unaffected. The process of ion-exchanging in zeolites is typically carried out by replacing Na^+ [1–3] with different ions, such as Ag^{2+}, K^+, Cs^+ and Sr^{2+} or through a pre-exchange of zeolite to its H-form [4] and further exchange the H-form with metal ions. Zinc-containing microporous materials (including natural zeolites) have drawn attention because of their antibacterial [5–7] and anti-tumor [8] properties. In contrast, formation of toxic ZnO-nanoclusters has been also reported [9]. Interestingly, results for ion-exchange of natural clinoptilolite (CPT) with Zn^{2+} salts, are almost missing [10–11] probably because of intrinsic difficulties of incorporation of Zn^{2+} in CPT structure at ambient temperatures (around 60–100 °C). Because of this, a classic liquid ion-exchange of Zn^{2+} in CPT commonly requires prolonged time for a sufficient high-rate Zn-exchange to take place. In this case, an alternative cation-exchange approach - the molten exchange was carried out. The molten exchange requires significantly less time – only a few hours [12, 13]. The major benefit of this approach is the improved stability of the initial CPT-structure at higher temperatures than the exchanged CPT-structure obtained by a common liquid ion-exchange [in preparation].

In this work, Zn-containing clinoptilolite (Zn-CPT) was produced by using a molten-exchange process. A NH_4^+ exchanged intermediate product (NH_4-CPT) was obtained from clinoptilolite rich tuff ("Beli plast", Khardjali) and $ZnCl_2$ was used as the Zn-source. The experimental results for the weight losses, the thermal stability of the CPT-structure under *in situ* heating, the unit cell variations and the diffusion of Zn^{2+} in clinoptilolite's structure are discussed below.

EXPERIMENTAL

Molten exchange

In our molten-exchange experiment, CPT was chosen as a substrate and $ZnCl_2$ (1:1 mass) - as the ion source. The CPT-substrate was subjected to preliminary removal of concomitant minerals such as quartz, plagioclase, mica, and then was NH_4^+ ex-

* To whom all correspondence should be sent:
E-mail: louiza.dimova@gmail.com

changed in order to ensure the optimal exchange conditions. The molten-exchange temperature and the processing times were varied (360–400 °C and 30 to 360 minutes). Optimal temperature and time were found to be 380 °C and 240 minutes.

X-ray diffraction

The structural properties of the samples were analyzed with *in situ* HT X-ray powder diffraction (equipment: Bruker D2 Phaser, Cu-Kα radiation and Dron 3M, Co-Kα radiation). The *in situ* heating was conducted from room temperature (RT) to 800 °C using an in house temperature device. The heating scheme was: 100 °C step and 30 minutes retention time. Data collection was carried out at each HT-step with scan speed 0.02 °/sec. on a range from 5–35° 2-theta.

Rietveld Refinement

Rietveld analysis on the powder X-ray diffraction patterns was carried out with Topas v.3.0 [14] suite of programs. A pseudo-Voight profile function was used. Profile parameters (2θ zero correction, background, cell parameters) were refined first and then the positional parameters (locations and site occupancies) of Zn^{2+} cations at various temperatures: RT, 300 °C and 500 °C. Unit cell parameters for all samples (RT to 800 °C) were calculated primary by Pawley-extraction.

DTA/TG-MS

The weight losses were monitored by DTA/TG-MS on Setaram Setsys DTA/TG equipment coupled with a Thermo Scientific mass spectrometer for evolved gas analysis (EGA). The experiment was carried out by placing approximately 15–20 mg of the Zn-CPT sample into a corundum crucible and heating at a rate of 10 °C min^{-1} from ambient temperature to 700 °C under flowing (20 mL min^{-1}) high purity argon gas. Baseline curves measured under the same experimental conditions were acquired to account for buoyancy effects on the balance. The mass to charge ratios selected for analysis were 18, 35.5 and 65.4 amu. A one second acquisition time for each mass unit was set, thus requiring 0.13 min (or 1.3 °C) for each cycle. The chemical composition of the samples was determined by ISP-OES, apparatus Varian Vista MPX CCD simultaneous analyses.

Chlorine determination

One of the most widely used methods for the determination of chlorides at relatively low levels and where the error is in the range of 1–2% is the Mohr's method [15]. It is based on the reactions and the formation of hardly soluble precipitates with the condition that the reaction of precipitation is fast and that there is a true indicator that shows the end of the titration. To determine the concentration of chloride, samples were prepared as follows: the sample has been transferred into Erlenmeyer flask and diluted by distilled water (about 100 ml) and added 2 ml of 5% K_2CrO_4. Titration of the sample prepared in this way was carried out with standard solution of 0.0975 mol l^{-1} $AgNO_3$ under constant steering of the solution. Titration was completed when a reddish solution appeared. The obtained concentration for Cl^- was 11 (±0.09) g l^{-1}.

The Fourier transform infrared (FTIR) spectra were recorded on a Bruker Tensor 37 spectrometer at a resolution of 4 cm^{-1} accumulating 50 scans (in this case the samples were prepared in the form of KBr pellets).

RESULTS AND DISCUSSION

The chemical compositions of the starting NH_4-CPT and molten exchanged Zn-CPT are shown in Table 1. It is obvious that the amount of cations in the NH_4-CPT is very low with respect to the natural poly-cationic CPT [16]. Interestingly, the Zn^{2+} content in the molten exchanged CPT is 14.32 wt.% – a value significantly higher compared with the one in liquid ion-exchanged CPT-Zn (2.2 wt.%, 30 days at 100 °C [16]). The incorporation of Zn^{2+} in the channels of CPT structure causes visible changes in the intensities of some diffraction peaks in the pattern, which is another ultimate proof for the conducted cation exchange. A comparison of the powder diffraction patterns of Zn^{2+} CPT and non-exchanged CPT are shown on Figure 1. The changes on the XRD patterns are basically the same as previously established [16]: in Zn-CPT the 220 peak disap-

Table 1. Chemical composition (ICP-OES) of initial CPT and after molten exchange process

Oxides	NH_4-CPT	Zn-CPT
	wt.%	
SiO_2	68.19	57.08
Al_2O_3	12.51	10.32
CaO	0.06	0.20
Na_2O	0.09	0.09
K_2O	0.19	0.19
MgO	0.26	0.10
ZnO	–	14.32
LOI (1000 °C)	18.7	17.70

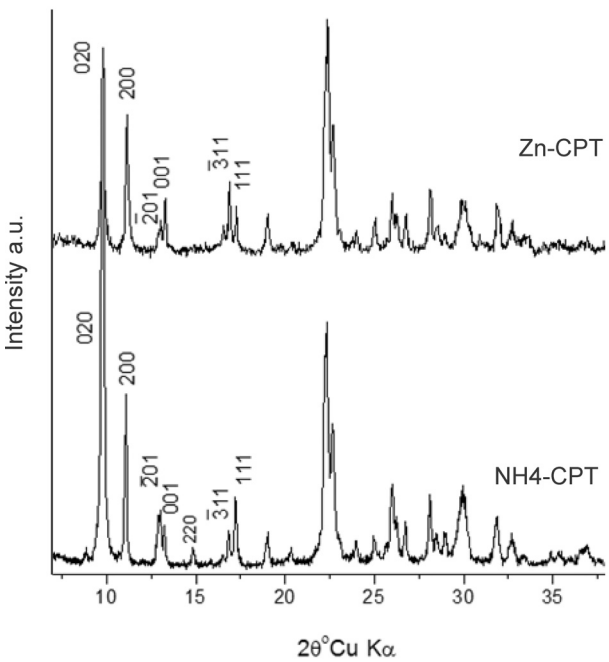

Fig. 1. XRD patterns of NH_4^+ and Zn exchanged CPT

pears, the intensities of 020, 311 and 001 increase while the intensity of 111 decreases. Our opinion is that the observed changes of the intensities of some diffraction peaks in Zn-CPT are due to the locations of the "heavy" Zn^{2+} cations in certain positions within the channels, which reasonably changes the structural factors of certain atomic plains (hkl).

The calculated from the chemical analysis formula of our molten exchanged Zn-CPT is:

$$Zn_{5.43}Na_{0.09}Ca_{0.11}K_{0.06}Mg_{0.08}Si_{29.33}Al_{6.25}O_{72} \times n.H_2O. \quad (1)$$

There are two remarkable features of this chemical composition:

1. Zn content is 5.43 APU, providing a theoretical positive charge of 10.86. This value is higher than the negative charge (from Al) of 6.25. However, "Cl^-" is not included in the above chemical formula as it was undetectable by ICP-OES.

2. The value of ~18 wt.% for the losses on ignition (LOI) is higher than the TG losses. Normally losses are associated with volatile compounds. In our case, such are: the water molecules located in the CPT channels, the residual NH_4^+ (the band at ~1400 cm^{-1} observed in the FTIR spectrum (Fig. 2.), and the Cl^- coming from $ZnCl_2$ source.

The results from the wet analysis (Mohr's titration) yield a presence of ~11% Cl. This value is quite close to one evaluated from the difference of the LOI-TG ($17.7_{LOI\ 1100°C} - 8.5_{\ TG\ 700°C} = 9.2$). Note that the humidity was not monitored and, therefore, the obtained value (for the "loss difference") is only an indicative one.

The DTA/TG-MS curves of the Zn-CPT sample are shown on Fig. 3. These curves show two distinct regions. Region 1 includes the data carried out from room temperature to 450 °C and Region 2 – above 450 °C. Each of these regions is characteristic of a mass loss step (TG), with combined mass losses of ~9%. The TG curve for Zn-CPT is plotted with a selected range of MS mass-to-charge ratio curves (in *amu*) on Fig. 3 for better visualization and characterization of each mass loss step.

Region 1 is linked to the evolution of water and/or NH_4^+ (18 *amu*) with peaks in the DTA curve observed at 68, 160, 213 and 314 °C. The maximum of the peak in the MS 18 *amu* curve is around 140 °C and continues up to ~ 400 °C. The observed DTA maxima may be accounted for different types of water-cations bonds and variations in water-framework molecular interactions.

Thermal decomposition of the analyzed Zn-CPT is not observed throughout the experiment.

Region 2 starts from ~500 °C and continues to 700 °C. The mass loss for Region 2 appears to be insignificant (~1%).

Remarkably, no Zn^{+2} or Cl^- could be detected up to 700 °C by TG-MS (the curves of the water/ammonium, Zn^{+2} and Cl^- mass-fragments have been shown for comparison) and no clear and pronounced decomposition (destruction) effect is observed on the DTA curve.

The diffraction patterns from *in situ*-HT XRD analysis are in good agreement with the DTA/TG-

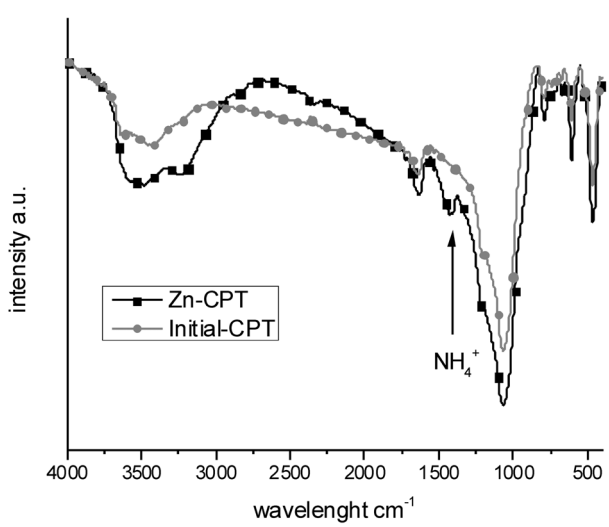

Fig. 2. FTIR for initial and Zn-CPT samples; the 1414 cm^{-1} mode is associated with NH_4^+ stretching

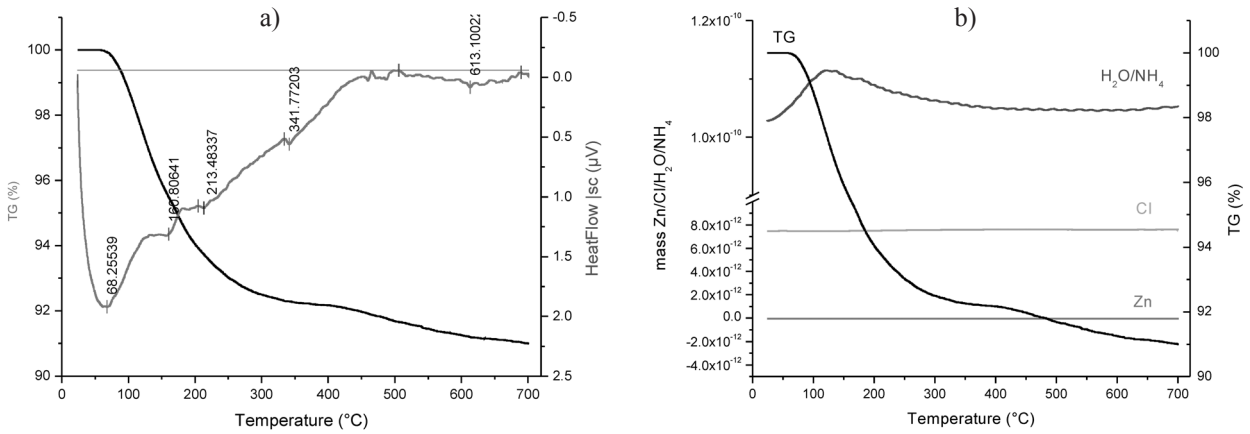

Fig. 3. (a) DTA/TG for Zn-CPT (b) TG-MS for Zn-CPT

MS results showing no collapse of the CPT structure up to 700 °C (Fig. 4). The diffraction patterns taken from heated Zn-CPT (from RT to 700 °C) clearly indicate that the overall structure remains unchanged up to 700 °C. Indeed, HT-diffraction patterns do not show any significant structural changes in the framework. As expected, there are some variations of the unit cell as a function of the temperature and they are shown on Fig. 5 and Table 2. It was found that the heating affects mainly *b* parameter, while *a*, *c* and *β* remain almost unchanged. The collapse of the Zn-CPT structure is not accompanied by a collapse of the B channel (Table 3). Some elongation of A-channel semi-major axis is observed but the values of the semi-axis for B-channel are basically unaffected. The variation of the eccentric-

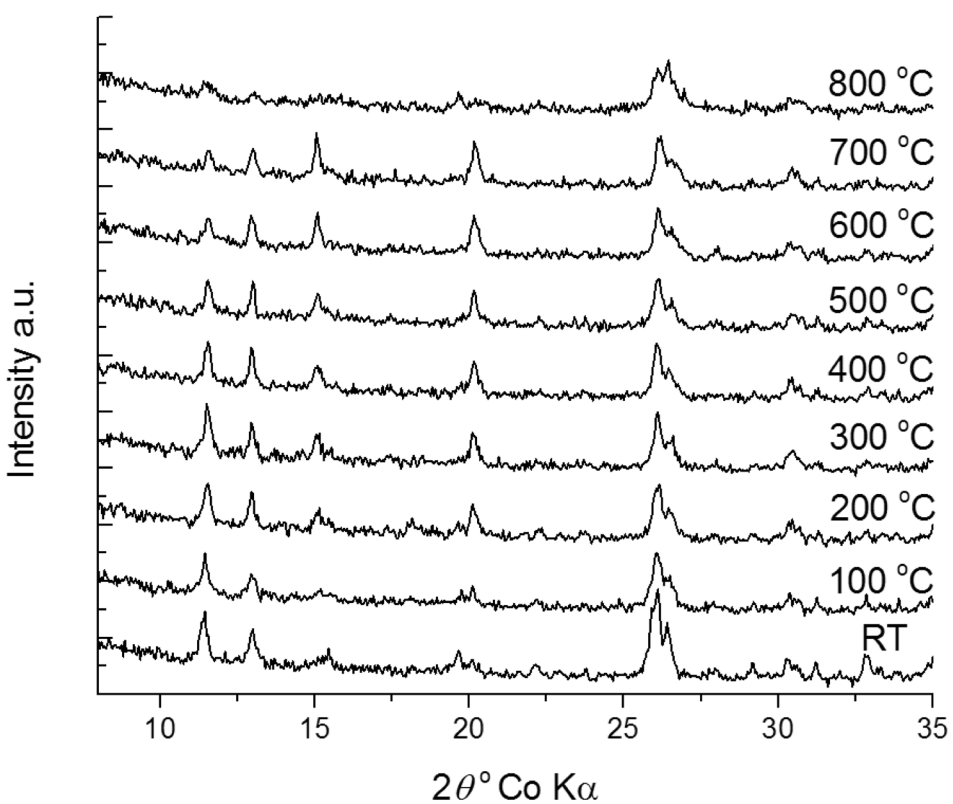

Fig. 4. Zn-CPT diffraction patterns from *in situ*-HT XRD analysis (RT –800 °C)

Table 2. Unit cell parameters for all samples (RT to 800 °C) calculated by Pawley-extraction[1] and by Rietveld method[2] along with R_{wp} value

°C	*a*	*b*	*c*	*β*	V	R_{wp}
RT[1]	17.664(12)	17.999(13)	7.404(3)	116.109(25)	2111.60(2.4)	11.136
RT[2]	17.642(15)	17.978(16)	7.401(4)	116.078(38)	2108.49(3.0)	11.201
100[1]	17.660(21)	17.941(23)	7.398(6)	116.162(41)	2104.12(2.3)	11.723
200[1]	17.685(10)	17.873(12)	7.405(3)	116.073(31)	2103.22(2.2)	12.821
300[1]	17.681(14)	17.900(17)	7.405(4)	116.049(33)	2105.53(2.6)	12.333
300[2]	17.688(16)	17.863(15)	7.401(4)	116.134(42)	2099.33(3.0)	11.351
400[1]	17.679(10)	17.850(15)	7.399(3)	116.103(33)	2096.92(2.5)	11.301
500[1]	17.659(12)	17.847(13)	7.395(4)	116.074(35)	2093.55(2.5)	12.192
500[2]	17.658(17)	17.823(21)	7.383(5)	116.08935)	2086.65(3.2)	12.981
600[1]	17.658(14)	17.815(18)	7.391(4)	116.161(32)	2086.72(3.1)	11.643
700[1]	17.639(17)	17.758(15)	7.391(4)	116.240(41)	2076.92(2.9)	12.176

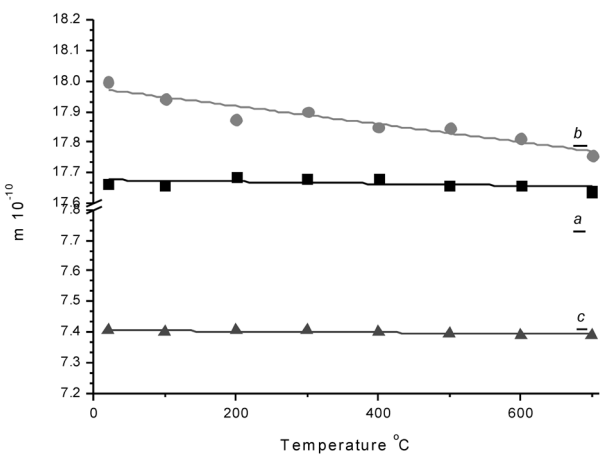

Fig. 5. Variations of the unit cell parameters of Zn-CPT in function of the temperature

ity is different for both channels: for A-channel it increases towards a value of 1 – thus, the shape is more compressed (elongated) along the semi-minor axis, while for B-channel the decrease leads to more spherical shape of the channel. Similarly to ref. [17], we could not associate a collapse phase or trend unit cell/channel shape to the collapse of the structure. However, as both *in situ*-HT XRD and DTA data have been collected for a relatively short period of time (4 hours of total heating time), the effect may have not been well expressed. One reason could be that the structure was not allowed to "relax" due to insufficient time.

Rietveld method was applied mainly for evaluating unit cell parameters and locating the atoms in the CPT channels. The performed Rietveld refinement of the XRD patterns locates water molecules in heated samples up to 200 °C. The location of water molecules by XRD cannot be evaluated correctly because most of the positions are not fully occupied and the heating increases their thermal displacement/diffusion inside the CPT channels. As a result, the electron density associated with water molecules is very shallow and is not clearly visible on the [F_o-F_c] difference map. On the other hand, as Zn^{+2} cation possesses more electrons than Si^{+4} and Al^{+3} (the main building units of the CPT framework), we expected its main locations in the CPT channels to be accessed by Rietvled analysis. The total amount of Zn located in the CPT channels is in agreement with the ICP-OES data (5.43 from ICP vs 5.64 at RT, 5.44 at 300 °C and 5.47 at 500 °C). The positions of Zn^{+2} cations, in both A- and B-channels as they were assigned from Rietveld refinement are shown on Fig. 6 and Table 4.

At ambient conditions (RT) four different Zn^{+2} positions are found: three in A-channel ("Zn1", "Zn2" and "Zn3") and one in B-channel ("Zn4"). The "Zn4" position in B-channel sits close to the well established Ca^{2+} (M2) position in natural clinoptilolite [18]. Two of the positions in A-channel, "Zn1" and "Zn2", are located close to its center. The "Zn1"

Table 3. Variation of major (h index) and minor (v index) semi-axes for A- and B-channels

Temperature [°C]	size [Å]			
	$A1_h$	$A2_v$	$B2_v$	$B1_h$
20 (RT)	9.08	6.02	6.07	6.44
300	9.45	5.99	6.34	6.43
500	9.49	5.95	6.31	6.45

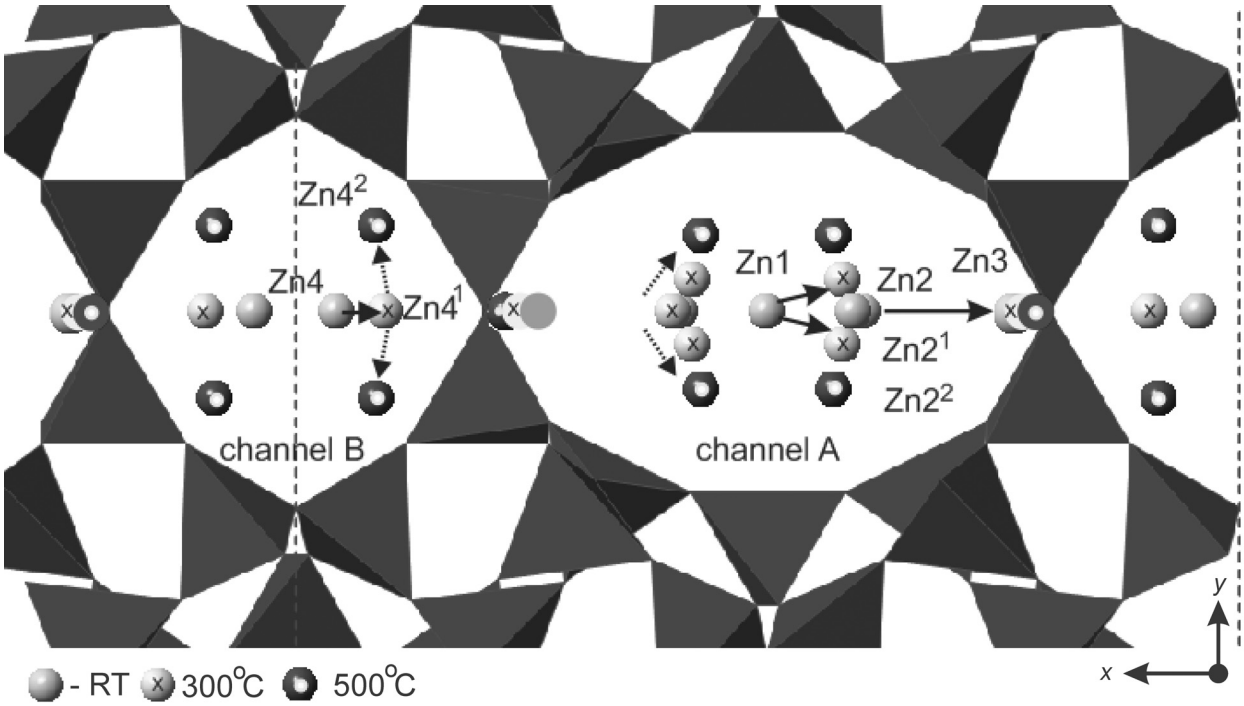

Fig. 6. The positions of Zn^{+2} cations in both A- and B-channels as they were assigned from Rietveld refinement. The positions of Zn at RT are shown in green/full circles; in yellow/x at 300 °C; and in red/● at 500 °C (colors are available in the online version of the manuscript)

Table 4. Positions of Zn sites for Zn-CPT at RT and heated at 300 and 500 °C

Zn positions	Atomic coordinates								
	RT			300 °C			500 °C		
A channel									
Zn1	0	0	0.5		–			–	
Zn2	0.092	0	0.464	0.1	0	0.444		–	
$Zn2^1$		–		0.580	0.468	0.104		–	
$Zn2^2$		–			–		0.070	0.072	0.76
Zn3	0.234	0.5	0.035	0.220	0.5	0.151	0.217	0.5	0.084
B channel									
Zn4	0.043	0.5	0.27		–			–	
$Zn4^2$		–		0.095	0.5	0.16		–	
$Zn4^2$		–			–		0.085	0.420	0.09

position is sited exactly in the center of the channel taking the position of Mg^{2+} [17]. The other centered position, "Zn2", corresponds to the one designated by Dimowa for ion-exchanged Zn-CPT [15]. The third position, "Zn3", is located very close to the intersection of A- and B-channels and matches the known "M3" position in non-exchanged clinoptilolite [18]. The estimated amounts of Zn^{+2} cations in A- and B-channel are 3.92 vs 1.72 respectively.

It was expected that at higher temperatures the Zn^{+2} cations will move (diffuse) and change their initial positions due water molecules expelling from the structure, which causes re-location of the cations to maintain the initial charge balance. This was confirmed by the performed Rietvled analyses on the diffraction patterns at various temperatures.

At 300 °C the Zn^{+2} cations are also located in four positions, but some of them change from the intial RT positions. Namely, "Zn1" position disappeared, "Zn2" position slightly shifts along *a* allowing the appearance of a new "$Zn2^1$" position. The "Zn3" position also shifted along *a* towards the B-channel.

The disappearance of "Zn1" [17] is associated with the loss of the coordination water surrounding the hydrated Zn^{+2} cations at RT. Zn4 position (B-channel) shifts along *c*, closer to the negatively charged framework producing Zn4'. A more general comparison of the positioning of the Zn atoms in the channels at RT and 300 °C shows that all Zn sites are located closer to the Si/Al framework. In order to compensate its surcharge, the Zn^{+2} shifts towards the negatively charged framework preserving the initial charge balance. At 300 °C, the distribution of Zn^{+2} cations in A and B-channel is 3.52 vs 1.92 APU respectively. The distribution of the Zn sites indicates a slight positive "shift" of the compensating charges towards the B-channel.

At 500 °C Zn^{+2} is found in three sites in the CPT framework. The already modified at 300 °C "$Zn2^1$" position in A-channel moves now closer to the CPT framework – "$Zn2^2$" position. The "Zn3" position situated at the intersection of the two channels is almost unchanged, but slightly migrates towards the B-channel. Finally, a new "$Zn4^2$" position appears as a result of the shift and splitting of Zn4 → $Zn4^1$ → $Zn4^2$ positions. At 500 °C the distribution of the Zn atoms in A and B channel is 2.55 vs. 2.92 APU respectively. Thus, the charge transfer from A to B channel, already noticed at 300 °C, is even more pronounced. Similarly to "RT vs. 300 °C" the "300 vs. 500 °C" general comparison of the Zn sites in the channels shows further displacement of the cations towards the framework. The distribution and Zn amounts in the channels, described above is shown on Fig. 7. The results indicate that there is a diffusion of Zn^{+2} from A to B-channel. The "Zn3" position is serving as a bridge between the channels [15]. On the other hand, the loss of Zn^{+2}-coordination seems to occur first in the A-channel (associated with the disappearance of "Zn1" site) and thus further promotes the diffusion of Zn^{+2}. The occupancy of the "Zn3" site in A-channel diminishes in favor of the Zn4/Zn4' and Zn4" located in the B-channel. As the amount of Zn remains the same at RT, 300 °C and 500 °C the observed changes and shifts of the Zn-sites are associated with the increased mobility (thermal motion) of the cations inside the channels.

The saturation of the $Zn4^2$ position (leading to the presence of 2.92 Zn APU in B channel at 500 °C) is probably responsible for the stabilization of the CPT framework. If we consider the systems of channels acting like interconnected vessels one can assume that the transfer of Zn to B-channel rigidifies it and preventing its structural deformation. This enhanced stability of B-channel also inhibits the deformation of A-channel (interconnected vessels).

The enhanced thermal motion and diffusion of both the CPT framework and cations profits the mutual compensation of the charges and prohibits the release of the cations. Thus, the overall effect is a relative stabilization of the CPT structure at high temperatures.

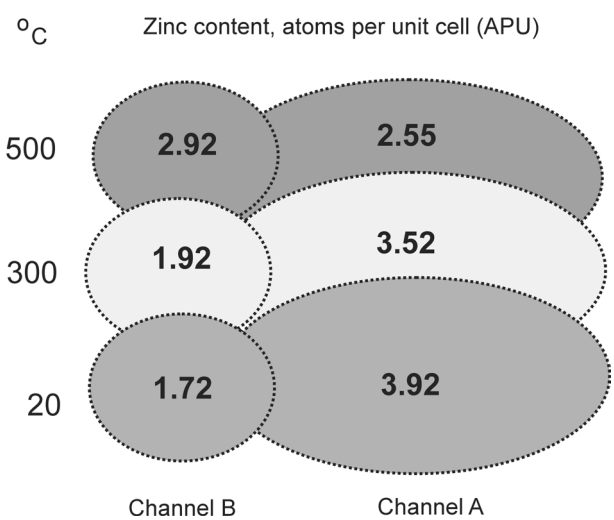

Fig. 7. The distribution of Zn amounts (APU) in the clinoptilolite channels

CONCLUSIONS

Molten exchange of $ZnCl_2$ in NH_4^+ exchanged clinoptilolite is reported. The amount of Zn incorporated in the CPT structure after four hours molten exchange is about five times greater than that one of the liquid ion-exchanged Zn-CPT for 30 days. The temperature of 380 °C required for the molten exchange does not affect the structural ordering. Instead, it was found out that Zn^{+2} presence in the channels improves the overall thermal stability of CPT structure. The stabilization occurs through a diffusion of Zn^{+2} cations from A to B-channel, which prevents the deformation of B channel. The CPT system of channels acts as interconnected vessels and the rigidified B-channel hampers the deformation of A-channel. The higher amount of Zn-cations achieved in the molten- exchange process and their locations and transport through the channels in CPT-structure at elevated temperature play an important role for this stabilization.

REFERENCES

1. A. Langella, M. Pansini, P. Cappelleti, B. de Gennaro, M. de. Gennaro, C. Collela, *Microporous and Mesoporous Materials,* **37**, 337 343 (2000).
2. T. Armbruster, P. Simoncic, N. Dobelin, A. Malsy, P. Yang, *Microporous and Mesoporous Materials*, **57**, 121 131 (2003).

3. J. Stolz, P. Yang, T. Armbruster, *Microporous and Mesoporous Materials,* **37**, 233 242 (2000).
4. A. Ssirkecioglu, A. Erdem-Senatalar, *Clays and Clay Minerals,* **44** 686 692 (1996).
5. L. Habbena, B. Koopmans, H. E. Menke, S. Doornweerd, K. de Boule, *British Journal of Dermatology,* **121**, 497 502 (1989).
6. K. T. Holland, R. A. Bojar, W. J. Cunliffe, A. G. Cutcliffe, E. A. Eady, L. Farooq, A. M. Farrel1, E. M. Gribbon, D. Taylor, *British Journal of Dermatology*, **126**, 505 509 (1992).
7. G. Cerri, M. de Gennaro, M. C. Bonferoni, C. Caramella, *Applied Clay Science,* 27, 141 150 (2004).
8. K. Pavelic, M. Katic, V. Sverko, T. Marotti, B. Bosnjak, T. Balog, R. Stojkovic, M. Radacic, M. Colic, M. Poljak-Blazi, *J. Cancer Res. Clin. Oncol.,* **128**, 37 44 (2002).
9. R. Brayner, R. Ferrari-Iliou, N. Brivois, S. Djediat, M. F. Benedetti, F Fievet, *Nano Letters* **6,** 4 866 870 (2006).
10. I. R. Iznaga, V. Petranovskii, F. Castillon, M. Farias, *Optical Materials,* **29**, 105 109 (2006).
11. A. Top, S. Ulku, *Applied Clay Science,* **27**, 13 19 (2004).
12. Park, M., C. S. Seung, L. C. Choy, D. H. Lee, W. T. Lim, S. Komarneni, M. C. Kim, J. Choi, N. H. Cheo, 2001, Role of framework on NH4NO3 occlusion in zeolite pores. Microporous and Mesoporous Materials, **50**, 91–99.
13. M. Liquornik, Y. Marcus, *J. Phys. Chem.,* **72**, 13, 4704 4705 (1968).
14. DiffracPlus TOPAS v. 3.0 (2008) Bruker AXS Karlsruhe – Germany.
15. X. M.A. Herrero, J. Atiemza, R. P. Maquieira, *Analyst,* 117 (1992) 1019.
16. L. Dimowa, PhD Thesis, IMC, Sofia, 2011.
17. T. Armbruster, *American Mineralogist,* **78**, 260 264 (1993).
18. K. Koyama, Y. Takeuchi, *Zeitschrift fur Kristallographie,* **145**, 216 239 (1977).

ОБМЕН НА КЛИНОПТИЛОЛИТ ОТ СТОПИЛКА $ZnCl_2$: СТРУКТУРНИ ОСОБЕНОСТИ И СВОЙСТВА ПРИ ВИСОКА ТЕМПЕРАТУРА

Л. Т. Димова[1]*, С. Л. Петров[2], Б. Л. Шивачев[1]

[1] Институт по Минералогия и кристалография, Българка Академия на Науките, „Акад. Георги Бончев“ бл. 107, София 1113, България
[2] Университет в Торонто, Химически факултет, ул. „Сейнт Джордж“ 80, Торонто, ON, M5S 3H6, Канада

Постъпила на 20 март, 2012 г.; приета на 5 май, 2012 г.

(Резюме)

За първи път е направен обмен на стопилка $ZnCl_2$ в клиноптилолит (Zn-CPT). Обменът се осъществява в твърдо-течно състояние и намалява значително времето, което е необходимо за постигане пълен цинков обмен в клиноптилолита. Методът е потенциална алтернатива на класическия йонен обмен от разтвор. Механизмът на включването на Zn^{2+} катиони в каналите на клиноптилолита структура е изследван с различни методи, като високо температурна рентгенова дифракция, инфрачервена спектроскопия, диференциално термичен анализ, и др. Показано е, че обменният на Zn клиноптилолит е термично по-устойчиви от природния, поради насищане на осем членния Б-канал на Zn^{2+} катиони.

Bulgarian Chemical Communications, Volume 44, Proceedings of the III[rd] National Crystallographic Symposium (pp. 63–69) 2012

ZnO thin films preparation on glass substrates by two different sol-gel methods

N. V. Kaneva*, C. D. Dushkin, A. S. Bojinova

Laboratory of Nanoparticle Science and Technology, Department of General and Inorganic Chemistry, Faculty of Chemistry and Pharmacy, University of Sofia, 1 James Bourchier Blvd.,1164 Sofia, Bulgaria

Received February 20, 2012; Revised March 29, 2012

Here we present thin films of ZnO with photocatalytic application in purifying water from organic pollutants. The films were obtained from stable colloidal precursor sol, prepared by two sol-gel methods (*A* and *B*) using zinc acetate and varying the solvents. These sols are deposited on glass substrates via dip-coating technique. The films are characterized by different methods (XRD, SEM, FTIR). By XRD was established that the zinc oxide is of hexagonal crystal structure.

A comparison of the determined morphology, composition and structure for the prepared by two different method films is studied. The morphology of films obtained with 1-propanol and 1-butanol, as shown is not homogeneous. The film surface is not uniform and there are many cracks and bubbles. Layers in such films is very easy to peel off after their ignition. Therefore, a third synthesis of the sol-gel method *A* is performed, with any changes in the formulation, only alcohol is substituted by 2-propanol. There is ganglia typical surface structure of the so obtained film, which is established by SEM. They are evenly distributed over the entire film surface. The film surface in the sol-gel *B* was investigated by SEM. The film surface has characteristic ganglia-like patterns.The resulting samples are more uniform, show much better adhesion of the layers and higher density, compared to films from the sol-gel method *A*. The difference in the films morphology has influence their photocatalytic performance.

Key words: zinc oxide, thin films, crystallites, glass substrate, dip coating, sol-gel method.

INTRODUCTION

The zinc oxide (ZnO) is an important II–VI group semiconductor material, with a hexagonal wurtzite crystal structure (c = 5.21 Å and a = 3.25 Å) [1], wide and direct band gap of 3.37 eV (at 300 K), large free-exciton binding energy (60 meV) [2], strong cohesive energy of 1.89 eV [3], high mechanical and thermal stabilities [4], and radiation hardness [5–7]. ZnO possesses a wurtzite structure similar to GaN [8, 9], which is widely used in high-performance optoelectronic devices.

Undoped and doped zinc oxide thin films have many interesting properties, such as, transparency in the visible and high infrared reflectivity [10], excellent piezoelectrical properties [11], hexagonal wurtzite structure n-type conductivity [12], etc. All these properties make them widely applied in many fields, such as, transparent conductors [13], solar cells [14], electrical, piezoelectric or luminescent devices and also as gas sensors, chemical sensors, surface acoustic wave devices (SAW) [15], UV laser and catalysts. Semiconductor catalysts have been studied extensively [16–18] to promote the degradation of potential organic pollutants present in waste water [19, 20].

ZnO films can be prepared by various methods, including vapor deposition [21], pulsed laser deposition [22], molecular beam epitaxy [23], metal organic chemical vapor deposition (MOCVD) [24], sputtering [25], electron beam evaporation [26], spray pyrolysis [27] and sol–gel [28,29]. Sol–gel is an attractive method for films preparation because of its easy control, low cost and low fabricating temperature [30]. It is well known that the sensing mechanism of semiconducting oxide gas sensors is based on the surface reaction and a high surface–volume ratio. The grain size and the porosity of the sensing material are the most important factors for high sensitivity and short response time sensors.

This paper presents preliminary results on the crystalline structure, morphology and photocatalytic properties of nanocrystalline ZnO thin films prepared by both sol–gel methods. When dip-coating sol–gel technique is used, the withdrawal

* To whom all correspondence should be sent:
E-mail: nina_k@abv.bg

speed is the most important processing parameter affecting the porosity of the films. It was found that higher withdrawal rates resulted in films of lower quality. The surface of films obtained with 1-butanol and 1-propanol were observed bubbles, cracks and haven't good photocatalytic properties. While films with 2-propanol manifest homogeneous ganglia-like surface structure. Nanostructured zinc oxide films with 2-methoxyethanol have improved ganglia-like structure, but much more developed. They degrade most completely the dye (97% for 3 hours) and have the highest photocatalytic activity.

EXPERIMENTAL SECTION

Preparation of ZnO films

Materials: Zinc acetate dihydrate $Zn(CH_3COO)_2.2H_2O$ (>99.5%), n-propanol (>99.0%), 2-propanol (>99.0%), n-butanol (>99.0%), glycerol (>99,0%), ethylene glycol (>99,0%), triethylamine (>99.5%), 2-methoxyethanol (>99.5%) and monoethanolamine (>99%) were supplied from Fluka. Malachite green (MG) oxalate was from Croma-G mbH & Co. The glass slides (ca. 76×26 mm), used for substrates of the ZnO films, were from ISO-LAB (Germany). All other reagents were of analytical grade. The soda-lime microscope glasses were cleaned with a chromerge solution (H_2SO_4/Cr_2O_3), then with a mixture of hydrochloric and nitric acid and finally with ethanol and acetone successively.

Sol-gel method (A): The sol was prepared using zinc acetate dihydrate ($Zn(CH_3COO)_2.2H_2O$), ethylene glycol ($C_2H_6O_2$), alcohols (1-propanol, 2-propanol, 1-butanol), glycerol ($C_3H_8O_3$) and triethylamine ($C_6H_{15}N$) (Fig. 1a). Ethylene glycol (2.5 ml) and zinc acetate dihydrate (10 g) were mixed in a round-bottomed flask and heated at 100 °C for 15 min to obtain a uniform transparent mixture. During the heating, water vapor evolved from the mixture equivalent to the water of hydration of zinc acetate dihydrate. After cooling down to room temperature the content of the flask solidifies to a transparent brittle solid, which is then dissolved in alcohol. The addition of glycerol (0.5 ml) enhances the solubility of zinc acetate as well as the film formation property of the sol. Triethylamine (1 mol eq.) is also added

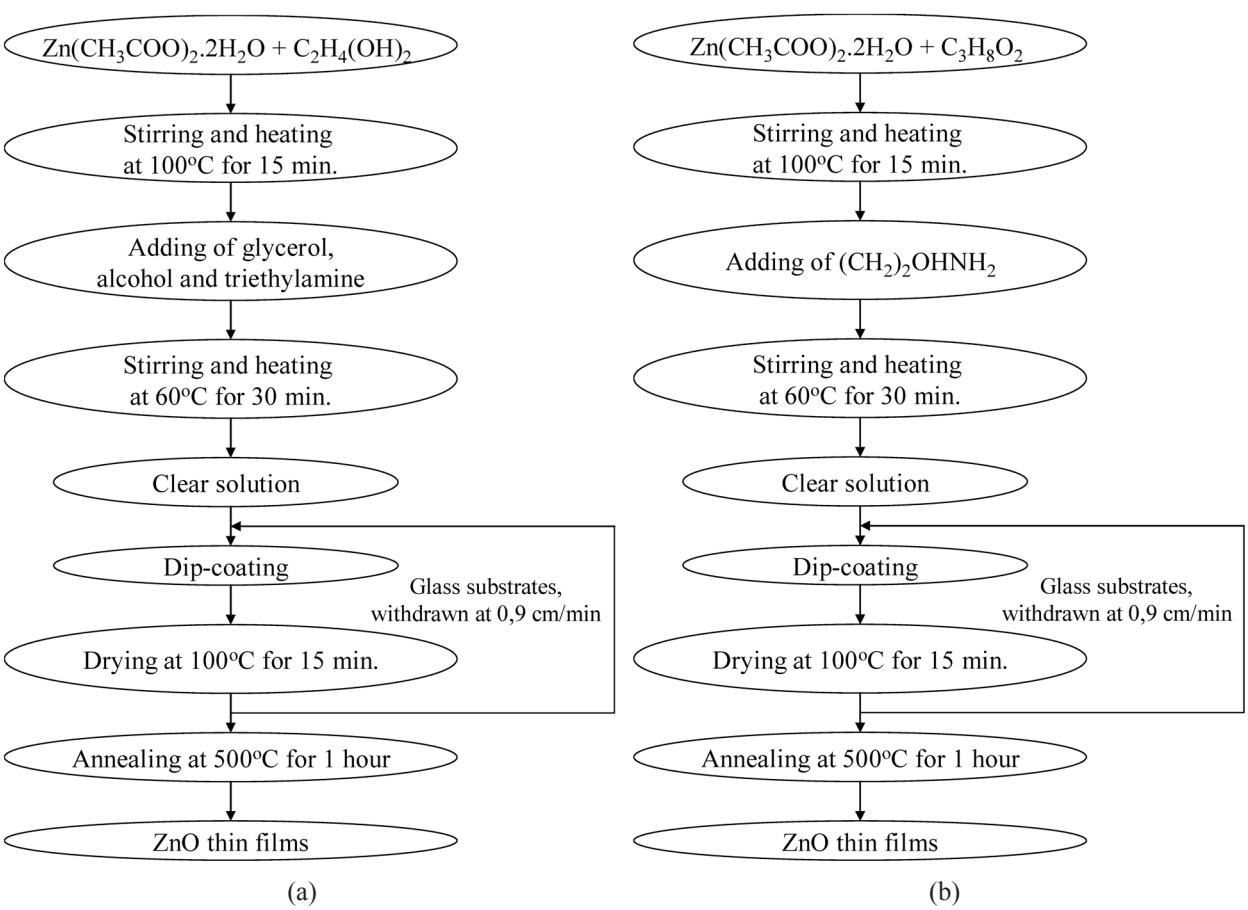

Fig. 1. Scheme of experimental procedures: (a) *sol A* and (b) *sol B*

to assist the hydrolysis of zinc acetate. The resultant solution is stirred at 60 °C for 1h to yield a clear and homogeneous solution, which serves as precursor coating sol.

Sol-gel method (B): The scheme of *sol B* is shown in Fig. 1b. Zinc acetate dihydrate (10 g) and 2-methoxyethanol (20 ml) are mixed together in a round-bottomed flask and heated at 100 °C for 15 min to obtain a uniform transparent mixture. Monoethanolamine (3.2 ml) is also added to assist the hydrolysis of zinc acetate. The obtained clear solution was heated up at 60 °C upon magnetic stirring for 1h and let aging overnight. The resultant solution was clear and homogenous to serve as the coating substance for film preparation.

The *sol A* and *sol B* was strongly hydrolyze and formed a thick gel after the addition of water. No visible changes were observed in the solution stored at room temperature for at least 2 months.

The deposition of ZnO films consisted of dip coating, drying and annealing of the material. The gel films were prepared by dipping glass substrates in the precursor solutions and next withdrawing at rates of 0.9 cm/min at room temperature. It was found that higher withdrawal rates resulted in films of lower quality. The films were deposited with 5 coatings and dried at 80 °C for 15 min after each successive coating. The final gel films were annealed at 500 °C for 60 min in order to obtain photocatalytic ZnO films.

Characterization of ZnO films

The obtained ZnO thin films were analyzed by scanning electron microscope (SEM) JSM-5510 (JEOL), operated at 10 kV of acceleration voltage. The investigated samples were coated with gold by JFC-1200 fine coater (JEOL) before observation. The phase composition and crystallinity of the samples is determined by XRD.

X-Ray diffraction (XRD) spectra were recorded at room temperature on a powder diffractometer (Siemens D500 with CuKα radiation within 2θ range 10–80 deg and step 0.05 deg 2θ and counting time 2 s/step). The average crystallite size was estimated according to Scherrer's equation:

$$d_{hkl} = k\lambda / \beta\cos(2\theta) \qquad (1)$$

where d_{hkl} is the average crystallite size (nm), λ is the wavelength of CuKα radiation applied (λ = 0.154056 nm), θ is the Bragg's angle of diffraction, β is the full-width at half maximum intensity of the peak observed at 2θ = 25.20 (converted to radians) and k is a constant usually chosen ~0.9.

Fourier transform infrared (FTIR) spectra were taken with Bruker Tensor 27 spectrometer, using KBr tablet technique. Spectra were taken in the interval 400–4400 cm^{-1}.

The photocatalytic action of the ZnO films was tested in photoinitiated bleaching of malachite green (MG) dye in aqueous solution. The photocatalytic reaction was conducted in a cylindrical glass reactor (volume 150 ml), equipped with a magnetic stirrer (rotating speed controlled by stroboscope) and UV-lamp (emission maximum at 370 nm; the light power density at the sample position was 0.66 mW/cm^2 as measured with Research Radiometer of Ealing Electro-optics, Inc.). The decay of MG concentration during the bleaching process was monitored by UV-vis absorbance spectroscopy after aliquot sampling at regular time intervals. Experiments were carried out with two series of ZnO films, prepared with *sol A* and *sol B*, respectively.

The decolorization and degradation efficiency, *D (%)*, was calculated as:

$$D = \left[\frac{C_0 - C}{C_0}\right] \times 100 \qquad (2)$$

where C_0 is the initial concentration of dye and C is the dye concentration after UV irradiation in selected time interval, t.

The initial concentration of MG is 10 ppm. All photocatalytic tests were performed at constant stirring rate (500 rpm) and room temperature (23±2 °C). The optical absorbance spectra were measured by spectrophotometer Jenway 6400 in the wavelength range from 400 to 800 nm.

RESULTS AND DISCUSSION

Structure characterization

The morphology of both films from *sol A* with 1-propanol and 1-butanol determined by scanning electron microscope is shown in Fig. 2a and b.

The SEM images of both films were made at the same magnification (x 1000) and the marker is 10 μm. As seen from the picture their morphology is not homogeneous. Even the appearance of the films does not look good, their surface is not uniform and there are many cracks and bubbles. Layers are very easy to peel off after their ignition. The photocatalytic tests with such films showed very low photocatalytic activity. Therefore, a third synthesis was performed – no other changes in the formulation only alcohol is 2-propanol. The as-prepared samples are more uniform and show much better adhesion of the layers and the higher density of the film. There is ganglia typical surface structure of the film. The surface morphology of the films (Fig. 2c) is represented by different ganglia-

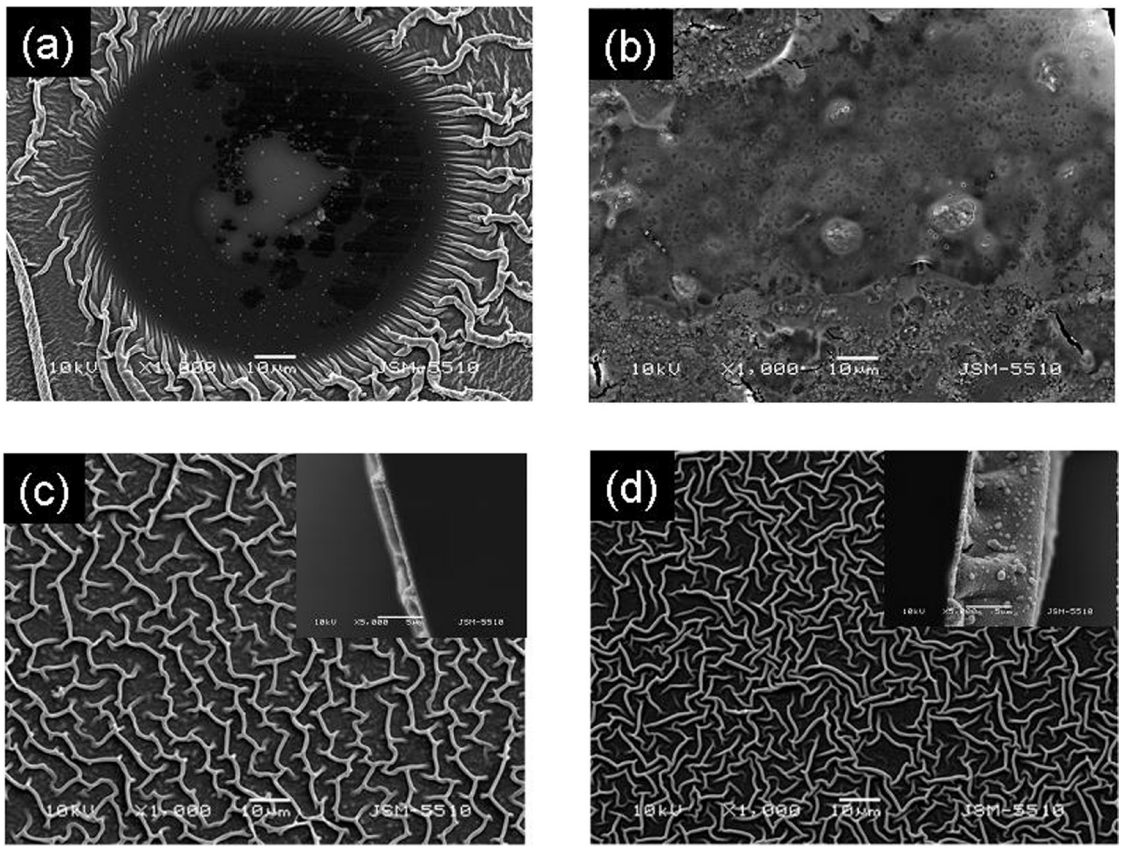

Fig. 2. SEM images of ZnO film prepared by *sol A* with (a) 1-propanol, (b) 1-butanol, (c) 2-propanol, (d) *sol B* with 2-methoxyethanol. The inset SEM images show the cross-section of the both last films

like hills with typical width of about 1 μm and a height of 1–2 μm. They are evenly distributed over the entire surface of the film. Cross-sectional SEM image inset picture allows us to determine the film thickness, which is about 0.5 μm. At the places whit intensively formed ganglia, the thickness can reach 2–2.5 μm.

Scanning electron microscope was also used to monitor and study the surface of films obtained by method B (Fig. 2d). Cross section of the films was also characterized using SEM. The SEM images show that the surface is homogeneous and much more developed. There are different ganglia with a typical width of about 1 μm and a length of 5 μm to 15 μm. The results show that the average film thickness is about 5–10 μm. Ganglia-like hills along the entire surface of the film and have a height of about 2.5–3μm. They are reproducible, regardless of the conditions under which films are obtained. They can be seen on the surface of various other movies. An example can be given to the first synthesis of films of ZnO. The surface of the samples obtained using different reagents can be observed ganglia similar entities. With the difference that in the first case they are not as wide and thick, but smaller and not so expressed. From cross section of the two films is clearly evident that ganglia-like formations are composed of very small nano-sized particles of ZnO.

The XRD spectra of thin ZnO films are presented in Figure 3. The blades resemble many spectra of literature on thin films of zinc oxide. The spectrum of both types nanostructured films consist of well-defined diffraction peaks showing good crystallinity. The three characteristic peaks clearly proof the existence of ZnO, which correspond to different crystallographic orientations of the crystal lattice of wurtzite (from left to right) (100) – at (2θ = 31.76°); (002) – at (2θ = 34.39°) and (101) – at 2θ = 36.24°. Almost the same peak height shows that the nanocrystallites are with different orientations of the axes. Crystalline structure of both films is hexagonal wurtzite. The size of crystallites, calculated by Scherer (Equation 1) is 30 nm. We assume that annealing for 1h at 500 °C leads to decomposition of Zn (II) hydroxide and its transformation into ZnO with hexagonal structure, which can be seen from diffraction spectra.

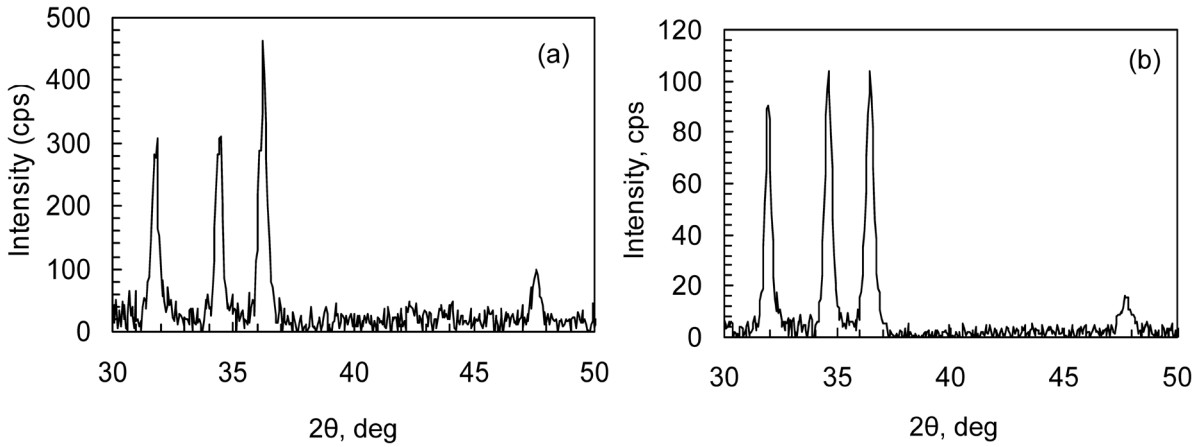

Fig. 3. XRD spectra of nanostructured films annealed for 1 hour at 500 °C (*sol A* with 2-propanol) (a) and *sol B* (b). The crystallite sizes are about 30 nm in both cases

Figure 3 are compared to the first peaks of spectrums of ZnO, obtained by both methods. The paintings are completely identical and correspond to the zinc oxide. Attempt was made to find, even small differences in half-width of the major peaks and their positions. For this purpose, the peaks were approximated with a Gaussian function. Within experimental error has been found only difference either in width or in the angular positions of the more intensive (three) peaks. An interesting phenomenon is the observed change in the relative intensity of three diffraction peaks, which increase with the movies, the first synthesis compared with those of the second method. The latter can be attributed to the different precursors, used in methods A and B (2-propanol and 2-metoxyethanol), favoring different orientation of the as grown crystallites.

FTIR spectra of gel films are shown in Figure 4. FTIR spectrum shows several interesting areas in both cases. The first is in the range 3000–3750 cm^{-1} with a maximum of 3436 cm^{-1} due to the absorption of O-H groups. The second area of absorption (in the range 1250–1750 cm^{-1}) corresponds to COO^- (1620 cm^{-1}) group. The third absorption region with a peak between 1000–1300 cm^{-1} due to CO stretching vibration absorption (1021 cm^{-1}). The maximum absorption peak in the range 440–450 cm^{-1} is attributed to ZnO. Some other groups absorption can also be found in the well ignited movies, for example, can give the group between 2988 and 1381 cm^{-1} CH, which indicates the presence of some organic products. The lack of such groups in the range 500–3000 cm^{-1} shows that there are only traces of other organic substances. Both films contain only ZnO.

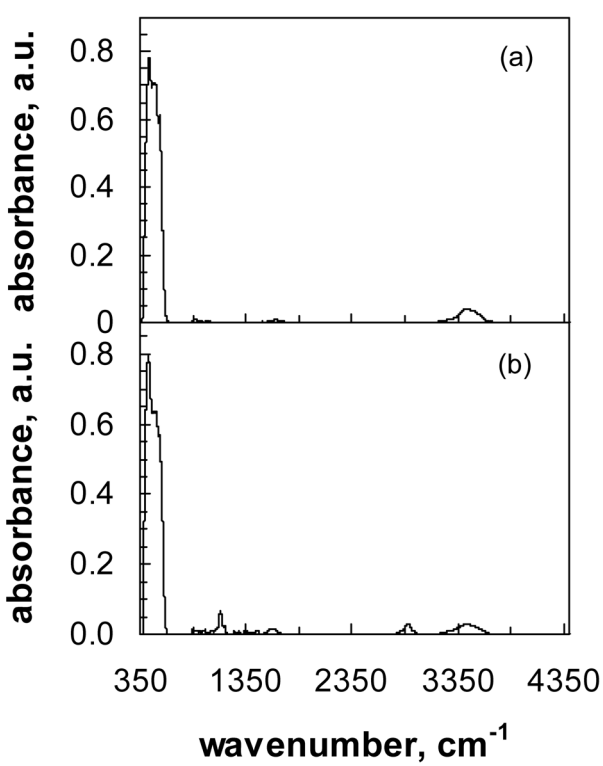

Fig. 4. FTIR spectrum of ZnO films obtained by *sol A* with 2-propanol (a) and *sol B* (b)

Characterization of the photocatalytic activity

The purification of wastewater from dyes in the textile industry is becoming a serious environmental problem because of their unacceptable color need high oxygen content, and their resistance to different methods of destruction – chemical, photochemical and biological. We have chosen photocatalytic degradation of malachite green (as a representative

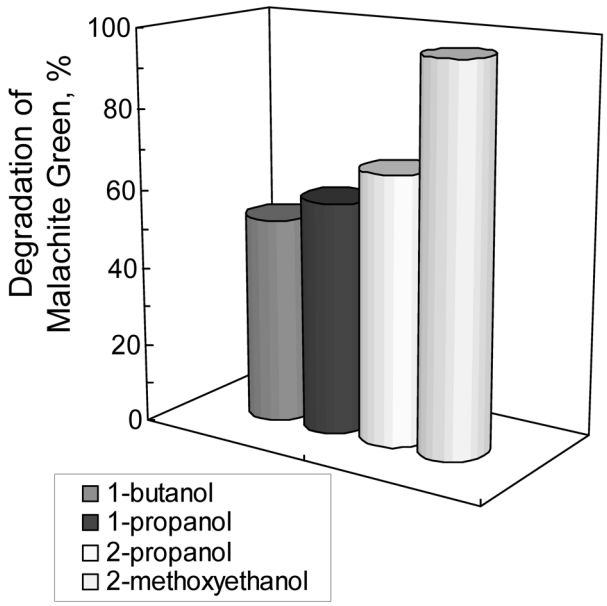

Fig. 5. Photocatalytic degradation of MG solution at 3 hour by ZnO films under UV-light illumination. The initial concentration of MG is 10 ppm

of such dyes) in the presence of a catalyst under UV-light illumination. This will be assessed the influence of photocatalysts. The initial dye concentration in these experiments is constant – 10 ppm.

Four types of experiments were made with four different types of films, obtained using different alcohols (*sol A* and *sol B*) for preparation of the precursor sol: 1-propanol, 2-propanol, 1-butanol and 2-methoxyethanol. The aim is to investigate kinetics of decolorization of the dye and to determine which of the four types of samples manifests higher photocatalytic effeciency and rates of dye photodegradation. Nanostructured films made with 2-methoxyethanol rapidly degrade dye (96.77%) and have the best photocatalytic efficiency compared to films with 2-propanol (67.88%). All the rates of dye degradation are calculated using (Equation 2) and the results are presented in Figure 5. Very clearly and distinctly visible trend of rapid degradation of the dye films with 2-methoxyethanol is seen from the date in Fig. 5. Thin films with 1-butanol degraded dye most slowly about 54% for period of three hours. Films with 2-methoxyethanol are better catalysts than those prepared with 2-propanol, are consistent with the observed surface morphology (SEM images). They have formation of ganglia-like hills on the films surface. The difference in morphology is that the ganglia formed in films obtained by the second method are larger in width, height and length as well as cash. This has a decisive influence on their photocatalytic properties.

The results show that the films that have significantly developed surface area are better photocatalysts. Thin ZnO films are promising and efficient catalysts for the decomposition of organic pollutants by photocatalytic oxidation.

CONCLUSION

Thin films of nanostructured ZnO are successfully prepared by two sol-gel methods from zinc acetate and different solvents. The sol is deposited on glass substrates by dip coating method and the obtained films are dried and annealed to form nanostructured zinc oxide. The film structure is characterized be means of XRD, FTIR spectroscopy and SEM. It is shown that the thin films are porous and formed of zinc oxide nanoparticles with an average diameter of 30 nm. The morphology of films obtained with 1-propanol and 1-butanol, as shown is not homogeneous. The film surface is not uniform and there are many cracks and bubbles. The prepared with 2-propanol and 2-methoxyethanol samples have typical ganglia structure, which is established by SEM. The resulting samples from *sol B* are more uniform show much better adhesion of the layers and higher density, compared to films from the first sol-gel method. All films pertain to the hexagonal wurtzite structure without preferred orientation irrespective to the manner of film preparation.

Further the obtained ZnO films are characterized by photo-initiated bleaching of malachite green in aqueous solutions. The photocatalytic activities of the films obtained by *sol A* are lower than those of the films obtained by *sol B*. The results obtained show that the films morphology has significant influence on the photocatalytic properties. The ZnO thin films prepared by us are promising and efficient catalyst for photocatalytic degradation of malachite green.

***Acknowledgements**: The authors are thankful to projects DDVU 02-36/10 of the Bulgarian Ministry of Education and Science.*

REFERENCES

1. Y. Kim, W. Tai, S. Shu, *Thin Solid Films*, **491**, 153 (2005).
2. H. Brown, *J. Phys. Chem. Solids*, **15**, 86 (1960).
3. R. Chuang, R. Wu, L. Lai, C. Lee, *Appl. Phys. Lett.*, **91**, 231113 (2007).
4. A. Ohtomo, M. Kawasaki, Y. Sakurai, I. Ohkubo, R. Shiroki, Y. Yoshida, T. Yasuda, Y. Segawa, H. Koinuma, *Mater. Sci. Eng. B*, **56**, 263 (1998).
5. D. Look, D. Reynolds, J. Hemsky, R. Jones, J. Sizelove, *Appl. Phys. Lett.*, **75**, 811 (1999).

6. C. Coskun, D. Look, G. Farlow, J. Sizelove, Semicond. *Sci. Technol.*, **19**, 752 (2004).
7. A. Burlacu, V. Ursaki, D. Lincot, V. Skuratov, T. Pauporte, E. Rusu, I. Tiginyanu, *Phys. Status Solidi (Rapid Res. Lett.)*, **2**, 68 (2008).
8. Ü. Özgur, Ya. Alivov, C. Liu, A. Teke, M. Reshchikov, S. Dogan, V. Avrutin, S. Cho, H. Morkoc, *J. Appl. Phys.*, **98**, 041301 (2005).
9. V. Karpina, V. Lazorenko, C. Lashkarev, V. Dobrowolski, L. Kopylova, V. Baturin, S. Pustovoytov, A. Karpenko, S. Eremin, P. Lytvyn, V. Ovsyannikov, E. Mazurenko, *Cryst. Res. Technol.*, **39**, 980 (2004).
10. B. Ismail, M. Abaab, B. Rezig, *Thin Solid Films*, **383**, 92 (2001).
11. J. Liu, W. Weng, W. Ding, K. Cheng, P. Du, G. Shen, G. Han, *Surf. Coating Technol.*, **198**, 274 (2005).
12. Y. Natsume, H. Sakata, *Thin Solid Films*, **372**, 30 (2000).
13. S. Chen, J. Zhang, X. Feng, X. Wang, L. Luo, Y. Shi, Q. Xue, C. Wang, J. Zhu, Z. Zhu, *Appl. Surf. Sci.*, **241**, 384 (2005).
14. J. Aranovich, D. Golmayo, A. Fahrenbruch, R. Bube, *J. Appl. Phys.*, **51**, 4260 (1980).
15. M. Wang, J. Wang, W. Chen, Y. Cui, L. Wang, *Mater. Chem. Phys.*, **97**, 219 (2006).
16. M. Hoffmann, S. Martin, W. Choi, D. Bahnemann, *Chem. Rev.*, **95**, 69 (1995).
17. J. Herrmann, C. Guillard, P. Pichat, *Catal. Today*, **17**, 7 (1993).
18. R. Mathews, *Water Res.*, **20**, 569 (1986).
19. N. Kaneva, D. Dimitrov, C. Dushkin, *Appl. Surf. Sci.*, **257**, 8113 (2011).
20. N. Kaneva, C. Dushkin, *Col. and Sur. A*, **382**, 211 (2011).
21. Y. Alivov, J. Nostrand, D. Look, *Appl. Phys. Lett.*, **83**, 2943 (2003).
22. R. Casero, A. Llorente, O. Moll, W. Seiler, R. Defourneau, D. Defourneau, E. Millon, J. Perriere, P. Goldner, B. Viana, *J. Appl. Phys.*, **97**, 054905 (2005).
23. D. Oh, T. Suzuki, J. Kim, H. Makino, T. Hanada, M. Cho, T. Yao, *Appl. Phys. Lett.*, **86**, 032909 (2005).
24. W. Xu, Z. Ye, Y. Zeng, L. Zhu, B. Zhao, L. Jiang, J. Lu, H. He, S. Zhang, *Appl. Phys. Lett.*, **88**, 173506 (2006).
25. D. Hwang, S. Kang, J. Lim, E. Yang, J. Oh, J. Yang, S. Park, Appl. *Phys. Lett.*, **86**, 222101 (2005).
26. A. Kuroyanagi, Jpn. *J. Appl. Phys.*, **28**, 219 (1989).
27. J. Bian, X. Li, X. Gao, W. Yu, L. Chen, *Appl. Phys. Lett.*, **84**, 541 (2004).
28. J. Lee, K. Ko, B. Park, *J. Cryst. Growth*, **247**, 119 (2003).
29. Y. Kim, W. Tai, S. Shu, *Thin Solid Films*, **491**, 153 (2005).
30. J. Liu, W. Weng, W. Ding, K. Cheng, P. Du, G. Shen, G. Han, *Surf. Coating Technol.*, **198**, 274 (2005).

ПОЛУЧАВАНЕ НА ТЪНКИ ФИЛМИ ОТ ZnO ВЪРХУ СТЪКЛО ПО ДВА РАЗЛИЧНИ ЗОЛ–ГЕЛ МЕТОДА

Н. В. Кънева*, Ц. Д. Душкин, А. С. Божинова

Лаборатория по наука и технология на наночастиците, Катедра по Обща и неорганична химия, Факултет по химия и фармация, Софийски университет, 1 Джемс Баучер Бул.,1164 София, България

Постъпила на 20 февруари, 2012 г.; приета на 29 март, 2012 г.

(Резюме)

В настоящето изследване представяме фотокаталитичното приложение на тънки филми от ZnO за пречистване на вода от органични замърсители. Филмите са получени от стабилен колоиден прекурсорен зол, приготвен по два различни зол-гел метода (*A* и *B*) от цинков ацетат и при вариране на разтворителите. Покритията са отложени на стъкло по метода на потапяне на подложката. Филмите са характеризирани чрез различни методи на анализ (XRD, SEM, FTIR). XRD показват, че цинковият оксид е с хексагонална кристална структура.

Сравнени са морфологията, състава и структурата на получените по двата метода филми. Морфологията на филмите, получени с 1-пропанол и 1-бутанол е нехомогенна. По повърхността се наблюдават множество балончета и пукнатини. Затова е направен трети синтез по метод *A*, като е използван 2-пропанол. Ганглийната структура на повърхността на така получените филми е установена със SEM. Подобна ганглийна структура е наблюдавана и при филмите, получени по метод *B.* was investigated by SEM. Получените образци са хомогенни, с по-добра адхезия и по-висока плътност, в сравнение с филмите, получени по метод *A*. Разликата в морфологията на филмите оказва влияние върху фотокаталитичната им ефективност.

Bulgarian Chemical Communications, Volume 44, Proceedings of the III[rd] National Crystallographic Symposium (pp. 70–76) 2012

Size and distribution of Pt nanoparticles in LDH nanocomposites at different temperatures

D. B. Karashanova[1]*, D. D. Kostadinova[2], S. V. Vasilev[2], N. L. Petrova[3]

[1] *Institute of Optical Materials and Technologies "Acad. Jordan Malinovski", Bulgarian Academy of Sciences, 1113 Sofia, Bulgaria*
[2] *Institute of Electrochemistry and Energy Systems, Bulgarian Academy of Sciences, 1113 Sofia, Bulgaria*
[3] *Institute of Mineralogy and Crystallography, Bulgarian Academy of Sciences, 1113 Sofia, Bulgaria*

Received February 15, 2012; Revised April 17, 2012

Nanocomposites were succesfully synthesized from multicationic layered double hydroxides (LDHs) and platinum nanoparticles (PtNPs). The features of the nanocomposite layer structure were characterized by XRD and IR analyses while the thermal behaviour by DTA-TG. The observed interlayer contraction can be explained by the grafting of interlayer organic anions onto the hydroxylated layers. The change of the mean size and the size distribution of the PtNPs after heat treatment of the samples at 500 °C and 1000 °C were observed by TEM. The intercalated in the support PtNPs were coalesced under heating. Spherical and highly dispersed nanopatricles were observed at room temperature while rough and granular aggregates were formed at 500 °C and large, dense and well-faceted particles at 1000 °C.

Key words: Pt-LDH nanocomposite, TEM of Pt nanoparticles, thermal treatment.

INTRODUCTION

A recent review has shown the great potential of layered double hydroxides (LDHs) as precursors of metal particles on basic supports with very unique properties [1, 2], as regards metal-support interaction ("electron transfer") and metal-support cooperation ("metal-base bifunctional catalysis"). It is known also that LDHs are good precursors for loading noble metals and non noble metals [3]. LDHs of general formula $[M^{2+}_{1-x}\ M^{3+}_{x}(OH)_2][A^{n-}_{x/n}.mH_2O]$ can contain different M^{2+} and M^{3+} metal cations in their brucite-like sheets, and various A^{n-} charge-compensating anions in their interlayer space. LDH compounds easily decompose into mixed oxides of the $M^{2+}M^{3+}(O)$ type after calcination [4–6]. These materials have both basic and redox functions as catalysts.

Three general routes are available for synthesis of LDHs precursors: first, the synthesis of LDHs containing M^{2+} and/or M^{3+}elements with redox behaviour within the sheets; second, the exchange with anionic metal precursors of the desired metal in the interlayer space of the LDHs; third, the deposition or grafting of inorganic or organometallic precursors onto the calcined precursor LDH. The advantage of the second route for synthesis is that the steric hindrance in the interlayer space prevents aggregation of the nanoparticles and allows the control of their growth. However these routes of catalysts preparation suffer from several limitations: (i) pure LDH phases cannot be obtained with a noble metal content larger than 5 at.% [7, 8]; (ii) catalytically active ions of too large ionic radius or without octahedral coordination cannot be accommodated in the brucite-like sheets [1, 4] and (iii) the sizes of the metal particles obtained after calcination and reduction of the LDH or mixed oxides are not easily controlled, aggregation often takes place leading to large particle sizes [9]. Keeping in mind these drawbacks, there is a demand to design new synthesis routes for obtaining highly loaded metal catalysts with control of noble metal particles in size and distribution starting from LDH precursors.

A recent report has described a novel preparation method of such materials by intercalation of preformed negatively charged Ni-based nanoparticles in Mg/Al LDH [10]. It has been shown that a better control of nanosized Ni^0 particles could be achieved. Three approaches are considered in order to prepare LDH nanocomposites incorporating

* To whom all correspondence should be sent:
E-mail: dkarashanova@yahoo.com

large negatively charged entities: the LDH co-precipitation and the reconstruction of the host LDH in the presence of the anionic species, and the anion exchange route of, for example, nitrate-containing LDH with the anions [10–11]. The first two methods yield poorly ordered layered structures, while the third yields well-ordered lamellar structures. Moreover, the anionic exchange route is the only one that allows us to tailor Ni particle sizes in the calcined and reduced materials.

The aim of the present work was therefore the preparation of highly disperse supported Pt-metal catalyst by intercalation of platinum nanoparticles into multicationic LDHs and fine control of the size and microstructure of Pt NPs at room temperature and after heat treatment at 500 °C and 1000 °C. For this purpose original Pt-containing LDH nanocomposites were prepared by exchange route of negatively charged Pt colloids with controlled sizes of the nanoparticles.

EXPERIMENTAL

Preparation of Pt-Colloid

Colloidal suspensions of Pt-based particles were obtained by hydrolysis of an aqueous solution of $(H_3O)_2PtCl_6$ (8%) and $Na_3(C_6O_7H_3)$ (1%) with NaOH (4%). This modified method of synthesis is created on the basis of works of Turkevich [12] and Harriman [13]. The molar ratio x = [citrate]/[Pt] was 3.45. Hydrolysis of Pt^{2+} ions was performed at a controlled platinum hydroxylation ratio h = [OH]/[Pt]=7,95 at alkaline pH =10 and temperature of 80 °C. The general equation of the reactions of formation of Pt-complex, followed by hydrolysis can be presented by:

$$(H_3O)_2PtCl_6 + x\,Na_3Citrate + h\,NaOH \rightarrow [Pt(Cit)_x(OH)_h]^{2-}$$

Preparation of LDH Host Structure, Pt-LDH nanocomposite and its conformations after heat treatment

(i) The host NO_3-Mg/Ni/Al sample (Mg/Ni/Al = 2:0.5:1) was prepared by co-precipitation at constant pH=10 of suitable amounts of $Mg(NO_3)_2.6H_2O$ (21.7%), $Al(NO_3)_3.9H_2O$ (15.8%) and $Ni(NO)_2.6H_2O$ (6.1%) with a solution of NaOH (4%). The addition of the alkaline solution was controlled by using a pH-STAT Titrino (Metrohm) apparatus to keep the pH constant. The suspension was stirred at 80 °C for 17 h, and then the solid fraction was separated by centrifugation, washed thoroughly with distilled water and dried overnight at 80 °C [14]. These samples will be hereafter labeled NO_3-LDH.

(ii) The Pt-LDH nanocomposite was prepared from the NO_3-LDH by anionic exchange of nitrate ions: 0.6 g of the host NO_3-LDH was dispersed in the required amounts of a 2% aqueous suspension of Pt-based nanoparticles ([citrate]/[Pt])=3.45; ([OH]/[Pt])=7.95). The exchange process was performed by stirring the mixture in air at temperature of 80 °C for 6 h. The solid fraction was then recovered and washed by dispersion and centrifugation in distilled water and finally dried at 80 °C for 12 h.

(iii) Two conformations of the Pt-layered nanocomposite were obtained after heat treatment at 500 °C – mixed oxide Mg/Ni/Al(O) and 1000 °C – spinel $MgNiAl_2O_4$ type phase.

Methods of characterization

Phase identification was performed using powder XRD data obtained by XRD patterns recorded on a Bruker D8 Advance instrument using the Cu $K\alpha_1$ radiation (λ= 1.542 Å, 40 kV, and 50 mA).

The infrared absorption spectra were measured with a Tensor 37, Bruker FTIR spectrometer in the MIR 400–4000 cm^{-1} spectral range with a 2 cm^{-1} spectral resolution, after averaging 72 scans on standard KBr pallets.

DTA-TG analyses were performed on Stanton Redcroft, STA 780 equipment operating at a heating rate of 10° min^{-1}, dynamic air conditions and Al_2O_3 used as a reference.

The microstructure of the samples was investigated by means of HRTEM JEOL JEM 2100, operated at 200 kV accelerating voltage. For the phase composition identification Selected Area Electron Diffraction (SAED) was applied. Pt-LDH nanocomposite and thermally treated powders were dispersed in ethanol. Micro-quantities of the colloids were dropped on standard Cu TEM grids, coated with carbon and dried for subsequent observation.

RESULTS AND DISCUSSION

Characterization of Pt-LDH nanocomposite

XRD patterns of the host NO_3-LDH and of the Pt colloid-exchanged LDH are shown in Figure 1. In all cases the XRD patterns are typical for LDHs structures. The reflections can be indexed in a hexagonal lattice with a *R*3hm rhombohedral symmetry. The two sharp and intense characteristic diffraction lines appearing as symmetric lines at 2Θ angles below 25 °C in the NO_3-LDH are ascribed to (003) and (006) planes (Fig. 1a). The basal spacing value of d_{003}=0.886 nm is consistent with the presence of

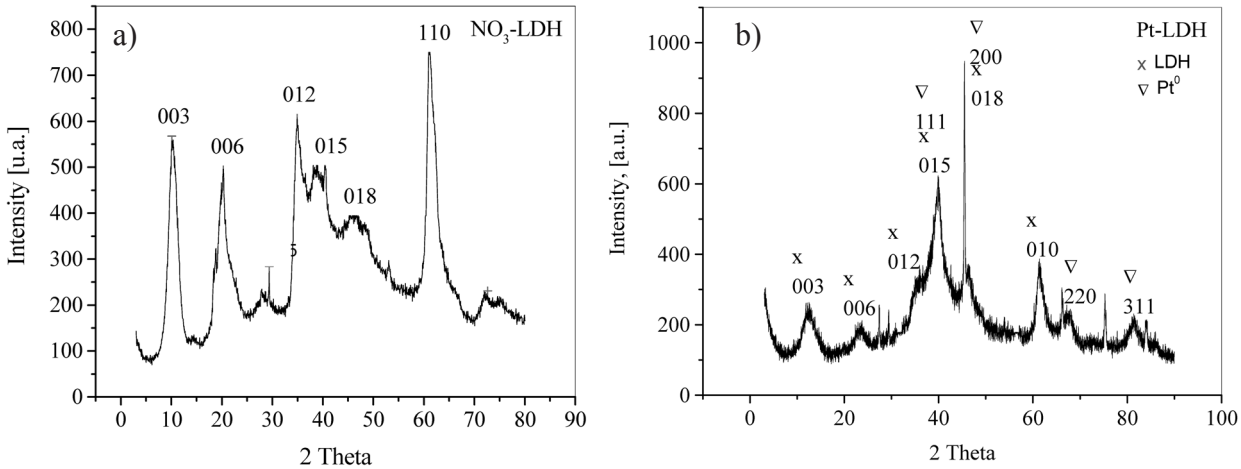

Fig. 1. XRD patterns of NO_3-LDH (a) and Pt-LDH nanocomposite (b)

nitrates as charge compensating anions in the interlayer space. Compared to the XRD patterns of the host LDH, those of the Pt colloid-exchanged LDH show several changes. The crystallinity greatly decreases indicating a lower ordering in the structural arrangement (Fig. 1b). At the same time the interlayer spacing d_{003} decreases from 0.886 to 0.706 nm, even less than that in the CO_3^{2-} – Mg/Al LDH (d_{003} = 0.760 nm) where the carbonate anion is the compensating anion in the interlayer space [15]. The reflections of metallic platinum are considerably broad (Fig. 1b), which indicates the formation of nanoparticles of the metal.

Thermal decomposition of both NO_3-LDH and Pt-LDH nanocomposite has been studied by DTA-TG analysis (Fig. 2) under dynamic air atmosphere. As it can be seen, three regions of mass losses from TG curves are observed, corresponding to different events in DTA profiles: dehydration, dehydroxylation and interlayer anion decomposition [15, 16]. The first weight loss, taking place between room temperature and 200 °C appears as a continuous step. It corresponds to a broad endothermic peak of H_2O release and accounts for the physisorption and interlayer water molecules. The second weight loss takes place between 200 and 300 °C and associates to an endothermic peak. This corresponds to the partial dehydroxylation of the brucite-like layers. A third step in the TG plots occurs between 300 and 600 °C. It gives a broad endothermic event corresponding to the full dehydroxylation of the layer and the nitrate decomposition in the case of NO_3-LDH

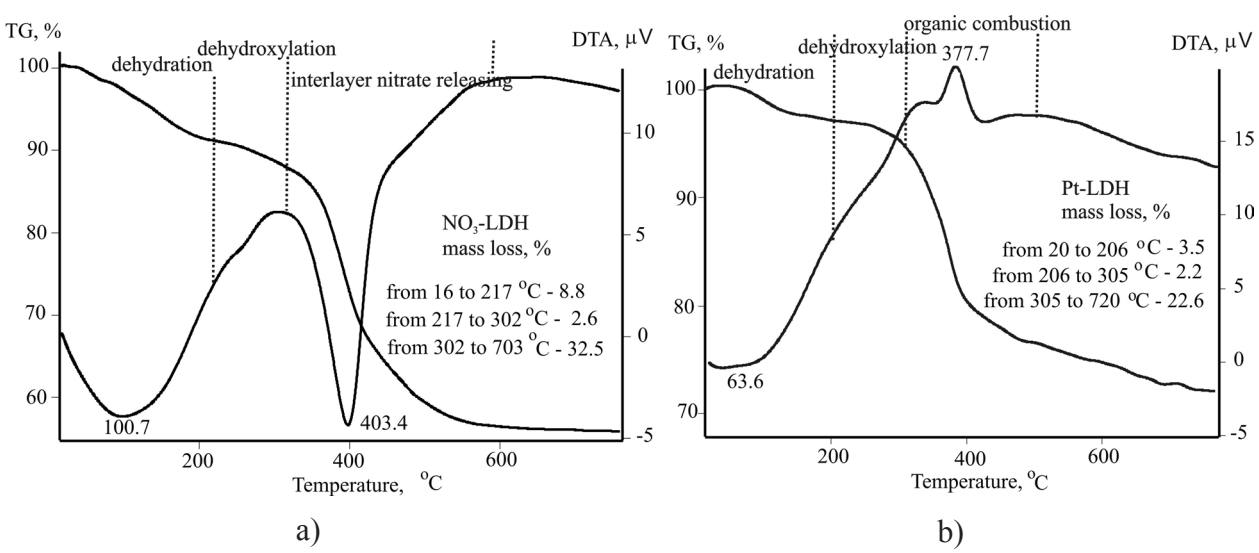

Fig. 2. DTA-TG of NO_3-LDH (a) and Pt-LDH nanocomposite (b)

(Fig. 2a), while in the case of Pt- nanocomposite an exothermic event is observed corresponding to the citrate species combustion (Fig. 2b). The amount of released both components interlayer water and volatile is higher in the case of the NO_3-LDH thermal decomposition comparing to that of the Pt-LDH nanocomposite. This fact confirms the reduced interlayer distance observed in XRD patterns of the Pt-LDH nanocomposite.

IR spectrum of the Pt-LDH nanocomposite presented on Figure 3 allows to identify bands associated with water and those associated with hydroxyl stretching vibrations. Water bending modes are situated around 1630 cm^{-1} accompanied by OH^- stretching vibrations in the 3000–4000 cm^{-1} region.

The lower wavenumber region of the infrared spectrum, 1000–400 cm^{-1}, is complicated due to the presence of lattice translational modes, librational modes of hydroxyl and water molecules, and O-M-O near 450 cm^{-1} [17]. Meanwhile, there are absorption bands, υ_3 at 1385 and 1420 cm^{-1}, which are associated with the symmetric vibration of the anionic carboxylate functions ($-CO_2^-$) of the interlayer citrate-complex. In addition, the broad and strong absorption band around 1630–1580 cm^{-1} centered at 1632 cm^{-1} should actually be associated with a superposition of water deformation, δ (H_2O), and anti-symmetric vibration of the anionic carboxylate functions ($-CO_2^-$). Di Cosimo et al. [18] have reported unidentate carbonate exhibited a symmetric O-C-O stretching vibration at 1360–1400 cm^{-1} and an asymmetric O-C-O stretching vibration at 1510–1560 cm^{-1}. These features correspond to the $C_{2\upsilon}$ carbonate group symmetry. Obviously, these groups became parts of both the interlayer and brucite-like layer. The interlayer contraction can be explained by the grafting of interlayer organic anions onto the hydroxylated layers through the substitution of OH groups on the layers. Such grafting process of organic Gly molecules on the hydroxylated layers of LDHs with a strong ion–covalent M–O-organic bonding has been reported [19] after moderate hydrothermal treatment.

Characterization of PtNPs shape transformations and size distribution at room temperature, 500 and 1000 °C

XRD patterns of Pt nanocomposites after heat treatment are presented on Fig. 4. The layer structure

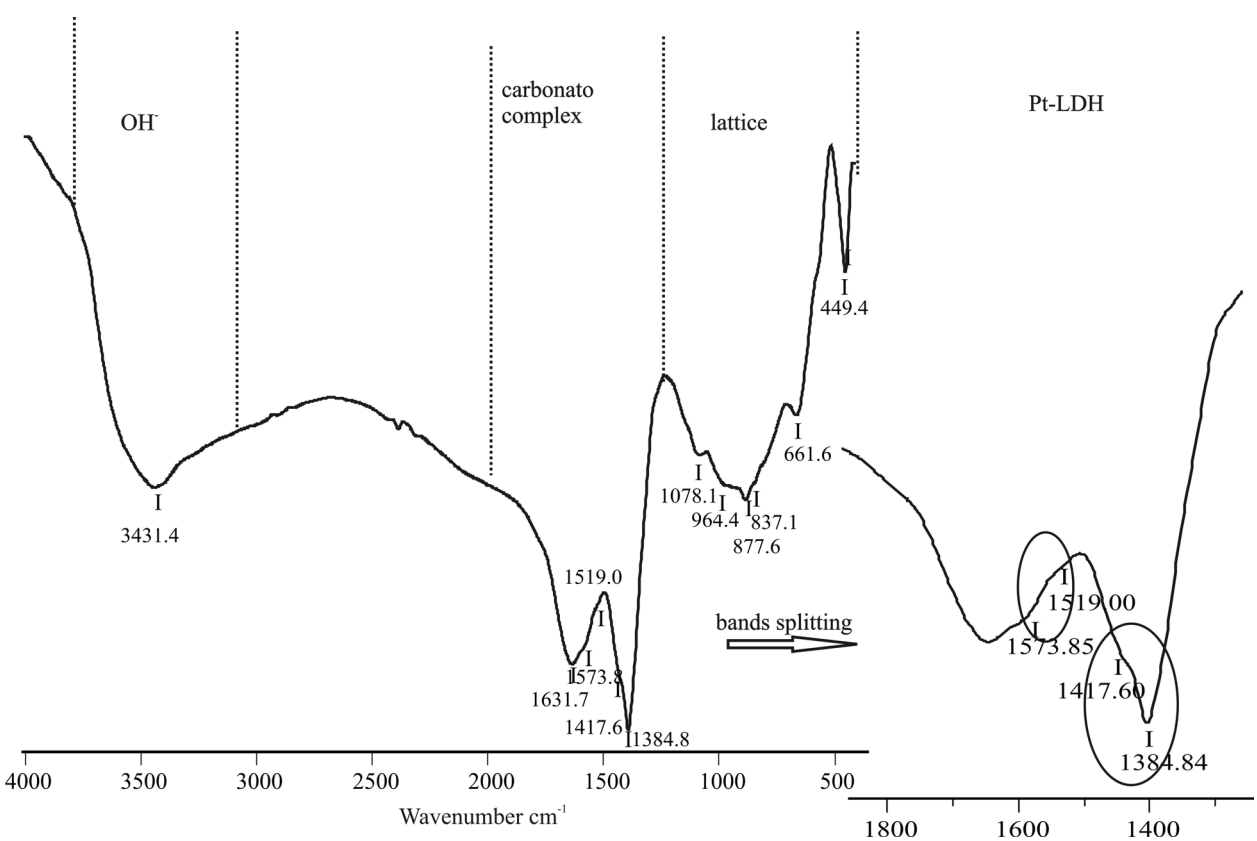

Fig. 3. IR spectrum of the Pt-LDH nanocomposite

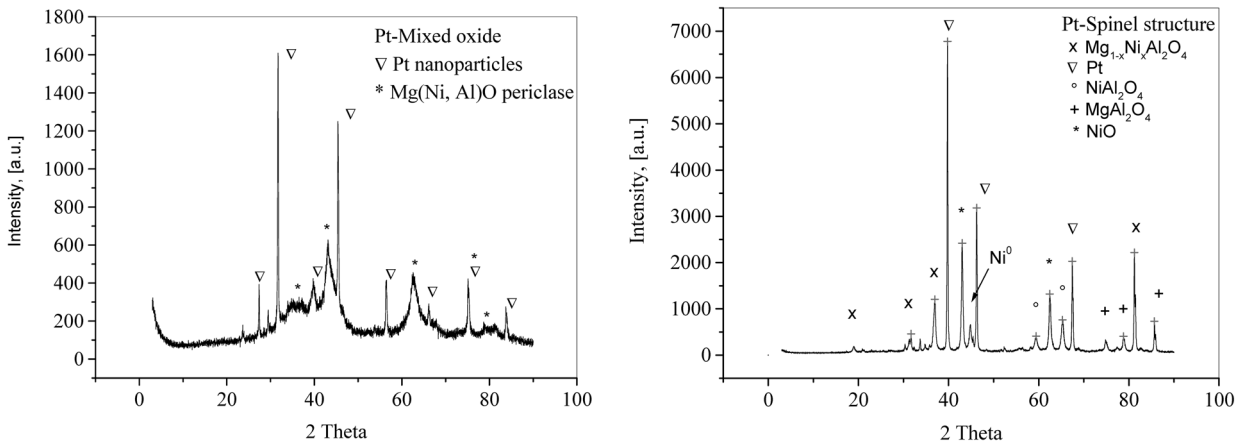

Fig. 4. XRD patterns of Pt- nanocomposites at 500 (a) and 1000 °C (b)

of the nanocomposite (Fig. 1b) transforms into mixed oxide (Fig. 4a) and spinel-like structure (Fig. 4b) at 500 and 1000 °C, respectively. At the same time, the reflections of metallic platinum become sharp, which indicates increasing of both the size and crystallinity of Pt particles with the heating temperature.

The microstructure of Pt nanocomposites, treated at the different temperatures is visualized on Fig. 5, where the bright field micrographs and corresponding SAED patterns as insets are presented. The phase composition identification confirms the presence of metal Pt phase in all three cases. A substantial increase of the mean Pt particle size is established as in [20]. The corresponding size distributions are presented on Fig. 6. The mean diameter is estimated to be 4 nm for the PtNPs at room temperature, 6 nm at 500 °C and about 120 and 200 nm at 1000 °C. It is seen that not only the size of the PtNPs, but their shape was also changed under the heating. Initially spherical, the particles intercalated in the support coalesced, thus forming rough and granular aggregates, still spherical at 500 °C while large, dense and well-faceted, particles appeared at 1000 °C. The last ones exhibit a shape anisotropy consisting of two different dimensions in the two mutually perpendicular directions. For more of the particles one of these dimensions was significantly larger than the other. To characterize this anisotropy, two independent measurements in the two perpendicular directions for each Pt NP, annealed at 1000 °C were performed. As a result two groups of columns on the histogram were formed – one between 100 and 150 nm, correspond-

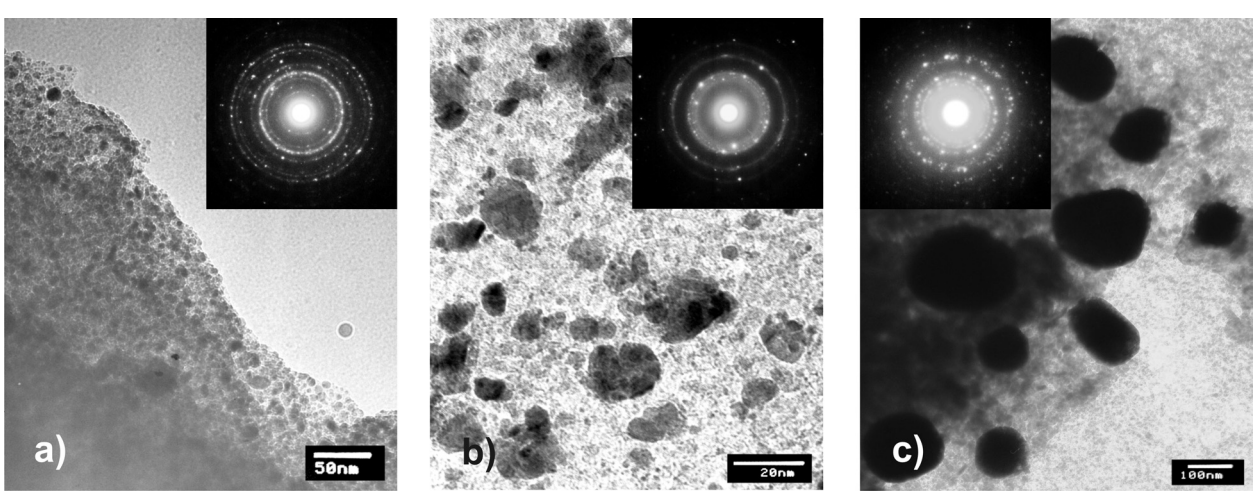

Fig. 5. Bright field TEM images and corresponding SAED patterns of Pt nanocomposites at room temperature (a), 500 °C (b) and 1000 °C (c)

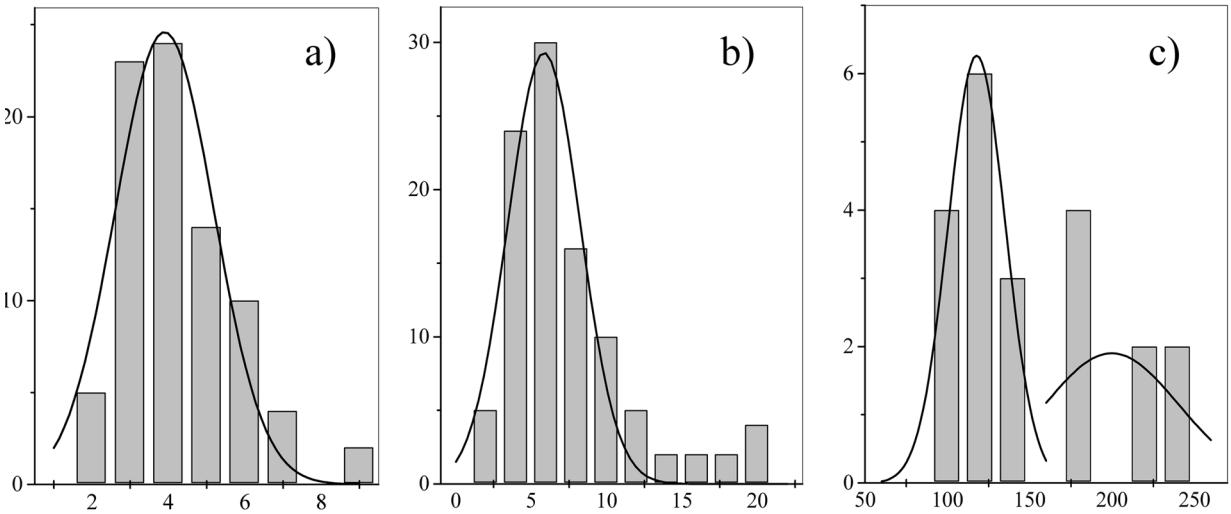

Fig. 6. Size distributions of PtNPs in the samples presented on Fig. 5

ing to the less dimension and one between 180 and 240 nm, due to the larger dimension.

CONCLUSIONS

An effective method for synthesis of PtNPs based nanocomposite as a promising material for catalytic applications was established. A thermal treatment for size and microstructure fine control of the PtNPs was applied. It was observed that intercalated in the precursor PtNPs were coalesced becoming dense and well-faced under heating. Thus, the layer structure of the catalytic nanocomposite favors in best way the fine distribution and nanosize control of the Pt particles.

REFERENCES

1. A. Vaccari, *Appl. Clay Sci.*, **14**, 161 (1999).
2. D. Tichit, B. Coq, B. *Cattech*, **7**, 206 (2003).
3. S. Narayanan, *Bulletin of the Catalysis Society of India*, **2**, 107 (2003).
4. F. Cavani, F. Trifiro, A. Vaccari, *Catal. Today*, **11**, 173 (1991).
5. A. De Roy, C. Forano, K. El Malki, J. P. Besse, in: *Synthesis of Microporous Materials*, M. L. Occelli, H. Robson (eds.), Van Nostrand Reinhold: New York, 1992, p. 108.
6. V. Rives, *Layered Double Hydroxides: Present and Future*, V. Rives (ed.), Nova Science Publishers: New York, 2001, p. 115.
7. F. Basile, L. Basini, G. Fornasari, M. Gazzano, F. Trifiro, A. Vaccari, *J. Chem. Soc.*, *Chem. Commun.*, 2435 (1996).
8. F. Basile, G. Fornasari, M. Gazzano, A. Vaccari, *Appl. Clay Sci.*, **16,** 185 **(**2000).
9. M. K. Titulaer, J. Ben, H. Jansen, J. Geus, *Clays Clay Miner*., **42,** 249 (1994)
10. C. Gerardin, D. Kostadinova, N. Sanson, D. Francova, N. Tanchoux, D. Tichit, B. Coq, *Stud. Surf. Sci*. *Catal*., **156**, 357 (2005).
11. V. Rives, M. Ulibarri, A. *Coord. Chem. Rev*., **61**, 181 (1999).
12. J. Turkevich, P. Stevenson, J. Hillier, *Discuss. Faraday. Soc*., **11**, 55 (1951).
13. A. Harriman, G. R. Millward, P. Neta, M.C. Richoux, J. M. Thomas, *J. Phys.Chem.*, **92**, 1286 (1988).
14. D. Kostadinova, G. Topalov, A. Stoyanova, E. Lefterova, I. Dragieva, *Bulgarian Chemical Communications*, **43**, 1, 150 (2011).
15. Ts. Stanimirova, I. Vergilov, G. Kirov, N. Petrova, *J. Mater. Sci.*, **34**, 4153 (1999).
16. C. Ge´rardin, D. Kostadinova, N. Sanson, B. Coq, D. Tichit, *Chem. Mater.*, **17**, 6473 (2005).
17. S. J. Palmer, L. Frost, T. Nguen, *Coordination Chemistry Reviews*, **253**, 250 (2009).
18. J. I. Di Cosimo, V. K. Diez, M. Xu, E. Iglesia, C. R. Apesteguia, *J. Catal.*, **178**, 499 (1998).
19. F. Li, L. Zhang, D. G. Evans, C. Forano, X. Duan, *Thermoch. Acta*, **424**, 15 (2004).
20. A. V. Lukashin, M. V. Chernysheva, A. A. Vertegel, Yu. D. Tret'yakov, *Doklady Chemistry*, **388**, 1–3, 19 (2003).

РАЗМЕР И РАЗПРЕДЕЛЕНИЕ НА Pt НАНОЧАСТИЦИ В LDH НАНОКОМПОЗИТИ ПРИ РАЗЛИЧНИ ТЕМПЕРАТУРИ

Д. Б. Карашанова[1]*, Д. Д. Костадинова[2], С. В. Василев[2], Н. Л. Петрова[3]

[1] Институт по оптически материали и технологии „Акад. Йордан Малиновски“, Българска академия на науките, 1113 София, България
[2] Институт по електрохимия и енергийни системи, Българска академия на науките, 1113 София, България
[3] Институт по минералогия и кристалография, Българска академия на науките, 1113 София, България

Постъпила на 15 февруари, 2012 г.; приета на 17 април, 2012 г.

(Резюме)

Успешно са синтезирани нанокомпозити от мултикатионни слоисти двойни хидроксиди (LDH) и платинови наночастици (PtNPs). Слоистата структура на нанокомпозитите е охарактеризирана с рентгенова дифракция (XRD) и инфрачервена (IR) спектроскопия, а термичните им свойства – посредством диференциален термичен и термогравиметричен (DTA-TG) анализ. Установено е свиване на междуслойното пространство, което може да бъде обяснено с вграждането на органичните аниони, разположени там, в хидроксилираните слоеве. С помощта на трансмисионна електронна микроскопия (TEM) е наблюдавана промяната на размера и разпределението на PtNPs след термично третиране на образците при 500 °C и 1000 °C. В резултат на нагряването, интеркалираните в подложката PtNPs коалесцират. При стайна температура те са сферични и силно диспергирани по повърхността на подложката, докато при 500 °C се групират в агрегати с неправилна форма, а при 1000 °C се трансформират в големи, плътни и добре остенени частици.

Bulgarian Chemical Communications, Volume 44, Proceedings of the III[rd] National Crystallographic Symposium (pp. 77–82) 2012

The thermal device of the Guinier image foil camera in the Geological Institute, BAS: calibration and usage experience

T. N. Kerestedjian*, I. Sergeeva

Geological Institute, Bulgarian Academy of Scieneces, 1113 Sofia

Received March 16, 2012; Revised April 17, 2012

Along with its normal (flat sample) mode, the unique for Bulgaria Guinier image foil camera in the Geological Institute (Bulgarian Academy of Sciences) can also be used in capillary mode. In this mode a dedicated ceramic heater can be attached, so that the whole setup is turned into a powerful thermal device. The possible uses of this device are numerous, most important of which are: determination of the thermal expansion coefficient(s) of the studied sample in each crystallographic direction; detect anomalous or negative thermal expansion trends; register phase transitions (reversible or non-reversible), witness purely temperature driven solid state reactions (formation or dissolution of ISS) etc. The successful use of the device, however, requires some preliminary experience and prompt calibration. For this type of thermal device calibration is crucial, since the sample in the glass capillary and the detecting thermo-couple react differently to the received infrared radiation and respectively experience different resultant temperature. Finding a function, well describing this difference for each given temperature in the technically applicable temperature range (ambient – 900 °C) is the aim of the calibration. Although the most important, calibration is not the only issue in using this thermal device. There are a whole lot of possible mistakes that a novice can do. Our experience in calibrating and first usage of the device is shared in the following paper.

Key words: X-ray diffraction, Guinier camera, capillary tube, thermal device, calibration.

INTRODUCTION

The Guinier image foil camera G-670 (Huber Diffraktiontechnik GmbH & Co. KG), available in the Geological Institute, Bulgarian Academy of Sciences, can be used with either swinging flat or rotating capillary specimen holders (Fig. 1 and 2).

Fig. 1. Swinging flat sample setup

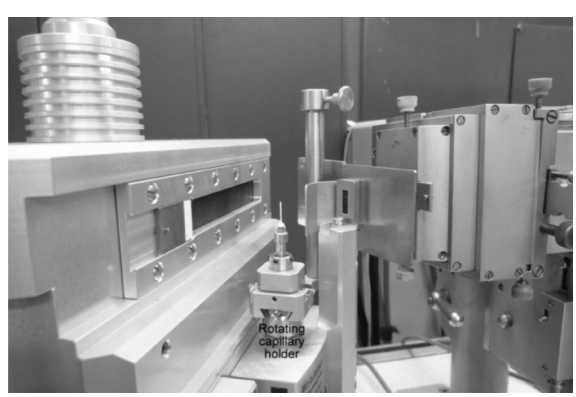

Fig. 2. Rotating capillary setup

In both cases the sample is radiated by monochromatic (pure $K\alpha_1$) beam, transmitted through the sample and diffracted beams in the range 3–100° 2θ are simultaneously registered on the reusable image foil, lying at the back wall of the cylindrical camera housing. The foil is then read by a laser reader and data recorded to file. Finally, the foil is erased and ready for the next data collection.

The capillaries used are 0.5 mm thick with 0.01 mm wall thickness. Commercially available capillary tubes of this size can be made of special

* To whom all correspondence should be sent:
E-mail: thomas@geology.bas.bg

Fig. 3. Capillary adjustment

Fig. 4. Heater device

glass, boron-rich glass, or quartz glass. The linear absorption coefficients of CuK_α in these materials vary from 110 (in special glass) to 76 cm^{-1} (in quartz glass). Respective values for MoK_α are approximately 10 times lower. Both boron- and quartz- glasses have comparable and acceptable for most purposes absorption coefficients, however, softening temperature of boron glass is about 820 °C, while for the quartz glass it is 1730 °C. Keeping in mind, that technically achievable temperature limit of the device is 900 °C, the use of quartz glass is economically reasonable only for studies in the higher-most end of the temperature range. In most other cases far cheaper boron-glass is the better choice.

Filling of the powdered sample in the capillary tube is facilitated by the funnel that it usually has on one end. However, some source of vibration should be applied on it too, in order to move all powder particles down to the capillary bottom. A dedicated vibrating device named "capillary boy" is offered by Huber Diffraktiontechnik GmbH & Co. KG.

Once filled, the capillary is to be glued in its holder. This is made using wax, if normal ambient temperature studies are to be done, and special, heat resistant, bi-component glue in case of high temperature studies. The holder is then adjusted in a special goniometric head, so that it is rotated strictly along its own axis, exposing all the sample particles simultaneously to the direct X-ray beam (Fig. 3).

High temperature setup is achieved by attaching a ceramic fork with built-in heating coil. The heater is adjusted over the capillary tube, containing the powdered sample (Fig. 4).

Adjustment is a rather tricky point. Following are some practical advices, from our experience:

• The length of the capillary must be chosen properly, so that the entire sample is placed fully inside the heater and its top is as close to the thermocouple (the ball in the upper-most part of the heater, Fig. 5) as possible. The latter is achieved also by proper adjustment of the heater height. If longer, part of the sample (outside the heater) will remain less heated and will produce inconclusive results. If shorter, the sample will either remain far from the thermocouple and its temperature will differ too much from that registered by it, or the heater has to be lowered too much and may be hit by the rotating capillary holder.

• Positioning the heater over the capillary should start with rotating the ceramic fork around its own axis, so that the line connecting its two legs passes through the axis, holding the heater shoulder (i.e. it is made strictly radial to the arc, drawn by moving the heater shoulder). Otherwise, adjustment will almost surely end up with broken capillary.

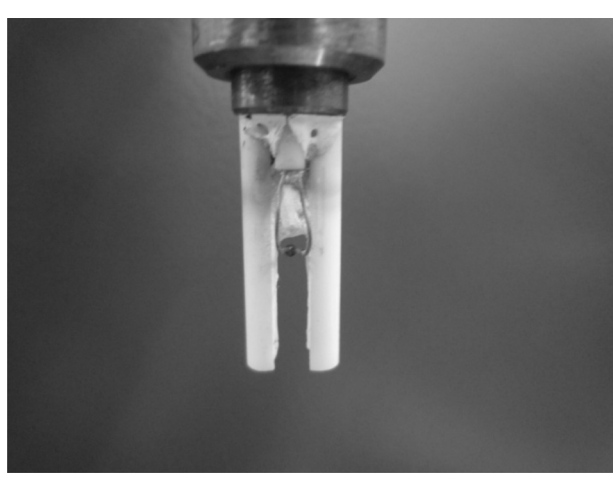

Fig. 5. Ceramic heater fork with the detecting thermocouple ball in the uppermost part of the opening

• Once in right position, the heater should be rotated around its own axis again, so that the opening between the legs of the fork is oriented towards the 2θ range of interest. One should keep in mind, that the heating device narrows the range of outgoing reflections to some 30 degrees 2θ. This is why the range of interest should be chosen in advance and targeted by proper rotation of the heater.

• In any case one should make sure, that the capillary is equally distant from both legs of the fork. This guarantees that the primary beam will not touch any of them. This rule should be followed also for the heat-keeping cover (Fig. 6). Otherwise, "alien" reflections will be detected.

• The overall setup of the device does not allow the operator to place his eye wherever necessary for all the adjustments. We found it very useful to place a handy mirror on the receiving window of the camera (just don't forget it there ☺).

Heating is controlled by a special heat controller, responsible for gaining and keeping the required sample temperature unchanged for the required period of time. This is achieved by periodically turning the heating coil current on and off. The duration and periodicity of the heating impulses are dynamically adjusted, depending on the values fed back by the thermocouple. Although the controller can be operated manually from its grip, it is normally communicated through the main system software. This software allows the user to plan his experiment, by creating a temperature profile, based on start, stop and step temperature values, using also desired durations for each step, with respective dwell time and diffraction pattern collecting time.

PID values are another important parameter of the experiment. Since PID is not anything specific to this device, but a parameter set, lying in the base of the general process control theory, it will not be described here. However, it is worth to mention, that correct choice of PID values is very important for the good operation of the heating device. If improper PID values are chosen, the sample temperature in the beginning can vary too widely around the chosen value, and many materials can be destroyed before required diffraction pattern is collected. Even few seconds of overheating can cause a loss of some phase transition pattern (a permanent loss if the transition is irreversible), or even complete melting or evaporation of the sample. Good sources of initial information on the topic are [12, 15].

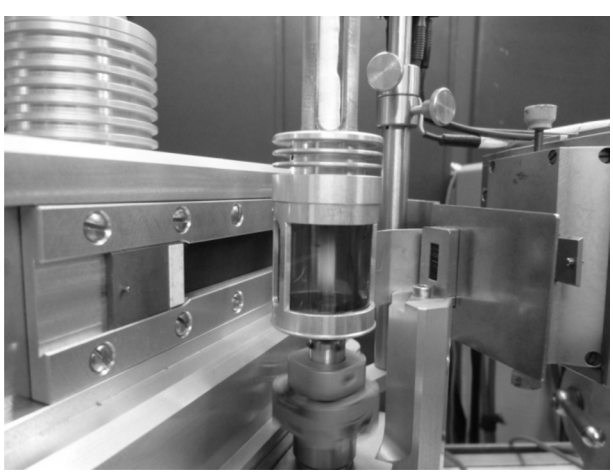

Fig. 6. The heat-keeping cover, preventing too much air convection and respectively fast cooling of the sample

Calibration. Both the sample and the thermocouple in this device receive the main part of their heat by direct infrared radiation from the ceramic mounted heating coil. Because of the open design of the device, the importance of the air flow as heat transferring agent is rather low. Even the role of the heat keeping cover, which slows down the air convection around the sample and thermocouple, is mostly to avoid pretty fast cooling of the sample, rather than helping to heat the device volume. Receiving equal amounts of heat, however, the sample and the thermocouple reach different resulting temperatures, because of their rather different heat capacities (45.3 J/mol.K for the quartz glass, opposed to 25.9 J/mol.K for the Pt/Rh thermocouple). Soundly, this difference is almost negligible at lower temperatures, but becomes rather significant with temperature rise.

Since the device operating software only receives the thermocouple temperature, finding an equation, well modeling the sample temperature for any given thermocouple temperature, is crucial for obtaining conclusive study results. This is the aim of the calibration procedure.

All *calibration approaches* are based on comparison of the thermocouple temperature with some independent evidence for the real sample temperature. Three kinds of physical phenomena can be employed as independent temperature evidences: known thermal expansion coefficients; known melting temperatures; known phase transition temperatures. The advantage of the first approach is that it can give a continuous series of d-values (and respective temperatures, calculated from the known expansion coefficient) to plot against the respective thermocouple temperatures, this way providing a smooth calibration curve in the whole temperature range of interest. Its disadvantage, however, is that the whole calibration curve depends on measurements of just one substance. If there is something wrong with the substance (chemical purity or physical conditions) or with the experiment (zero shift, sample displacement

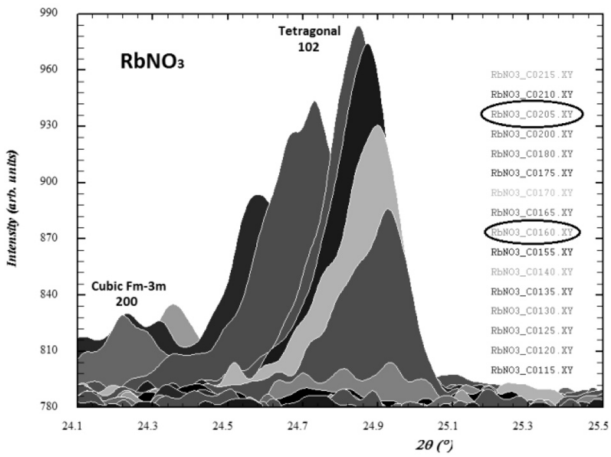

Fig. 7. Example of RbNO3. Tetragonal phase appears on flat background at 160 °C. So does the cubic phase at 205 °C

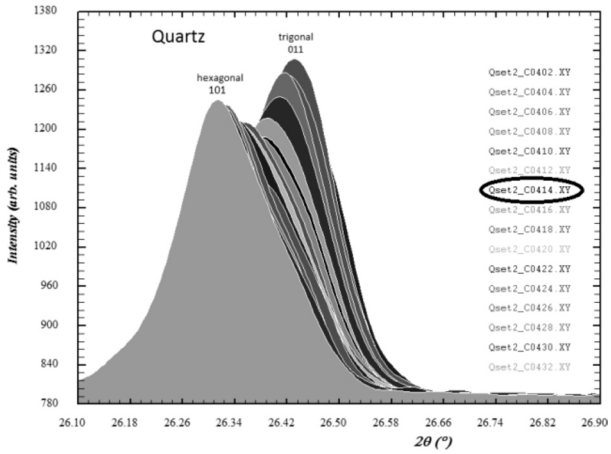

Fig. 8. Typical saddle shape of the stacking diagram for the trigonal/hexagonal transition in quartz

etc.) these errors are cast over the whole range of results as systematic errors.

A big disadvantage of the second approach is that melting is not an abrupt phenomenon. It always takes a temperature range with smooth disappearance of the diffraction lines and hence the accuracy of the calibration curve, created this way, is pretty poor.

For the reasons expressed above, we choose the third approach – using phase transitions in our calibration experiments.

In this approach, each point of the calibration curve is determined by the results of a separate experiment, using proper substance with well known phase transition effect. Before each experiment, available reference data have been carefully investigated, to make sure that there is no discrepancy in the literature, about the character and the temperature at which the targeted phase transition occurs. Another important information to collect before the experiment was to learn at what Bragg angle the most visible transition effect should be expected. This was done in order to adjust the heater and its cover, so that reflections in the respective 2 theta range are to be observed.

Since preliminary reference data showed that the thermocouple systematically shows temperatures lower than the real sample temperature, and at the high end of the range (900 °C) this discrepancy can even reach 250 °C, we used to start stepwise heating far before the expected phase transition. The step was chosen larger at the beginning and was decreased with approaching the expected transition point. The result was a series of diffraction data, which could be plotted in some stacking diagram, to visualize the changes.

Duration of the heating step. Structural and respective diffraction pattern changes, which appear on heating, require some time to take place. Since the required tempering time is specific for each substance and each phase transition, no general suggestion for the proper step duration can be drawn out. This is why we used to adjust step duration experimentally, by consecutive collection of diffraction patterns at constant temperature, until they remain unchanged.

The character of the change in the diffraction pattern depends on the character of the structural change. Since phase transitions usually refer to slight distortions of the atomic arrangement and respective slight displacements of the diffraction peaks, they are best recognized, when extinction conditions are changed. In this case, a new peak appears right from the flat background (Fig. 7). In most cases, however, the change is expressed by deformation of some peaks, loss of intensity and finally growth of new peak at the foothills of an existing one. Often the new and old peaks coexist over some temperature range, forming a typical saddle shape on the stacking diagram (Fig. 8), but we need certain strict temperature value to assign to the phase transition. We choose to assign it the temperature of first appearance of the new peak, since presumably this should be the point of symmetry change.

The set of substances, used for the creation of the calibration curve, was chosen on the grounds of available reference data, temperature of phase transition and of course – availability in accessible labs. Our choice is given in the following Table 1.

Table 1. List of used substances and respective reference data

Substance	Reference	Substance	Reference
$TlNO_3$	[3, 4, 5, 6]	Quartz	[3, 13]
KNO_3	[3, 5, 6, 7, 8]	KCl	[3, 15]
$RbNO_3$	[3, 5, 6, 9, 10, 11, 12]	NaCl	[3, 15]
Ag_2SO_4	[3]	$SrCO_3$	[5, 14]

Substance	reference	set	sample
Ambient temp	0	0	0
$TlNO_3$ Orth↔Trig	79	73	79
KNO_3 Orth↔Trig	128	108	128
$TlNO_3$ Trig↔Cub	143	112	143
$RbNO_3$ Hex↔Cub(Pm-3m)	164	125	164
$RbNO_3$ Cub (Pm-3m)↔Tetr	219	160	219
$RbNO_3$ Tetr↔Cub (Fm-3m)	291	205	291
Ag_2SO_4 Orth↔Hex	427	304	427
Quartz Trig↔Hex	573	410	573
KCl melting	776	555	776
NaCl melting	804	575	804
$SrCO_3$ Orth↔Trig	930	680	930

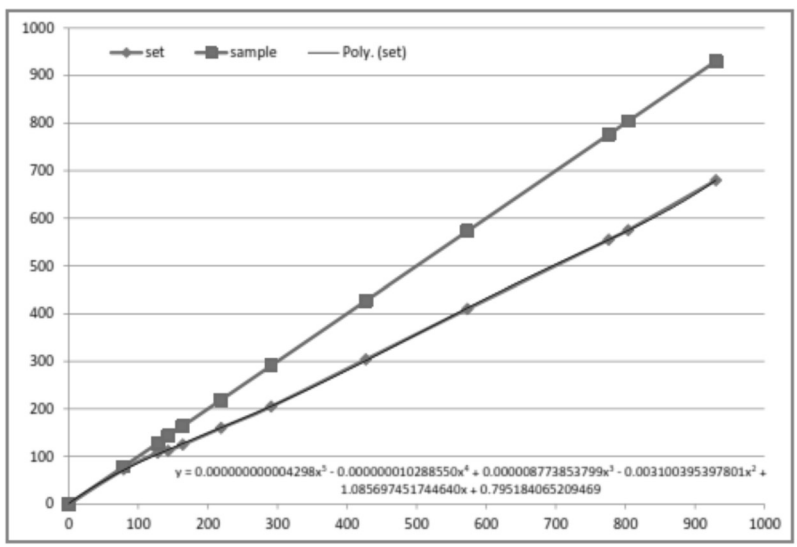

Fig. 9. Constructed calibration curve, with the underlying data base (on the left): list of used substances with known phase transitions; sample (presumably equal to reference) and set (read from the thermocouple) temperatures for each phase transition. Polynomial equation of the approximating curve is given below the set curve

The calibration curve was built on the base of the data, obtained from the above described experiments on the above listed substances. The results are given in Figure 9.

Discussion. The obtained calibration curve confirms the observation of [16], that set temperatures (those sensed by the thermo-couple) are always lower than actual sample ones and at the hot end of the range (900 °C) this difference can reach 250 °C. It is very similar to that in the unpublished study of M. Nippus (2000) from Huber GMBH, who proposes the following approximation function: $T_{set} = T_{sample} - A*(1 - \exp(B*T_{sample}\text{^}2))$, where A and B are fitting parameters, specific for each individual heating device. Instead, we found a pretty good fit of the obtained results with a polynomial of order 5. The most satisfying result, however, is that the obtained dependence differs from a simple linear function $T_{set} = 0.7*T_{sample} +10$ within an accuracy range of ±10 °C, which is acceptable, for many purposes.

REFERENCES

1. K. J. Åström, PID Control, in: Control System Design, (2002).
2. http://en.wikipedia.org/wiki/PID_controller
3. *Table of Calibration Standards* by Dr. M. Emrich. http://www.mpi-stuttgart.mpg.de/xray/html/temperature_calibration.html
4. R. N. Brown, A. C. McLaren, *Acta Cryst.*, **15**, 977 (1962).
5. C. N. R. Rao, B. Prakash, M. Natarajan, *NSRDS-NBS* 53, (1975).
6. K. H. Stern, *J. Phys. Chem. Ref. Data*, **1,** 747 (1972).
7. A. Paar, XRD Temperature Calibration with Phase Transitions. Sources of errors, advantages and limitations.
8. J. K. Nimmo, B. W. Lucas, *Acta Cryst.*, B**32**, 1968 (1976).
9. E. L. Charsley, P. G. Laye, H. M. Markham, J. O. Hill, B. Berger, T. T. Griffiths, *Thermochim. Acta*, **469**, 65 (2008).

10. R. N. Brown, A. C. McLaren, *Acta Cryst.*, **15**, 974, (1962).
11. S. Wacharine, D. Hellali, H. Zamali, J. Rogez, M. Jemal, *J. Therm Anal Calorim*, DOI 10.1007/s10973-011-1544-3, (2011).
12. B. W. Lucas, *Mater. Sci. For*., **27-28**, 95 (1988).
13. P. J. Heaney, D. R. Veblen, *Amer. Miner*., **76**, 1018 (1991).
14. S. M. Antao, I. Hassan, *Can. Min.,* **47**, 1245, (2009).
15. http://www.gcsescience.com/imeltcomplz.htm
16. G. E. Brown, S. Sueno, C. T. Prewitt, *Am. Mineral*. **58**, 698 (1973).

ТЕРМИЧНАТА ПРИСТАВКА НА ЦИФРОВАТА ГИНИЕ КАМЕРА В ГЕОЛОГИЧЕСКИЯ ИНСТИТУТ НА БАН: КАЛИБРИРАНЕ И НАТРУПАН ОПИТ

Т. Н. Керестеджиян*, И. Сергеева

Геологически институт, Българска академия на науките, 1113 Sofia

Постъпила на 16март, 2012 г.; приета на 17 април, 2012 г.

(Резюме)

Наред с нормалния (с плосък препарат) режим, уникалната за България цифрова Гиние камера в Геологическия институт (БАН), може да бъде използувана и с препарат в капилярна тръбичка. В този режим е възможно към системата да се добави специален керамичен нагревател, превръщащ установката в мощен инструмент за in-situ термична дифрактометрия. Има множество възможните приложения на тази система, най-важните от които са: определяне на коефициента(ите) на термично разширение на материала по всяко кристалографско направление, установяване на аномални или отрицателни трендове на термично разширение, регистрация на фазови преходи (обратими или необратими), проследяване на термично предизвикани, твърдотелни реакции (образуване на междинни твърди разтвори) и др. Успешната употреба на системата, обаче, изисква някои предварителни знания и внимателно калибриране. За този тип термична приставка калибрирането е от решаващо значение, доколкото препаратът в капилярната тръбичка и отчитащата температурата термодвойка реагират различно на постъпващото инфра-червено облъчване и постигат различна резултатна температура. Целта на калибрирането е да се намери подходяща функция, добре описваща температурното състояние на образеца, за всяка избрана температура на термодвойката в рамките на работния интервал (0–900 °C). Въпреки че калибрирането е основната, то не е единствената трудност при работа с термичната приставка. Има множество възможни грешки, които неопитният изследовател може да допусне. В тази работа авторите споделят резултатите от калибрирането и първоначалния си опит от използуването на системата.

Bulgarian Chemical Communications, Volume 44, Proceedings of the III[rd] National Crystallographic Symposium (pp. 83–89) 2012

Two-stage protonation of a small-pore microporous zirconosilicate $Na_2ZrSi_2O_7.H_2O$

V. V. Kostov-Kytin*, R. P. Nikolova, N. L. Lihareva

Institute of Mineralogy and Crystallography, Bulgarian Academy of Science, Acad. G. Bonchev Str., Bl. 107 Sofia, Bulgaria

Received February 15, 2012; Revised March 27, 2012

The crystal chemical changes occurring upon protonation of the small-pore zirconosilicate $Na_2ZrSi_2O_7.H_2O$ have been studied. It has been noticed that variations of the reaction's medium initial pH influence the degree of sodium leaching of this material. It is found that this dependence is closely related to the structural positions of the Na atoms. The crystal structures of partially and completely protonated samples were refined and compared with the one of the as-synthesized material. In general, the protonation process preserves the framework topology but, however, it noticeably causes mutual shifting of the adjacent layers, which affects the unit cell parameters. Initially, the unit cell volume increases from 673.56Å^3 (as-synthesized phase) to 684.9 Å^3 (partially protonated sample) and next shrinks to 660.8(1) Å^3 (completely protonated material). The monoclinic arrangement becomes pseudo-orthorhombic with values of β = 89.519(9)° and 89.872(3)° for the partially and fully protonated samples, respectively. The evaluation of the framework deformation evidences that protonation causes higher degree of framework deformations than the dehydration process.

Key words: zirconosilicate, protonation, crystal structure, framework deformation.

INTRODUCTION

A new microporous phase was hydrothermally synthesized in the system Na_2O–ZrO_2–SiO_2–H_2O [1]. Subsequently, the structure of this powdered material was successfully solved based on the Rietveld refinement routine carried out with the GSAS program [2] and EXPGUI [3] and using the suitably modified atomic coordinates of the topologically identical $Na_3ScSi_2O_7$ as a starting structural model [4]. It has been found that $Na_2ZrSi_2O_7.H_2O$ is a small-pore compound with framework built up of ZrO_6 octahedra and SiO_4 tetrahedra in a manner that results in the formation of layers (alpha-ZrP type [5]) parallel to (001), where silicate groups lie both above and below the plane of the zirconium atoms. The adjacent layers are related by rotation and are connected to each other *via* oxygen atoms creating $[Si_2O_7]$ pyrogroups. The structure is thus a three-dimensional framework and possesses system of two interconnected channels running parallel to (001). The sodium ions and water molecules reside within the channels. Sodium occupies two crystallographic positions – general and special ones. While the occupied in half "general" Na resides together with the water molecules almost in the central parts of the channels, the "special" Na lies in cavities set up between the alpha-ZrP type of layers building up the polyhedral ($ZrSi_2O_4$) framework [4]. Lately, it was found that upon heating the monoclinic structure of the title compound converts into orthorhombic one, however preserving the initial topology. The process is accompanied by water release and a slowly rehydration is possible for this material only up to 300 °C. Above this temperature the orthorhombic structure is preserved up to 800 °C and next an irreversible transition into a phase with denser triclinic structure occurs thus, precluding the ion-exchange properties of this compound [6]. Further on, the ion-exchange properties of $Na_2ZrSi_2O_7.H_2O$ have been investigated (unpublished data). Upon exchange on Sr, substantial changes of the peaks intensity ratios in the powder XRD patterns of the final products have been detected being more pronounced at lower initial pH of the reaction media. Chemical analyses and simulated XRD pattern of "fully exchanged" on Sr material have been indicative that such drastic peak ratio differences could not be obtained only on the account of Sr uptake. Thus, it has become clear

* To whom all correspondence should be sent:
E-mail: vkytin@abv.bg

that the observed changes are due to Na leaching. Taken alone this fact confirms the microporosity of the title compound. However, our attention was attracted by the possibility to investigate the mechanism and degree of protonation of $Na_2ZrSi_2O_7.H_2O$ upon various experimental conditions (initial pH) as well as the structural changes occurring upon these processes.

EXPERIMENTAL

Sample preparation

The starting compound $Na_2ZrSi_2O_7.H_2O$ was hydrothermally synthesized following a procedure described by Kostov-Kytin and Kalvachev [1]. Best results were achieved from gels with the following starting composition (moles): $37.5Na_2O$ – $2.5ZrO_2$ – $8SiO_2$ – $675H_2O$ and 480 hours synthesis duration at 200 °C.

Protonation procedure

Several samples of the as-synthesized material of one gram each were stirred in distilled water for 7 hours at 60 °C and solid –to- liquid ratio of 1:200. The initial pH was adjusted by adding HNO_3. Subsequently, only two of the samples were chosen for further investigations designated as HM-1 and HM-2, 1 and 2 meaning 0.1 and 0.2N acid solution used in each experiment, respectively.

Analytical Procedures

Initial characterization of the HNO_3 treated samples were performed by powder X-ray diffraction (XRD) analysis using a Bruker D2Phaser diffractometer with CuKα radiation in the 2θ range from 5 to 90° and in a step-scan regime (step 0.015° and time 6 s). Sodium content in the run products after the treatment was determined by AAS (Perkin Elmer 3030) under conditions prescribed by the manufacturer. TG and DTA studies were performed on a Stanton Redcroft thermal analyzer (STA 780) at a heating rate 10 deg/min in static air.

Structure Refinement

The atomic coordinates of $Na_2ZrSi_2O_7.H_2O$ were used as a starting structural model for Rietveld refinement of HM-1 and HM-2 carried out with the GSAS program [2] and EXPGUI [3]. Initial chemical compositions for the acid-treated phases were adjusted in accordance with the number of water molecules and sodium content obtained from the TG-DTA data and the chemical analyses, respectively - a procedure, which will be described in details in the following section. Both structures were initially refined with soft constraints imposed on the Zr-O and Si-O bond distances and in the final refinement cycles they were released. In the case of HM-2 this did not cause substantial structural distortions before convergence achievement. However, unrealistic bond distances and angles were received for HM-1, whereas no substantial improvement of the statistical Rietveld parameters was achieved. Thus, only the results for the constrained structural refinement of HM-1 are presented, here. The bond restraints χ^2 contribution for each one of the 10 restraints inserted is 6.71. In addition, a small 2θ range from 17.615 to 18.245° has been excluded from the refinement of HM-1 due to the presence of a negligible amount of impurity phase. In both refinements: (i) all atoms in the structures were refined isotropically, (ii) expecting similar U_{iso} values for the O atoms these ones were refined in a group, (iii) neutral atomic scattering factors, as stored in GSAS, were used for all atoms, and (iv) no corrections were made for absorption.

RESULTS

Figure 1 presents the powder XRD patterns of the as-synthesized $Na_2ZrSi_2O_7.H_2O$ and the two acid-treated samples together with the final difference plot of the XRD Rietveld refinement. Results from DTA-TG analyses of the investigated materials are shown in Figure 2. The 1.79% weight loss after 500 °C (Fig. 2a) is assumed to be due to decomposition of some nitrogen-containing products. Whereas water liberates HM-1 within a single stage, two distinct stages of water release are detected for HM-2, most probably being due to the interrelation peculiarities of the sodium cations and H_2O molecules. Based on the chemical analyses and assuming that weight losses in the temperature range of 100–500 °C are being totally due to water release the following empirical formulas have been calculated: $H_2ZrSi_2O_7.2.6H_2O$ for HM-1 and $H_{0.5}Na_{1.5}ZrSi_2O_7.1.4H_2O$ for HM-2, respectively. Further on, taking into consideration the crystallographic position peculiarities of sodium atoms in the initial phase and assuming that Na from the general position (Na_g) is more susceptible to the protonation process than the structurally more "hidden" Na from the special position (Na_p) occupying the cavities attached to the structural layers we have suggested the following formula for HM-2: $H_{0.5}Na_{g0.5}Na_pZrSi_2O_7.1.4H_2O$. Initially, no other crystallographic position has been suggested for the excessive water in this structure. As for the totally protonated HM-1 we have assumed three crystallographically distinct positions for the H_2O

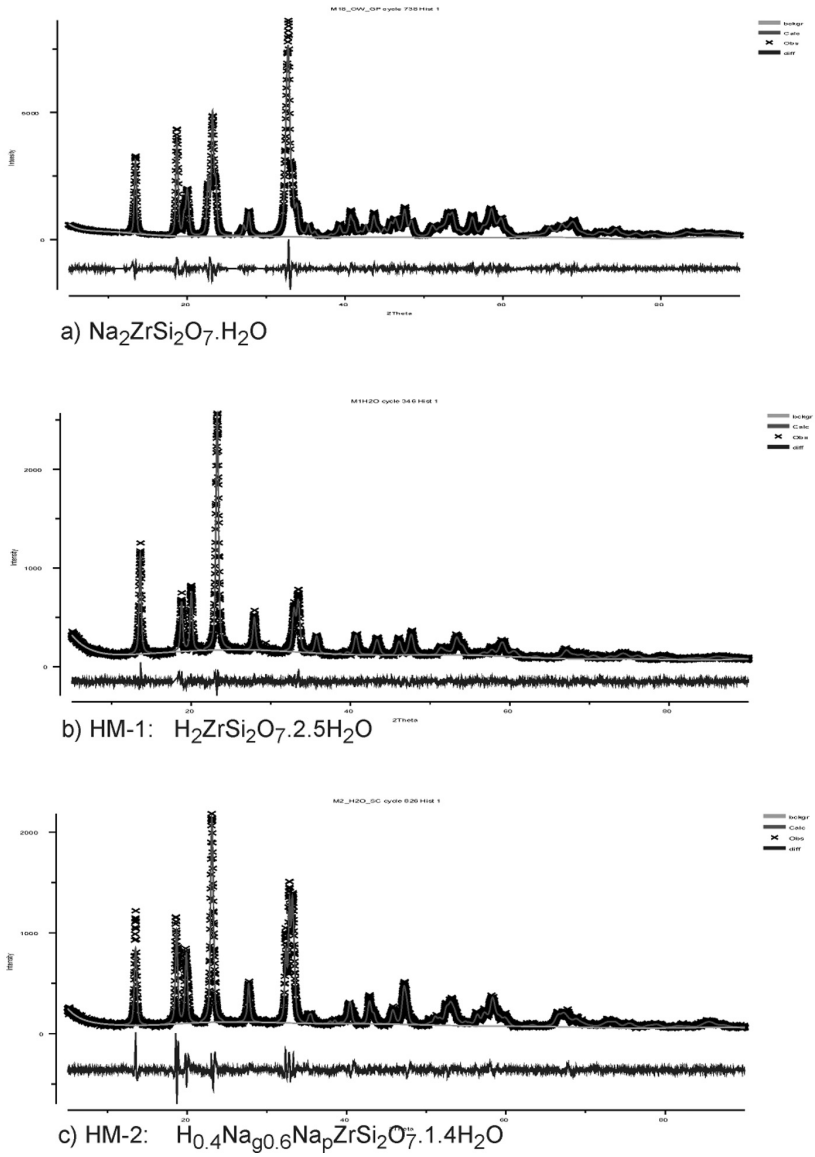

Fig. 1. Powder XRD patterns of: a) as-synthesized $Na_2ZrSi_2O_7.H_2O$; b) HM-1; c) HM-2; The difference (bottom line) of the observed (crosses) *vs.* calculated (continuous line) profiles for each sample after the final XRD Rietveld refinement are plotted bellow each pattern

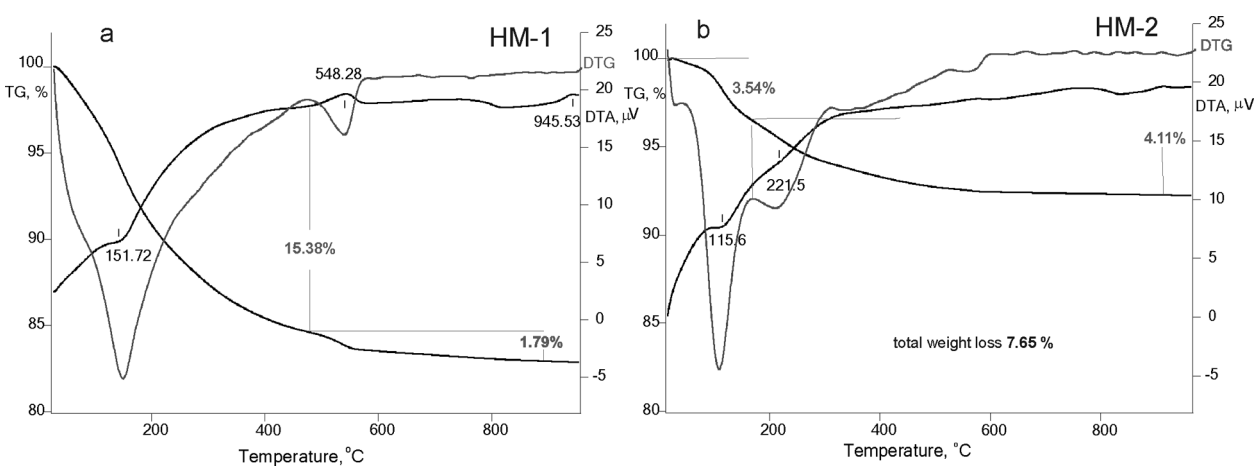

Fig. 2. TG-DTA curves of: a) HM-1 and b) HM-2

molecules: first of them coinciding with that one of the water in the structure of the as-synthesized compound, and the other two have been placed in the positions of Na_p and Na_g, respectively. Namely these considerations have been used to prepare the structural models of both acid-treated phases for the Rietveld procedure. In the final stages of the structure refinements structural positions and occupancies of the two sodium atoms in the partially protonated HM-2 and the same for the water molecules in both phases have been refined. In contrast to the completely protonated phase an unrealistic excess of water has been established for HM-2. Then we inserted additional H_2O molecule (Ow_g) there and constrained its coordinates and occupancy with those ones of Na_g taken from the structure of the as-synthesized compound. The subsequent refinement of atomic coordinates and occupancies of the extra-framework species completed with a structural model, which crystal chemistry stays very close to our notion about the occurring changes and the mechanism of protonation. The resulting compositions are in perfect agreement with the obtained chemical analyses. The final crystallographic and Rietveld parameters for the studied compounds are listed in Table 1. The crystal structures of the initial and the protonated samples are presented in Fig. 3.

DISCUSSION

As seen from Figure 3 the investigated material preserves its framework topology despite the intensity of the applied treatment. As it was pointed out

Table 1. Crystallographic data and results of the Rietveld refinement of $Na_2ZrSi_2O_7 \cdot H_2O$

	Reference [4]	HM-2 this study	HM-1 this study
Space group	*C*2/*c*	*C*2/*c*	*C*2/*c*
Cell parameters:			
a (Å)	5.4715(4)	5.4552(6)	5.4227(7)
b (Å)	9.4111(6)	9.6215(13)	9.4160(27)
c (Å)	13.0969(8)	13.0505(19)	12.9418(21)
α	90.0000	90.0000	90.0000
angles (°) β	92.851(7)	89.519(9)	89.872(3)
γ	90.0000	90.0000	90.0000
V (Å^3)	673.56(7)	684.9(2)	660.8(3)
Empirical formula	$Na_2ZrSi_2O_7$ (H_2O)	$H_{0.4}Na_{g0.6}ZrSi_2O_7$ 1.4(H_2O)	$H_2ZrSi_2O_7$ 2.5(H_2O)
Fw	1285.46	1276.98	1198.49
Z	4	4	4
P_{calc} (g cm^{-3})	3.17	3.096	3.012
Wavelength (Å)	1.5419	1.5419	1.5419
2θ range (deg)	5–90	5–90	5–90
Step-scan increment (2θ), deg	0.01	0.015	0.015
Step-scan time, s	5	6	6
No of data points	4089	5665	5632
No of contributing reflections	514	594	583
No of structural parameters	29	43	33
No of profile parameters	7	5	5
Profile function	Pseudo-Voight	Pseudo-Voight	Pseudo-Voight
R_{wp}	0.0914	0.1249	0.0911
R_p	0.0713	0.0962	0.0707
R_F^2	0.0207	0.1053	0.2132
χ^2	4.33	2.6	1.468
Occupancies of extra-framework species:			
Na_g		0.29	–
Na_p		1	–
Ow		0.52	0.49
Ow_g		0.21	0.49
Ow_p		–	0.55

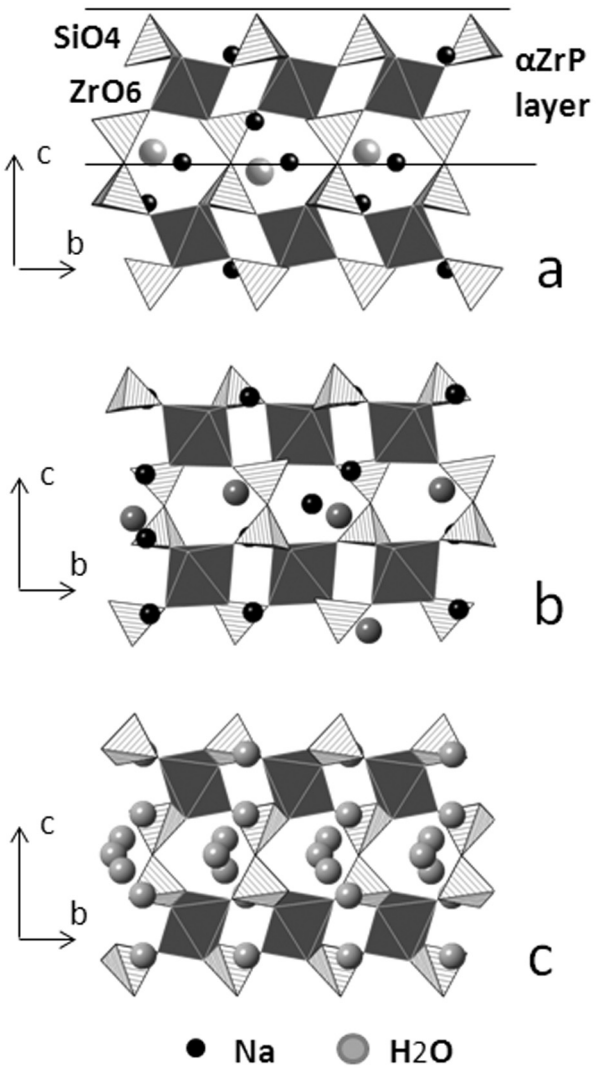

Fig. 3. Crystal structure of initial (a) and protonated samples HM-2 (b) and HM-1 (c)

earlier [4] such kind of framework is very flexible with respect to the exhibited geometrical features of the $[Si_2O_7]$ pyrogroup. Its configuration can be described by two angles: T-O-T' (τ) angle corresponding to the tilting of the TO_4 tetrahedra over the common oxygen atom and O_p-T_p-O_p' (ρ) angle indicating the twisting of the triangular faces set by the terminal oxygen atoms (Fig. 4). Such approach was applied before to describe the degree of structural deformations occurring upon thermal treatment of the studied material [6]. Thus, we can now compare the values of the tilting and twisting angles for the as-synthesized compound with those ones obtained after its heating and/or protonation. As mentioned in the "Introduction" section water releasing upon heat treatment of the as-synthesized phase causes framework relaxation and the initially monoclinic structure converts into an orthorhombic one without topological changes. The tilting and twisting angles for monoclinic and orthorhombic structures do not differ substantially and have values: τ = 156.9°, ρ = 7.53° and τ = 145.07°, ρ = 0°, respectively. Similar structural behavior has been observed for $Na_2ZrSi_2O_7.H_2O$ upon its acid-treatment. The crystal structures of the protonated samples exhibit pseudo-orthorhombic symmetry with β = 89.51(1) and 89.87(1)° for HM-2 and HM-1, respectively. Cell volume increase from 673.56Å^3 (as-synthesized phase) to 684.9 Å^3 (partially protonated sample) is observed when the reaction's media concentration has been adjusted to 0.2N HNO_3. The successful refinement of the structure of HM-2 confirms our initial assumption that the "mid channel located" sodium (Na_g) is more susceptible to the protonation process than the stronger bound to the framework oxygen atoms "cavity located" (Na_p) one. Leaching would hardly be possible on Na atoms of special position before this process has been totally completed for sodium placed in general position. Attempts to refine the structure with partial decrease of Na_p occupancy or total elimination of this position failed. When all of the sodium ions are leached (c ≈ 0.1N HNO_3) from the structure the cell volume decreases to 660.8(1) Å^3. These data suggest a two-stage protonation mechanism for the studied material that could be controlled through adjustment of the reaction's media pH. The values of τ =179.18°, ρ =27° and τ =152.37°, ρ =22° for HM-2 and HM-1 respectively confirm the enlargement of the framework channels during the first protonation stage and subsequent relaxation upon further protonation. The obtained values for the twisting angles of both protonated samples characterizing the mutual rotation of the adjacent layers differ substantially from those ones found in the initial and dehydrated samples

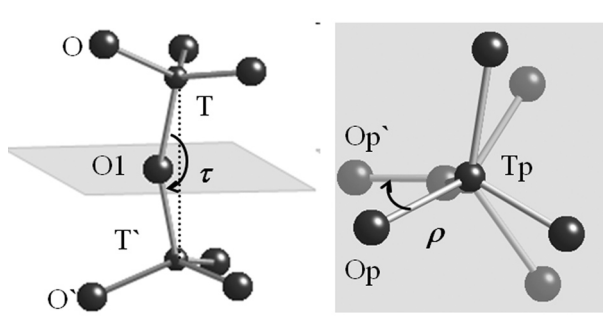

Fig. 4. Angles indicating the degree of pyrogroups deformation. Op, Op' and Tp are projections of O, T, T' and O' on the plane perpendicular to T-T'

Table 2. Comparison of the values of the tilting and twisting angles of the as-synthesized compound and its dehydrated and protonated forms

Material	Tilting angle (τ) °	Twisting angle (ρ) °
as-synthesized $Na_2ZrSi_2O_7.H_2O$	156.9	7.53
dehydrated $Na_2ZrSi_2O_7$	145.07	0
partially protonated HM-2	179.18	27
completely protonated HM-1	152.37	22

(Table 2). This suggests that protonation process causes higher degree of framework deformations as compared to the dehydration one. Although this process is accompanied with increase of the water content in the channels this could not compensate for the lack of "inner" stabilization caused by leaching of sodium from them.

CONCLUSION

An experimental procedure for controlled protonation of a new small-pore microporous zirconosilicate is reported. The occurring compositional and structural changes have been studied and described by means of atomic absorption spectroscopy, TG-DTA, and Rietveld refinement routine. Two pH-dependent protonation stages of the $Na_2ZrSi_2O_7.H_2O$ have clearly been defined. Crystal structures of the partially and completely protonated samples have been refined. Evaluation of the framework deformation in terms of tilting and twisting angles of the Si_2O_7 groups has given evidence that the protonation process causes stronger deformations as compared to those ones occurring upon dehydration of the same structure. Apparently, sodium leaching deprives the channels from their "inner" stabilization causing substantial mutual shifting of the neighboring building layers, however without changing the initial topology of this material.

Acknowledgements: *This study is part of the co-operation within the frames of Joint Research Project between Bulgarian Academy of Sciences and Academy of Sciences of the Czech Republic, as well as by the Joint Research Project between the CLMC-BAS, Sofia and the ISPE-UAS, Kiev and financially supported by the National Science Fund - Bulgarian Ministry of Education, Youth and Science under contract DO02-38.*

REFERENCES

1. V. Kostov-Kytin, Yu. Kalvachev, *Meeting "Micro- and mesoporous mineral phases" Rome*, December 6-7, 2004, Extended Abstracts, 235 (2005).
2. A. C. Larson, R. B. Von Dreele, Report LAUR 86-748, Los Alamos National Laboratory (2000).
3. B. H. Toby, *J. Appl. Crystal.* **34**, 210 (2001).
4. R. P. Nikolova, K. Fujiwara, N. Nakayama, V. Kostov-Kytin, *Solid State Sci.*, **11**, 2, 382 (2009).
5. P. Pertierra, M. A. Salvado, S. Garcia-Granda, C. Trabajo, J. R. Garcia, A. Y. Bortun, A. Clearfield, *Journal of Solid State Chemistry*, **148** (1), 41 (1999).
6. N. R. Petrova, N. Nakayama, S. Bakardjieva, P. Bezdicka, V. Kostov-Kytin, *Solid State Sciences*, **13** (5), 1187 (2011).

ДВУСТАДИЙНО ПРОТОНИРАНЕ НА МИКРОПОРЕСТ ЦИРКОНОСИЛИКАТ $Na_2ZrSi_2O_7.H_2O$

В. В. Костов-Китин*, Р. П. Николова, Н. Л. Лихарева

Институт по минералогия и кристалография, Българска академия на науките, ул. „Акад. Г. Бончев“, бл. 107, София, България

Постъпила на 15 февруари, 2012 г.; приета на 27 март, 2012 г.

(Резюме)

Изследвани са кристалохимичните промени настъпващи в процеса на протониране на микропорестия цирконосиликат $Na_2ZrSi_2O_7.H_2O$. Показано е, че степента на киселинност на първоначалния разтвор влияе върху степента на излужване на натрия от пробата. Уточнени са кристалните структури на частично и напълно протонирани проби и получените данни са сравнени с аналогичните за изходната фаза. В процеса на протониране кристалната структура запазва своята топология, но се наблюдава взаимно завъртане на съседните слоеве, което рефлектира съответно в промяна на параметрите на елементарна клетка. В първия етап обемът на елементарна клетка се увеличава от 673.56Å^3 (синтезирана фаза) до 684.9 Å^3 (частично протонирана фаза) а при втория намалява до 660.8(1) Å^3 (напълно протонирана фаза). Доказано е, че в процеса на протониране, кристалната структура релаксира до псевдо-орторомбична със стойности за ъгъл β = 89.519(9)° и 89.872(3)° съответно за частично и напълно протонираната фаза. Данните показват, че процесът на протониране води до по-значителни промени в кристалната структура от процеса на дехидратация на изследвания материал.

Bulgarian Chemical Communications, Volume 44, Proceedings of the III[rd] National Crystallographic Symposium (pp. 90–97) 2012

Synthesis and characterization of magnetic nano-sized Fe_3O_4 and $CoFe_2O_4$

D. Kovacheva[1*], T. Ruskov[2], P. Krystev[2], S. Asenov[2], N. Tanev[2], I. Mönch[3], R. Koseva[3], U. Wolff[3], T. Gemming[3], M. Markova-Velichkova[1], D. Nihtianova[1], K.-F. Arndt[4]

[1] *Institute of General and Inorganic Chemistry, Bulgarian Academy of Sciences, 1113 Sofia, Bulgaria*
[2] *Institute for Nuclear Research and Nuclear Energy, 1784 Sofia, Bulgaria*
[3] *Leibniz Institute of Solid State and Materials Research Dresden, D-01069, Dresden, Germany*
[4] *Department of Chemistry, Physical Chemistry of Polymers, TU Dresden, D-0162, Dresden, Germany*

Received February 20, 2012; Revised April 2, 2012

The synthesis of Fe_3O_4 and $CoFe_2O_4$ nanomaterials was performed by co-precipitation of corresponding metal hydroxides and their further decomposition to oxides under ultrasonic irradiation. The particles were characterized by X-Ray diffraction (XRD), transmission electron microscopy (TEM) and vibrating sample magnetometry (VSM). The crystallite sizes were 7.1 nm for the Fe_3O_4 sample and from 1.9 to 21 nm for the $CoFe_2O_4$ sample depending on the synthesis conditions. Mössbauer spectra of Fe_3O_4 and $CoFe_2O_4$ were measured at room temperature and 77 K. They revealed that samples show either superparamagnetic behavior or a mixture of superparamagnetism and ferrimagnetism depending on the crystallite sizes and temperature. Cation distribution for 10.4 nm $CoFe_2O_4$ was obtained from the Mössbauer spectra as well.

Key words: nanoparticle, spinel ferrites, sonochemical synthesis.

INTRODUCTION

Nano-sized materials made of magnetite (Fe_3O_4) and cobalt ferrite ($CoFe_2O_4$) are attractive both from fundamental point of view and for various physical, chemical and biological applications. The general formula of spinel ferrites is $MO.Fe_2O_3$ (where M is usually a divalent transition metal ion with an ionic radius, $r < 1$Å). The spinel ferrite structure consists of a cubic close-packed oxygen arrangement, in which cations occupy tetrahedral and octahedral interstices. Occupation of tetrahedral sites with divalent metal ions yields a normal spinel structure typical for $M^{2+} = Zn^{2+}$, Cd^{2+}, Mn^{2+}, while occupation of octahedral sites with divalent metal ions results in an inverse spinel structure when $M^{2+} = Fe^{2+}$, Co^{2+}, Ni^{2+}, Cu^{2+}. Ferrites comprise a broad and important class of magnetic materials, with important technological applications. Recently it was found that magnetic properties of nanosized spinel ferrites differ strongly from those of the corresponding bulk materials. For example magnetic saturation and coercitivity change drastically when the size of the particles becomes very small. Nanoparticle's physical and chemical characteristics are interesting not only from a fundamental point of view but also from a practical, since they offer possibilities for various new physical, chemical and biological applications. Special attention was paid to their application in medicine, where they can be used as magnetic resonance imaging agents in diagnostic, heat mediators in hyperthermia treatments as well as magnetic guidance for drug delivery [1–6].

Various synthetic methods have been developed to synthesize oxide nanoparticles, among them co-precipitation, thermal decomposition, sol-gel, microemulsion and other techniques [7–14]. It was established that the degree of crystallinity, particle size and particle morphology of oxide nanoparticles are strongly dependent on the method used for their preparation. The simplest synthetic procedure is based on the co-precipitation method, which involves the co-precipitation of M^{2+} and M^{3+} ions in basic aqueous media. Recently, the sonochemical method started to be applied widely in material science because it allows obtaining a wide range of functional materials such as magnetic nanocomposites, catalysts, molecular sieves etc. [15–18]. The mechanism of sonochemical reactions in aqueous and non-aqueous solutions is governed by two ma-

* To whom all correspondence should be sent:
E-mail: didka@svr.igic.bas.bg

jor effects accompanying the interaction of ultrasonic radiation with liquid media. The first one is the intensification of mass-transfer processes and the second one is cavitation. The collapse of cavitation bubbles results in an enormous rise of local temperatures and pressures leading to the decomposition of dissolved volatile compounds and the formation of amorphous and crystalline nanopowders.

In the present work we applied the sonochemical method for the synthesis of nanosize spinel oxide materials, namely Fe_3O_4 and $CoFe_2O_4$ samples with particle sizes in the range from 1.9 to 21 nm and investigated their size dependent structural and magnetic characteristics.

EXPERIMENTAL

The synthesis was performed by co-precipitation of corresponding metal hydroxides and their further decomposition to oxides under ultrasonic irradiation. As starting compounds $FeCl_2.6H_2O$, $Fe(NO_3)_3.9H_2O$, $Co(NO_3)_2.6H_2O$ and NaOH in a molar ratio of 1:2 were used. Metal nitrates and NaOH were dissolved separately in appropriate amount of distilled water. To obtain materials with different particle sizes for the $CoFe_2O_4$ samples the concentration of the initial solutions was varied. The co-precipitation took place while metal salt solutions were dropwise added to the solution of NaOH. The sonication of the precipitate was performed at 20 KHz, and 750 W in an ultrasonic processor SONIX, USA. The total sonication time was 1 hour. The obtained products were repeatedly washed with distilled water, filtered and finally dried at 50 °C.

Materials were first characterized by X-ray diffraction. Powder X-ray diffraction patterns were collected within the range from 10 to 80° 2θ with a constant step of 0.02° 2θ on a Bruker D8 Advance diffractometer with Cu Kα radiation and a LynxEye detector. Phase identification was performed with the Diffrac*plus* EVA using the ICDD-PDF2 Database. The powder diffraction patterns were evaluated with the Topas-4.2 software package using the fundamental parameters peak shape description including appropriate corrections for the instrumental broadening and diffractometer geometry. Unit cell parameters were obtained by whole powder XRD pattern fitting using as a starting values the data taken from the files in ICDD-PDF2 (#79-416 for magnetite and #70-8729 for $CoFe_2O_4$). Unit cell parameters, profile parameters as well as zero shift were varied to obtain a good fit with the experimental data. The mean crystallite domain sizes were determined using the same whole powder XRD pattern fitting mode of the program. For this purpose the integral line breadth approach for the generalized treatment of the domain size broadening – $\beta_i = \lambda / L_{vol} cos\theta$ was employed, where β_i is the integral breadth of the diffraction line i and L_{vol} is the volume weighted mean column height.

The specific surface area was determined by low temperature adsorption of nitrogen according to the B.E.T. method [19].

The particle size and morphology were determined using a TEM JEOL 2100 at 200 kV. The specimens are prepared by grinding the samples in an agate mortar and dispersing them in acetone by ultrasonic treatment for 6 min. A droplet of the suspension is dripped on standard carbon films on Cu grids. Additional crystal structure data are obtained using the selected area electron diffraction method (SAED). Particle size distributions were calculated on 100 to 200 particles in different images in bright field mode.

Magnetization measurements of the magnetite and $CoFe_2O_4$ samples were performed in a Quantum Design superconducting magnet system (PPMS) with vibrating sample magnetometer (VSM) option in fields up to 5 T at room temperature and 5 K.

^{57}Fe Mössbauer measurements were performed using a constant acceleration spectrometer. A source of ^{57}Co(Rh) with an activity of 50 mCi was used. The Fe_3O_4 and $CoFe_2O_4$ spectra were taken in the transmission mode at room temperature and at liquid nitrogen temperature (77 K). The Mössbauer absorbers with a thickness of 40 mg cm^{-2} were made by mixing the studied nanomaterial powder with polyvinyl alcohol (glue material) and then pressed into disk pellets. Each experimental Mössbauer spectrum was decomposed either through the so-called "thin sample approximation" when the spectrum is represented as a sum of few simple spectra (sextets or doublets) or to avoid thickness effect it was fitted using an integral Lorentzian line shape approximation [20, 21]. When such decomposition is not possible one needs to take into account a distribution of spectra over a range of effective magnetic fields and/or electric field gradients. The geometric effect is taken into account as well.

RESULTS AND DISCUSSION

Figure 1 shows the XRD pattern of the nanosized magnetite material. The pattern was indexed within the cubic Fd-3m space group typical for the spinel structure. The unit cell parameter was measured to be 8.388(1) Å, which is closer to the value of 8.394 Å (ICDD-PDF2 #79-416 of crystalline magnetite (Fe_3O_4)), but differs from the unit cell parameter of maghemite 8.351 Å (ICDD-PDF2 #89-3850 cubic non-stoichiometric spinel γ-Fe_2O_3). The measured value for the unit cell parameter sug-

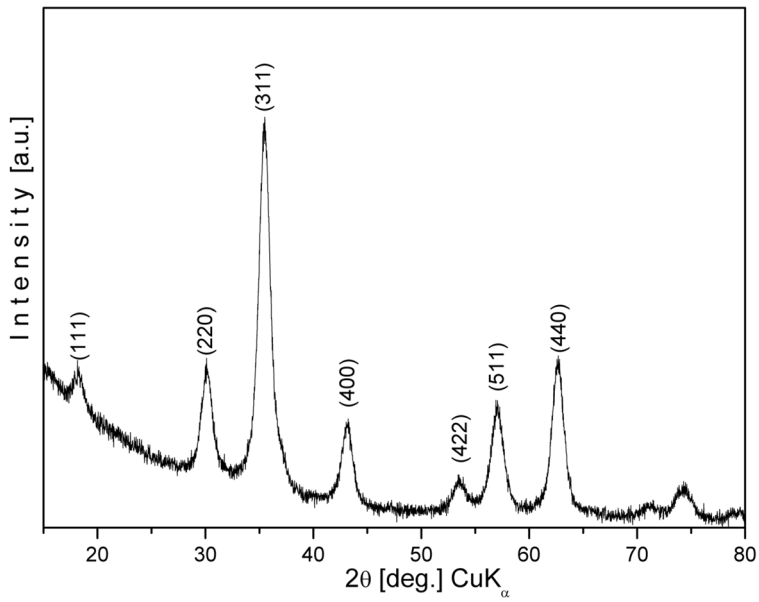

Fig. 1. XRD pattern of Fe_3O_4 with a particle size of 7.1 nm

gests a possibly non stiochiometric Fe^{2+}/Fe^{3+} ratio with some excess of Fe^{3+}. Analysis of the diffraction peak broadening resulted in a mean crystallite size of about 7.1 nm. This value agrees well with the high specific surface area of 180 m^2/g measured for this sample. Such high specific surface area corresponds to a mean particle size of 6.4 nm assuming not aggregated spherical particles. Powder diffraction patterns for $CoFe_2O_4$ samples synthesized from the same amount of initial compounds dissolved at different volumes are presented in Fig. 2. The corresponding mean crystallite sizes are shown in Table1.

Bright field TEM micrographs of Fe_3O_4 and $CoFe_2O_4$ samples together with the corresponding particle size distributions are presented in Fig. 3. Mean particle sizes obtained from TEM are given in Table 1. The spherical particles of Fe_3O_4 are distributed over a region from 3 to 11 nm. Polycrystalline SAED pattern of this sample shows that it is single phase and consists only of Fe_3O_4 (magnetite) ICDD-PDF2 #79-416. The spherical particles of $CoFe_2O_4$ with mean size of 2.7 nm (3.4 nm from XRD) are seen on Fig. 3b. It is worth to mention that these small particles produce a crystalline SAED pattern,

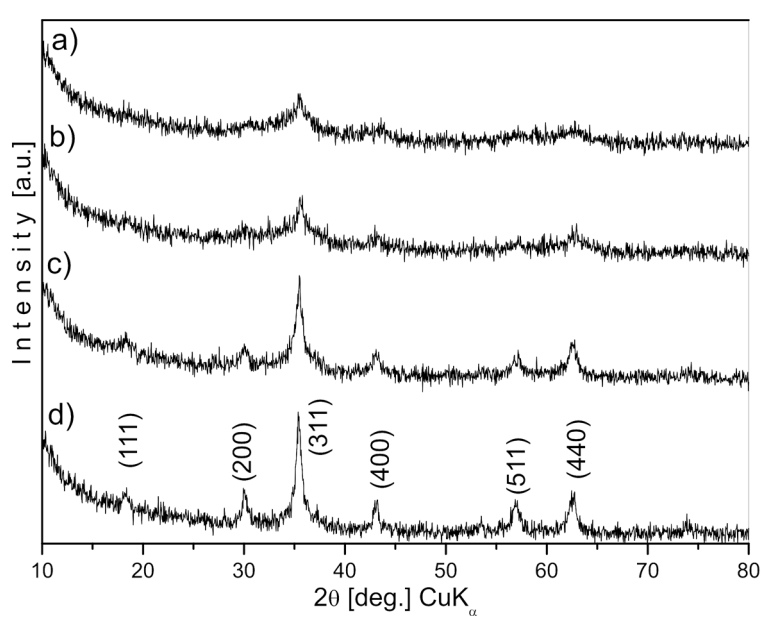

Fig. 2. XRD patterns of samples of $CoFe_2O_4$ obtained at different sonicated volumes: (a) – 300 ml, (b) – 200 ml, (c) – 100 ml and (d) – 50 ml

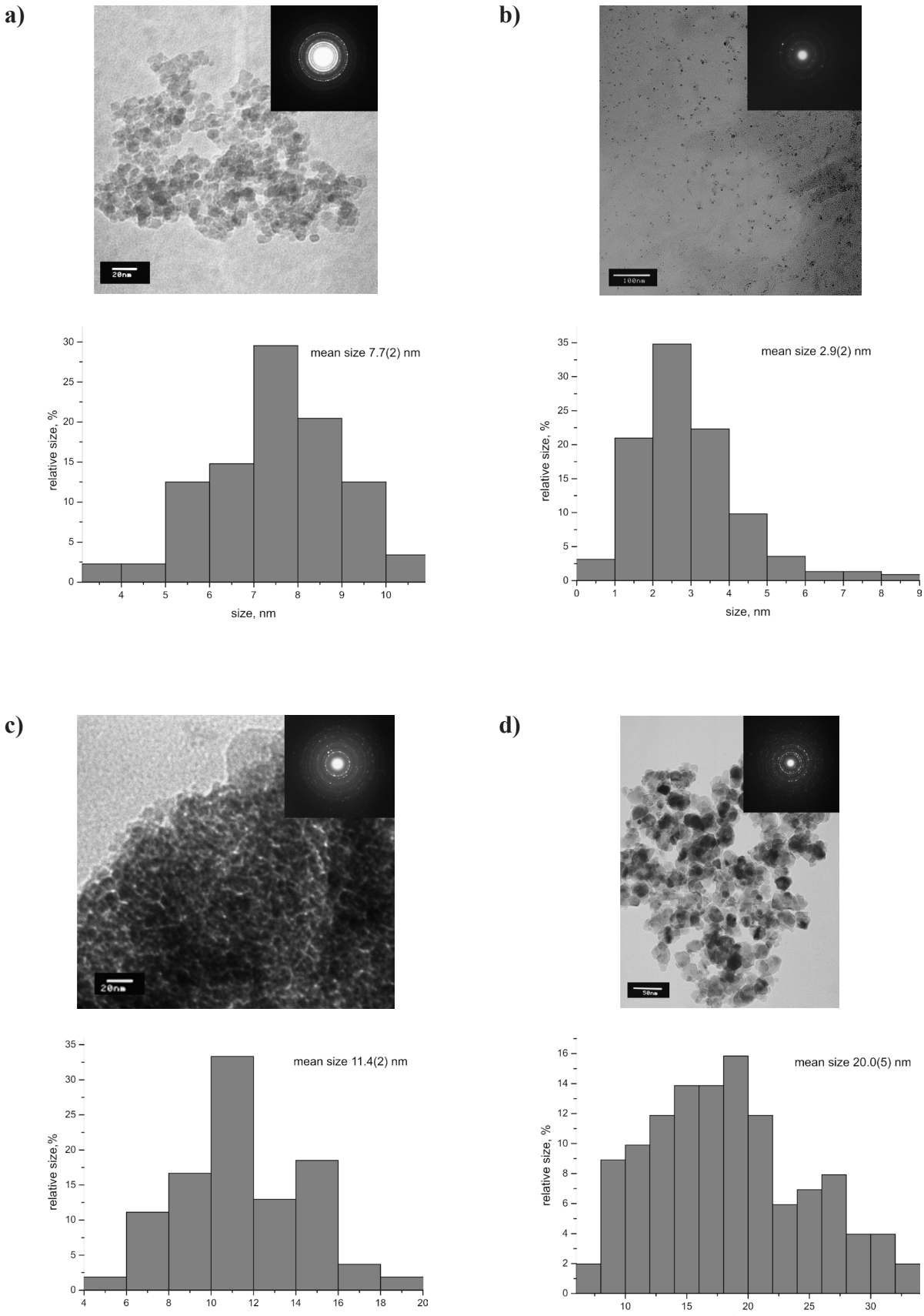

Fig. 3. TEM images and particle size distribution of (a) – Fe_3O_4 and $CoFe_2O_4$ obtained at different sonicated volumes: (b) – 200 ml, (c) – 100 ml and (d) – 50 ml

Table 1. Dependence of the coercitivity on the crystallite size of the samples

Sample	Crystallite size [nm] XRD	Particle diameter [nm] TEM	Coercivity H_C [mT] at room temperature	Coercivity H_C [mT] at 5 K
Magnetite	7.1(2)	7.7(2)	70	
$CoFe_2O_4$	1.9(2)		0	
$CoFe_2O_4$	3.4(2)	2.9(4)	0	264
$CoFe_2O_4$	10.4(3)	11.4(2)	30	1157
$CoFe_2O_4$	21.0(5)	20.0(5)	105	

which corresponds to $CoFe_2O_4$ (spinel) phase ICDD-PDF2 #70-8729. On Fig. 3c and 3d we present spherical particles of $CoFe_2O_4$ samples with larger mean sizes. SAED patterns of these samples unambiguously show that they are crystalline and consist only of one phase: $CoFe_2O_4$ (spinel) ICDD-PDF2 #70-8729. For $CoFe_2O_4$ samples it can be seen that with increasing the mean size of the particles their distribution becomes wider.

Saturation magnetization M_s, remanent magnetization M_r, and coercivity H_c are the main technical parameters to characterize the magnetism of a ferromagnetic sample. The magnetization curves at room temperature of the magnetite sample and different $CoFe_2O_4$ samples are shown in Fig. 4a,b respectively. At room temperature the coercivity as well as the remanent magnetization of the $CoFe_2O_4$ samples is decreasing with smaller particle size (Table 1). The change of the magnetization of the nanoparticles (small particle sizes) follows spontaneously the orientation of the applied magnetic field. The samples with the smallest particle size of 1.9 and 3.4 nm exhibit a complete superparamagnetic behaviour (Fig. 4b), which was also confirmed by Mössbauer spectroscopy (Fig. 7a). $CoFe_2O_4$ nanoparticles show typical hysteresis for their field-dependent magnetization below the blocking temperature. Fig. 5 is showing the hysteresis curves of two $CoFe_2O_4$ samples with a particle size of 3.4 and 10.4 nm measured at 5 K. The magnetization of the nanoparticles is not following the applied magnetic field simultaneously, but has to overcome a certain magnetic field value. This coercive field represents the value which is needed to surpass the anisotropy barrier [22–24]. Therefore, the coercivities for the $CoFe_2O_4$ samples strongly increased with lower temperature. The measurements show clearly that the coercivity H_C is strongly size and temperature dependent [25, 26].

The Mössbauer spectrum of nanosized magnetite (Fe_3O_4) taken at room temperature is shown in Fig. 6a. The extremely broadened six lines indicate that the sample consists of a mixture of superparamagnetic and ferrimagnetic phases rather than a

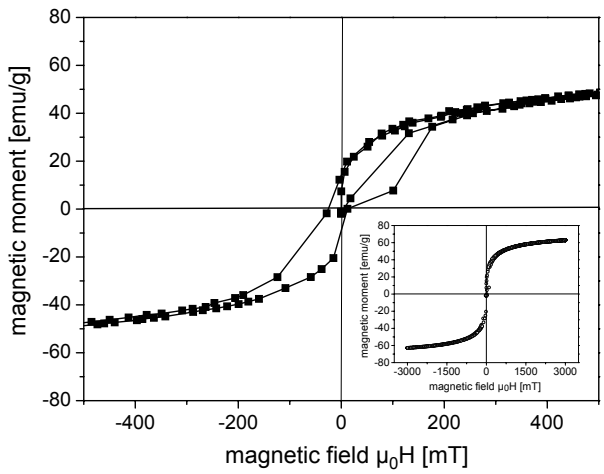

Fig. 4a) Room temperature magnetization curve of Fe_3O_4 (7 nm). The majority of particles are in an intermediate region (between the superparamagnetic and ferromagnetic state). The inset shows the hysteresis curve measured up to ± 3 T

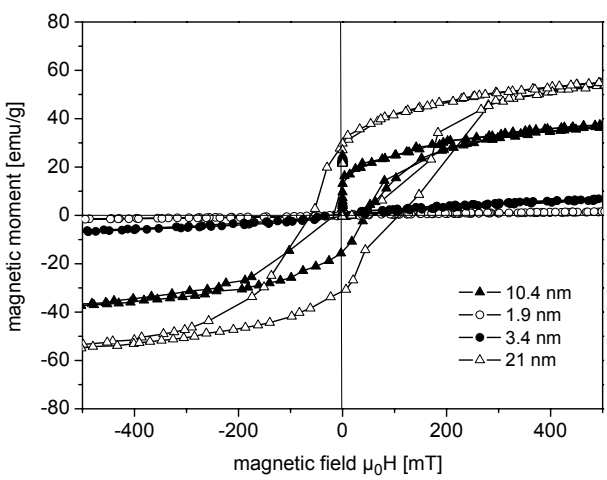

Fig. 4b) Magnetization curves of $CoFe_2O_4$ nanoparticles, measured at room temperature: 1.9 nm – open circles, 3.4 nm – filled circles, 10.4 nm – filled triangles, and 21 nm – open triangles. The first two groups of nanoparicles are completely in the superparamagnetic state, while the third and the fourth are in an intermediate region of a mixed superparamagnetic and ferrimagnetic state

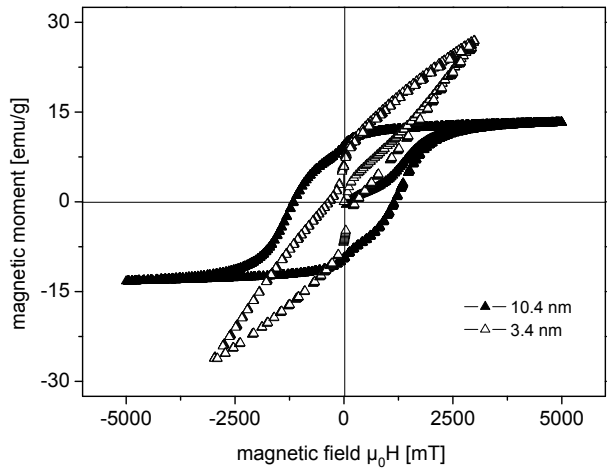

Fig. 5. Hysteresis loops at 5 K for $CoFe_2O_4$ samples with a particle size of 3.4 nm – open triangles and 10.4 nm – filled triangles

pure superparamagnetic. The spectrum was fitted as a magnetic sextet's distributions of 100 closely spaced sextets with a hyperfine magnetic field distribution (Fig. 6b). The average isomer shift and hyperfine magnetic field are: IS=0.41 mm/s and H = 364 kOe. The Mössbauer spectrum of the same sample at liquid nitrogen temperature (Fig. 6c) was fitted as a superposition of two magnetic sextets. At this temperature the superparamagnetic relaxations are blocked for the majority of the magnetic nanoparticles, however the broadening of the resonance lines for both sextets still could be explained as small influence of the superparamagnetism. The isomer shifts for sextets (1) and (2) are 0.46 mm/s and 0.38 mm/s respectively showing that the Fe^{2+} in the magnetite sample is partially oxidized to Fe^{3+}, forming some part of maghemite (γ-Fe_2O_3). The hyperfine magnetic fields derived from the sextets (1)

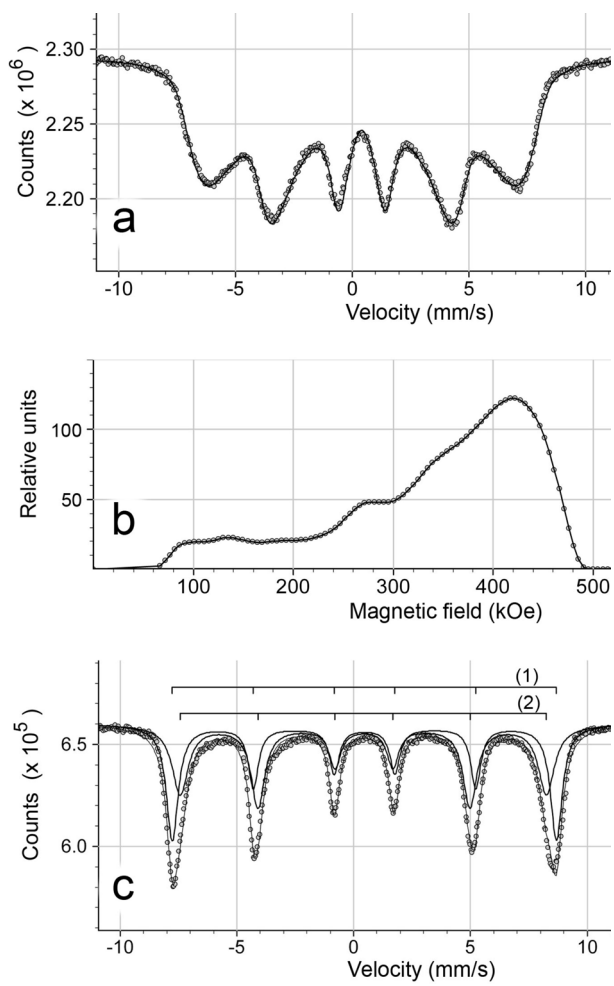

Fig. 6. Mössbauer spectrum of Fe_3O_4 taken at room temperature – fitted as a magnetic sextet's distribution (a); the hyperfine magnetic field distribution (b); Mössbauer spectrum of the sample taken at 77 K – fitted as a superposition of two magnetic sextets (c)

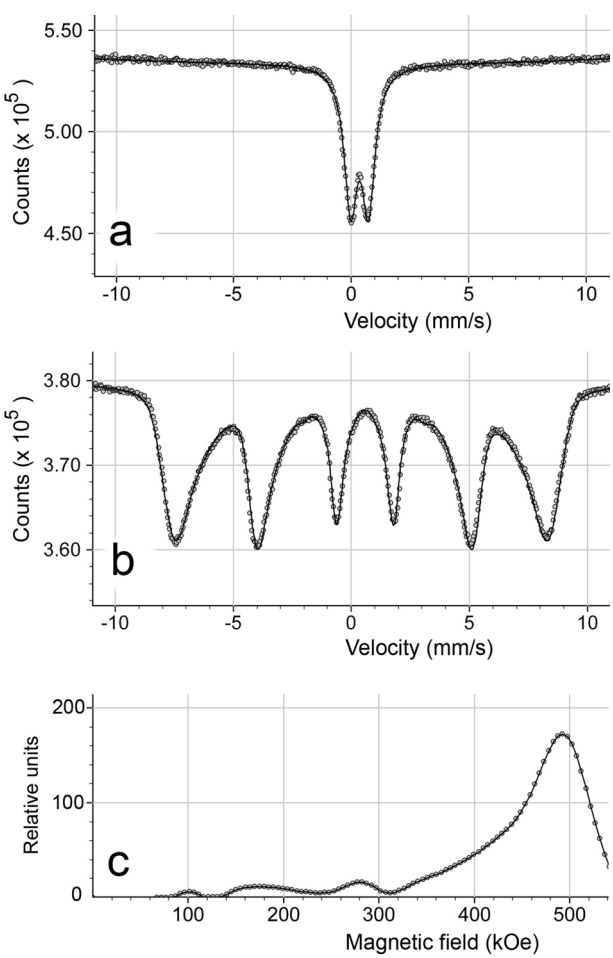

Fig. 7. Mössbauer spectrum of $CoFe_2O_4$ (3.4 nm) taken at room temperature – fitted as a quadrupole doublet (a); Mössbauer spectrum of the same sample taken at 77 K – fitted as a magnetic sextet's distribution (b); the hyperfine magnetic field distribution (c)

and (2) are 511 kOe and 487 kOe respectively. On the basis of these data and taking into account the Mössbauer data for 6.2 nm magnetite (Fe_3O_4) obtained by A. D. Arelaro et al. [27] we could assign the sextet (1) to Fe^{3+} in octahedral (B-site) and the sextet (2) to Fe^{3+} in tetrahedral (A-site).

In Fig. 7a the Mössbauer spectrum of $CoFe_2O_4$ (3.4 nm) at room temperature is shown. The superparamagnetic behavior of these nanoparticles leads to a complete lack of magnetic hyperfine splitting of the spectrum and represents a quadrupole doublet with broadened lines with an isomer shift of 0.36 mm/s and a quadrupole splitting of 0.76 mm/s. The origin of the quadrupole doublet line broadening is connected with the surface of the particle and the layers in the immediate vicinity of the surface, creating different electric field gradients on the Fe nucleus as compared to the electric field gradient from the core of the nanoparticle.

The Mössbauer spectrum of $CoFe_2O_4$ (3.4 nm) taken at 77 K represents a sextet with broadened lines (Fig. 7b). The fluctuations of the magnetization direction are partially blocked and the magnetic hyperfine splitting takes place. The spectrum was fitted as a magnetic sextet's distribution of 100 sextets with a hyperfine magnetic field distribution with an average magnetic hyperfine field of 442 kOe (Fig. 7c).

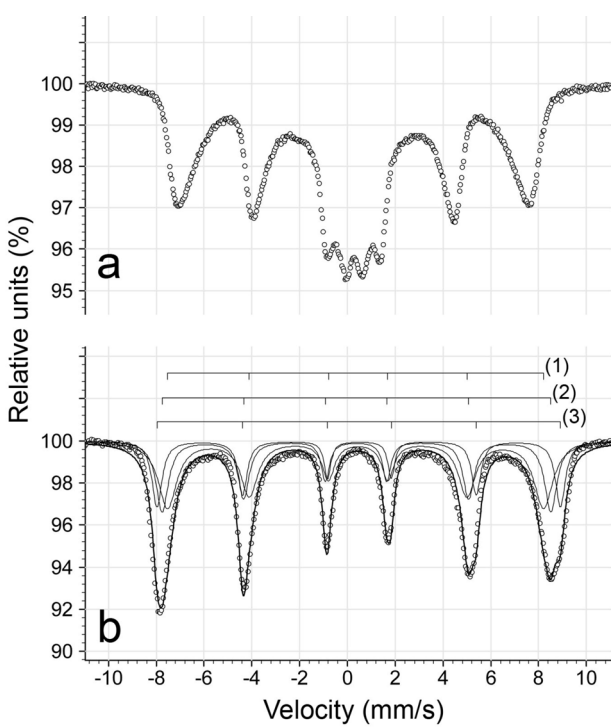

Fig. 8. Mössbauer spectra of $CoFe_2O_4$ (10.4 nm) taken at room temperature (a), and taken at 77K and fitted as a superposition of three magnetic sextets (b)

Fig. 8 shows the Mössbauer spectra of $CoFe_2O_4$ (10.4 nm) taken at room temperature (a) and at 77 K (b) respectively. The RT spectrum (a) shows a high percentage of superparamagnetic behavior of the sample, and therefore it is not possible to extract information about the cation distribution from such a spectrum. In contrast, the second spectrum (b), taken at 77 K, shows that the contribution of the superparamagnetic component is negligible and the spectrum can be fitted quite well with three magnetic sextets. The isomer shifts for the sextets (1), (2), and (3) are 0.37 mm/s, 0.49 mm/s and 0.39 mm/s, respectively. The hyperfine magnetic fields derived from the sextets (1), (2), and (3) are 489 kOe, 505 kOe, and 524 kOe, respectively. From these parameters one can conclude that sextet (1) corresponds to the Fe^{3+} cation in A-site, while the sextets (2) and (3) correspond to Fe^{3+} placed in B-site (B2 and B3). From the measured relative spectral areas of the sextets (1), (2), and (3) we can derive the formula for the cation distribution of $CoFe_2O_4$ (10.4 nm), namely: $(Co_{0.1}Fe_{0.9})[Co_{0.9}Fe_{1.1}]O_4$. Possible explanation for the two octahedral sites B2 and B3 is given in the paper of Lopes et al. [28] where the Mössbauer spectrum for cobalt ferrite nanoparticles (7.2 nm), taken at 5 K was fitted with three subspectra related to Fe^{3+} in A-site and Fe^{3+} in B2 and B3-sites. The two B-sites correspond to different surroundings of Fe^{3+} in the B-positions of the spinel structure.

CONCLUSIONS

Nanoparticles of two different ferrite materials, Fe_3O_4 and $CoFe_2O_4$, have been obtained by ultrasound assisted co-precipitation. The method allows producing oxide materials with a preliminary desired mean particle size within the nanoscale range by simple control of synthesis governing parameters, such as reactant concentration, power input and reaction time. Magnetic measurements at room temperature and 5 K have shown that the magnetization behaviour changes clearly with temperature. At room temperature the $CoFe_2O_4$ samples with the smallest particle size of 1.9 and 3.4 nm exhibit a complete superparamagnetic behaviour, while samples with bigger particles show a mixed state of superparamagnetic and ferrimagnetic behaviour. Mössbauer spectroscopy measurements provide the formula for cation distribution of $CoFe_2O_4$ (10.4 nm), namely $(Co_{0.1}Fe_{0.9})$ $[Co_{0.9}Fe_{1.1}]O_4$.

Acknowledgment: *The financial support of National Science Fund – contract DTK02/77/09 is gratefully acknowledged. The authors thank Ivan Spirov for the fitting of the Mössbauer spectra.*

REFERENCES

1. L. Babes, B. Denizot, G. Tanguy, J. Le Jeune, P. Jallet, *J Colloid Inter Sci*, **212**, 474 (1999).
2. I. Safarik, M. Safarikova, *Monats Chem*, **133**, 737 (2002).
3. Q. Pankhurst, J. Connolly, S. Jones, J. Dobson, *J Phys D: Appl Phys*, **36**, 167 (2003).
4. X. Wang, H. Gu, Zh. Yang, *J Magn Magn Mater*, **293**, 334 (2005).
5. M. Lin, H. Kim, H. Kim, M. Muhammed, K. Kim Do, *Nano Reviews*, **1**, 4883 (2010).
6. A. Figuerola, R. Di Corato, L. Manna, T. Pellegrino, *Pharmacological Research*, **62**, 126 (2010).
7. K. Haneda, A. Morrish, *J de Physique*, **38**, C1-321 (1977).
8. T. Hosono, H. Takahashi, A. Fijita, R. Justin Joseyphus, K. Tohji, B. Jeyadevan, *J Magn Magn Mater*, **321**, 3019 (2009).
9. V. Blaskov, V. Petkov, V. Rusanov, Li. Martinez, B. Martinez, J. Monos, M. Mikhov, *J Magn Magn Mater*, **162**, 331 (1996).
10. P. Sraravanan, S. Alam, G. Mathur, *J Mater Sci Lett*, **22**, 1283 (2003).
11. D. Maity, S. Kale, R. Kaul-Ghanekar, Xue Jun-Min, J. Ding, *J Magn Magn Mater*, **321**, 3093 (2009).
12. Z. Hua, R. Chen, C. Li, S. Yang, M. Lu, B. Gu, Y. Du, *J Alloys Comp*, **427**, 199 (2007).
13. M. Liu, X. Li, H. Imrane, Y. Chen, T. Googrich, Z. Cai, K. Ziemer, J. Huang, N. Sun, *Appl Phys Lett*, 152501 (2007).
14. S. Santra, R. Tapes, N. Theodoropoulou, J. Dobson, A. Hebard, W. Tan, *Langmuir*, **17**, 2900 (2001).
15. J. Bang, K. Suslick, *Adv Mater*, **22**, 1039 (2010).
16. I. Ray, S. Chakraborty, A. Chowdhury, S. Majumdar, A. Prakash, R. Pyare, A. Sen, *Sensors and Actuators B*, **130**, 882 (2008).
17. E. Kim, H. Lee, H. Shao, *Key Eng Mater*, **277-279**, 1044 (2005).
18. S. Park, J. Kim, C. G. Kim, C. O. Kim, *Current Appl Phys*, **8**, 784 (2008).
19. S. Brunauer, H. Emmett, E. Teller, *J. Am. Chem. Soc*., **60**, 309 (1938).
20. G. Shenoy, J. Friedt, H. Maleta, S. Ruby, *Mössbauer Effect Methodology*, **9**, 277 (1974).
21. T. Cranshaw, *J Phys E*, **7**, 122 (1974).
22. S. Laureti, G. Varvaro, A. M. Testa, D. Fiorani, E. Agostinelli, G. Piccaluga, A. Musinu, A. Ardu, D. Peddis, *Nanotechnology*, **21**, 315701 (2010).
23. Ch. Liu, Z. J. Zhang, *Chem. Mater*., **13**, 2092 (2001).
24. Ch. Liu, B. Zou, A. J. Rondinone, Z. J. Zhang, *J. Am. Chem. Soc*., **122**, 6263 (2000).
25. G. Herzer, *IEEE Trans Mag*, **26**, 1397 (1990).
26. G. Herzer, *J Magn Magn Mater*, **112**, 258 (1992).
27. A. Arelaro, L. Rossi, H. Rechenberg, *Journal of Physics: conference series*, **217**, 012126 (2010).
28. J. L. Lopez, H. D. Pfannes, R. Paniago, J. P. Sinnicker, M. A. Novak, *J Magn Magn Mater*, **320**, e327 (2008).

СИНТЕЗ И ХАРАКТЕРИЗИРАНЕ НА МАГНИТНИ НАНОРАЗМЕРНИ Fe_3O_4 И $CoFe_2O_4$

Д. Ковачева[1], Т. Русков[2], П. Кръстев[2], С. Асенов[2], Н. Танев[2], И. Мьонж[3], Р. Косева[3], У. Волф[3], Т. Геминг[3], М. Маркова-Величкова[1], Д. Нихтянова[1], К.-Ф. Арндт[4]

[1] Институт по обща и неорганична химия, Българска академия на науките, 1113 София, България
[2] Институт за ядрени изследвания и ядрена енергетика, 1784 София, България
[3] Лайбниц институт за изследвания на твърдо състояние и материали, Дрезден, D-01069, Дрезден, Германия
[4] Катедра по химия, Физикохимия на полимери, ТУ - Дрезден, D-0162, Дрезден, Германия

Постъпила на 20 февруари, 2012 г.; приета на 2 април, 2012 г.

(Резюме)

Синтезът на наноразмерните Fe_3O_4 и $CoFe_2O_4$ бе проведен чрез съутаяване на съответните метални хидроксиди и тяхното по-нататъшно разлагане до оксиди под въздействие на ултразвуково облъчване. Получените материали са характеризирани с рентгенова дифракция (XRD), трансмисионна електронна микроскопия (TEM) и вибрационна магнитометрия (VSM). Получените материали са със средни размери на кристалитите 7.1 нанометра за Fe_3O_4 проба и от 1.9 до 21 нанометра при $CoFe_2O_4$ проби в зависимост от условията на синтез. Мьосбауеровите спектри на Fe_3O_4 и $CoFe_2O_4$, измерени при стайна температура и 77 K показаха, че пробите проявяват или суперпарамагнитно поведение или смес от суперпарамагнитно и феримагнитно в зависимост от на размера на кристалитите и температурата. Чрез Мьосбауеровата спектроскопия е определено и катионното разпределение за образец от $CoFe_2O_4$ с размер на кристалитите 10.4 nm.

Bulgarian Chemical Communications, Volume 44, Proceedings of the III[rd] National Crystallographic Symposium (pp. 98–108) 2012

Rare-earth doped optical waveguides in $LiNbO_3$

M. Kuneva

Institute of Solid State Physics – Bulgarian Academy of Sciences,
72 Tzarigradsko Chaussee Blvd, Sofia 1784, Bulgaria

Received February 15, 2012; Revised March 26, 2012

Doping of dielectric hosts with laser-active ions, such as the rare earth ones, is widely researched recently. The great interest has been provoked by the miniature waveguide solid state lasers obtained that way, and the opportunity for monolithic integration of these lasers and other elements on a common substrate.

The present article is a data review on the doping of $LiNbO_3$ with ions of rare-earth elements. Here, an attempt is made to summarize the most important results on technologies for doping with rare earths of optical waveguides in $LiNbO_3$ substrates and for obtaining of optical waveguides in rare-earth doped $LiNbO_3$. The sequence of the technological steps depends on the methods of doping and particularly on the temperature. The main methods of doping are described: ion implantation, diffusion from a layer deposited on the $LiNbO_3$ crystal substrate, diffusion from a melt. The main points of consideration are the effect of substrate orientation and of the initial doping on the subsequent diffusion processes, mechanism of rare-earth ion penetration and the possible positions they occupy in the lattice, structural changes due to the doping versus technological parameters, etc. A special attention is paid to the low-temperature methods of diffusion; they imply ion exchange or diffusion without ion exchange when the doping ions are situated in existing vacations of the host. The influence of the melt composition, temperature and duration of the diffusion on the concentration of the dopant in the waveguide is discussed, as well as the conditions at which that kind of anisotropic diffusion process becomes self-restricted.

Key words: Rare earths, Optical waveguides, $LiNbO_3$

INTRODUCTION

Being a crystal with strong electro-optical and non-linear properties, lithium niobate (LN) is one of the main materials having application in integrated optics. Of particular interest in recent years are the possibilities to obtain waveguide lasers based on LN doped with rare-earth elements, since the lifetime of their excited states in crystal matrices vary from 1 to 23 ms – a time sufficient for inverse population to appear [1]. The integrated-optical technologies based on the use of LN make possible the monolithic integration of waveguide lasers with other functional elements on a common substrate. An entire family of waveguide lasers already exists [2, 3–5] having excellent parameters, mainly based on erbium-doped LN, and emitting in the range 1530 nm < λ < 1610 nm. This range belongs to the third telecommunication spectral window, in which the losses in fiber-optical cables are the lowest. It is also important to note that, unlike rare-earth-doped glass fibers, the dopant positions occupy particular sites in the crystal lattice, which reduces band broadening due to inhomogeneities, i.e. the pumping and amplification efficiencies are increased [6].

The obtaining of waveguide lasers consists of two technological steps: (1) doping with a rare-earth element, and (2) obtaining of a waveguide.

METHODS OF RARE EARTH CRYSTAL DOPING

Doping during crystal growth (Nd^{3+}, Er^{3+}, Yb^{3+}, Er^{3+}+Yb^{3+}, Yb^{3+}+Pr^{3+})

The doping takes place by adding the activating compound – usually an oxide (e.g. Er_2O_3 for erbium doping [7]) – to the melt, in which the growth of the crystal starts (usually a congruent melt composition with Li^+ to Nb^{5+} concentration ratio of the order of 0.945). The congruent melt gives rise to Li-defficient crystals that need intrinsic defects to satisfy the overall charge compensation.

* To whom all correspondence should be sent:
E-mail: kuneva@issp.bas.bg

The doping of LN with erbium is the most extensively studied one. The erbium concentration changes the parameters of the lattice and the intensity of the absorption band. Erbium-doped LN crystals with an erbium concentration of 0.5 to 8 mol% have been grown by Czochralski's method in order to study the integration of erbium in the lattice of LN [7]. It was observed that the erbium concentration in the crystal changes linearly depending on the melt concentration up to a concentration which remains constant, independent of the increase of the dopant concentration in the melt. The maximal amount of erbium ions integrated in the lattice is about 3 mol%. This value should correspond to the concentration limit of presence of erbium in LN. The research of other authors indicates that the rare-earth component occupies random places in LN's lattice and that, when the concentration limit is reached (the limit of solubility of the dopant in the crystal, corresponding to non-clustered or axially-positioned erbium ions), the possibility appears that chaotically positioned clusters or precipitates form [8, 9]. Their formation is stimulated also by the large ion radius of rare-earth elements. As shown in [8], the clusters formed above the saturation point cause distortions of the lattice and change the matrix's crystallography. The presence of clusters is proven experimentally in [10, 11]. When the erbium concentration increases, radiation trapping effect of the emission at 1.5 μm is observed, which decreases the lifetime of the excited states.

The doping of LN with ytterbium is also well-studied experimentally [6, 12] and theoretically [13] regarding the concentration and the sites occupied by the dopant in the lattice during the crystal growht, which is of particular importance, as it was shown above. The concentrations of the dopant considered in this case are relatively low (1.0 wt.% and 0.8 wt.% for LN: Yb, and LN: Yb, Pr, respectively [14]). The results show that the rare-earth ions occupy mainly Li^+ sites, and when co-doping with another element takes place (e.g. Pr), Yb^{3+} ions may also occupy Nb^{5+} sites [13] or form Yb^{3+} pairs in an LN matrix with one Yb^{3+} ion placed at the Li^+ site and another one at the Nb^{5+} site, while the rest of the Yb^{3+} ions are randomly distributed over the Li^+ sites [15, 16].

More research is also needed to clarify the influence of rare-earth elements on the crystal of the incongruent LN [7].

Since the domain structure also strongly depends on the concentration of the dopant in the crystal, the concentration of Er and Yb influences the formation of PPLN (periodically poled LN). The best PPLN structures are formed by doping with 0.5 mol% with erbium as well as ytterbium. Below 0.5 mol%, a regular domain structure is observed, whereas at dopant concentrations over 1 mol% the domain structure is distorted and becomes non-periodic [7].

A very important conclusion from the technological point of view is the one that at very low concentrations of the rare-earth element (below 0.1 at.%) the doping does not lead to luminescent activation of the crystal, and at higher concentrations (above 0.6 at.%) effects appear which lead to quenching of the luminescence. Due to these reasons, the most effective concentration of the rare-earth element happens to be in the range from 0.1 to 0.6 at.%.

The simultaneous doping of LN with more than one rare-earth element is used to avoid effects harmful to optical amplifiers and lasers such as photorefraction and luminescence quenching. Also, at co-doping with erbium and ytterbium, the Yb^{3+} ions act as sensitizers of the Er^{3+} luminescence, absorbing the pumping light and effectively transmitting it to the erbium which then emits it [17]. With this co-doping, compact and highly efficient waveguide lasers and amplifiers are obtained. The proportions in the quantity of co-doping elements for growing $LiNbO_3:Er^{3+}/Yb^{3+}$ and the parameters of the growing process are also described elsewhere [18]. The structural analysis performed by these authors shows that both types of rare-earth ions occupy sites in the crystal lattice slightly shifted towards lithium sites (ca. 0.25 Å). The doping with both ion types changes the refractive indices of the crystal so that their values are maximal at concentration of 1.1–1.2 mol% in the crystal.

However, it has to be emphasized that it is not at all easy to dope the crystal homogeneously during its growth, especially when a low concentration of the dopant is required (e.g. 0.5 mol%), since in that case the relative inhomogeneity reaches high values. Besides, the doping of the bulk material is not the best solution for waveguide integrated optics, because, at excitation, all parts of the waveguide will absorb. The integrated-optical devices are thin-layer ones and they do not require bulk doping. Therefore, the methods for local doping of LN are preferred [19]. The bulk-doped crystals are of interest mainly with regard to the construction of high-gain-switched lasers; they operate at concentrations up to 2%, which cannot be reached with the methods for local doping (indiffusion).

Ion implantation followed by annealing (Nd^{3+}, Eu^{3+}, Er^{3+})

The attractiveness of ion implantation as a method for local doping is mainly due to the fact that it provides the possibility to adjust better the obtained profile of the dopant in the layer with the profile of

the optical waveguide which is obtained thereafter [20]. High-energy (MeV) ion implantation is used for doping of LN with erbium ions at ion beam energy of 2.0 or 3.5 MeV and surface density of the beam of 2×10^{14} and 7.5×10^{15} cm^{-2}. The obtained doped layers after annealing do not differ in their optical properties from bulk-doped LN. The erbium ions occupy optically active sites, so the photoluminescent spectra and the lifetime of the $I_{13/2}$ level are the same. No luminescence quenching is observed at erbium ion concentrations up to 0.12 at.% in the layer, which is the maximal concentration obtained under these conditions. Ion implantation could be used also for the modification of already obtained waveguides in order to introduce laser/amplifier-active ions such as Er^{3+} which offers attractive possibilities for new devices.

Since the ion beam damages the structure of the crystal close to the surface and causes amorphization of the 50–60 nm thick subsurface layer, the implantation always requires subsequent annealing for recrystallization. The recrystallization may not always be complete. It takes place at high temperatures (800–1250 °C), close to the Curie temperature for LN, so the electro-optical properties of the material may be lost. At the annealing, along with recrystallization, the diffusion of the rare-earth element in depth also continues, and the profile of its distribution changes from steplike to Gaussian [21]. This ensures a better overlap of the doped region and the field in the optical waveguide formed thereafter. On the other hand, the amorphized region provides higher mobility for the dopant ions and hence, at the thermal treatment, they migrate more to the surface and less in the depth of the crystal, so that the effective doping does not coincide with the field of the optical mode propagating in the waveguide. This increases the losses of erbium fluorescence. Also, the annealing requires special attention since the higher concentrations of the doping element combined with the higher temperatures raise the risk of formation of nano-sized atomic metal clusters of the dopant, which leads to luminescence quenching [2]. This makes ion implantation not only an expensive method, but also a risky one [22].

Indiffusion

The doping by diffusion allows avoiding the use of expensive equipment for doping during crystal growth as well as the high energy in ion implantation. It allows local control of the doping element concentration by using photolithographic techniques and the obtaining of a large variety of integrated-optical devices in any combination on a common substrate at a higher rate of integration.

a) Thermal diffusion from a metal layer deposited onto LN substrate (Nd^{3+}, Er^{3+}, Tm^{3+}, Yb^{3+})

The doping by diffusion of rare-earth ions from a metal layer deposited on the crystal surface takes place at high temperatures (1050–1130 °C) for a quite long time (50–250 h depending on the crystal orientation of the substrate) in a flow of dry oxygen. These high temperatures and time are required due to the relatively large ion radii of rare-earth elements and their harder entry into the LN crystal. Since the Curie temperature (T_c = 1142 °C for congruent LN) is close to the diffusion one, the risk exists that during the diffusion the crystal loses its ferrooelectric and electro-optical properties. The diffusion creates a homogeneously doped but very thin surface layer (nm) in the substrate, so additional annealing is required for the dopant to enter deeper into the crystal. At the beginning of the process, while the source is not yet exhausted, the distribution of the dopant from the surface to the depth of the crystal has the shape of an erfc-function. After that, at further thermal treatment after the diffusion of the layer, the profile transforms to a Gaussian one [23, 24]. In an aerial atmosphere the metal oxidizes and forms a hard matte layer. It worsens the optical quality of the crystal. In that case, either the diffusion should be continued until the metal oxide transfers entirely to the substrate, or the crystal surface should be polished carefully to minimize the losses from surface scattering in the optical waveguide to be obtained thereafter in the rare-earth-doped layer [23]. Due to the low mobility of the ions of rare earth elements, the doping with them is always the first step of the obtaining of doped waveguides. The above discussed shows that the thermal diffusion from a layer deposited on the surface is also a process quite difficult from the technological point of view. Nevertheless, this method has a number of advantages which will be discussed below with the example of the thermal diffusion of erbium ions from a thin vacuum-deposited metal layer.

Besides having the most appropriate emission spectrum for optical communications, erbium is also the rare-earth element most frequently used for diffusion due to its low ion diameter compared to other rare-earth elements which provides it with a relatively good mobility during the diffusion process [25]. The electron transitions of Er^{3+}:$LiNbO_3$ used for laser generation with a wavelength of 1550 nm are a quasi three level system with ground state absorption. Therefore the erbium doping has to be limited to these regions of the integrated-optical device for the function of which pumping is required; otherwise strong absorption takes place and the efficiency of the device decreases strongly. Such selective doping cannot be performed during the crystal

growth but only by indiffusion from a structured vacuum-deposited layer [23]. This method allows avoiding the clustering of erbium ions in the matrix and is compatible with the diffusion methods for obtaining of waveguides. It allows concentration values to be reached close to the solubility limit for a solid solution (ca. 0.18 at.% at 1060 °C) without fluorescence quenching [21]. This is a prerequisite for a significant optical amplification in a short distance (experimentally achieved up to 2 dB/cm). For example, the diffusion of an erbium layer (23 Å thick) for 40 h at 1060 °C results in a subsurface layer with erbium concentration of 3.6×10^{19} cm^{-3} [26].

To understand the physical mechanisms behind the optical properties of the doped LN, it is necessary to be known which sites the dopant occupies in that pseudo-perovskite matrix. The authors of [27] have found that in the diffusion from a metal layer, the Er atoms occupy sites located at 0.46 Å from the lithium sites in a ferroelectric state directed along the optical axis; at higher erbium concentrations the diffusion resembles an exchange, where Li and Nb ions are replaced by erbium ions, thus changing considerably the structure of the crystal. It remains well-ordered, with strongly coherent fractions of erbium and niobium atoms located in the respective positions as in [27].

Varioius waveguide lasers have been obtained by thermal diffusion from a metal layer: Distributed Bragg Reflector (DBR) laser [3], Distributed Feedback (DFB) laser [4], DFB-DBR coupled cavity laser [5], etc.

b) Diffusion from a melt (Er^{3+})

Although the methods described above allow the obtaining of high-quality doped waveguides, they are time-consuming, require high temperatures or high energy and are risky and technologically complicated. Very promising seems the doping by diffusion from melts of eutectic mixtures of nitrates [28] or sulphates [29], where the diffusion quite probably takes the form of an ion exchange. The process takes place by dipping the substrate in the doping mixture at relatively low temperatures (a few hundred degrees). Until now this technology has been studied and applied only for doping of LN with erbium. It has to be noted that the diffusion coefficient of erbium with this method is twice higher than with diffusion from a metal layer [30]. Melts with the following composition have been proposed (I–III):

$$76\ CsNO_3 + 14\ Ba(NO_3)_2 + 10\ Er(NO_3)_3\ [28] \quad (I)$$

The diffusion takes place at a temperature of about 400 °C and for about 5 h. This way, a very thin doped surface layer is obtained having an erbium concentration of up to 9 wt%. The post-diffusion annealing at 400 °C for 20–40 hours increases the depth of the doped region and lowers the dopant concentration in the subsurface layer. The temperature should not exceed 500 °C since higher temperatures cause microcracks to appear on the sample surface, probably due to the too fast relaxation of the tensions in the diffused region [28]. The best results are obtained for X-cut samples.

$$90\ KNO_3 + 10\ Er(NO_3)_3\ [28] \quad (II)$$

The diffusion lasts about 5 hours at a temperature of 350–400 °C in a platinum crucible. Under these conditions, in X-cut samples, a thin (50 nm) doped layer is obtained having a dopant concentration up to 20 at.%. Erbium ions have a homogeneous (steplike) distribution. The erbium concentration in the different cuts differs significantly – from ca. 3 at.% for Y- and Z-cut to 20 at.% for X-cut. Erbium ions may diffuse into the crystal when additional annealing is applied at 350 °C, and their distribution becomes Gaussian [28].

The change in lithium concentration in the doped layer (i.e. lithium decrease) is studied by the Neutron Depth Profiling (NDP) method. The distribution of the integrated erbium atoms is determined using Rutherford Backscattering Spectrometry (RBS) [19]. The RBS spectrum shows that erbium ions are located in a ca. 100 nm thick layer (after annealing) on the surface of the crystal, and that there is a strong anisotropy when doping substrates having different crystal orientations. While with Y- and Z-cut substrates the erbium concentration does not exceed 5 at.%, in the cases of an X-cut it could easily reach 20 at.%. This may be explained, to some extent, as owing to the known different wettability of the Z-cut compared to the X- and Y-cut by the melt. The wettability of Z-cuts by the melt is impeded most probably due to the pyroelectric effect (the pyroelectric axis of LN is perpendicular to the Z-cut substare). This cannot, however, explain the different behaviour of X- and Y-cuts.

The study on concentration profiles of lithium shows that no lithium decrease is observed in the doped layer, therefore erbium ions do not occupy lithium sites during low-temperature doping, and it does not take the form of an exchange, but of an interstitial diffusion. Erbium ions most probably occupy the majority of vacancies, which explains the higher concentration of erbium ions in the X-cut samples [28].

Other authors have an interpretation slightly opposing the above – they assume that the diffusion has the form of an ion exchange [30]. These authors use sulphate melts instead of nitrate ones (III) [29]. Ion exchange is a transfer of different types of ions

between phases brought to a contact. The gradient in chemical potential at their interface leads to movement and exchange of the different ion types, so that electrical neutrality is preserved. When ion exchange is not isovalent, the diffusion coefficient depends on many parameters and it is not easy to predict the profile of the doping element (i.e. of its distribution in depth). Within this exchange, a complex rearrangement of the crystal structure takes place, for which no thorough model has been created yet [31].

$$19.4K_2SO_4+9.9Na_2SO_4+70.7Li_2SO_4 +0.125 \text{ wt.\% } Er_2(SO_4)_3 \text{ [29]} \quad \text{(III)}$$

The diffusion lasts 24 hours at 680 °C. The exchange takes place at temperatures of 560–700 °C. The profile of erbium distribution depends on the speed of melt heating – fast (300 °C/h) or slow (150 °C/h). The diffusion time varies from 4 to 24 hours. Additional annealing at 900 °C for 15 h is also performed. By varying the amount of erbium sulphate in the melt from 0.002 wt.% to 5 wt.%, it has been found that below 0.002 wt.% the exchange is inefficient even at longer times and higher temperatures. Above 5 wt.% the thickness of the ion-exchange layer decreases. A thickness of a few micrometers is achievable at a concentration of 0.6 %, time below 10 hours and temperature about 600 °C. At concentrations of erbium sulphate between 0.1–0.6 wt.% the luminescence intensity increases linearly with concentration, i. e. within this range there is still no luminescence quenching. The systematic study done by these authors to establish the dependence of erbium profile on diffusion parameters shows that it is preferable to use lower temperatures and shorter times, since the process seems to be self-limiting. The authors state that, due to the higher mobility of lithium compared to erbium, a local unbalanced charge appears which limits the further diffusion of erbium into the matrix. The gradient in ion concentration leads to the formation of a barrier layer which blocks the diffusion of ions involved in the process. As a possible explanation for the fact that in X-cut samples the exchange layer is thicker than in Z-cut ones, these authors also point out the better wettability of X-cut substrates. It is harder in terms of energy for erbium to enter Z-cut substrates due to its lower concentration on the surface.

The analysis of concentration profiles using SIMS and RBS shows complete lithium depletion of the subsurface layer, and a stoichiometry close to $Er_1Nb_1O_{4.5}$ which corresponds to a mixture of erbium and niobium oxides. Under the subsurface layer, a multivalent Er^{3+}-$3Li^+$ exchange takes place. Thicker layers are formed in X-cut substrates than in Z-cut ones, i.e. these authors also find anisotropy of diffusion. Moreover, they also find that in the case of X-cut samples, both surfaces of the sample dipped in the melt are equally and homogeneously doped, whereas with Z-cut, active erbium agglomerates are formed, probably due to the different orientation of the ferroelectric domains in the crystal, which results in doping with active erbium ions of only one surface of the substrate.

Ion exchange in a salt melt is the most convenient technology for local doping, if no co-doping with another element is needed. With this method the thermal stress upon the crystal is minimal and the risk of depolarization and loss of electro-optical properties is avoided.

To use rare-earth doped substrates in integrated-optical circuits, after the doping it is necessary to obtain high-quality optical waveguides.

WAYS FOR OBTAINING ACTIVE WAVEGUIDES

Creation of the the waveguide by the doping itself

It has been found with erbium diffusion from nitrate melts [28], that all samples regardless of their crystal orientation have waveguiding properties stemming from a change in the extraordinary refractive index in the range 0.003–0.005 for wavelength of 0.633 μm. The waveguides obtained this way are quite thick – up to 9 μm [19]. This waveguide effect of the diffused layer results solely from the presence of erbium ions. However, due to a number of reasons, the waveguides so obtained do not have a practical application.

Creation of an optical waveguide in a rare-earth doped crystal

For the formation of optical waveguides in LN previously doped with rare-earth elements, ion implantation, diffusion from a metal layer, and proton exchange have been used. It has to be mentioned that the rare-earth doping also changes the refractive index, and if it is a local one, it also creates a waveguide itself.

The two widely accepted technologies for obtaining of optical waveguides in LN by diffusion are titanium diffusion and proton exchange. Proton exchange has the advantage of increasing the photorefractive resistance and the generation of a strong waveguide effect, but the obtained waveguides maintain only one polarization, since only the extraordinary refractive index rises. This makes some authors state that the waveguides obtained by proton exchange are not suitable for laser action, since

the fluorescence of the system La^{3+}:LN has both polarizations [32]. Many authors however consider proton-exchanged waveguides as a good alternative to titanium ones for the obtaining of integrated-optical lasers [28, 33].

a) In-diffusion of Ti or Zn from a metal layer

The most frequently used and approved technology is the diffusion of Ti in $LiNbO_3$. Until now, this is the technology providing the highest quality of waveguides formed in LN previously doped with rare-earth ions. A thin layer of titanium with a thickness of 20-200 nm is deposited onto a crystal substrate and after that, the thermal diffusion takes place at ca. 950–1100 °C for several (5–20) hours in flowing Ar gas atmosphere (to prevent oxidation of the metal) replaced by O_2 during cool-down to allow reoxidation. If the diffusion takes place in an argon atmosphere, the ions directly enter the substrate and diffuse from the metal layer until its exhaustion. If the diffusion is carried out in an oxygen atmosphere, the layer is first oxidized to TiO_2 or ZnO_2 respectively, and the metal ions enter the substrate from the oxide layer. In this case, as with the rare-earth activation from a metal layer deposited onto the crystal surface, it is very important that the diffusion of Ti/Zn is complete. If the metal layer diffuses incompletely, it is necessary to polish the surface in order to obtain a high-quality, low-loss waveguide.

Diffusion gives a profile which is typically half-Gaussian or error-function in shape, with a maximal change at the surface.

The formation of the waveguide structure is performed by photolithography, followed by deposition of a Ti layer and thermal diffusion. Due to the high losses and the instability of the obtained waveguides, additional annealing in an oxygen atmosphere or periodic poling is needed [32]. The obtained optical waveguide overlaps the rare-earth doped region. Since the diffusion temperature and the duration of the process of waveguide formation also allow the rare-earth element to enter deeper into the crystal, it is best to consider this process as an additional annealing of the doped layer when calculating the final diffusion depth of the rare-earth element. At the same time, titanium has a faster diffusion (due to its shorter ion radius) and this way it provides the necessary larger width of the waveguide channel compared to the width of the rare-earth region.

In Figure 1, the transverse section of a crystal is shown, surface-doped with a rare-earth element surrounded by a stripe waveguide, obtained by titanium diffusion or proton exchange. The rare-earth doped area has a smaller width than the waveguide and a smaller doping depth than the waveguide channel depth. The maximal concentration of the rare-earth dopant is located in the center below the surface of the crystal.

A good combination of the technologies for obtaining of erbium-doped LN and for the formation of optical waveguides by titanium diffusion is demonstrated by the authors of [34-36], as well as optical amplifiers and lasers based thereon [2].

The obtaining of waveguides by diffusion of titanium or zinc in the activated systems (Nd/Er/Tm/Yb):$LiNbO_3$ has been described [37]. Single-mode waveguides are formed by diffusion of 7 μm wide, 100 nm thick Ti-stripes for 9 hours at 1060 °C. The crystal orientation of the substrates is selected with regard to the type of laser device to be obtained: for DBR/DFB lasers or for acoustooptically tunable lasers, X-cut substrates are used, and a propagation of the light beam along Z in the first case, and along Y in the second one. For the obtaining of Q-switched and modelocked lasers, Z-cut substrates are selected and a propagation of the light beam along X, in order to use the highest value of the electro-optical coefficient for more efficient modulation.

The main advantages of the formation of optical waveguides by thermal indiffusion of a metal layer in LN are: high reproducibility, increase of both ordinary and extraordinary refractive indices, high stability of waveguide parameters and low losses in the obtained waveguides. As disadvantages,

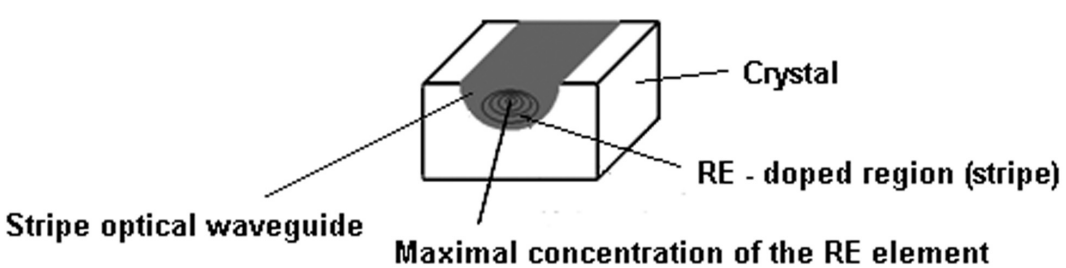

Fig. 1. A transverse section of a rare-earth doped waveguide channel in LN

the following may be cited: the high temperature required and the parasitic waveguides formed by out-diffusion, as well as the 100-fold reduction in the optical damage threshold power density from the bulk value.

b) Proton exchange

Proton exchange (PE) takes place in a surface layer of a substrate immersed in an appropriate acidic melt [38]. PE modifies the surface layer (several μm in depth) by Li-H ion exchange at a relatively low temperature (160–250 °C) causing a large extraordinary index change Δn_e ($\Delta n_e \cong 0.12$ at 0.633 μm). The PE layers show complex phase behavior depending on the hydrogen concentration. Strong protonation considerably worsens electro-optical properties of the waveguiding layer [39] and causes higher losses (2 to 5 dB/cm) [40] and some instability of the parameters over time. However, taking into consideration that other methods (melt buffering and/or annealing) exist for the adjustment of phase composition [41], these drawbacks can be corrected or even turned into advantages for the possibility to modify the electro-optical properties. These can also be avoided by using the methods for optimization of proton concentration [42]. Waveguide fabrication by PE has multiple variations, including post-exchange annealing (APE) [42]. Proton-exchanged LN waveguide devices are preferred over Ti-diffused LN ones in cases where high optical powers are to be transmitted and/or single polarization operation is desired.

Considering proton exchange of rare-earth doped LN, it should be taken into account that radiative lifetime reduction and strong fluorescence quenching occur because of the coupling to OH-phonons [43, 44]. Due to these reasons, some authors do not find the combination of rare-earth doping with subsequent obtaining of the optical waveguide by proton exchange a good one for waveguide lasers, since the presence of hydrogen has a killing effect on the excited erbium electrons, shortening their lifetimes, which then results in a drastically reduced optical gain [2, 24, 36, 44, 45]. Promising results have been obtained with selection of appropriate conditions for carrying out proton exchange with subsequent annealing for the formation of the optical waveguide [19, 28, 29], or with using reverse proton exchange (RPE) [46]. Waveguide lasers have been described based on stripe waveguides obtained in erbium-doped LN by proton exchange for 2 h in benzoic acid buffered with 1 mol% lithium benzoate at 200 °C, with subsequent annealing for 3–4 hours at 350 °C [47]. Continuous-wave laser action at 1084.5° nm at room temperature in $LiNbO_3$:Nd^{3+} channel waveguides, fabricated by RPE, is reported.[46]. Yb-diffused $LiNbO_3$ annealed/proton-exchanged waveguide lasers are also demonstrated. A Fabry-Pérot waveguide laser of 3-cm length is fabricated and characterized. For optical pumping at 918-nm wavelength, stable continuous-wave laser oscillation is achieved at 1061 nm with a threshold power of 40 mW. [33]. It has been demonstrated that Er-doped optical waveguides produced by a moderate temperature process (APE, for example) are quite effective [19]. With appropriately chosen parameters of the APE technology [43], the hydrogen content in the waveguides could be decreased to a level not causing photoluminescent quenching, so that such waveguides could be used in active integrated-optical structures.

The results of the study of APE layers in LN doped with erbium or erbium+ytterbium show also that during the APE process, no loss of rare-earth elements from the substrate previously doped with them is observed. The waveguide properties and the PE process itself in doped samples do not differ from those of non-doped ones. The presence of doping ions (rare-earth as well as hydrogen ones) leads to worsening of the electro-optical properties of LN, but a carefully designed APE technology may restore them almost to the degree of a non-doped LN. This may be done by modeling the distribution of lithium in the waveguide area, since a correlation between the uniform distribution of lithium and the high values of the electro-optical coefficient r_{33} has been found. A homogeneous distribution of lithium and a very low content of hydrogen has been obtained in the long-time-annealed waveguiding layers [48].

It has to be mentioned that the problems with luminescence quenching are observed only with protonation of erbium-doped LN, whereas, for example, after protonation of a neodymium-doped LN, a very effective luminescence has been registered around 1 μm wavelength and no quenching problems are reported [44, 49]. Besides, luminescence quenching after the proton exchange has not always been observed in the case of erbium activation of LN. This effect has been reported when the doping has been performed either during crystal growth by ion implantation, or by diffusion from a metal layer [2, 24, 44, 45] and does not take place when the doping has been performed with a low-temperature process in a melt [19, 28–29, 50–52].

The advantages of proton exchange as a method for obtaining of optical waveguides in LN are: a fast and simple waveguide formation procedure; non-toxicity and lower cost; possibility of thermal tuning of the refractive index; a strong waveguiding effect; an increased photorefractive resistance; flexibility and compatibility with other technologies; a large variety of optimization steps. Its main

disadvantages are: multiphase composition of the waveguide layer; deterioration of electro-optical properties in strongly protonated layers; some instability over time.

Doping of a previously obtained optical waveguide with laser-active ions (rare earths)

Since for the formation of laser-active waveguides the opposite procedure is also generally possible – proton exchange and subsequent diffusion of a rare-earth element – the influence of proton exchange on the following erbium-ion doping has been studied, in the case that the obtaining of the optical waveguide is chosen as the first step in the fabrication of the waveguide light amplifier or laser [19, 28]. It has been found that with the diffusion of erbium the amount of diffused erbium depends not only on the crystal orientation but also on the history of the substrate – untreated or previously proton-exchanged. This dependence is strongest with X-cut samples, in which the proton exchange lowers about 15 times the amount of erbium ions compared to that in non-protonated subtstrates under identical conditions [28]. This is most probably due to the gradual transition of the structure of LN towards monocline one after PE. Although the lattice parameters do not change significantly, that suppresses the diffusion of erbium ions. Due to these reasons, the erbium doping should be performed before the APE process, since the completely changed structure of APE layers impedes the process of rare-earth doping [19].

In Figure 2-A, the steps for the obtaining of a stripe optical waveguide activated by a rare-earth element are schematically shown. The first step is the deposition of structured photoresist (PR) onto the crystal surface, thereby obtaining photoresist-free channels in the area subjected to rare-earth doping. The second step is the deposition of the rare-earth element (RE) by sputtering or vaccum evaporation in the form of a metal or a metal oxide, after which the photoresist (PR) together with the overlying layer are removed by the lift-off technique. This results in a small rare-earth stripe (RE) deposited onto the surface of the crystal substrate (S); the stripe would diffuse in S in the next step. This diffusion takes place during the first thermal treatment (T1) in an atmosphere of Ar-O_2, the temperature and duration being so chosen that a controlled diffusion depth is achieved which has to be smaller than the depth of the waveguide channel, which should be inserted thereafter. It has been shown, for example [49] that with Z-cut substrates, an average diffusion depth of 5 μm is reached after 100 h at 1050 °C, and at 1080 °C the depth is 7.2 μm. The diffusion depth is defined as 1/e of the surface concentration. The next step is the deposition of silica-gel (sol-gel) (SG) onto the crystal surface, followed by the second thermal treatment (T2) which leads to partial out-diffusion of the dopant close to the surface through the sur-

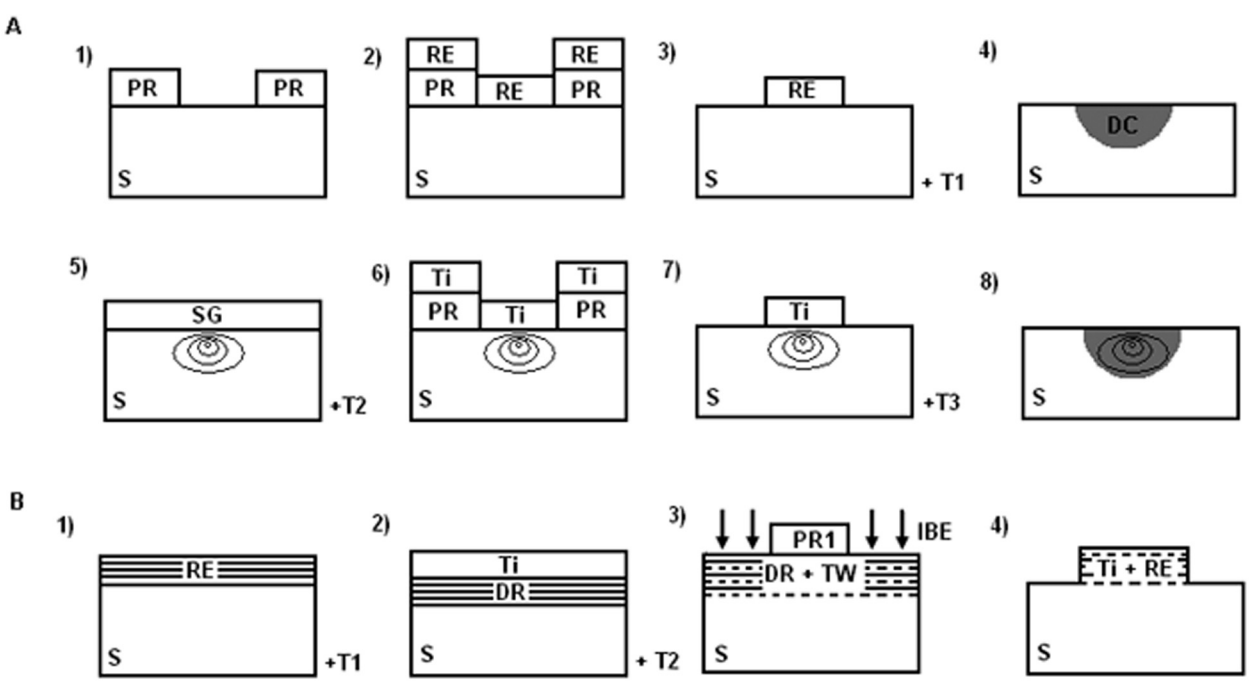

Fig. 2. Scheme of the technological steps for obtaining an active waveguide

face in the gel. This way, an area with a maximal dopant concentration is formed under the surface of the crystal. At the same time, the rare-earth doped area becomes deeper. The next step is the deposition of titanium (Ti) onto the structured photoresist (PR) onto the surface of S and its diffusion in the crystal during the third thermal treatment (T3), again in an atmosphere of Ar-O_2. A titanium stripe is deposited over the center of the rare-earth doped area, and as a result, the axis of the waveguide channel is parallel to that of the rare-earth channel. With a 95 nm thick titanium layer and a diffusion of 10 h at 1050 °C, a single-mode waveguide is obtained.

In Figure 2-B, another method is shown for the formation of the lateral borders of the waveguide channel. This process comprises an initial deposition of a rare-earth layer (RE) onto a wide area of the crystal substrate (S) and its diffusion during the first thermal treatment (T1). After that, again over a wide area, a waveguide is formed by Ti diffusion or PE. The next step is the deposition of photoresist (PR) onto the doped area (DR), the photoresist being so structured that a small stripe of photoresist (PR1) remains where the waveguide channel should be formed. In the following step, the surplus doped material at both sides of the stripe is etched by ion etching, and the photoresist is removed in the next step. This way a small stripe – a narrow stripe waveguide doped with a rare-earth element – stays on the crystal.

Ion implantation (He^+, Ne^+)

Ion implantation is performed usually at energies from 7 keV to 2 MeV. The change of the refractive index depends on the ion energy and is relatively large – from 0.02 to 0.08 [53]. After the implantation, annealing is always performed to restore the crystal structure [2, 25]. The implantation of H^+ in erbium-doped LN easily leads to chemical reactions, for example formation of OH-groups, and they are important centers of luminescence quenching [2]. In this case, for ion-implanted waveguides, co-doped LN substrates are used, for example with MgO, which avoids the quenching by OH-groups. Waveguides with a high optical quality have been obtained with implantation of H^+ in $LiNbO_3$ bulk-doped with Eu^{3+} and MgO [54]. There, no luminescence quenching is observed and the fluorescence in the waveguide is the same as bulk fluorescence.

The method has the advantages of preserving the bulk material properties, depth control and possibility for obtaining multilayer structures, as well as an opportunity of writing optical circuits by ion beam. However, it is a very expensive method and some instability of waveguide parameters over time has been demonstrated.

CONCLUSIONS

• The choice of technological conditions for rare-earth doping of LN affects the dopant penetration and location as well as the structural changes of the doped layers.

• The concentration of the dopant and the sites its ions occupy in the crystal lattice of the LN matrix are crucial for both the dopant's luminescent activation and its optical properties.

• The local doping of $LiNbO_3$ exhibits strong anisotropy.

• In many cases lasing efficiency and optical properties of the waveguides obtained could be improved by co-doping.

• The most convenient and promising methods for obtaining waveguide lasers are the diffusion ones – for rare-earth doping as well as for the subsequent fabrication of the optical waveguides.

• Better results are achieved when the doping with rare-earth ions precedes the fabrication of the optical waveguides, although in some cases the reverse procedure is also possible.

REFERENCES

1. L. Tsonev,*Optical Materials*, **30**, 892 (2008).
2. Ch. Buchal, S. P. Withrow, C. W. White, D. B. Poker, *Annual Revue of Materials Science*, **24**, 125 (1994).
3. B. K. Das, H. Suche, W. Sohler,*Appl. Phys. B*, **73**, (2001).
4. B. K. Das, R. Ricken, W. Sohler, *Appl. Phys. Lett*., **l82**, 1515 (2003).
5. B. K. Das, R. Ricken, V. Quiring, H. Suche,W. Sohler, *Opt. Lett*., **29**, 165 (2004).
6. G. Burns, D. F. O'Kane, R. S. Title, *Phys. Rev.,* **167**, 314 (1968).
7. V. Bermudez, M. D. Serrano, J. Torento, E. Diegues, *Solid State Communications*, **112**, 699 (1999).
8. L. Rebouta, M. F. Da Silva, J. C. Soares, D. Serrano, E. Diéguez, F. Agulló-López, J. Tornero. *Appl. Phys. Lett.* **70**, 1070 (1997).
9. B. Herreros, PhD Thesis, UAM, Madrid, Spain, 1997.
10. L. Nuñez, R. Duchowicz, M. Voda F. Cussó, *J. Physique IV*, **4**, C4–443 (1994).
11. D. M. Gill, J. C. Wright and L. McCaugan, *Appl. Phys. Lett.* **64**, 2483 (1994).
12. C. Bonardi, C. J. Magon, E. A. Vidoto, M. C. Terrile, L. E. Bausa, E. Montoya, D. Bravo, A. Martin, F. J. Lopez, *J. Alloy Comp.*, **323-324**, 340 (2001).
13. H.-N. Dong, S.-Y. Wu , W.-C. Zheng, *J. Phys. Chem. Solids*, **64**, 695 (2003).
14. I. Pracka, M. Malinowski, A. L. Bajor, B. Surma, Z. Galazka, M. Swirkowicz, M. Mozdzonek, *Proc. SPIE*, **3178**, 295 (1997).
15. E. Montoya, O. Espeso, L. E. Bausa, *J. Lumin*., **87-89**, 1036 (2000).
16. E. Montoya, L. E. Bausa, B. Schaudel , P. Goldner, *J. Chem. Phys.*, **114**, 3200 (2001).

17. C. Huang, L. McCaughan, *IEEE Photonics Technology Letters*, **9**, 599 (1997)
18. V. A. Fedorov, Yu. Korkishko, J. A. Sanz-Garcia, E. Cantelar, R. Nevado, G. Lifante, F. Gusso, in: Proc. ECIO'01, Padeborn, April 2001, 297 (2001).
19. V. Perina, J. Vacik, V. Hnatovicz, J. Cervena, P. Kolarova, J. Spirkova-Hradilova, J. Schröfel, *NIM-B*, **139**, 208 (1998).
20. M. Fleuster, Ch. Buchal, H. Holzbrecher, E. Snoeks, A. Polman, *J. Appl. Phys.*, **75**, 173 (1994).
21. M. Fleuster, Ch. Buchal, E. Snoeks,A. Polman, *Appl. Phys. Lett.*, **65**, 225(1994).
22. P. Moretti, B. Canut, S. M. M. Ramos, P. Thevenard, D. Poker, J. B. M. Da Cunha, L. Amaral, A. Vasquez, *J. Mater. Res.,* **8**, 2679 (1993).
23. I. Baumann, R. Brinkmann, M. Dinand, W. Sohler, L. Beckers, Ch. Buchal, M. Fleuster, H. Holzbrecher, H. Paulus, K.-H. Müller, Th. Gog, G. Materlick, O. Witte, H. Stolz, W. von der Osten, *Appl. Phys. A*, **A64**, 33 (1997).
24. I. Baumann, S. Bosso, R. Brinkmann, R. Corsini, M. Dinand, A. Greiner, K. Schäfer, J. Söchtig, W. Sohler, H. Suche, R. Wessel, *IEEE J. Select. Topics in Quantum Electron*, **2**, 355 (1996).
25. W. Sohler, B. K. Das, D. Dey, S. Reza, H. Suche, R. Ricken,*IEICE Trans. Electron.*, **E88–C**, 990 (2005).
26. I. Baumann, R. Brinkmann, Ch. Buchal, M. Dinand, M. Fleuster, H. Holzbrechel, W. Sohler, H. Suche, in: Proc. ECIO'93, Neuchatel, 1993, p. 3.
27. Th. Gog, M. Griebenow and G. Materlik, *Physics Letters A*, **181**, 417 (1993).
28. J. Hradilova, P. Kolarova, J. Schröfel, J. Ctyroky, J. Vacik, V. Perina, *Proc. SPIE*, **2775**, 647 (1996).
29. C. Sada, E. Borsella, F. Caccavale, F. Gonella, F. Segato, Yu. N. Korkishko, V. A. Fedorov, T. M. Morozova, G. Battaglin, R. Polloni, *Appl. Phys. Lett.*, **72**, 3431 (1998).
30. F. Caccavale, C. Sada, F. Segato, B. Allieri, L. E. Depero, L. Sangaletti, V. A. Fedorov, Yu. N. Korkishko, T. V. Morozova, *J. Non- Cryst. Solid*s, **280**, 156 (2001).
31. F. Caccavale, C. Sada, F. Segato, in: Properties of Lithium Niobate, K. K. Wong (ed.), INSPEC Inc., 2002, p. 300.
32. J. K. Jones, J. P. de Sandro, M. Hempstead, D. P. Shepherd, A. C. Large, A. C. Tropper, J. S. Wilkinson, *Optics Letters*, **20**, 1477 (1995).
33. M. Fujimura, H. Tsuchimoto, T. Suhara, *Photonics Technology Letters, (IEEE **17**)*, 130 (2005).
34. A. Lorenzo, L. E. Bausa, J. Garcia-Sole, *Phys. Rev. B*, **51**, 16643 (1995).
35. K.A. Winick, *Proc.SPIE*, **3280**, 88 (1998).
36. A. Fukumi: PhD Thesis, Hiroshima University, June 2002.
37. E. Cantelar, R. Nevado, G. Martin, J. A. Sanz-Garcia, G. Lifante, F. Cusso, M. J. Hernandez, P. L. Pernas, *J. Luminesc.*,**87/ 89**, 109 (2000).
38. J. Jackel, C. Rice, J. Veselka, *Appl. Phys. Lett.*, **41**, 607 (1982).
39. M. Rottschalk, A. Rash, W. Karthe, *J. Opt. Commun.*, **9**, 19 (1988).
40. A. Loni, R. De La Rue, J. Winfield, in: Technical Digest Series 5 (Proc. Topical Meeting on Integrated & Guided Wave Optics, March 28-30, Santa Fe, New Mexico), 1988, p. 84.
41. K. Wong , *Gec. J. Research*, **3**, 243 (1985).
42. S. M.Al-Shukri, S., A. Dawar, R. De La Rue, A. Nutt, M. Taylor, J. Tobin, in: Proc. 7th Top. Meet. on Integrated and Guided Wave Optics, Florida, April 1984, PD7/1.
43. J. K. Jones, J. P. De Sandro, M. Hempstead, D. P. Shepherd, A. C. Tropper, J. S. Wilkinson, in: Proc. Symp. on Materials for Advanced Solid State Lasers, Boston, 1993, publ. by, Materials Research Society, Pittsbourgh, PA, 1994, p. 233.
44. Marc P. De Micheli, *Proc. SPIE*, **2996**, 62 (1997).
45. A. C. Cino, S. Riva Sanseverino, M. P. De Micheli, K. El Hadi, F. Cusso, G. Lifante, *Proc. SPIE*, **3280,** 152 (1998).
46. E. Cantelar, G. Lifante, F. Cussó, M. Domenech, A. Busacca, A. Cino, S. Riva-Sanseverino, *Optical Materials*, **30**, 1039 (2008).
47. W. Sohler, H. Suche,*US Patent* 5 473 722 (1995).
48. P. Nekvindova, J. Cervena, P. Capek, A. Mackova, V. Perina, J. Schröfel, J. Spirkova, *Optical Materials*, **24**, 527 (2003).
49. M. Hempstead, J. S. Wilkinson, L. Reekie, *IEEE Photon. Technol. Lett.*, **4**, 852 (1992).
50. P. Nekvindova, J. Spirkova-Hradilova, J. Schroefel, M. Slunecko, V. Perina, J. Vacik, *Proc. SPIE*, **3858**, 180(1999).
51. F. Zhou, Y. Zhou, *Singapore J. Phys*. **12**, 21 (1996).
52. J. Spirkova-Hradilova, P. Nekvindova, J. Vacik, J. Cervena, V. Perina, A. Mackova, J. Schroefel, M. Budnar, A. Raspet, B. Zorko, P. Pelicon, *Proc. SPIE*, **4277**, 200 (2001).
53. A. Polman, E. Snoeks, G. N. van den Hoven, M. L. Brongersma, R. Serna, J. H. Shin, P. Kik, E. Radius, *Nucl. Instr. Meth. Phys. Res. B*, **106**, 393 (1995).
54. C. Mignotte, P. Moretti, K.E. Lipinska-Kalita, G. Boulon, J. Mugnier, *J. Optics*, **27**,259 (1996).

ОПТИЧНИ ВЪЛНОВОДИ В ЛИТИЕВ НИОБАТ, ДОТИРАН С РЕКОЗЕМНИ ЕЛЕМЕНТИ

М. Кънева

Институт по физика на твърдото тяло „Акад. Г. Наджаков“ – Българска академия на науките, бул. „Цариградско шосе“ № 72, София 1784, България

Постъпила на 15 февруари, 2012 г.; приета на 26 март, 2012 г.

(Резюме)

Дотирането на диелектрици с лазерно-активни йони, каквито са йоните на редкоземните елементи, е предмет на широко изследване през последните години. Големият интерес се дължи на възможността за получаване по този начин на миниатюрни твърдотелни лазери и за монолитно интегриране на тези лазери и други елементи върху обща подложка.

Настоящата публикация представлява обзор на по-важните изследвания в областта на дотирането на литиев ниобат с йони на редкоземни елементи. Направен е опит за обобщаване на резултатите по отношение на технологиите за дотиране на $LiNbO_3$ с лазерно-активни йони и за получаване на оптични вълноводи в дотираните с редкоземни елементи подложки от $LiNbO_3$. Основните методи за дотиране са: въвеждане на примеса при израстването на кристала, йонна имплантация, дифузия от слой, отложен върху кристалната подложка, дифузия от стопилка. Разгледано е влиянието на ориентацията на подложката върху дотирането, влиянието на дотирането върху следващи дифузионни процеси, възможните позиции на примесните йони в решетката на $LiNbO_3$-матрица, структурните промени в нея и зависимостта им от технологичните параметри на дифузионния процес и т.н. Специално внимание е отделено на нискотемпературните методи за дифузия, при които се извършва йонен обмен или дифузия без йонен обмен, при която дотиращите йони се разполагат в съществуващите ваканции в кристалната решетка на $LiNbO_3$. Обсъдено е влиянието на състава на стопилката, температурата и продължителността на дифузията върху концентрацията на дотиращия елемент, както и условията, при които анизотропната дифузия става самоограничаващ се процес.

Bulgarian Chemical Communications, Volume 44, Proceedings of the III[rd] National Crystallographic Symposium (pp. 109–114) 2012

Synthesis and characterization of zinc phosphates doped with samarium and manganese

G. I. Patronov[1]*, I. P. Kostova[1], Z. Y. Stoeva[2], D. T. Tonchev[1, 2]

[1] *Dept. Chem. Technology, Plovdiv University "Paisii Hilendarski", 4000 Plovdiv, Bulgaria*
[2] *DZP Technologies Ltd.*, *22 Signet Court, Cambridge CB5 8LA, United Kingdom*

Received February 15, 2012; Revised April 6, 2012

Samarium and manganese doped zinc phosphate compositions were prepared by high-temperature ceramic synthesis where ZnO, $NH_4H_2PO_4$ and Sm_2O_3 (or MnO) of pre-determined ratios were powdered, mixed and placed in alumina crucibles. The synthesis was performed at 950 °C for 3 hours in a muffle furnace. Samples were quenched out of the melt to room temperatures and after that annealed at 250 °C for 2 hours. Sm_2O_3 and MnO doping varied between 0.03 and 0.28 mol percentage.

Using powder X-ray diffraction, we have found that the observed fundamental crystalline phase is iso-structural with α-$Zn_2P_2O_7$, where samarium and manganese ions most probably substitute for Zn^{2+}. This is supported by the obtained photoluminescence spectra. The lattice parameters obtained from the Le Bail calculations for the doped zinc phosphate crystalline phase are very similar to the lattice parameters of α-$Zn_2P_2O_7$. Deviation of lattice parameters is associated with different ionic radius of dopant Sm^{3+} and Mn^{2+}.

Key words: doped zinc phosphates, samarium, manganese, crystal structure, photoluminescence.

INTRODUCTION

Recently there has been significant interest in materials based on phosphates (P_2O_5), doped with rare earths and others elements (such as transition elements) due to their unique optical and electrical properties and related photo-, electro-, luminescent effects and others. These materials have potential applications in advanced devices such as laser sources, sensors, photodiodes, X-ray imaging plates, anti-counterfeit printing additives etc.

These compositions, stoichiometric or alloys, have been synthesized by different methods – sintering, melting, sol – gel and others. They may have polycrystalline, amorphous or amorphous-crystalline mixed phase composition. The amorphous state provides technological and functional advantage in many cases. Attention is directed to changing their optical, mechanical and thermal properties for different ratio of ZnO and P_2O_5 and different contents of doped elements [1–4].

Our research on samarium and manganese doped zinc phosphates has demonstrated that UV and X-ray exited photo-luminescence in the visible spectra and glass ceramics materials are formed in the ZnO – rich compositions. We believe the strong photoluminescence is due to the stabilisation of samarium and manganese ions within both the glass matrix and within the crystalline phases dispersed into these scintillating materials. It is of particular interest to investigate crystalline phases in this glassy matrix and to study their structures, in order to understand their relationship with the photo-luminescence properties.

In our work we present synthesis and characterisation studies of samarium and manganese doped ZnO-rich zinc phosphate material of composition $yM - (72-y)ZnO - 28P_2O_5$ where: M = Sm_2O_3 or MnO, y varied between 0.03 and 0.28 mol%. We examine the difference between the two dopant structures, and we correlate them to the observed photo-luminescence properties.

EXPERIMENTAL

Sample preparation

All samples were prepared by high-temperature ceramic methods using $NH_4H_2PO_4$, ZnO and Sm_2O_3 (or MnO) as starting materials. The reagents were

* To whom all correspondence should be sent:
E-mail: patron@uni-plovdiv.bg

thoroughly mixed, placed in alumina crucibles and heated at 950 °C for 3 hours in a muffle furnace. The obtained homogeneous melts were then poured onto a graphite plate and annealed at 250 °C for two hours. The obtained materials are easily reproducible. Synthesis of the doped zinc phosphate samples (samarium or manganese) is schematically presented on Fig. 1. Sm_2O_3 or MnO doping varied between 0.03 and 0.28 mol percentage.

Density measurements

Density measurements were carried out according to the Archimedes method using deionised water of density 1g/cm^3 as an immersion liquid.

Photoluminescence measurements

The photoluminescence spectra were measured by optical CCD Aventes spectrometer Ave-Spec 2048, operating at 25 MW in the range 250–1100 nm at room temperature. Two light sources were used: 405 nm laser diode and 365 nm light emitting diode.

Powder X-ray diffraction analysis

Powder X-ray diffraction data were collected on TUR M62 diffractometer operating with a Cu Kα radiation source (λ = 0.15405 nm), in steps of 0.04° over the range of 10–60° 2θ, with a time per step of 2.8 sec.

Modelling of the powder X-ray diffraction patterns was carried out using Powder Cell software [5]. The Le Bail method [6] implemented within the General Structure Analysis Software (GSAS) [7] was used to extract structure factors and refine the cell parameters. The Le Bail refinements were carried out based on the reported crystal structure of α-$Zn_2P_2O_7$ [8, 9, 10].

RESULTS AND DISCUSSION

Lists of the samples and the data obtained from density measurements of the same are presented in Table 1 and Table 2. There are some variations in the density as a function of Sm_2O_3 or MnO doping. This may be related to the changes in atomic masses, ionic size, cross-linking densities and occupied positions of the constituent dopant elements in glass-ceramics [11]. A somewhat similar trend was observed by Eraiah *et al.* [1] who found that the density of samarium doped zinc phosphate glasses reached a minimum at Sm_2O_3 doping level of 0.03 mol %. This trend is explained by the fact that Sm_2O_3 acts as

Table 1. List of samarium doped zinc phosphate samples

№	Composition			Density (ρ), g/cm^3
	Sm_2O_3, mol %	ZnO, mol %	P_2O_5, mol %	
1	0.03	72.28	27.69	4.60
2	0.09	72.17	27.74	4.46
3	0.14	72.06	27.80	4.26
4	0.28	71.79	27.93	4.74

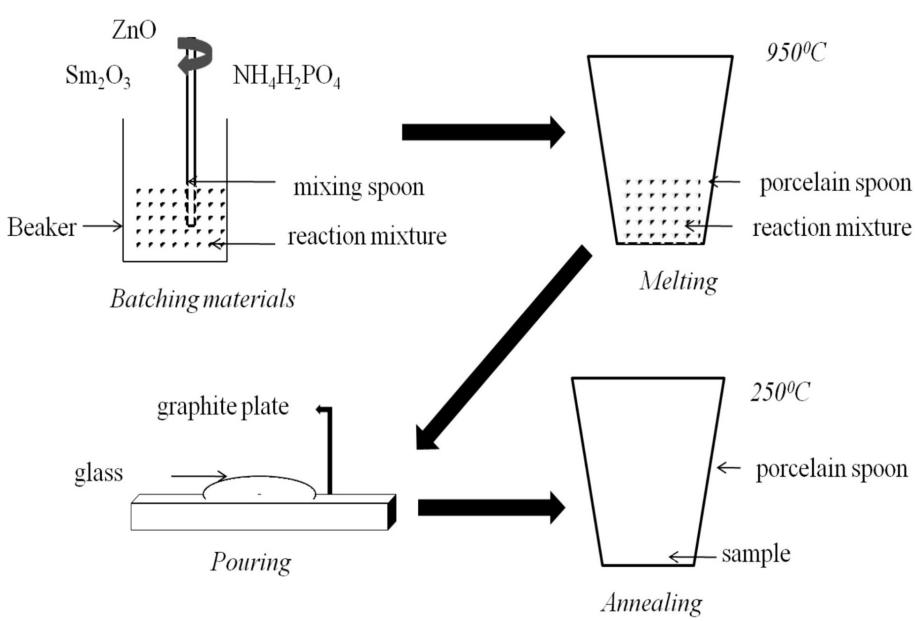

Fig. 1. Preparation of the samarium and manganese doped zinc phosphate samples

Table 2. List of manganese doped zinc phosphate samples

№	Composition			Density (ρ), g/cm^3
	MnO, mol %	ZnO, mol %	P_2O_5, mol %	
5	0.03	72.28	27.69	3.95
6	0.09	72.17	27.74	3.89
7	0.14	72.06	27.80	3.68
8	0.17	72.01	27.82	3.25
9	0.23	71.90	27.87	3.68
10	0.28	71.79	27.93	3.76

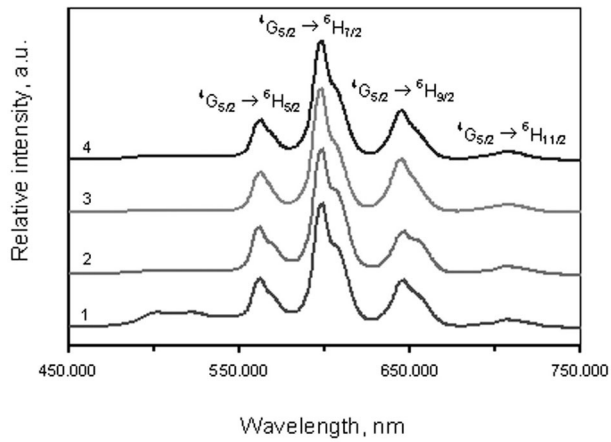

Fig. 2. Photoluminescence spectra of samples 1–4 at excitation wavelength 405 nm

a glass modifier that increases the fraction of non-bridging oxygen atoms and leads to increased porosity and reduced density of the glass.

The densities of the samples in our work are higher than the densities reported for samarium doped zinc phosphate glasses by Eraiah *et al.* [1]. This could be expected, given the higher molar fraction of ZnO in our material (70%), compared to the glasses studied by Eraiah *et al.* [1] where the molar fraction of ZnO was 60%.

All synthesized materials display photoluminescence. Representative emission spectra for samples 1–4 are illustrated in Figure 2 and reveal four emission bands in the wavelength range be-

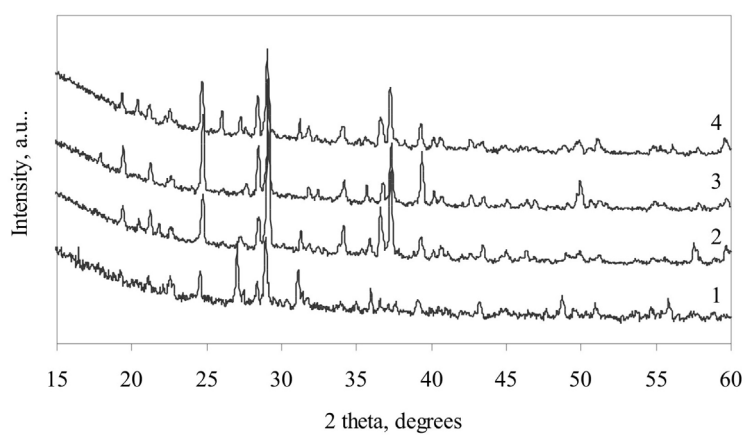

Fig. 3a

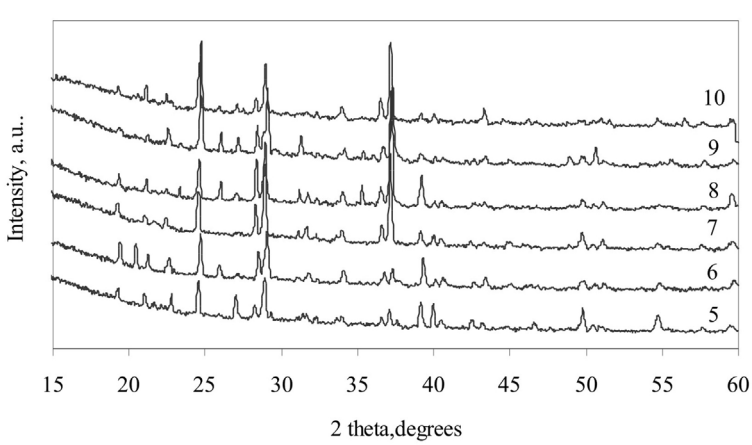

Fig. 3b

Fig. 3. Powder X-ray diffraction patterns for samarium (Fig. 3a) and manganese (Fig. 3b) doped zinc phosphate samples: No1 (0.03 mol% Sm_2O_3), No2 (0.09 mol% Sm_2O_3), No3 (0.14 mol% Sm_2O_3), No4 (0.28 mol% Sm_2O_3) No5 (0.03 mol% MnO), No6 (0.09 mol% MnO), No7 (0.14 mol% MnO), No8 (0.17 mol% MnO), No9 (0.23 mol% MnO), No10 (0.28 mol% MnO)

tween 450 and 750 nm, namely 564 nm, 600 nm, 645 nm and 710 nm. The band at 600 nm which corresponds to orange emission is the most intense. As shown in Figure 2, the emission bands can be assigned to the *4f–4f* transitions from the excited $^4G_{5/2}$ level to the ground state $^6H_{5/2}$ and higher levels ^6H_J ($J > 5/2$) of the trivalent Sm^{3+} ions which have $4f^5$ configuration. The spectra indicate that the luminescence reddish colour of UV irradiated (LED 365 and 405 nm) Zn-phosphate materials are due to Sm^{3+} ions only (no Sm^{2+} ions present) [12, 13].

Powder X-ray diffraction was used to identify the crystalline phases present in the obtained samples. The X-ray diffraction patterns, presented in Figure 3, confirm that all samples contain one or more crystalline phases. However, the poorly defined peak shapes and the presence of a high background, which is attributable to an amorphous phase, indicate the formation of mixed amorphous-crystalline (glass ceramic like) material.

Inspection of the powder patterns using Powder Cell software shows that the observed crystalline phases are iso-structural with α-$Zn_2P_2O_7$ [8, 9, 10], illustrated in Figure 4, where samarium and manganese ions most likely substitute for Zn^{2+}. The material crystallises with monoclinic symmetry in space group I2/c with unit cell parameters a = 20.068(15) Å, b = 8.259(6) Å, c = 9.099(8) Å, β = 106.35(5)°. Some of Zn^{2+} sites in the structure are 5-coordinated and others are 6-coordinated. The structure is composed of layers of PO_4 tetrahedra alternating with layers of Zn atoms. The suggestion that the Sm and Mn dopant ions substitute for the Zn sites in the structure is in agreement with the observed photo-luminescence spectra that confirm that all samarium ions are present in 3^+-valence state, as shown in Figure 2.

In order to further investigate the crystalline phase that was present in all samples, the Le Bail method was used to compare the calculated powder X-ray diffraction pattern of α-$Zn_2P_2O_7$ against the experimental pattern of sample 2 and sample 8. The resulting fit is shown in Figure 5 and the lattice parameters obtained from the Le Bail calculations for sample 2 and sample 8 are listed in Table 3. It is evident that they are very similar to the lattice parameters of α-$Zn_2P_2O_7$ but slightly increased because of the Sm^{3+} and Mn^{2+} doping. Deviation of lattice parameters is associated with different ionic radius of Sm^{3+} and Mn^{2+}.

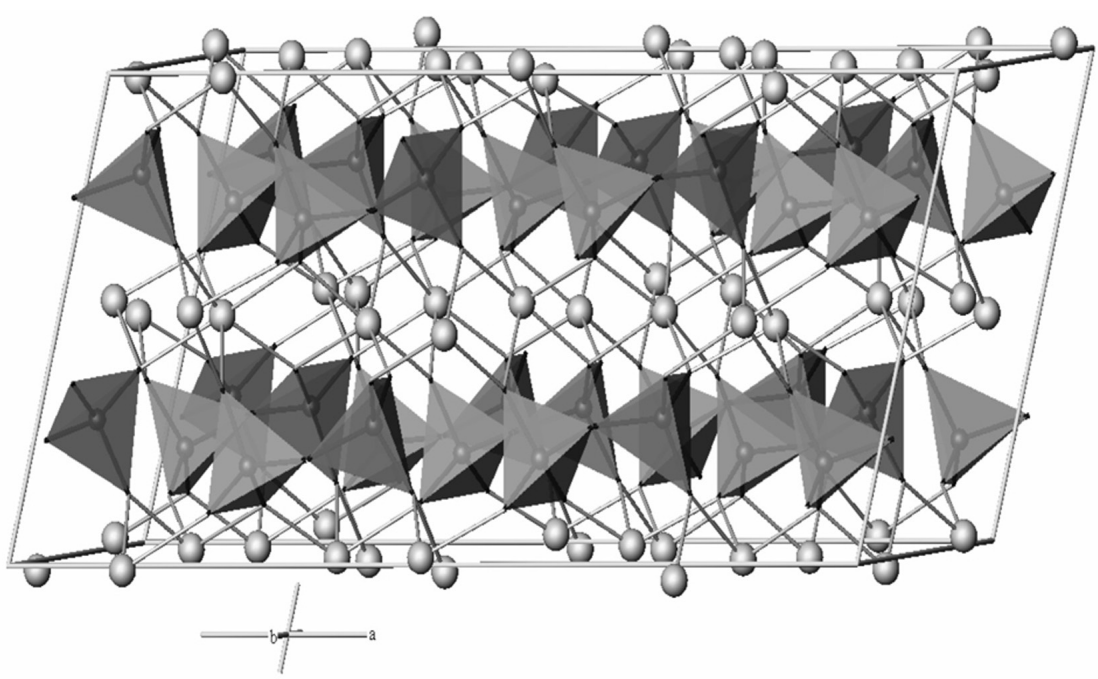

Fig. 4. Crystal structure of α-$Zn_2P_2O_7$ according to Robertson *et al* [8]
The picture shows the content of a single unit cell. The phosphorous atoms are shown by small circles that are located inside corner-sharing PO_4 tetrahedra, shown in grey. The zinc atoms, presented by light grey circles, occupy two different cites in the structure

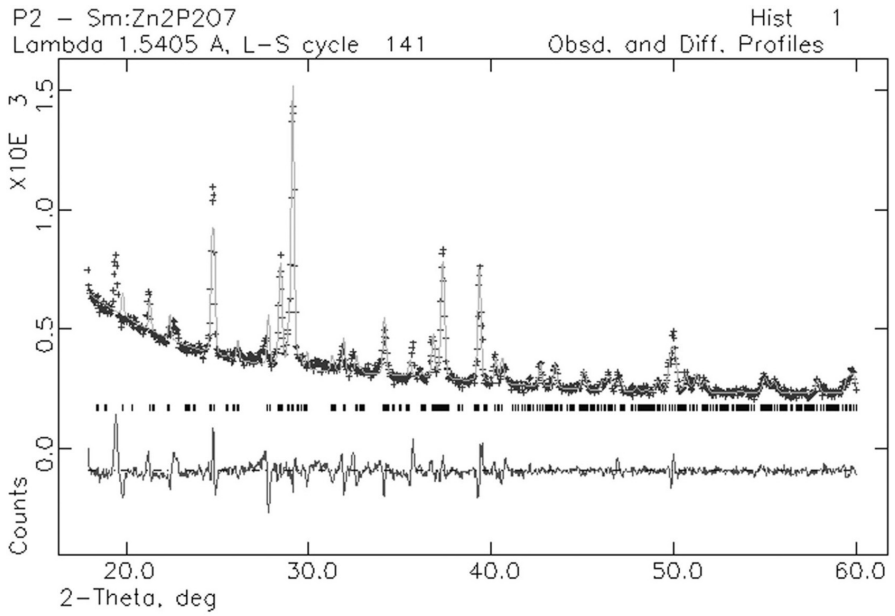

Sample 2

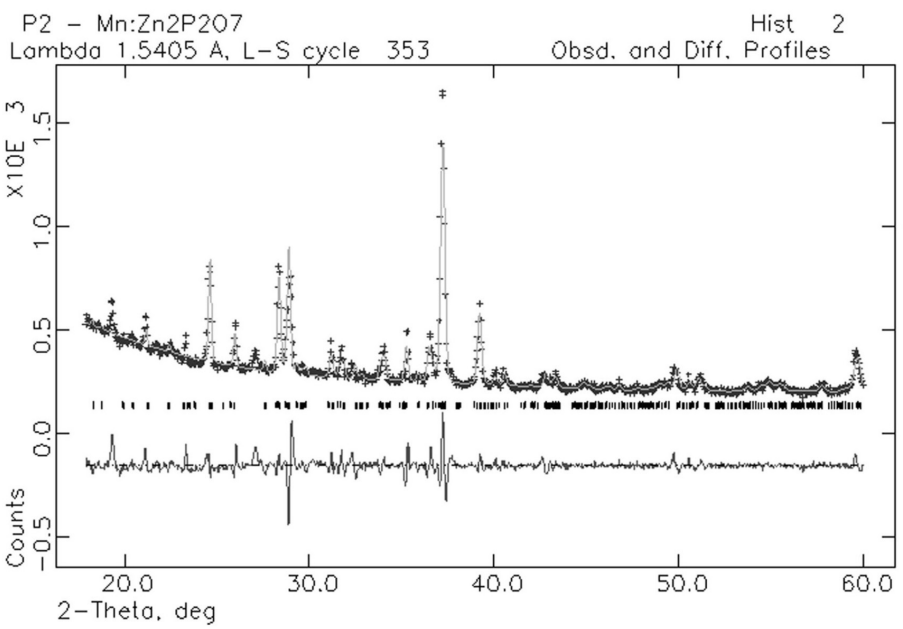

Sample 8

Fig. 5. Le Bail calculations for sample 2 and sample 8 Grey crosses show the observed data points, solid grey line represents the calculated diffraction pattern and difference profile is shown at the bottom of the plot. Black vertical marks represent the calculated reflection positions

Table 3. Lattice parameters for the crystalline phase in samples 2 and 8

Lattice parameters of Sm^{3+} doped $Zn_2P_2O_7$ (sample 2)	Lattice parameters of Mn^{2+} doped $Zn_2P_2O_7$ (sample 6)	Lattice parameters of α-$Zn_2P_2O_7$ from reference [4]
space group I2/c	space group I2/c	space group I2/c
a = 20.071(2) Å	a = 20.126(3) Å	a = 20.068(15) Å
b = 8.261(9) Å	b = 8.328(2) Å	b = 8.259(6) Å
c = 9.101(2) Å	c = 9.015(2) Å	c = 9.099(8) Å
β = 106.42(1)°	β = 106.07(1)°	β = 106.35(5)°
V = 1447.3(3) Å^3	V = 1451.8(3) Å^3	V = 1447.1 Å^3

CONCLUSIONS

In our work, we present synthesis and characterisation studies of samarium and manganese doped zinc phosphate materials, we examine the difference between the two doped structures, and we correlate them to the observed photo-luminescence properties.

X-ray diffraction studies of the crystalline phases shows that they are iso-structural with α-$Zn_2P_2O_7$, where samarium and manganese ions most likely substitute for Zn^{2+}. The lattice parameters obtained from the Le Bail calculations for doped zinc phosphate materials are very similar to the lattice parameters of α-$Zn_2P_2O_7$. Deviation of lattice parameters is associated with different ionic radius of Sm^{3+} and Mn^{2+}.

Acknowledgments: *This research was funded by the "Scientific Research" fund at Plovdiv University, Grant № NI 11 HF 007. We are grateful to Mr Zlatkov of Plovdiv University for his help with the powder X-ray diffraction measurements.*

REFERENCES

1. B. Eraiah, S. G. Bhat, *J. Phys. Chem. Solids*, **68**, 581 (2007).
2. R. Seema, P. Suri, P. K. Shishodia, R. M. Mehra, *Solar Energy Materials & Solar Cells*, **92**, 1639 (2008).
3. M. Kawano, H. Takebe, M. Kuwabara, *Opt. Materials*, **32**, 277 (2009).
4. L. Gacem, A. Artemenko, D. Ouadjaout, J. P. Chaminade, A. Garcia, M. Pollet, O. Viraphong, *Solid St. Sci.*, **11**, 1854 (2009).
5. G. Nolze, W. Kraus, *J. Appl. Cryst.*, **29**, 301 (1996).
6. A. Le Bail, H. Duroy, J. L. Fourquet, *Mat. Res. Bull.*, **23**, 447 (1988).
7. A.C.Larson, R.B.von Dreele, The General Structure Analysis System, Los Alamos National Laboratories, Report LAUR 086-748; LANL:Los Alamos, NM, 2000.
8. B. E. Robertson, C. Calvo, *J. Solid St. Chem.*, **1**, 120 (1970).
9. M. A. Petrova, V. I. Shitova, G. A. Mikirticheva, V. F. Popova, E. Malshikov, *J. Solid St. Chem.*, **119**, 219 (1995).
10. L. N. Ji, J. B. Li, J. K. Liang, B. J. Suna, Y. H. Liu, J. Y. Zhang, G. H. Rao, *Journal of Alloys and Compounds*, **459**, 481 (2008).
11. S. M. El-Rabie, *J. Optoelectr. Adv. Mat.*, **9**, 2046 (2007).
12. G. Lakshminarayana, H. Yang, Y. Teng, J. Qiu, *J. Luminesc*., **129**, 59 (2009).
13. G. Belev, G. Okada, D Tonchev, C. Koughia. C. Varoy, A. Edgar, T. Wysokinski, D. Chapman, S. Kasap, *Phys. St. Solidi C*, 8 (9), 2822 (2011).

СИНТЕЗ И ХАРАКТЕРИСТИКА НА ЦИНКОВИ ФОСФАТИ, ДОТИРАНИ СЪС САМАРИЙ И МАНГАН

Г. И. Патронов[1], И. П. Костова[1], З. Й. Стоева[2], Д. Т. Тончев[1,2]

[1] Катедра Химична технология, Пловдивски Университет „Паисий Хилендарски", 4000 Пловдив, България
[2] DZP Technologies Ltd., 22 Signet Court, Cambridge CB5 8LA, United Kingdom

Постъпила на 15 февруари, 2012 г.; приета на 6 април, 2012 г.

(Резюме)

Дотираните със самарий и манган цинк фосфатни композиции са получени чрез високотемпературен синтез от ZnO, $NH_4H_2PO_4$ и Sm_2O_3 (или MnO) в определено съотношение. Изходните реагенти са стрити, смесени и сместа е поставена в керамичен тигел. Синтезът е извършен при температура от 950 °C за 3 часа в муфелна пещ. Пробите са охладени до стайна температура и след това темперирани при 250 °C за 2 часа. Дотирането със самарий и манган варира между 0,03 и 0,28 mol%.

Извършен е рентгеноструктурен анализ, който показва че получената основна кристална фаза е изоструктурна с α-$Zn_2P_2O_7$, в която самариевите и манганови йони най-вероятно заместват частично Zn^{2+}. Това се потвърждава от получените фотолуминесцентни спектри. Определените в резултат на изчислителния метод на Le Bail параметри на кристалната решетка на дотираната цинк фосфатна кристална фаза са много близки до тези на α-$Zn_2P_2O_7$. Тази разлика в параметрите на кристалната решетка се свързва с различния йонен радиус на дотиращите йони Sm^{3+} и Mn^{2+}.

Bulgarian Chemical Communications, Volume 44, Proceedings of the III[rd] National Crystallographic Symposium (pp. 115–119) 2012

The optical influence of Cr^{3+} and P^{5+} ions on the properties of doped $Bi_{12}SiO_{20}$

P. Petkova*

Shumen University "Konstantin Preslavsky", 115 Universitetska street, 9712 Shumen, Bulgaria

Received February 15, 2012; Revised April 20, 2012

The absorption coefficient of $Bi_{12}SiO_{20}$:Cr+P and $Bi_{12}SiO_{20}$:P single crystals is measured in the visible and far IR spectral regions. The influence of P^{5+} ions is determined in double doped sillenite. The energy level diagram of Cr^{3+} is produced. The Jahn-Teller effect is explained in the concrete crystals. The Racah parameters have been calculated also. The magnitude of the composite oscillations is determined in far IR region.

Key words: doped sillenites, Jahn-Teller effect, energy level diagram, composite oscillations.

INTRODUCTION

The sillenite-type $Bi_{12}SiO_{20}$ (BSO) crystals have applications in the dynamic holography, optical information processing, optical phase conjugation and real-time interferometry [1]. This is the reason of the investigation of their optical properties. The determination of the valence and the local symmetry of the involved dopants in the crystal structure is very important for optimization of the synthesis conditions of these materials. That is why the aim of the present work is to be presented the energy level diagram of Cr^{3+} in BSO:Cr+P and to be determined the composite oscillations in the crystals BSO:P and BSO:Cr+P.

EXPERIMENTAL

The investigated BSO crystals, either undoped or doped with Cr, P and co-doped with Cr+P were grown from stoichiometric melts Bi_2O_3:SiO_2 = 6:1 using the Czochralski method under conditions described in detail elsewhere [2]. High purity Bi_2O_3, SiO_2, Cr_2O_3 and P_2O_5 were used for syhthesis and doping. The concentration of P^{5+} is 1.6×10^{20} N/cm^{-1} in BSO:P and the concentration of this ion is 1.13×10^{20} N/cm^{-1} in BSO:Cr+P. The Cr^{3+} ions are inculcated on the co-doped crystal with the concentration 8.1×10^{16} N/cm^{-1}. The thickness of the samples is as follows: $d_{BSO:Cr+P}$ = 0.101 cm, $d_{BSO:P}$ = 0.062 cm.

The experimental set up for measurement of the absorption coefficient in the visible region consists of the following: a halogen lamp with a stabilized 3H-7 rectifier, a SPM-2 monochromator, a system of quartz lenses, a polarizer, a crystal sample holder, and a Hamamatsu S2281-01 detector. The measurements in the far IR region are performed by use of an IRAffinity-1Shimadzu Fourier Transform Infrared Spectrophotometer.

The absorption spectrum is measured in the spectral region 1.55–2.6 eV for BSO:Cr+P (Fig. 1a). The energetic level diagram of Cr^{3+} ion is presented in Fig. 2. The two-phonon absorption of BSO, BSO:P and BSO:Cr+P is shown in the spectral region 400–2000 cm^{-1} (Fig. 3a and 4a). The electron-vibrational interaction in far IR region of these crystals is measured in the spectral region 5000–6000 cm^{-1} (Fig. 3b and 4b).

RESULTS AND DISCUSSION

The absorption coefficient is calculated using the formula: $\alpha = (1/d)\ln(I_0/I)$, where I_0 is the intensity of the incident light, I is the intensity of the passing light and d is the sample thickness (Fig. 1a). The first derivative of the absorption coefficient at photon energy is calculated to be in the 1.5–2.6 eV spectral region (Fig. 1b). The $[d\alpha/d(h\nu)]$ determines only the number of electron transitions in a Cr^{3+} ion and it does not give an exact information about the energy position of these transitions. This is the reason for the calculation of the second derivative of the absorption coefficient $[d^2\alpha/d(h\nu)^2]$ (Fig. 1c).

* To whom all correspondence should be sent:
E-mail: Petya232@abv.bg

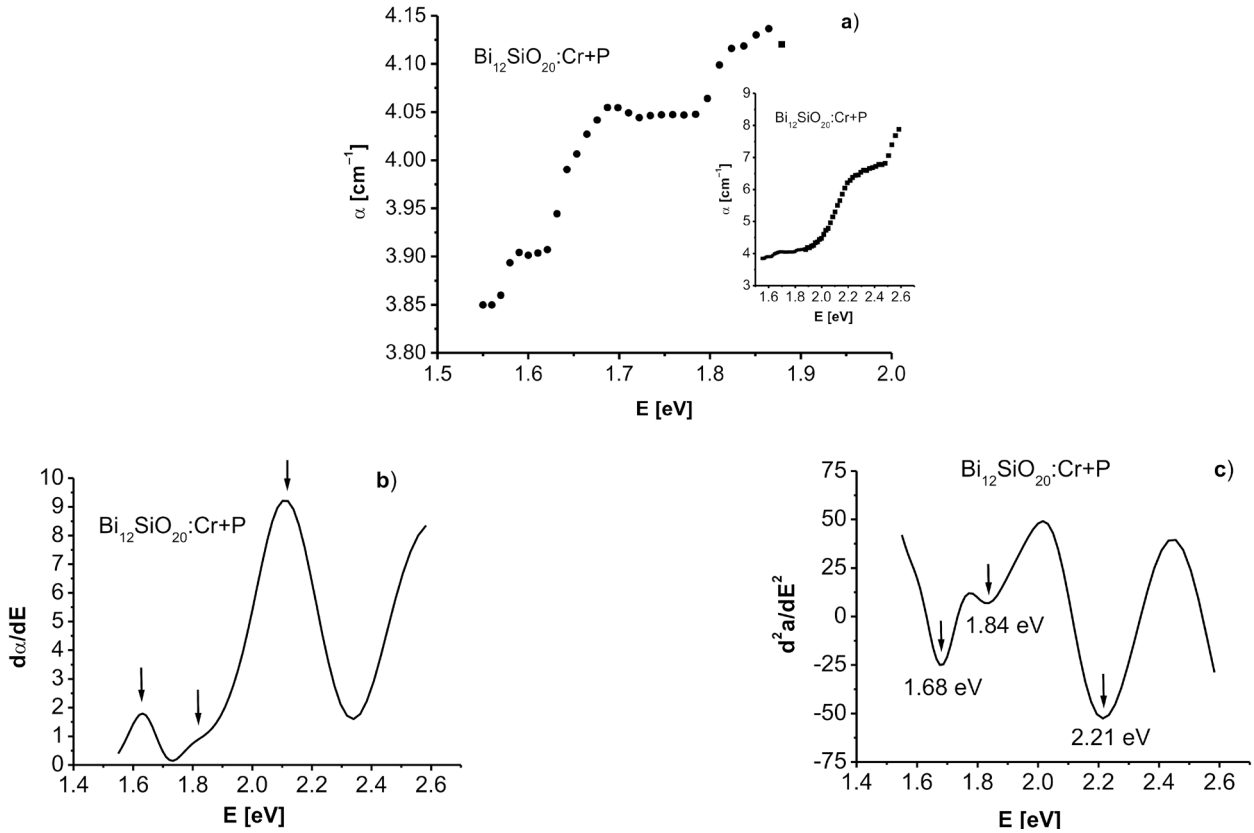

Fig. 1. The absorption coefficient (a), the calculated first derivative of α(E) (b) and the second derivative of absorption coefficient (c) for BSO:Cr+P in the spectral region 1.55–2.6 eV

The d-orbital e_g is split of $e_{\pm2}(\delta)$ and the d-orbital t_{2g} is split of the two orbitals $e_{\pm1}(\pi)$ and $a_1(\sigma)$, when the symmetry changes from T_d to C_{3v} [3] (Fig. 2). The transformation of the symmetry due to the Jahn-Teller effect. The radial parameters Ds and Dt are conditioned by the potential $V_{tetr.}$ [4]. In the case of C_{3v} symmetry the distance between $e_{+2}(\delta)$ and $e_{-1}(\pi)$ is $\Delta_1 = 3Ds - 5Dt = 129$ cm^{-1} = 0.16 eV. This is the distance between the first and the second electronic transition in the Cr^{3+} ion (Fig. 2). The distance between $e_{+1}(\pi)$ and $a_1(\sigma)$ is $\Delta_2 = Ds + 10Dt = 299$ cm^{-1} = 0.37 eV. This is the distance between the second and the third 3d-electronic transition in the chromium (Fig. 2). The values of these two parameters are calculated by our experiment. Thus the values of the parameters Dt and Ds are as follow 21.94 and 79.6. McClure [5] has determined the next parameters $\delta\sigma = \sigma_z - \sigma_{xy} = -1.5Ds - 1.88Dt$ and $\delta\pi = \pi_z - \pi_{xy} = 1.5Ds + 2.5Dt$. The values of these two parameters for the complex $[CrO_4]^{6-}$ are $\delta\sigma = -161$ and $\delta\pi = -65$ and they can be considered as indirect indicators for the antibonding properties of σ- and π- ligands. The literature [6] informs us of the Nephelauxetic parameter β = B (complex)/B (free ion). If the value of β is in the interval 0.54–0.81, it manifests the metal ligand σ bond. The calculation of this parameter for BSO:Cr+P ($\beta = 0.4$) shows that the metal ligand π bond is done. The spin-orbit interaction splits the state $^4T_1$ (^4F) of one sextet (J = 5/2), one quartet (J = 3/2) and one doublet (J = 1/2) (Fig. 2).

The high-frequency part of the spectrum of the two-phonon absorption (Fig. 3 and 4) is given by the phonons related to vibrations of $[SiO_4]$ and $[PO_4]^{3-}$ complexes. The frequency of the two-phonon transition is equal to the sum or the difference of the frequencies ω_i and ω_j of the fundamental oscillations [7]. The oscillations of the crystal lattice are due to oscillations of $[MO_4]$. The tetrahedrons are surrounded by heavy Bi atoms and this is the reason for the absence of absorption structure displacements. That is why Cr does not shift the position of the absorption maxima at 1616 cm^{-1}, 1662 cm^{-1}, 1868 cm^{-1} and 1934 cm^{-1}. The Cr^{3+} ions make the absorption maxima at 1616 cm^{-1} and 1662 cm^{-1} more intensive and the phosphorus removes completely these two maxima in this spectral region. The doping of the crystal lattice with P^{5+} ions leads to the observation of the maxima at 1868 cm^{-1} (965 + 903) and at 1934 cm^{-1} (967 × 2). The Cr^{3+} ions make these two maxima only more intensive. The next two maxima at 1361 cm^{-1} (680.5 × 2) and 1397 cm^{-1} (679 + 718) are due only to the influence

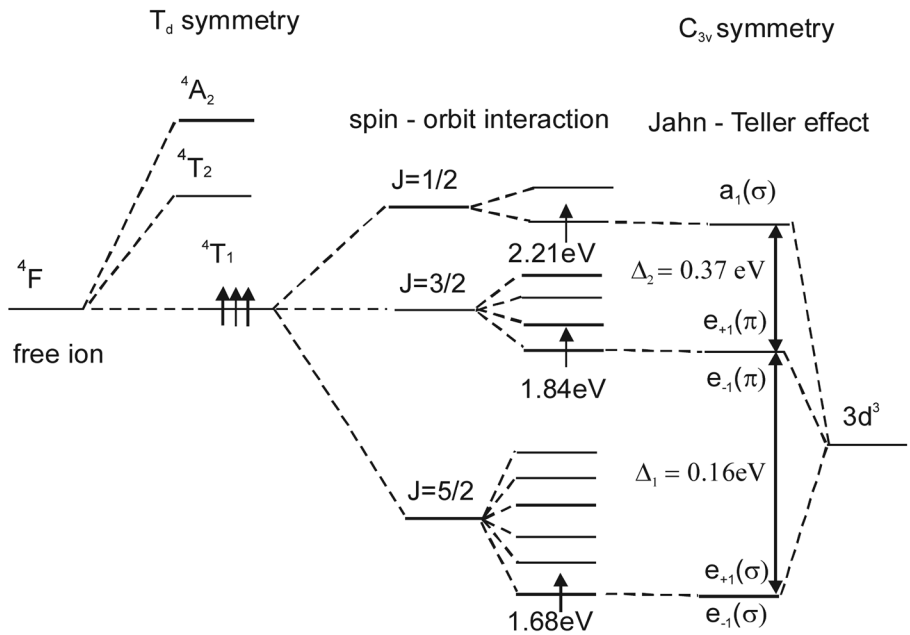

Fig. 2. The energetic level diagram of Cr^{3+} ion

of the phosphorus in the crystal lattice. The first of them consists of the overtone ($T_M \times 2$) and the second one consists of the composite oscillations ($T_M + A_M$). The absorption maximum at 1260 cm^{-1} (668 + 603) consists of the composite oscillations (T_M + F). The phosphorus completely removes this maximum (Fig. 3a) and the chromium makes the same maximum more intensive (Fig. 4a). The

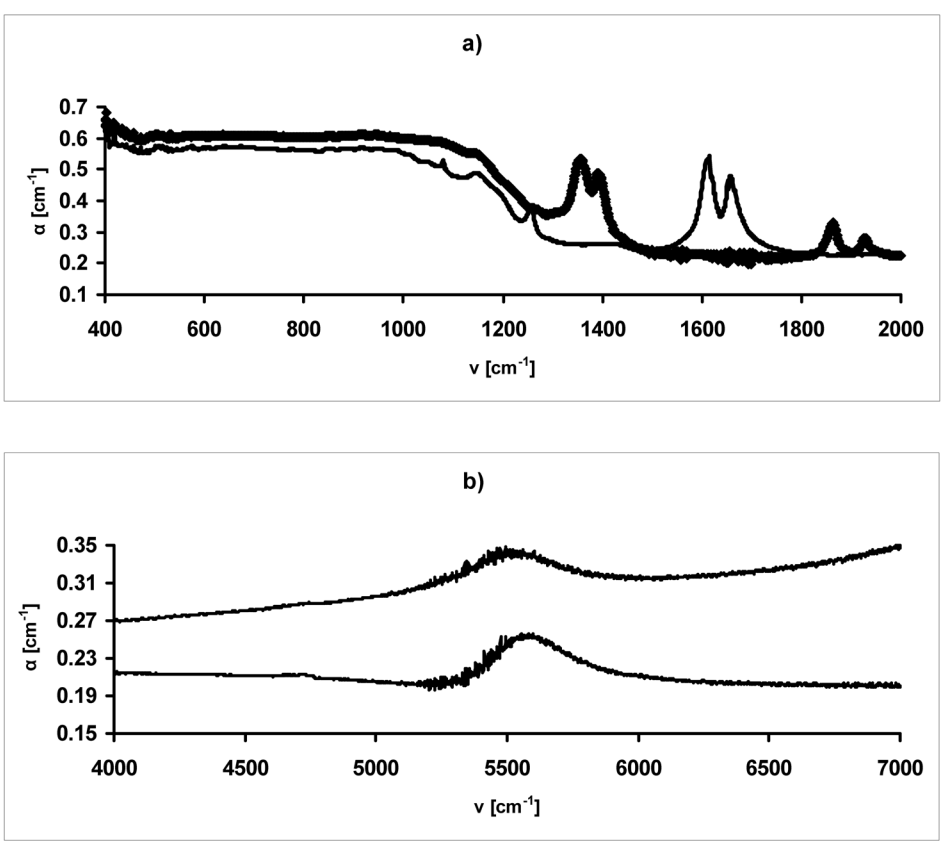

Fig. 3. a) Two-phonon absorption of BSO and BSO:P in the spectral region 400–2000 cm^{-1}; b) electron-vibrational interaction in far IR region of these crystals in the spectral region 5000–6000 cm^{-1}

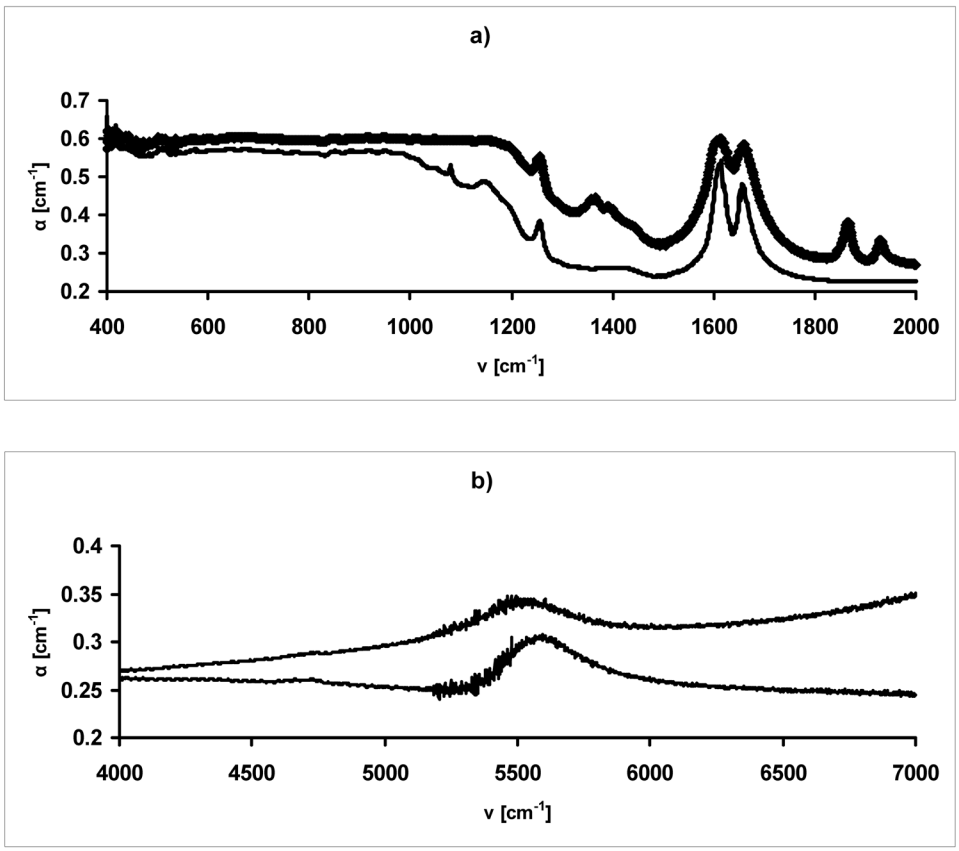

Fig. 4. a) Two-phonon absorption of BSO and BSO:Cr+P in the spectral region 400–2000 cm^{-1}; b) electron-vibrational interaction in far IR region of these crystals in the spectral region 5000–6000 cm^{-1}.

maxima at 5508 cm^{-1} (Fig. 3b and 4b) is determined by the two-phonon transition that is caused by $[SiO_4]$ oscillations. The chromium and phosphorus shifts this maximum to the larger frequencies and the values of the absorption coefficient are lower there.

We can observe direct and indirect mechanism of excitation of the two-phononic transitions. The first of them is determined by the optical anharmonicity and the second one is determined by the mechanical anharmonicity [8]. In the first case, the crystal changes its state when the photon passes through it. This state of the crystal differs from its initial state with the energy equal to twice the energy of the photon. The two-phonon excitation for the molecule MO_4 is due to an anharmonicity and it consists of an overtone and a composite tone. The absorption maximum at 1616 cm^{-1} (827 + 789) consists of the composite oscillations ($T_M + A_M$) (Fig. 3a and 4a). The second absorption maximum at 1662 cm^{-1} (831×2) consists of the overtone oscillation (T_M×2) (Fig. 3a and 4a). The presence of phosphorus leads to the disappearance of these two maxima and the presence of chromium leads to increased intensity of these maxima.

CONCLUSIONS

1. The calculations of the first and the second derivative of α(E) give three electron transitions in Cr^{3+} ions which are inculcated on the tetrahedral complexes.

2. The strong Jahn-Teller effect manifests and the tetrahedral complexes are distorted. The new symmetry of these complexes is C_{3v}.

3. The parameters D_s and D_t are determined. This is important, because we can conclude that the π-bond is stronger than the σ-bond in the tetrahedral complexes. This fact is due to the presence of the P^{5+} ions in the doped and co-doped crystals.

4. The P^{5+} ions have strong influence on the two-phononic transitions in the far IR region for BSO:P and BSO:Cr+P.

REFERENCES

1. G. Raciukaitis, V. Gavryushin, V. Kubertavicius, G. Puzonas, *Jpn. J. Appl. Phys.*, **32**, 645 (1993).
2. I. Ahmad, V. Marinova, H. Vrielinck, F. Callens, E. Goovaerts, *Journal of Applied Physics*, **109**, 083506-1 (2011).

3. G. S. Nikolov, Structure and properties of the coordination compounds, Book Company "Science and Art", Sofia, 1977.
4. R. Drago, Physical Methods in Chemistry, University of Illinois, Urbana, 1981.
5. D. S. McClure, Advances in the Chemistry of Coordination Compounds, Macmillan, New York, 1961.
6. S. Chandra, L. Gupta, *Spectrochimica Acta Part A* **62**, 1125 (2005).
7. V. Burkov, V. Gorelik, A. Egorysheva, Yu. Kargin, *Journal of Russian Laser Research* **22,** 243 (2001).
8. H. Poulet, J. P. Mathieu, Spectres de Vibration et Symétrie des Cristaux, Gordon and Breach, Paris – Londres – New York, 1970.

ОПТИЧНО ВЛИЯНИЕ НА ЙОНИТЕ Cr^{3+} И P^{5+} ВЪРХУ СВОЙСТВАТА НА ЛЕГИРАНИ КРИСТАЛИ ОТ $Bi_{12}SiO_{20}$

П. Петкова*

Шуменски Университет „Епископ Константин Преславски", ул. „Университетска" № 115, 9712 Шумен, България

Постъпила на 15 февруари, 2012 г.; приета на 20 април, 2012 г.

(Резюме)

Измерен е коефициентът на поглъщане на единични кристали от $Bi_{12}SiO_{20}$, легирани с фосфор и двойно легирани с хром и фосфор във видимата и в далечната ИЧ област. Определено е влиянието на йоните P^{5+} в двойно легирания силенит. Представена е енергетичната диаграма на нивата на йона Cr^{3+}. Обяснен е ефектът на Ян-Телер в конкретните кристали. Изчислени са също и параметрите на Рака. Определен е директният и индиректният механизъм на двуфононното поглъщане в далечната ИЧ област.

Bulgarian Chemical Communications, Volume 44, Proceedings of the III[rd] National Crystallographic Symposium (pp. 120–123) 2012

The electron-phonon interaction in $Bi_{12}SiO_{20}$ doped with Fe^{3+}, Cr^{3+} and P^{5+} ions

P. Petkova*

Shumen University "Konstantin Preslavsky", 115 Universitetska street, 9712 Shumen, Bulgaria

Received February 15, 2012; Revised April 23, 2012

The absorption coefficient of $Bi_{12}SiO_{20}$:Fe, $Bi_{12}SiO_{20}$:P and $Bi_{12}SiO_{20}$:Cr+P single crystals is measured in the spectral region of Urbach's rule (2.5–3.1 eV) at room temperature. The parameters of electron-phonon interaction, Urbach's energy and the constants of Urbach's rule are calculated. It is established the behavior of the donors Fe^{3+} and Cr^{3+} and this of the acceptor P^{5+} in Urbach's rule region.

Key words: doped sillenites, Urbach's rule, electron-phonon interaction, Urbach's energy.

INTRODUCTION

The crystals $Bi_{12}SiO_{20}$ are piezoelectric, electro- and magnetooptic materials. The optical activity, photoconductivity and photorefractivity are a characteristic for BSO and their combination allow the use of these materials in various acousto and optoelectronic devices (piezo sensors, space-time light modulators etc.) [1, 2, 3, 4]. The doping of these crystals with different impurities change their physical and chemical properties. Therefore, the electron-phonon interaction is discussed in doped BSO and then it is compared with the same interaction in these materials in the frame of this work.

EXPERIMENTAL

The investigated BSO crystals, either undoped or doped with Cr, P and co-doped with Cr+P were grown from stoichiometric melts Bi_2O_3:SiO_2 = 6:1 using the Czochralski method under conditions described in detail elsewhere [5]. High purity Bi_2O_3, SiO_2, Cr_2O_3 and P_2O_5 were used for syhthesis and doping. The concentration of P^{5+} is 1.6×10^{20} N/cm^{-1} in BSO:P and the concentration of this ion is 1.13×10^{20} N/cm^{-1} in BSO:Cr+P. The Cr^{3+} ions are inculcated on the BSO:Cr with the concentration 8.6×10^{18} N/cm^{-1} and these ions are inculcated on the co-doped crystal with the concentration 8.1×10^{16} N/cm^{-1}. The thickness of the samples is as follows: $d_{BSO:Cr+P}$ = 0.101 cm, $d_{BSO:P}$ = 0.062 cm.

The Fe^{3+} ions were inculcated on the crystal lattice as Fe_2O_3 oxide. The concentration of Fe dopant $1.4x10^{18}$ N/cm^{-3} into the grown crystal was determined by flame (Zeeman 3030) and electro-thermal atomic (Varian 240) absorption spectrometry. The thickness of BSO:Fe is $d_{BSO:Fe}$ = 0.152 cm and the thickness of the undoped sample is d_{BSO} = 0.04 cm. The experimental set up for measurement of the absorption coefficient in the visible region consists of the following: a halogen lamp with a stabilized 3H-7 rectifier, a SPM-2 monochromator, a system of quartz lenses, a polarizer, a crystal sample holder, and a Hamamatsu S2281-01 detector.

The experimental dependence lnα(E) for all the investigated crystals is presented in Fig. 1. Urbach's rule for undoped and doped BSO in the spectral region 2.5–3.1 eV is shown in Fig. 2. Urbach's energy for the undoped and doped $Bi_{12}SiO_{20}$ is presented in Fig. 3.

RESULTS AND DISCUSSION

The behaviour of the absorption coefficient α has been investigated at the absorption edge using the Urbach's formula $\ln\alpha = A+B(\hbar\omega/T)$, where A and B are the constants, T is the temperature. The constant B is expressed by the dependence $B = \sigma(T)/k$, where $\sigma(T)$ is the parameter characterizing the slope of the absorption edge, k is the Boltzmann constant. The value of $\sigma(T)$ is 0.27 for $Bi_{12}SiO_{20}$ and $\sigma(T)$ var-

* To whom all correspondence should be sent:
E-mail: Petya232@abv.bg

Table 1. The parameters which are characterized the Urbach's rule region

sillenites at T = 300 K	σ	σ_0	g	W_d [meV]	E_0 [meV]	σ_a[cm^2]
$Bi_{12}SiO_{20}$	0.27	0.27	2.47	96	301	–
$Bi_{12}SiO_{20}$:Fe	0.32	0.32	2.08	81	239	1.83×10^{-18}
$Bi_{12}SiO_{20}$:Cr+P	0.52	0.52	1.28	50	154	7.91×10^{-17}
$Bi_{12}SiO_{20}$:P	0.88	0.88	0.76	29	97	4.87×10^{-17}

ies from 0.32 to 0.88 in the case of doped $Bi_{12}SiO_{20}$ (Table 1). The BSO:Fe has a value of σ(T) close to that of undoped sample. The value of the parameter σ(T) is biggest for P^{5+} ions. This is the reason for the bigger value of this parameter for co-doped BSO.

On the other hand, we have the next equation $W_d = kT/\sigma$ [6]. The magnitude W_d describes the broadening of the absorption edge due to the dynamic disorder. When the temperature is higher, the absorption edge is wider due to the dynamic disorder in the crystal lattice. W_d = 96 meV for undoped BSO and W_d = 29–81 meV for doped BSO (Table 1). Therefore, we can generalize that the absorption edge of BSO:P has smallest dynamic disorder in the crystal lattice due to the phosphorus. Therefore this fact, the dynamic disorder has small value in BSO:Cr+P. The Fe^{3+} leads to the large dynamic disorder in the doped sillenites. The σ(T) and W_d are calculated at room temperature (T = 300 K).

The approximation of the experimental data shows that $\sigma(T) = \sigma_0(2kT/h\nu_0)\text{th}(h\nu_0/2kT)$, where $h\nu_0$ is the energy of the effective phonons, strongly interacting with photons, and σ_0 is the high temperature constant [7]. The magnitude $h\nu_0$ for our investigated crystals corresponds to the energy $h\nu_0$ = 31.7 meV of the longitudinal optical phonons (ω = 257 cm^{-1}) which are observed in the IR absorption spectra of BSO [8].

In our case, the obtained values of σ_0 are as follows: σ_0 = 0.27 ($Bi_{12}SiO_{20}$) and σ_0 = 0.32 – 0.88 (doped $Bi_{12}SiO_{20}$) (Table 1). When we compare the values of σ_0 for our samples with the values of the same constant, obtained in [9], we can summarize that our undoped sillenite has a small surplus of Bi ions in the crystal lattice.

The dependence $g = 2/3\sigma_0$ determines the strength of the electron-phonon interaction [8]. When g > 1, the electron-phonon interaction is strong. This strength has a highest value (g = 2.47) for undoped BSO and g = 0.76 – 2.08 for doped BSO (Table 1). Therefore, we can conclude that the impurity ions reduce this interaction in the crystal lattice. The P^{5+} ions make the electron-phonon interaction very weak in the sillenites. Therefore the electron-phonon interaction is a weaker in BSO:Cr+P. On the other hand, the Fe^{3+} ions lead to the strong electron-phonon interaction in BSO:Fe.

The Urbach's region for undoped BSO is almost the same as for the sample BSO:Fe (Fig. 2). The Urbach's region is shifted (2.8–3.1 eV) for BSO:P

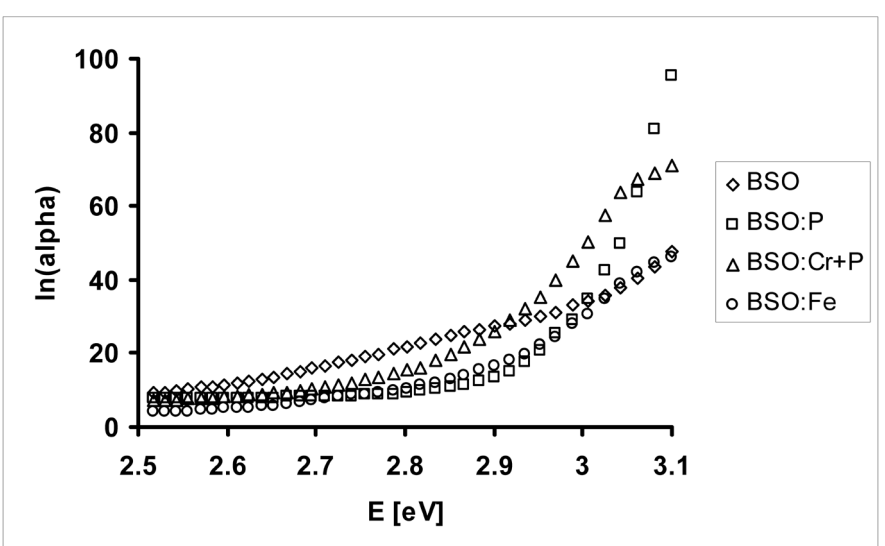

Fig. 1. The experimental dependence lnα(E) for all the investigated crystals

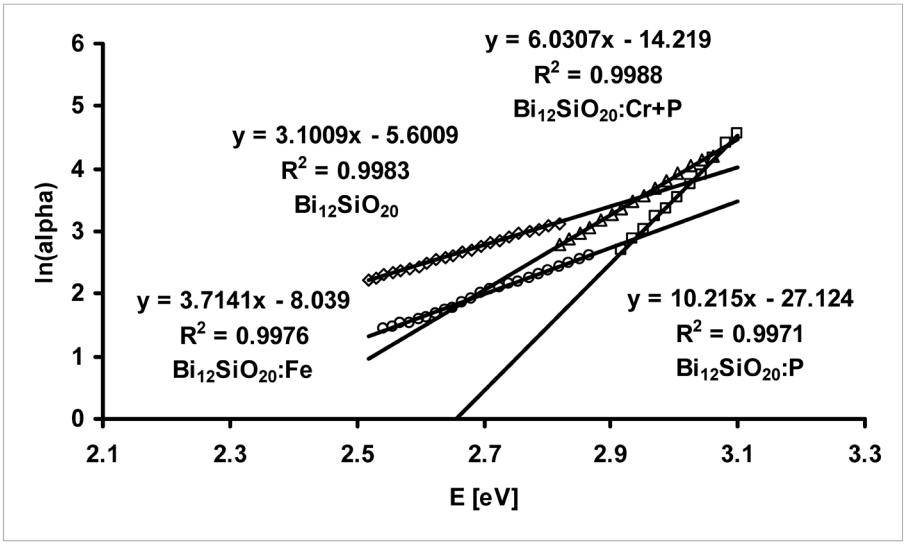

Fig. 2. Urbach's rule for undoped and doped BSO in the spectral region 2.5–3.1 eV

and BSO:Cr+P. It is interesting that the phosphorus shifts the Urbach's region to the biggest energies. Therefore the absorption edge is shifted to the smallest wavelengths for BSO:P (Fig. 1).

The Urbach's energy is connected with the carrier impurity interaction, the carrier–phonon interaction and the structural disorder [10]. That is why this energy is calculated by the formula Eu = α(E)/(dα/dE). The Eu is not a constant for undoped and Fe doped crystals in the spectral region 2.5–3.1 eV. The values of the Urbach's energy of the BSO:Fe are smaller than the Eu of the BSO (Fig. 3a). The parameter $E_0 = 1/[d(\ln\alpha)/d(h\nu)]$ is known as Urbach's slope [11]. We can see the values of E_0 at T = 300 K in Table 1 for undoped, doped and co-doped BSO. Next step in the calculations is the determination of

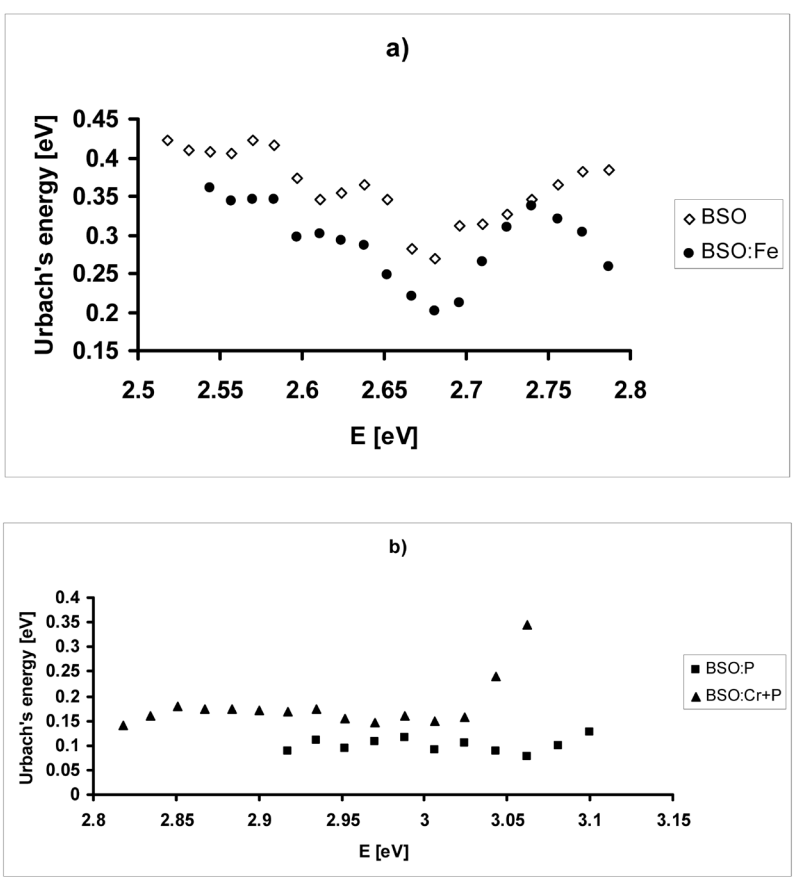

Fig. 3. Urbach's energy for the undoped and doped $Bi_{12}SiO_{20}$

the cross-section of the impurity absorption [12]. It is very important to establish how the radiation is absorbed by the impurity ions in the crystals. The total cross-section σ_a of the impurity absorption is defined by the integration within the absorption band of the impurity ions

$$\sigma_a = (1/N)\int_{E_1}^{E_2} \alpha(E)dE ,$$

where N is the number of the impurity ions in the unit volume, α is the impurity absorption coefficient typical of an energetic interval from E_1 to E_2. For the investigated crystals here E_1 = 2.5 eV and E_2 = 3.1 eV. The cross-section σ_a can vary significantly from one absorption band to another. The value of σ_a is smallest for the crystal BSO:Fe and it is biggest for the co-doped BSO (Table1).

CONCLUSIONS

1. The parameter σ has the biggest value for BSO:P, but the electron-phonon interaction is the lowest in this case. The dynamic disorder in the crystal lattice is the smallest again in BSO:P. The value of the parameter E_0 is the smallest for the same crystal.

2. The acceptor P^{5+} has the greatest impact on the value of the cross-section σ_a.

3. The Urbach's energy for BSO:Fe in the spectral region 2.5–2.8 eV follows the shape of this energy for BSO. The shape of the Urbach's energy for BSO:Cr+P and BSO:P is the same.

REFERENCES

1. T. Panchenko, K. Strelets, *Condensed Matter Physics*, **10**, 289 (2007).
2. D. Nesheva, Z. Aneva, M. Gospodinov, *J. Phys. Chem. Solids*, **54**, 857 (1993).
3. D. Nolte, *Condensed Matt.* News, **1**, 17 (1992).
4. N. Vainos, M. Gower, *Opt. Lett.*, **16**, 363 (1991).
5. I. Ahmad, V. Marinova, H. Vrielinck, F. Callens, E. Goovaerts, *Journal of Applied Physics*, **109**, 083506-1 (2011).
6. V. Kunets, N. Kulish, Vas. Kunets, M. Lisitsa, *Semiconductor Physics, Quantum Electronics & Optoelectronics* **5,** 9 (2002).
7. M. Kurik, *Phys. Status Solidi (a)* **8,** 9 (1971).
8. W. Woidovsky, T. Lukasiewicz, W. Nazariwicz, J. Zmija, *Phys. Status Solidi (b)* **94**, 649 (1979).
9. T. Panchenko, S. Kopylova, Yu. Osetskié, *Solid State Physics* **37**, 1415 (1995).
10. Sk. Faruque Ahmed, Myoung-Woon Moon, Kwang-Ryeol Lee, *Thin Solid Films* **517**, 4035 (2009).
11. I.A. Vainshtein, A.F. Zatsepin, V.S. Kortov, *Glass Phys. Chem.* **25**, 67 (1999).
12. Optical Properties of Condensed Matter and Applications, Edited by Jai Singh, John Wiley & Sons, 2006.

ЕЛЕКТРОН-ФОНОННО ВЗАИМОДЕЙСТВИЕ В $Bi_{12}SiO_{20}$, ЛЕГИРАН С ЙОНИТЕ Fe^{3+}, Cr^{3+} И P^{5+}

П. Петкова*

Шуменски Университет „Епископ Константин Преславски“, ул. „Университетска“ №115, 9712 Шумен, България

Постъпила на 15 февруари, 2012 г.; приета на 23 април, 2012 г.

(Резюме)

Измерен е коефициентът на поглъщане на единичните кристали $Bi_{12}SiO_{20}$:Fe, $Bi_{12}SiO_{20}$:P и $Bi_{12}SiO_{20}$:Cr+P в спектралния диапазон на правилото на Урбах (2,5–3,1 eV) при стайна температура. Изчислени са параметрите на електрон-фононното взаимодействие, енергията на Урбах и константите, участващи в правилото на Урбах. Установено е влиянието на донорите Fe^{3+} и Cr^{3+}, както и това на акцептора P^{5+} в областта на Урбах.

Bulgarian Chemical Communications, Volume 44, Proceedings of the III[rd] National Crystallographic Symposium (pp. 124–130) 2012

Classification of step bunching phenomena

V. Tonchev

Institute of Physical Chemistry, Bulgarian Academy of Sciences, 1113 Sofia, Bulgaria

Received March 20, 2012; Revised May 15, 2012

The classification of bunching of straight steps on vicinal crystal surfaces identifies two types according to the behavior of the minimal step-step distance in the bunch l_{min} with increasing the number of steps N in it. In the B1-type l_{min} remains constant while in the B2-type it decreases. Both types are illustrated by new results for well-known models. The precise numerical analysis is aimed at the intermediate asymptotic regime where self-similar spatiotemporal patterns develop. In the model of Tersoff et al. the regular step train is destabilized by step-step attraction of infinite range. It is shown that this model belongs to the B1-type and the same time-scaling exponent of 1/5 for N, terrace width and bunch width is obtained. An extended set of scaling exponents is obtained from the model of S.Stoyanov of diffusion-limited evaporation affected by electromigration of the adatoms. This model is of B2-type and shows a systematic shift of the exponents with respect to the predictions of the hypothesis for universality classes in bunching thus requiring further modification of it.

Key words: Vicinal crystal surface, Step-step interactions, Step bunching, Modeling and simulation, Scaling and universality, classification.

RETROSPECTIVE

The most intensive studies of the bunching of straight steps on vicinal crystal surfaces were initiated by the discovery of Latyshev et al. [1] – equally spaced steps gather in groups in result of resistive DC-heating of Si(111)-vicinals (surfaces of a monocrystal that are slightly deviated from the (111)-plane and the result is sequence of straight equidistant monoatomic steps). A theoretical explanation of the phenomenon was suggested by Stoyanov [2] who identified as source of the instability the electromigration of Si-adatoms which causes bias of the surface diffusion and thus uneven contribution of the two terraces adjacent to a step to its motion. In these initial years the theoretical efforts were focused on understanding and predicting the initial stages of the process – the way the instability arises and grows further. More recently were addressed [3–5] also the late stages of the process when the instability is well developed and enters into the so called intermediate asymptotic regime [6] in which the surface morphology becomes self-similar both in space and in time. The adequate description of this regime is given in terms of scaling laws which include a combination of model parameters, length-scale(s) of the phenomenon and time. There are several reasons for the continuing interest in bunching studies: (i) the so called step flow growth mode is the important one from technological point of view; (ii) bunched surfaces are nowadays used as templates for bottom-up strategies to grow nanostructures [7]; (iii) this is a clear and very rich case of surface self-organization after the system is driven out of equilibrium [8] and opposite tendencies compete – surface destabilization due to various kinetic or thermodynamic factors opposed by the omnipresent step-step repulsion which favors the equidistant step distribution.

CLASSIFICATION

The classification was introduced recently by Staneva et al. [9]. The step bunching phenomena are classified according to the behavior of the minimal step-step distance in the bunch l_{min} with increasing the number of step N in it as shown in the Table 1.

There are several reasons that hindered formulation of the classification in the years: (i) the communities that carry out active research on the two types practically do not overlap; (ii) the property of constant l_{min} was not explicitly recognized in the model studies of the B1-type [10, 11]; (iii) the number of necessary length-scales to describe the step bunch-

* To whom all correspondence should be sent:
E-mail: tonchev@ipc.bas.bg

Table 1.

When increasing the number of steps N in the bunch ..	.. the minimal step-step distance in the bunch l_{min} ..	Number of characteristic length-scales
B1-type	.. remains constant	1
B2-type	.. decreases	2

ing thoroughly was not instituted firmly in the protocol for the B2-type studies. In what follows I describe briefly the computational protocol and then present the two types with numerical results from well-known models stressing on the new findings.

Numerical procedure. – There are two general ways to obtain the system of ordinary differential equations (ODE's) for the velocities of steps. The usual one, of extended Burton-Cabrerra-Frank type (essentially 1D approach), is to deduce these by rigorous considerations - solving the proper diffusion equation on a single terrace with diffusion bias entering the equation, i.e. the drift of adatoms due to electromigration, and/or the asymmetry in kinetics of attachment/detachment entering the boundary conditions (BC) on the steps through unequal kinetic coefficients. The step-step repulsion also enters the BC modifying the equilibrium (reference) concentrations used to calculate the actual deviation from equilibrium. Step velocity is proportional to the diffusive fluxes entering the step from both terraces. Another approach is to construct velocity equation(s) *ad hoc* [12]. Once a system of ODE's is defined it is solved numerically by a suitable routine, usually fourth order Runge-Kutta but other modern integration strategies could be adopted as well [13]. The non-trivial part of the study is to design and implement a procedure to recognize the evolving surface pattern and to extract the information needed [14, 15]. Usually not less than 1000 steps (=equations) are included in the calculation in order to ensure smoothness of the quantities that describe the evolution of the system. Our computational protocol [14, 15] consists of gathering statistics based on the step-step distances with two monitoring schemes (MS) running simultaneously with the important definition in the background of what is *bunch distance*. We define a step-step distance to be a *bunch distance* always when it is smaller than the initial (vicinal) one, usually denoted by l. Other choices are also possible[16] but these are not justified by physical considerations. The first monitoring scheme, MS – I, is designed to follow the temporal evolution of the system. It calculates at every time step of the integration the number of bunches in the system and then the average number of steps in bunch N, the average bunch width L_b, average terrace width between bunches TW, etc. plus an individual quantity – the global minimal step-step distance in the system l_{min_g}. These quantities are written in files versus time. The second monitoring scheme, MS - II, cumulates separately information for any bunch size – average bunch width L_b, average minimal step-step distance in the bunch l_{min}, first and last step-step distances l_1 and l_{last}, see Figures 1 and 6 for some definitions, that would appear during the whole simulation and at every time step this information is updated and written in files versus the bunch size. Thus at every time step integral information is available from MS - II that reflects the whole surface evolution up to this moment. The coincidence of the results from the two schemes for a matching dependence as the bunch width vs. bunch size is considered non-trivial and mutual validation of the two schemes, see Figure 7. Mostly used are the N vs. time dependence from MS – I (plus bunch width L_b vs. time when studying B2-type) and l_{min} vs. N from MS – II. The combination of the two schemes could be used also for structuring the data from experiments in order to plot it in the same coordinates as the data from calculations and make a direct comparison.

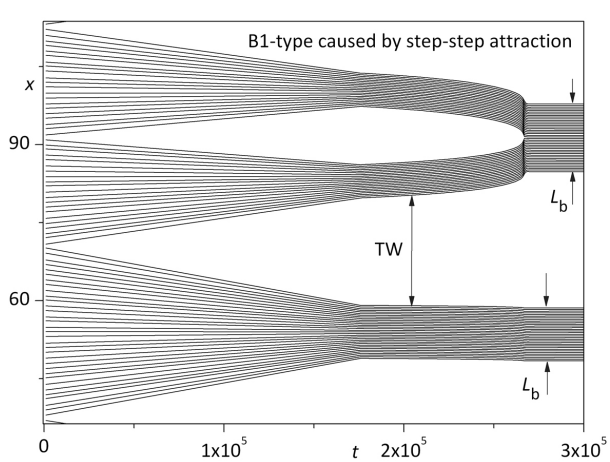

Fig. 1. TE-model, step trajectories as obtained when solving numerically the equations for step velocity [10]. It is seen that when two bunches coalesce the resulting bunch has a width being the sum of the bunch widths before the coalescence

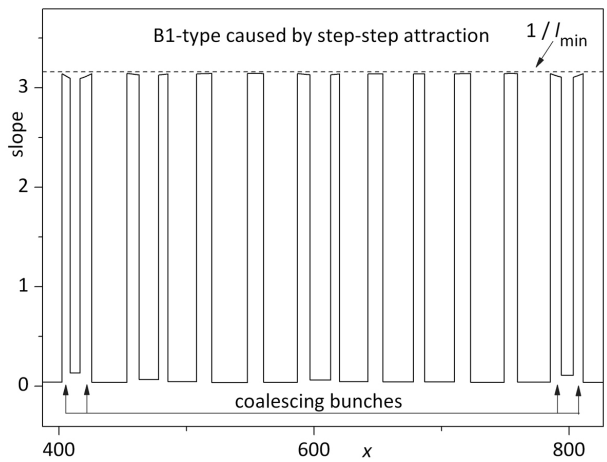

Fig. 2. TE-model, surface profile (inverse of the step-step distances) for well-developed instability. The width of the 'peaks' is the bunch width L_b. Interesting dynamic phenomenon is observed – when two bunches coalesce the slope of each is lower from the side of the other bunch (the double arrows from the bottom)

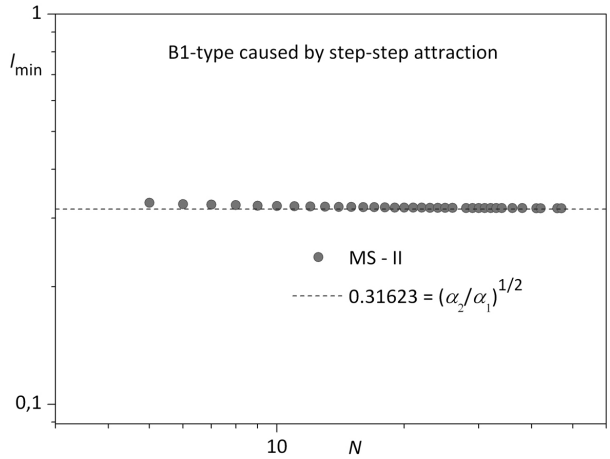

Fig. 3. TE-model, MS-II, the minimal step-step distance in the bunch, measured in units of initial vicinal distance l, is not function of the number of steps in the bunch N and thus the model is attributed to the B1-type

B1-type – Examples for experimental systems that show B1-type step bunching are the Si(113) surface, high temperature annealing of TaC(910) [17], vicinal Ag(111) in electrolyte [18], etc. I will illustrate this type with results from the model of step bunching due a step-step attraction of infinite range, proposed by Tersoff et al.[10], we will call this TE-model. The other limiting case of zero-range step-step attraction called 'sticky steps' was introduced quite recently [19, 20] and the surface slope behavior in this model is still under investigation. The physical origin of the step-step attraction in the TE-model is identified as the strain cumulated during heteroepitaxial growth which remains uncompensated at the steps and forms force monopoles. As a result instability develops mediated by mass diffusion which breaks the equidistant step distribution, thus being a vicinal analogue to the Asaro-Tiller-Grinfeld instability [8]. The equations for step velocity are published[10] and here only a comment is provided instead – this model and two more [12, 21] have a specific property of the equations, namely, they consist of two mathematically identical terms with opposite effect, destabilizing and stabilizing, and with different notation of the parameters. The second term introduces the effect of the omnipresent step-step repulsion and the first one – the effect of the emerging step-step attraction. In the original model of Tersoff et al. [10] the energy of step-step repulsion decays inversely proportional to the square of the step-step distance and the energy of step-step attraction increases with the logarithm of the step-step distance – the bigger is the distance between the steps, the larger is the uncompensated strain. The results are obtained with same values of the parameters: $\alpha_1 = 10$ (destabilizing), $\alpha_2 = 1$ (stabilizing), the first one contains the magnitude of the step-step attraction and the second one – the magnitude of step-step repulsion. In Figure 1 are plotted the step trajectories and some of the elements of the monitoring schemes are marked. Figure 2 contains data on the surface profile for well-developed instability – as seen the slope is constant along the surface while on Figures 3 and 4 it is seen that the slope does not change with the increase of the bunch size N and in time. Figure 4 demonstrates that only one

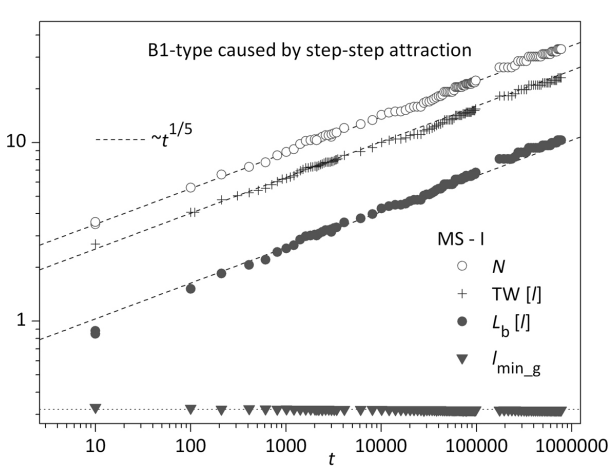

Fig. 4. TE-model, MS-I, the number of steps in the bunch N, the terrace width TW and the bunch width L_b share the same time-scaling exponent of 1/2, hence only one length-scale is needed what is typical for the B1-type. Data from several runs are used

time-scaling exponent is found for three different quantities – N, terrace width and bunch width and it is 1/5, different from 1/4 as found by Tersoff et al. [10]. The reasons for this difference are still unclear and subject to further studies.

B2-type – Some typical examples for experimental systems that show B2-type of step bunching, besides the most studied one – that of evaporating Si(111)-vicinals [1], are the KDP crystal growth [22, 23] and SiC epitaxial growth [24] although the latter shows quite rich bunching behavior and attribution to the B1-type is also possible after careful analysis of the experimental data using our systematic approach. I will illustrate this type with results on the model of diffusion limited vicinal evaporation already studied by Stoyanov and Tonchev [3] (called here EvEm-model) and the reason for this revisit is that the original study was restricted by the computational power at that time to the method of *single* bunch. Later on specially designed experiments [25] have shown that the process of Si(111) vicinal evaporation is actually controlled by the diffusion of the Si-adatoms on the terraces rather than by the attachment/detachment kinetics at the steps as suggested by a later study [16]. Very recently sophisticated experimental setup was developed [26] that would permit to study the time dependencies describing thoroughly the bunching process. As usually, systematic numerical studies play important role in planning experimental strategy and understanding its results.

The equations for step velocity are rather complex [3] and I will not adduce them here. Also, the original values of the parameters are preserved and only the parameter that contains the magnitude of the step-step repulsion is increased approximately thrice in order to permit faster computations. The reason is that in the method of *single bunch* used [3] one deals with systems of maximum 60–70 equations (steps) while in the present computation are included 1000 steps. The initial vicinal geometry comprises steps randomly deviated from their equidistant positions in order to permit development of the instability in a way similar to the real one. As for the previous, TE-model, these calculations include only the value n=2 from the step-step repulsion law, i.e. the repulsion energy decays with the inverse square of the step-step distance. The bunching process in the EvEm model is illustrated qualitatively by the step trajectories, Figure 5, and surface slope, Figure 6, and quantities that are monitored are marked.

Next are shown the studies of the size-scaling (MS-II), first of the bunch width L_b, Figure 7, and then of the minimal, first and last step-step distance, Figure 8. Together with the studies of the time-scaling (MS-I) of the relevant quantities, Figure 9, these

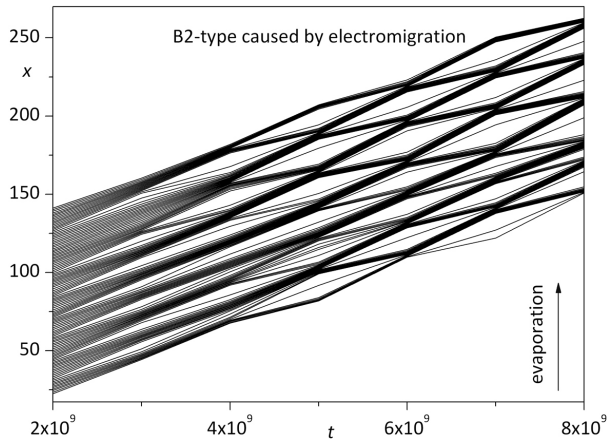

Fig. 5. Step trajectories in the model of diffusion limited vicinal evaporation affected by electromigration of the adatoms (EvEm-model). Every step moves in the up direction mediating the vicinal surface evaporation. It is well seen how bunches split in two

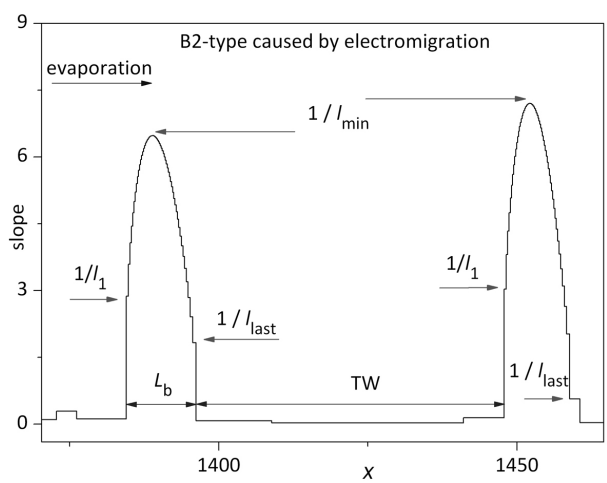

Fig. 6. EvEm-model, surface profile for well developed instability. With arrows are shown the places where appear some of the quantities used by the monitoring schemes. The higher slope is in the bunch with more steps (the right one), hence B2-type

scaling exponents form a set that could be compared with the predictions of the universality classes in bunching hypothesis [16, 27]. Here I will only stress that the comparison leads to the following conclusion: the set of *obtained* exponents with n=2, corresponds to the originally *predicted* for n=0 and thus is systematically shifted down in n with 2. There is still no explanation for such a shift and thus the present results are a challenge for further modification of the continuum equation which reflects the hypothesis of universality.

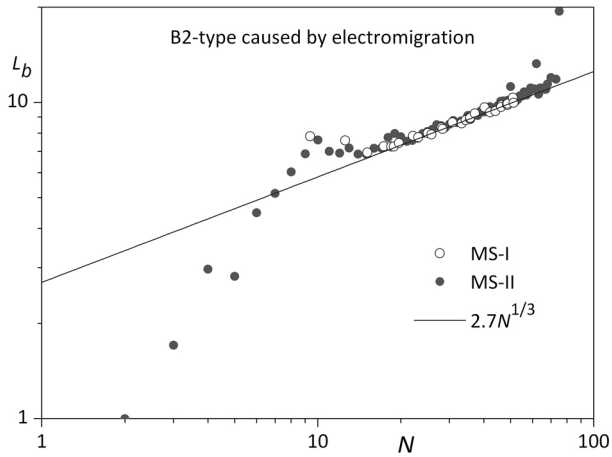

Fig. 7. EvEm-model, bunch width L_b versus number of steps N from both monitoring schemes. The slope of the guiding-eye line corresponds to size-scaling exponent of 1/3 (note the log-log character of the plot)

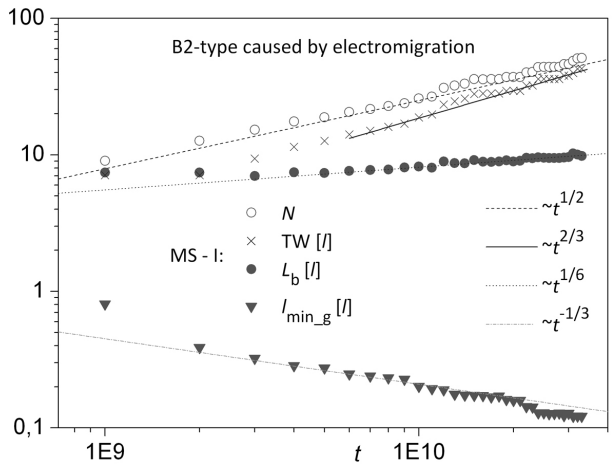

Fig. 9. EvEm-model, MS-I, time dependencies of the number of steps N, terrace width TW, bunch width L_b, and the globally minimal step-step distance l_{min_g}. The slopes of guiding-eye lines correspond to time-scaling exponents of 1/2, 2/3, 1/6 and –1/3, respectively

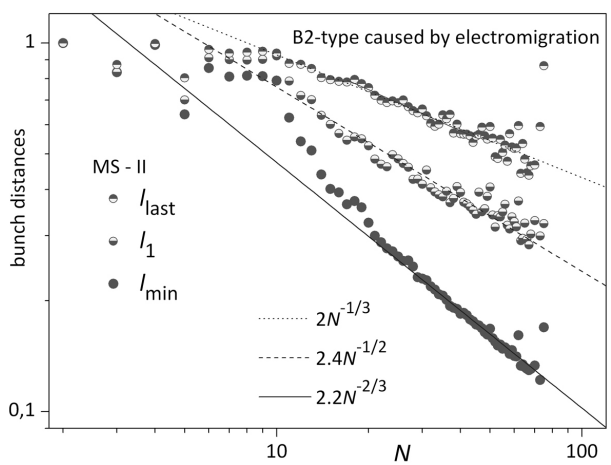

Fig. 8. EvEm-model, MS-II, bunch distances - minimal, first and last, versus number of steps N as obtained from MS-II. The slopes of the guiding eye lines correspond to size-scaling exponents of –2/3, –1/2 and –1/3 correspondingly. Note that also the last bunch distance decreases when N increases

Further comment on the results in this subsection is needed concerning the time-scaling exponent of the globally minimum step-step distance which is –1/3 as shown on Figure 9. The same exponent could be obtained if plugging in $t^{1/2}$ instead of N (time-scaling of N, shown on Figure 6) in the size-scaling relation of l_{min} (as found on Figure 8):

$$l_{\min} \sim N^{-2/3} \sim \left(t^{1/2}\right)^{-2/3} \sim t^{-1/3}$$

Thus one could argue that only the resulting scaling is enough to describe the spatiotemporal evolution of the vicinal surface but I will show in a subsequent study that the scaling above is invariant across two different B2-type models while the other scaling relations – in particular the size-scaling of l_{min} and the time-scaling of N still distinguish unambiguously between the models.

PERSPECTIVE

The nearest future of our computational studies of step bunching phenomena is to find the exact time-scaling of the number of steps in the bunch N, including the pre-factor, for the three models of B1-type available, all these having mathematically identical stabilizing and destabilizing terms in the equations for step velocity. As a preliminary study shows [21] namely the time-scaling of N could distinguish between the models and thus serve as a reference frame to plan, carry and understand experiments. In progress are also studies of three models of B2-type: diffusion and attachment-detachment limited evaporation affected by electromigration of the adatoms and a minimal model called MM0 which has the same destabilizing part in the equation(s) for step motion as in the latter but the stabilizing part is restricted to depend only on the widths of the two adjacent to the step terraces. Third direction of our studies comprises models that would eventually lead to what we now call B2m-type – simultaneous bunching *and* meandering (the steps are

no more straight but wavy or *meandered*), which phenomenon is still anti-paradigmatic in a sense that in the paradigm the preconditions for bunching – normal Ehrlich-Schwoebel effect in (vicinal) evaporation *or* inverse Ehrlich-Schwoebel effect in (vicinal) growth, and meandering – normal Ehrlich-Schwoebel effect in growth *or* inverse Ehrlich-Schwoebel effect in evaporation cannot be realized simultaneously (downstep electromigration of the adatoms destabilizes both growing and evaporating vicinal surfaces). Nevertheless, there is sufficient experimental evidence both on metal [28, 29] and semiconductor [30] vicinal surfaces for simultaneous bunching *and* meandering although the instability scenario is somewhat different. The bunches of B2m-type are expected to have their minimal step-step distance (largest slope) in the beginning of the bunches [14] rather than in the middle as seen on Figure 6 for the B2-type. Quite recently similar type of behavior was reported [31] in a KMC study of evaporating vicinal surface of GaN(0001).

Acknowledgments: *Our present HPC facility MADARA was built with the prevailing financial support from the Bulgarian National Science Fund through grant No. ДОО02-52/RNF01/0110. Some financial support from the same fund through IRC CoSiM grant is also appreciated.*

REFERENCES

1. A. V. Latyshev, A. L. Aseev, A. B. Krasilnikov, S. I. Stenin, *Surf. Sci*., **213,** 1, 169 (1989).
2. S. Stoyanov, *Jap. J. Appl. Phys*., **30**, 1, 1 (1991).
3. S. Stoyanov, V. Tonchev, *Phys. Rev. B*, **58**, 3, 1590 (1998).
4. D.-J. Liu, J. D. Weeks, *Phys. Rev. B*, **57**, 23, 14891 (1998).
5. M. Sato, M. Uwaha, *Surf. Sci.*, **442**, 318 (1999).
6. G. I. Barenblat, Scaling, self-similarity and intermediate asymptotics, CUP, Cambridge, 1996.
7. I. Berbezier, A. Ronda, *Surf. Sci. Rep*., **64,** 47 (2009).
8. C. Misbah, O. Pierre-Louis, Y. Saito, *Rev. Mod. Phys*., **82**, 981 (2010).
9. D. Staneva, B. Ranguelov, V. Tonchev, CR Acad. Bulg. Sci., **65**, 8, 1051, (2012).
10. J. Tersoff, Y. H. Phang, Z. Zhang, M. G. Lagally, *Phys. Rev. Lett*., **75**, 2730 (1995).
11. F. Liu, J. Tersoff, M. G. Lagally, *Phys. Rev. Lett*., **80,** 1268 (1998).
12. B. Ranguelov, V. Tonchev, C. Misbah, in: Nanoscience and Nanotechnology **6**, E. Balabanova and I. Dragieva (eds.), Heron Press, Sofia, 2006.
13. W. H. Press, S. A. Teukolski, W. T. Vetterling, B. P. Flannery, Numerical Recipes in Fortran 77, CUP, Cambridge, 1997.
14. V. Tonchev, B. Ranguelov, H. Omi, A. Pimpinelli, *Eur. Phys. J. B*, **73**, 539 (2010).
15. D. Staneva, B. Ranguelov, V. Tonchev, in: Nanoscience and Nanotechnology **10**, E. Balabanova and I. Dragieva (eds.), Heron Press, Sofia, 2010.
16. J. Krug, V. Tonchev, S. Stoyanov, A. Pimpinelli, *Phys. Rev. B*, **71**, 045412 (2005).
17. J. K. Zuo, T. Zhang, J. F. Wendelken, D. M. Zehner, *Phys. Rev. B*, **63,** 334041 (2001).
18. S. Baier, H. Ibach, M. Giesen, *Surf. Sci*., **573**, 17 (2004).
19. N. Akutsu, *J. Cryst. Growth*, **318**, 1, 10 (2011).
20. N. Akutsu, *J. Phys.: Cond. Matt*., **23**, 485004 (2011).
21. V. Tonchev, B. Ranguelov, D. Staneva, arXiv:1011. 1863v1.
22. N. A. Booth, A. A. Chernov, P. G. Vekilov, *Journal of Crystal Growth*, **237-239**, 1818 (2002).
23. P. Vekilov, private communication.
24. M. Syväjärvi, R. Yakimova, E. Janzén, *Journal of Crystal Growth*, **236,** 297 (2002).
25. B. J. Gibbons, S. Schaepe, J. P. Pelz, *Surf. Sci*., **600,** 2417 (2006).
26. V. Usov, C. O. Coileain, I. V. Shvets, *Phys. Rev. B*, **82,** 153301 (2010).
27. A. Pimpinelli, V. Tonchev, A. Videcoq, M. Vladimirova, *Phys. Rev. Lett.*, **88**, 206103 (2002).
28. N. Neel, T. Maroutian, L. Douillard, H.-J. Ernst, *Phys. Rev. Lett.*, **91**, 226103 (2003).
29. N. Neel, T. Maroutian, L. Douillard, H.-J. Ernst, *J. Phys-Cond. Matt.*, **15**, S3227 (2003).
30. H. Omi, Y. Homma, V. Tonchev, A. Pimpinelli, *Phys. Rev. Lett*., **95,** 216101 (2005).
31. M. A. Załuska-Kotur, F. Krzyżewski, *J. Appl. Phys.*, **111**, 114311 (2012).

КЛАСИФИКАЦИЯ НА ЯВЛЕНИЯТА НА ГРУПИРАНЕ

В. Тончев

Институт по Физикохимия, Българска Академия на Науките, 1113 София, България

Постъпила на 20 март, 2012 г.; приета на 15 май, 2012 г.

(Резюме)

Класификацията на групирането на прави стъпала върху вицинални кристални повърхности обособява два типа според поведението на минималното разстояние в групата l_{min} с нарастване на броя стъпала в нея N. В B1-типа l_{min} остава постоянно докато в B2-типа то намалява. Двата типа са илюстрирани с нови резултати за известни модели. Точният числен анализ е насочен към режима на междинна асимптотика, в който се формират самоподобни пространствено-времеви структури. В модела на Терсоф и сътр. поредицата равноотдалечени стъпала е дестабилизирана от междустъпално привличане с безкраен обхват. Показано е, че този модел принадлежи към B1-типа и степента 1/5 е получена за времевото поведение на N, ширината на терасата между групите и ширината на самите групи. Една разширена поредица от степени е получена за модела на С. Стоянов на дифузионно-контролирано изпарение, повлияно от електромиграция на адатомите. Този модел е от B2-тип и показва систематично отместване на степените спрямо предсказанията на хипотезата за класове на универсалност в групирането, което налага по-нататъшна ѝ модификация.

Bulgarian Chemical Communications, Volume 44, Proceedings of the III[rd] National Crystallographic Symposium (pp. 131–136) 2012

Parawollastonite (wollastonite-2M polytype) from the skarns in Zvezdel pluton, Eastern Rhodopes – a single crystal study

Y. Tzvetanova*, M. Kadyiski, O. Petrov

Institute of Mineralogy and Crystallography, Bulgarian Academy of Sciences, 1113 Sofia, Acad. Georgi Bonchev Str., Bl. 107

Received June 20, 2012; Revised July 9, 2012

The wollastonite polytype in three samples from different zones of skarns in Zvesdel pluton was determined by single-crystal XRD structure refinement. The studied wollastonite crystals are nearly pure $CaSiO_3$ but containing a few tenths of FeO wt.% (determined using microprobe analysis). The structure refinement confirmed the monoclinic symmetry of the studied samples (space group $P2_1/a$ and unit cell parameters a = 15.413(17) Å, b = 7.336(5) Å, c = 7.070(3) Å, β = 95.24(5)° for the crystal from the plagioclase-pyroxene-wollastonite+garnet zone; a = 15.409(7) Å, b = 7.320(3) Å, c = 7.063(2) Å, β = 95.36(3)° – wollastonite from the plagioclase-pyroxene-wollastonite zone, and a = 15.3770(11) Å, b = 7.2990(4) Å, c = 7.0491(5) Å, β = 95.340(6)° – wollastonite from the plagioclase-pyroxene-wollastonite+epidote zone). The latter structure was refined to R_1 = 0.0521 and $R_{(all)}$ = 0.0754 using 1970 unique reflections. The Si–O bond lengths vary between 1.580(3) and 1.667(3) Å (mean 1.624 Å), Ca–O bond lengths between 2.251(3) and 2.662(3) Å (mean 2.390 Å), and the Si–O–Si angles are 140.03(17), 139.39(18), and 150.81(18)° (mean 143.31°).

The proved monoclinic wollastonite (wollastonite-2M) is regarded as a higher temperature polytype with respect to the triclinic one. The presence only of the wollastonite-2M polytype in the studied skarns indicates longer duration of the thermal influence at the contact of carbonate xenoliths with monzonite magma or could be a result of an external stress, which is probably the stretching of the crystals due to differences in the thermal expansion coefficient of wollastonite with respect to the surrounding matrix.

Key words: skarn, wollastonite-2M, single crystal X-ray diffraction.

INTRODUCTION

Wollastonite ($CaSiO_3$) occurs in two structurally different forms: high-temperature α-wollastonite stable above ca. 1150 °C and low-temperature β-wollastonite that is the common $CaSiO_3$-polymorph found in crustal rocks. The low-temperature wollastonite contains dreier single chains, i.e. chains with three [SiO_4]-tetrahedra in the repeat unit (pyroxenoid type). The chains are linked to three columns of Ca-centred octahedra. Because of the size mismatch of the tetrahedral repeat units and the octahedral bands, the tetrahedra are tilted to accommodate their apices to the octahedral apices [1–4]. Both chains and bands run parallel to the *b*-axis.

A series of natural polytypes have been reported [3–11] with different packing arrangements of the single chains: triclinic polytypes (1T, 3T, 4T, 5T, 7T) and monoclinic parawollastonite (wollastonite-2M). The structure of wollastonite-1T was determined by Mamedov and Belov [5] and refined by Buerger and Prewitt [6], and Ohashi and Finger [3]; that one of wollastonite-2M was solved by Tolliday [7], Trojer [8], Ohashi [4], and Hesse [9]. The structures of the higher polytypes 3T, 4T, 5T and 7T were described by Henmi et al. [10] and Henmi et al. [11]. The structural difference between triclinic wollastonite and monoclinic parawollastonite has been interpreted to be due to different modes of stacking along the direction of the *a*-axis. These forms are not easily distinguishable except by single-crystal XRD refinement, since they differ only in the reflexions with *k* odd, which are always weak [7]. The structural state of wollastonite is a useful petrogenetic indicator for the deformation and cooling history of a rock. The aim of this study is to identify the polytypic modification of wollastonite

* To whom all correspondence should be sent:
E-mail: yana.tzvet@gmail.com

from different skarn zones and to interpret its occurrence at Zvezdel-Pcheloyad ore deposit (Eastern Rhodopes, Bulgaria).

MATERIALS

The studied wollastonite crystals were collected from zoned skarn nodules included in monzonites of the Zvezdel pluton. The following zones are determined from the proximal parts of the nodules towards the contact with the monzonites: garnet, pyroxene-garnet, plagioclase-pyroxene-wollastonite+garnet (Pl-Px-W-Gt), plagioclase-pyroxene-wollastonite (Pl-Px-W), plagioclase-pyroxene-wollastonite+epidote (Pl-Px-W-Ep), and plagioclase-pyroxene. Wollastonite, clinopyroxene, plagioclase, calcite, and grossular-andradite garnet are the major constituents of the wollastonite-bearing zones. Quartz is a subordinate phase and the associated minor minerals include epidote, prehnite, and chlorite. Titanite, apatite and magnetite are present as accessories.

The wollastonite-bearing zones exhibit massive or banded fabrics (Fig. 1a, b, c) with no visible preferred orientation of the crystals. The content of wollastonite averages 25–30%, but locally attains 70%. Wollastonite occurs mainly as nodular aggregates or forms prismatic grains up to about 3 mm in length along *b* (Fig. 1d, e, f). Wollastonite displays an overlapping composition among the three zones. It is nearly pure $CaSiO_3$ typically containing a few tenths of FeO wt.% (determined with microprobe analysis).

EXPERIMENTAL

Three wollastonite crystals from the zones Pl-Px-W-Gt, Pl-Px-W, and Pl-Px-W-Ep were selected for single-crystal XRD study. The specimens used in this study have prismatic habit, 0.2–0.3 mm long (along *b*), and cross sections of 0.1–0.2 mm. The crystals were mounted on glass fibres and measured on an Oxford diffraction Supernova diffractometer equipped with an Atlas CCD detector. X-ray data collection was carried out at room temperature with monochromatized Mo-Kα radiation (λ = 0.71073 Å). Data collection strategy was chosen for 100% completeness and redundancy of 4. Data reduction and analysis were carried out with the CrysAlisPro program [12]. Lorentz and polarization corrections were applied to intensity data using WinGX [13]. Reliable model with satisfactory R-values was obtained using the $P2_1/a$ space group and it was chosen for the refinement. Starting atomic coordinates were taken from [9]. Structure refinements were performed using the program SHELXTL [13], employing neutral atom scattering factors. At the final stage of refinement, anisotropic temperature factors were introduced.

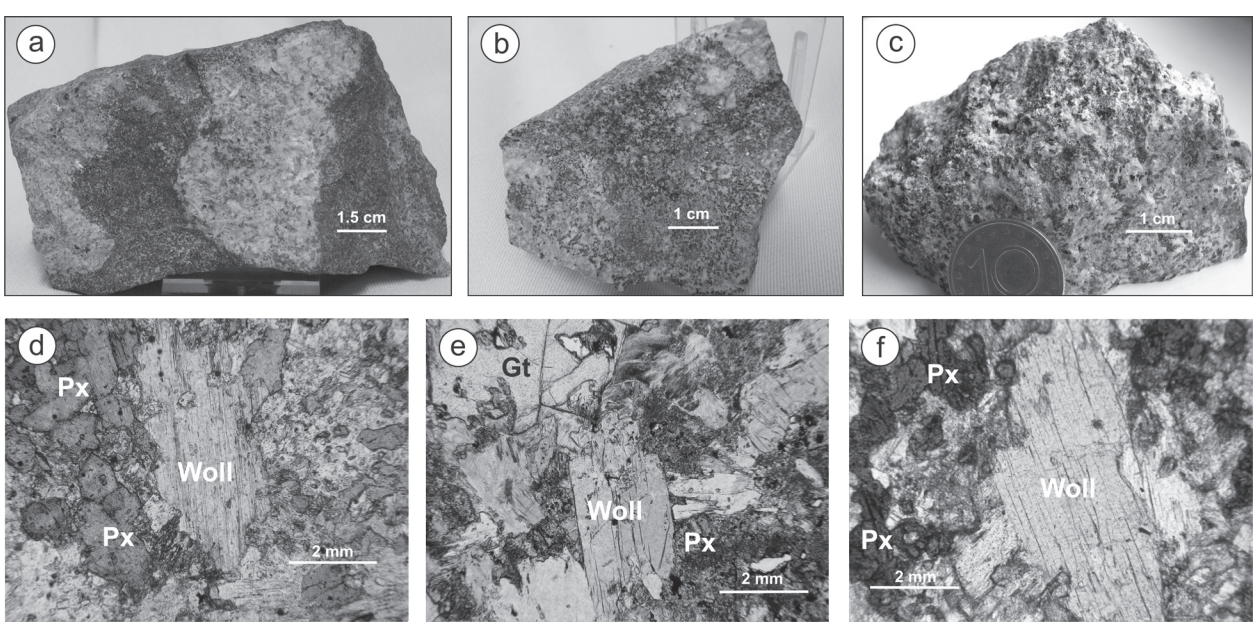

Fig. 1. Hand specimens of wollastonite-bearing skarn zones showing banded and massive texture (a–c); Photomicrographs (plane polarised light) showing wollastonite crystals of: (d) plagioclase-pyroxene-wollastonite-epidote skarn zones, (e) plagioclase-pyroxene-wollastonite-garnet zone; and (f) plagioclase-pyroxene-wollastonite zone. Woll – wollastonite, Px – clinopyroxene, Gt – garnet.

RESULTS AND DISCUSSION

The results after the refinement confirmed the monoclinic symmetry of the studied samples with space group $P2_1/a$ (Fig. 2). The final refinement unit cell dimensions are presented in Table 1.

The structure of a crystal selected from the Pl-Px-W-Ep zone was refined to $R_1 = 0.0521$ and $R_{(all)} = 0.0754$ using 1970 unique reflections. The experimental details are given in Table 2. Final atomic coordinates and thermal displacement parameters are listed in Tables 3 and 4. The Si–O bond lengths vary between 1.580(3) and 1.667(3) Å (mean 1.624 Å), Ca–O bond lengths are between 2.251(3) and 2.662(3) Å (mean 2.390 Å), and Si–O–Si angles are 140.03(17), 139.39(18) and 150.81(18)° (mean 143.31°) (Table 5). The results are in good agreement with those obtained by Hesse [9] and Ohashi [4].

Wollastonite-2M polytype was established for all wollastonite-bearing zones in the skarns at Zvezdel. This polytype is regarded as a higher temperature polytype with respect to the triclinic one [e.g. 10, 14]. Interesting results were reported by Henmi et al. [10]. The authors studied wollastonites from zoned skarns, which were formed around andesite dike at Kushiro, Hiroshima Prefecture, Japan and determined 1T, 2M, 3T, 4T, and 5T polytypes. The ratios of 2M to 1T in the skarns decrease gradually with increasing distances from the dike, and that 3T, 4T and 5T polytypes were found only at localities where both 1T and 2M exist. Mazzucato and Gualtieri [14] studied experimentally the wollastonite polytypes in the system $CaO–SiO_2$ in the temperature range

Table 1. Unit cell parameters of the studied samples

Parameter \ Sample	wollastonite from Pl-Px-W-Gt zone	wollastonite from Pl-Px-W zone	wollastonite from Pl-Px-W-Ep zone
a [Å]	15.413(17)	15.409(7)	15.3770(11)
b [Å]	7.336(5)	7.320(3)	7.2990(4)
c [Å]	7.070(3)	7.063(2)	7.0491(5)
β [°]	95.24(5)	95.36(3)	95.340(6)
V [Å^3]	796.0(7)	793.2(7)	787.68(9)

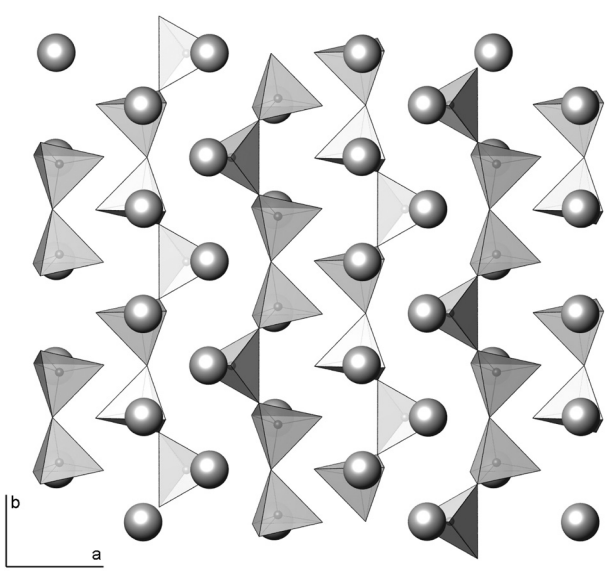

Fig. 2. Polyhedral model of the crystal structure of wollastonite-2M showing the stacking sequence of the *a* [(100) module] slabs (crystal from the Pl-Px-W-Ep zone)

Table 2. Experimental details for wollastonite-2M from the Pl-Px-W-Ep zone

№ of reflections	6826
R_{int}	0.0541
R_{sigma}	0.0446
h min	–20
h max	19
k min	–9
k max	10
l min	–9
l max	8
theta min [°]	3.75
theta max [°]	29.68
unique reflections	1970
Ref. $F_o > 4sigF_o$	1290
№ of parameters	131
R_1	0.0521
$R_{(all)}$	0.0754
GooF	1.081

Table 3. Atomic coordinates, $U_{iso}(U_{eq})$ parameters and occupancies for wollastonite-2M from the Pl-Px-W-Ep zone

Label	x	y	z	U_{iso} or U_{eq}	Occ.
Si1	–0.69845(7)	0.12375(16)	–0.44502(14)	0.0107(3)	1
Si2	–0.59235(7)	–0.15867(15)	–0.23179(15)	0.0101(3)	1
Si3	–0.59227(7)	0.40752(15)	–0.23147(15)	0.0105(3)	1
Ca1	–0.59925(6)	–0.12739(15)	–0.74079(11)	0.0117(2)	1
Ca2	–0.60095(5)	0.37808(15)	–0.73757(11)	0.0119(2)	1
Ca3	–0.74879(5)	–0.37530(17)	–0.02460(11)	0.0109(2)	1
O1	–0.6527(2)	–0.1142(5)	–0.0375(4)	0.0143(6)	1
O2	–0.6510(2)	0.3645(5)	–0.0365(4)	0.0146(6)	1
O3	–0.4912(2)	–0.1210(5)	–0.2326(4)	0.0150(6)	1
O4	–0.7856(2)	0.1246(5)	–0.3011(4)	0.0143(6)	1
O5	–0.7008(2)	0.1259(5)	–0.6727(4)	0.0123(6)	1
O6	–0.4903(2)	0.3720(5)	–0.2350(4)	0.0162(6)	1
O7	–0.6355(2)	0.3033(4)	–0.4073(4)	0.0147(6)	1
O8	–0.63592(19)	–0.0552(4)	–0.4087(4)	0.0143(6)	1
O9	–0.6082(2)	–0.3755(4)	–0.2759(4)	0.0202(7)	1

Table 4. Anisotropic displacement parameters for wollastonite-2M (sample from the Pl-Px-W-Ep zone)

Label	U11	U22	U33	U23	U13	U12
Si1	0.0093(6)	0.0122(5)	0.0114(6)	0.0000(4)	–0.0044(4)	0.0004(5)
Si2	0.0062(6)	0.0139(7)	0.0105(6)	0.0002(4)	–0.0021(4)	0.0002(4)
Si3	0.0061(6)	0.0140(7)	0.0117(6)	–0.0002(4)	–0.0024(4)	–0.0004(4)
Ca1	0.0147(4)	0.0133(4)	0.0074(4)	–0.0015(5)	0.0045(3)	–0.0020(5)
Ca2	0.0104(5)	0.0131(4)	0.0125(4)	0.0025(3)	–0.0032(3)	–0.0028(3)
Ca3	0.0070(5)	0.0115(4)	0.0148(4)	0.0006(3)	–0.0048(3)	–0.0002(3)
O1	0.0099(16)	0.0200(15)	0.0127(14)	0.0023(15)	0.0001(11)	0.0044(15)
O2	0.0119(16)	0.0190(14)	0.0126(14)	0.0009(15)	0.0003(11)	–0.0031(16)
O3	0.0072(15)	0.0165(13)	0.0221(16)	0.0016(17)	–0.0048(12)	–0.0003(17)
O4	0.0113(16)	0.0176(13)	0.0140(15)	–0.0004(13)	–0.0013(12)	0.0004(14)
O5	0.0097(15)	0.0139(12)	0.0138(14)	0.0004(13)	–0.0038(11)	–0.0035(14)
O6	0.0061(15)	0.0179(14)	0.0246(16)	0.0007(17)	–0.0015(12)	0.0008(18)
O7	0.0137(17)	0.0135(13)	0.0174(16)	–0.0012(11)	–0.0032(12)	–0.0032(12)
O8	0.0131(16)	0.0152(13)	0.0151(15)	0.0033(11)	–0.0053(12)	0.0043(12)
O9	0.0216(17)	0.0116(13)	0.0294(17)	–0.0009(13)	–0.0134(13)	0.0002(13)

700–1000 °C using *in situ* synchrotron X-ray powder diffraction data for determination of the kinetics of phase transformation. The authors observed the following reaction sequence of crystallisation of the $CaO–SiO_2$ parent glass: 1T-wollastonite forms first and progressively transforms in an intermediate 1Td-wollastonite metastable disordered form. Both phases in turn transform into 2M-wollastonite polytype at 950–1000 °C.

The presence only of a higher temperature polytype (wollastonite-2M) in the studied skarn samples could be interpreted as a result of a longer duration of thermal influence at the contact of carbonate xenoliths with monzonite magma by infiltration of hot fluids that were derived during the crystallisation of the pluton. The crystallisation temperature of the second monzonite phase of the Zvezdel pluton according to the two-feldspar geothermometer

Table 5. Si–O bond lengths [Å], Ca–O bond lengths [Å], and Si–O–Si angles [°] for polyhedra of wollastonite-2M (sample from the Pl-Px-W-Ep zone)

Si–O bond	Distance [Å]	Ca – O bond	Distance [Å]
Si1 – O4	1.604(3)	Ca1 – O6	2.251(3)
Si1 – O5	1.608(3)	Ca1 – O3	2.283(3)
Si1 – O8	1.656(3)	Ca1 – O1	2.319(3)
Si1 – O7	1.667(3)	Ca1 – O8	2.414(3)
mean	1.634(3)	Ca1 – O5	2.436(3)
Si2 – O3	1.580(3)	Ca1 – O4	2.530(3)
Si2 – O1	1.613(3)	Ca2 – O6	2.301(3)
Si2 – O9	1.634(3)	Ca2 – O2	2.311(3)
Si2 – O8	1.653(3)	Ca2 – O3	2.347(3)
mean	1.620(3)	Ca2 – O7	2.404(3)
Si3 – O6	1.586(3)	Ca2 – O5	2.415(3)
Si3 – O2	1.605(3)	Ca2 – O4	2.501(3)
Si3 – O9	1.637(3)	Ca3 – O1	2.325(3)
Si3 – O7	1.644(3)	Ca3 – O5	2.339(2)
mean	1.618(3)	Ca3 – O2	2.345(3)
Si–O–Si angle	Angle [°]	Ca3 – O4	2.406(3)
Si3–O7–Si1	140.03(17)	Ca3 – O1	2.408(3)
Si2–O8–Si1	139.39(18)	Ca3 – O2	2.418(3)
Si2–O9–Si3	150.81(18)	Ca3 – O9	2.662(3)

is estimated at about 675 °C [15]. The occurrence of wollastonite+plagioclase assemblages in the skarn zones indicates that the temperature was in excess of 600 °C [16] during the formation of early anhydrous minerals in the skarns. This temperature supplies the energy needed for the shift of the tetrahedral chains by 1T→2M polytype transition in wollastonite. This is possible through breaking Ca–O bonds bridging the chains with the 2M-polytype remaining stable during cooling of the system in the late stages of the skarn processes. Swami and Dubrovinsky [17] observed indications of Ca–O bonds breaking by 1T→2M polytype transition in Raman spectra. The estimated lower temperature of formation of wollastonite-2M polytype compared to the experimentally obtained results [14] could be interpreted as due to other factors like inhomogeneity of the rock, the chemical composition of the protolith and the fluid.

These polytype transformations have been explained as a result of deformation under conditions of shear stress or strain by some authors [18–21]. Guggenheim [19] stated that a combination of several processes may be necessary to produce the periodic faulting that yield polytypes with a repeat unit along [100] greater than one. During the field observation we could not find evidence for shear stress at the time of formation of that polytype, but we cannot exclude the possibility that the shear displacement leading to the formation of wollastonite-2M could be a result of an external stress. The latter explains the stretching of the crystals due to difference in the thermal expansion coefficient of wollastonite with respect to the surrounding matrix.

REFERENCES

1. D. R. Peacor, C. T. Prewitt, *Am. Mineral*., **48**, 1527 (1963).
2. F. J. Trojer, *Zeitschrift für Kristallographie*, **127**, 291 (1968).
3. Y. Ohashi, L. W. Finger, *Am. Mineral.*, **63**, 274 (1978).
4. Y. Ohashi, *Physics and Chemistry of Minerals*, **10**, 217 (1984).
5. K. S.Mamedov, N. V. Belov, *Dokl. Acad. Sci. USSR*, **107**, 463 (1956).
6. M. J. Buerger, C. T. Prewitt, *Proc. Natl. Acad. Sci*., **47**, 1884 (1961).
7. J. Tolliday, *Nature*, **182**, 1012 (1958).
8. F. J. Trojer, *Zeitschrift für Kristallographie*, **127**, 291 (1968).
9. K. F. Hesse, *Zeitschrift für Kristallographie*, **168**, 93 (1984).

10. C. Henmi, A. Kawahara, K. Henmi, I. Kusachi, Y. Takeuchi, *Am. Mineral.*, **68**, 156 (1983).
11. C. Henmi, I. Kusachi, A. Kawahara, K. Henmi, *Mineral. Journal*, **9**, 169 (1978).
12. Oxford Diffraction, CrysAlis PRO. Oxford Diffraction Ltd, Yarnton, England, 2010.
13. G. M. Sheldrick, *Acta Crystallographica A*, **64**, 112 (2008).
14. E. Mazzucato, A. F. Gualtieri, *Physics and Chemistry of Minerals*, **27**, 8, 565 (2000).
15. R. Nedialkov, B. Mavroudchiev, in: Proceedings of the XV Congress of the Carpatho-Balcan Geological Association. Geol. Soc. Greece, Sp. Publ., 1995, No 4/2, September 17–20, Athens, Greece, p. 561.
16. T. M. Gordon, H. J. Greenwood, *Amer. Mineral.*, **56**, 1674 (1971).
17. V. Swamy, L. S. Dubrovinsky, *Geochim. Cosmochim. Acta*, **61**, 1181 (1997).
18. H. R. Wenk, *Contributions to Mineralogy and Petrology*, **22**, 238 (1969).
19. S. Guggenheim, *Amer. Mineral*., **63**, 1260 (1978).
20. R. S. Coe, *Contrib. Mineral. Petrol.*, **26**, 3, 247 (1970).
21. R. Milke, R. Wirth, *Physics and Chemistry of Minerals*, **30**, 4, 230 (2003).

ПАРАВОЛАСТОНИТ (ПОЛИТИП ВОЛАСТОНИТ-2M) ОТ СКАРНИТЕ В ЗВЕЗДЕЛСКИЯ ПЛУТОН, ИЗТОЧНИ РОДОПИ – МОНОКРИСТАЛНО РЕНТГЕНОСТРУКТУРНО ИЗСЛЕДВАНЕ

Я. Цветанова, М. Кадийски, О. Петров

Институт по минералогия и кристалография, Българска академия на науките, ул. „Акад. Георги Бончев“, бл. 107, 1113 София

Постъпила на 20.06.2012 г.; приета на 09.07. 2012 г.

(Резюме)

Структурните разлики между политипите на триклинния воластонит и моноклинния параволастонит се състоят в различния начин на подредба на пироксеноидния тип вериги по посока на *a*-оста. Тези форми са трудно различими, освен с монокристална рентгенова дифрактометрия, тъй като се различават само по рефлексите с k-нечетно число, които обикновено са много слаби.

С монокристална рентгенова дифрактометрия е изследвана политипията на воластонит от три различни скарнови зони от Звезделския плутон. Химичният състав на изследваните монокристали се доближава до идеалния – $CaSiO_3$, като данните от рентгеноспектралния микроанализ показват незначително присъствие на FeO (0,n тегл.%). Структурните уточнения показват моноклинна симетрия на анализираните воластонитови кристали (пространствена група $P2_1/a$ и параметри на елементарната клетка a = 15.413(17) Å, b = 7.336(5) Å, c = 7.070(3) Å, β = 95.24(5)° за воластонита от зоната плагиоклаз-пироксен-воластонит+гранат; a = 15.409(7) Å, b = 7.320(3) Å, c = 7.063(2) Å, β = 95.36(3)° – от зоната плагиоклаз-пироксен-воластонит, и a = 15.3770(11) Å, b = 7.2990(4) Å, c = 7.0491(5) Å, β = 95.340(6)° – от зоната плагиоклаз-пироксен-воластонит+епидот). При рафинацията са достигнати удовлетворителни стойности на R_1 = 0.0521 и $R_{(all)}$ = 0.0754. Връзките Si–O варират между 1.580(3) и 1.667(3) Å (средно 1.624 Å), дължината на връзките Ca–O – между 2.251(3) и 2.662(3) Å (средно 2.390 Å), а ъглите между Si–O–Si са 140.03(17), 139.39(18) и 150.81(18)° (средно 143.31°).

По експериментални данни моноклинната модификация воластонит-2M се определя като по-високотемпературния политип по отношение на триклинния. Присъствието само на моноклинния политип във всички скарнови зони (независимо от тяхната отдалеченост от монцонита) би могло да се обясни с по-продължителното времетраене на термичното влияние на монцонитовата магма на контакта с карбонатните ксенолити. Възможно е образуването му да е резултат и от външни напрежения, възникващи при растежа на кристалите, поради разлики в термичния коефициент на разширение на воластонита по отношение на заобикалящата го матрица по време на прогресивния етап на метасоматичния процес.

Bulgarian Chemical Communications, Volume 44, Proceedings of the III[rd] National Crystallographic Symposium (pp. 137–145) 2012

Synthesis and crystal structure of new $PbBaFe_{2-x}Mn_xO_5$ perovskite-type compounds

P. Tzvetkov[1]*, D. Kovacheva[1], D. Nihtianova[1,2], N. Velichkova[1], T. Ruskov[3]

[1] *Institute of General and Inorganic Chemistry, Bulgarian Academy of Sciences*
1113 Sofia "Acad. Georgi Bonchev" str. bld.11
[2] *Institute of Mineralogy and Crystallography, Bulgarian Academy of Sciences*
1113 Sofia "Acad. Georgi Bonchev" str. bld.107
[3] *Institute for Nuclear Research and Nuclear Energy, Bulgarian Academy of Sciences*
1784 Sofia "Tzarigradsko chaussee" 72 Blvd.

Received March 22, 2012; Revised April 27, 2012

New perovskite-based compounds with general formula $PbBaFe_{2-x}Mn_xO_5$ ($0 \le x \le 1.5$) were synthesized by solid-state reaction under argon atmosphere. The compounds were characterized by X-ray powder diffraction, TEM (SAED) and ^{57}Fe Mössbauer spectroscopy. The crystal structure of $PbBaFeMnO_5$ and $PbBaFe_{0.5}Mn_{1.5}O_5$ members of the series is determined by Rietveld refinement method. The basic crystallographic sections in orientations [100] and [010] are obtained by SAED method. The Rietveld refinement results are in good agreement with the SAED data. The compounds crystallize in the orthorhombic space group *Pnma* with unit cell parameters $a \approx \sqrt{2}a_p$, $b \approx a_p$, and $c \approx 4\sqrt{2}a_p$ (a_p – the parameter of the perovskite subcell). The crystal structure of the studied phases consists of perovskite blocks separated by $\frac{1}{2}[110]_p(\bar{1}01)_p$ (p – the perovskite subcell) crystallographic shear planes. Inside the blocks the octahedral B–position is occupied by Fe^{3+} and Mn^{3+} ions and the twelve coordinated A–position is fully occupied by Ba^{2+} ions. The perovskite blocks are connected to each other by double chains of edge-sharing $(Fe, Mn)O_5$ distorted tetragonal pyramids running along the *b*–axis. The double chains delimit six-sided tunnels fully occupied by Pb^{2+} cations. The pyramidal chains adopt two mirror-related configurations ("left" L and "right" R) and layers consisting of chains of the same configuration alternate along the *c*–axis in –L–R–L–R– sequence. The Mössbauer spectroscopy reveals a transition from magnetic ordering to paramagnetic state in $PbBaFe_{1.5}Mn_{0.5}O_5$ at room temperature with the substitution of Fe^{3+} by Mn^{3+} cations. The measurements at 77 K show that the Mn^{3+} cations replace the Fe^{3+} cations for the octahedral (1) and the pyramidal (2) sites in equal proportions.

Key words: perovskites, crystallographic shear planes, cation substitutions.

INTRODUCTION

Perovskite-type compounds with general formula ABO_3 are extensively studied for many years due to their various electric and magnetic properties: dielectrics, high temperature superconductors, ion conductors, colossal magneto-resistant materials, optical materials, etc. The perovskite structure consists of cubic close packing of oxygen atoms and A-cations, with ¼ of the octahedral interstices occupied by B-cations. Many structures can be derived from that of perovskite by various ways: by mixed occupancy and cation ordering in A and B positions; vacancy ordering in the cation and anion sublattices; intergrowth of perovskite and other structure type blocks (NaCl, CaF_2 and other structure types) and the formation of hexagonal perovskite polytypes. The oxygen vacancies ordering in the perovskite structure gives rise to many compounds with different structures ($Ca_2Mn_2O_5$, $La_2Ni_2O_5$, $Ca_2Fe_2O_5$) [1, 2]. Recently, new class of oxygen deficient perovskite-type compounds incorporating periodically ordered translational interfaces was synthesized. The first published member of the class is $Pb_{1.33}Sr_{0.67}Fe_2O_5$ (*Pnma*, a = 5.687 Å, b = 3.920 Å, c = 21.075 Å) [3] with relations to the perovskite subcell (a_p): $a \approx \sqrt{2}a_p$, $b \approx a_p$, $c \approx 4\sqrt{2}a_p$. The structure can be described as an anion deficient perovskite in which half of the B^{3+} cations are located in octahedral coordination as in the prototype perovskite structure and the other half are five-coordinated in distorted tetragonal pyramids. The pyramids

* To whom all correspondence should be sent:
E-mail: p-tzvetkov@gmx.net

share common edges and form double chains and channels between them along the b-axis, alternating with perovskite blocks along the c-axis. Inside the channels the Pb^{2+} cations are coordinated by six oxygen atoms and one $6s^2$ electron lone pair of the lead atom. The A^{2+} cation position is situated within the perovskite block and has mixed occupancy by Pb^{2+} and Sr^{2+} ions. The introduction of periodically ordered translational interfaces into the perovskite structure was based on the basis of detailed transmission electron microscopy investigations of Pb and Fe-containing compounds [4, 5, 6]. The translational interfaces were found to have similar crystallographic properties as the crystallographic shear planes (CS planes) in ReO_3 structure type. The structure of $Pb_{1.33}Sr_{0.67}Fe_2O_5$ incorporates alternating CS planes and perovskite blocks along the *c* – axis. The shear planes remove a layer of oxygen atoms and displace the perovskite blocks with respect to each other by $1/2[110]_p$ vector. Derivative compounds of $Pb_{1.33}Sr_{0.67}Fe_2O_5$ with different chemical composition and thickness of the perovskite block are part of the homologous series $A_nB_nO_{3n-2}$ (n = 4, 5, 6) (A = Pb, Ba, Bi; B = Fe, Co, Mn, Ti, Sn) [7]. Chemical compositions $Pb_{1.33}Sr_{0.67}Fe_2O_5$ [3], $Pb_{1.33}Sr_{0.67-x}Ba_xFe_2O_5$ ($0 \le x \le 0.67$) [8], $Pb_{2-x}Ba_xFe_2O_5$ ($0.6 \le x \le 1.0$) [9], $Pb_2Mn_2O_5$ [10] and $PbBaFe_{2-x}Co_xO_5$ ($0 \le x \le 1$) [11] represents the n = 4 member of the homologous series. Partial replacement of B^{3+} by other cation with formal charge 4+ can enlarge the thickness of the perovskite block as compared to the prototype $Pb_{1.33}Sr_{0.67}Fe_2O_5$ structure. The members of the series $Pb_{2.9}Ba_{2.1}Fe_4TiO_{13}$ and $Pb_{2.85}Ba_{2.15}Fe_4SnO_{13}$ (n = 5) [12, 13] and $Pb_{3.8}Bi_{0.2}Ba_2Fe_{4.2}Ti_{1.8}O_{16}$ (n = 6) [12] represent 1.5 (n = 5) and 2 (n = 6) times the thickness of perovskite block.

In this work we report on the synthesis and crystal structure of $PbBaFe_{2-x}Mn_xO_5$ ($0 \le x \le 1.5$) solid solution, a new member of the homologous series $A_nB_nO_{3n-2}$ (n = 4).

EXPERIMENTAL

Polycrystalline samples with chemical composition $PbBaFe_{2-x}Mn_xO_5$ ($0 \le x \le 1.5$, $\Delta x = 0.25$) were prepared by high temperature solid state reaction. Analytical grade PbO, $BaCO_3$, Fe_2O_3 and MnO were used as starting compounds. Stoichiometric mixtures of the reagents were homogenized in agate mortar with acetone and pressed into pellets. The pellets were heated at 800 °C for 24 hours in argon flow with intermediate regrinding every 6 hours. After each regrinding the samples were annealed at 400 °C for 1 hour in air.

Powder X-ray diffraction (XRD) patterns were collected at room temperature on Bruker D8 Advance diffractometer using CuKα radiation and LynxEye PSD detector within the range 13–130° 2θ, step 0.02° 2θ and 6 sec/strip (total of 1050 sec/step) counting time. To improve the statistics, sample rotating speed of 30 rpm was used. The crystal structure parameters were refined using TOPAS 4.2 program [14].

The TEM (SAED) investigations were performed by transmission electron microscope JEOL 2100 at 200 kV accelerating voltage. The specimens were grinded and dispersed in ethanol by ultrasonic treatment for 6 min. The suspensions were dripped on standard holey carbon/Cu grids.

Mössbauer measurements were performed using a constant acceleration spectrometer. A source of $^{57}Co(Rh)$ with activity of 50 mCi was used. The $PbBaFe_{1.5}Mn_{0.5}O_5$ spectra were taken in the transmission mode at room temperature and at 77 K. The sample with a thickness of 50 mg cm^{-2} was mounted in a cryostat of He exchange cooling gas. The Mössbauer spectra were fitted using an integral Lorentzian line shape approximation or thin sample approximation [15, 16]. The isomer shifts are referred to the centroid of α-iron foil reference spectrum at room temperature. The geometric effect is taken into account as well.

RESULTS AND DISCUSSION

Single phase samples of $PbBaFe_{2-x}Mn_xO_5$ were obtained for x = 0, 0.25, 0.5, 0.75, 1.0, 1.25 and 1.5. The powder XRD patterns of all samples were indexed in orthorhombic symmetry, space group *Pnma* and unit-cell parameters $a \approx \sqrt{2}a_p$, $b \approx a_p$, $c \approx 4\sqrt{2}a_p$. To prevent the oxidation of Mn^{3+} to Mn^{4+} and the formation of $BaMnO_3$ as additional phase, all manganese containing samples were synthesised in argon flow. Since lead oxide starts to evaporate at temperatures above 800 °C to compensate possible losses an excess of 3% wt. was added to the stoichiometric mixture. The samples with higher Mn content (x > 1.5) are beyond the homogeneity range and contain PbO (Massicot) and $BaFeO_{2.25}$ as impurity phases. Samples $PbBaFeMnO_5$ and $PbBaFe_{0.5}Mn_{1.5}O_5$ were chosen for detailed structural investigation. The starting unit cell parameters and zero shift value were determined during the preliminary characterization using the whole powder pattern matching procedure (Pawley fit) (Table 1). The XRD phase analysis of $PbBaFeMnO_5$ and $PbBaFe_{0.5}Mn_{1.5}O_5$ revealed a single phase for the first sample and small impurities of PbO – Massicot in the last one. The determined amount of PbO from the Rietveld refinement is 2.73% wt. The Pawley fit of XRD patterns during the preliminary characterization of both samples revealed considerable

Table 1. Unit-cell parameters for $PbBaFe_{2-x}Mn_xO_5$ ($0 \le x \le 1.5$)

x	*a* (Å)	*b* (Å)	*c* (Å)
0.00	5.7656(2)	3.9920(1)	21.1433(6)
0.25	5.7661(4)	3.9733(3)	21.176(2)
0.50	5.7806(4)	3.9510(3)	21.281(2)
0.75	5.7839(6)	3.9382(4)	21.311(2)
1.00	5.7994(3)	3.9095(3)	21.407(1)
1.25	5.8123(3)	3.8962(2)	21.4752(8)
1.50	5.8182(2)	3.8816(1)	21.5115(5)

anisotropic peak shape broadening. The structure refinement without introducing a model for describing the anisotropic peak shapes leads to $R_B = 2.28$ and $R_B = 2.21$ respectively. Satisfactory results were achieved by using 8-th order spherical harmonics [17]. The reliability factors show considerable improvement of $R_B = 1.59$ and 1.76 for $PbBaFeMnO_5$ and $PbBaFe_{0.5}Mn_{1.5}O_5$, respectively. The observed anisotropic line broadening is probably due to relatively high level of structural disorder in the samples under investigation. The unit cell parameters of the solid-solution series $PbBaFe_{2-x}Mn_xO_5$ ($0 \le x \le 1.5$) are given in Table 1. With the increase of the manganese content the parameters *a* and *c* increase monotonically, while the *b* parameter decreases. This result has not straightforward explanation, because the ionic radii of Fe^{3+} and Mn^{3+} in octahedral and five fold pyramidal coordination are almost equal – 0.645 Å and 0.58 Å, respectively [18]. One possible explanation is the Jahn-Teller effect of Mn^{3+} atoms.

The experimental and calculated selected area electron diffraction (SAED) patterns of sample $PbBaFeMnO_5$ are given in Fig. 1. The indexing of the patterns was performed in orthorhombic lattice. The unit cell parameters were taken from powder XRD data measurements in Table 1. The reflection

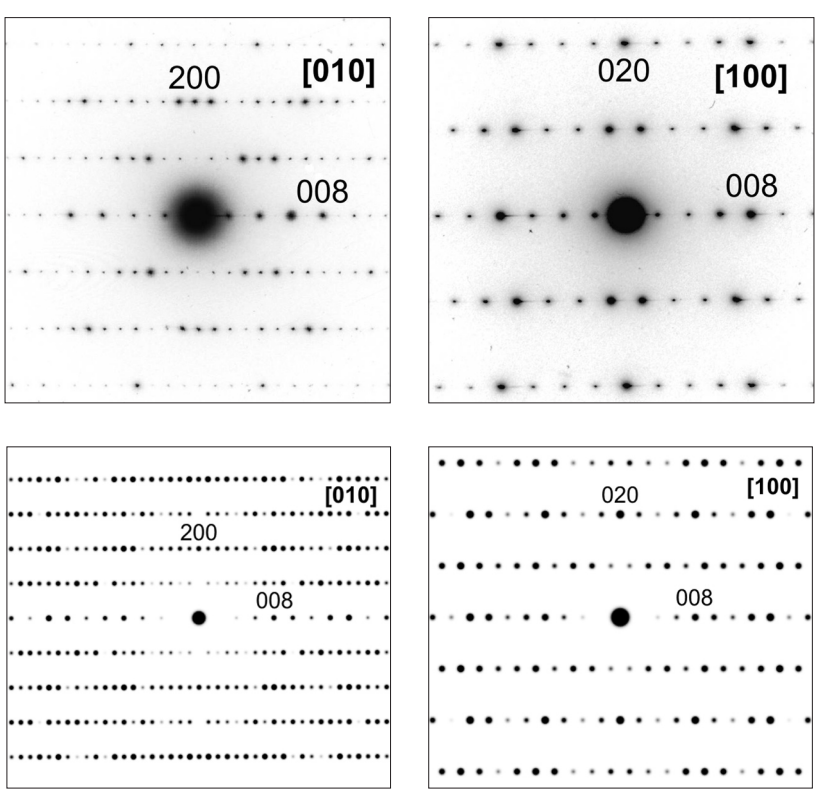

Fig. 1. Experimental (above) and calculated (below) SAED patterns of $PbBaFeMnO_5$ in [100] and [010] directions

conditions: 0kl:k+l = 2n, hk0:h = 2n, h00:h = 2n, 0k0:k = 2n, 00l:l = 2n determined from the electron diffraction patterns, are in agreement with the proposed *Pnma* space group. The Rietveld refinement structural parameters of $PbBaFeMnO_5$ were used for the calculated SAED patterns in Fig. 1. The experimental data are in very good agreement with the proposed structural data.

The crystal structures of $PbBaFeMnO_5$ and $PbBaFe_{0.5}Mn_{1.5}O_5$ were refined using powder XRD data. The atomic positions for $Pb_{1.08}Ba_{0.92}Fe_2O_5$ [9] were used as initial parameters for the refinement. Since the X-ray atomic scattering factors of manganese and iron are very close, their population in the mixed occupancy positions can not be determined precisely from the Rietveld refinement data. Therefore, statistical distribution of Fe and Mn atoms in the octahedral – $Fe2(Mn)O_6$ and pyramidal – $Fe1(Mn)O_5$ sites was used.

The refined structural parameters of both samples are given in Table 2 and 3. Typical Rietveld plot of $PbBaFe_{0.5}Mn_{1.5}O_5$ is shown in Fig. 2. Table 4 represents calculated metal-oxygen distances and bond-valence sums in comparison with the corresponding values calculated for $Pb_{1.2}Ba_{0.8}Fe_2O_5$ [9]. The average metal-oxygen distances around the Pb1 position inside the double chains of pyramids slightly increase with the manganese substitu-

Table 2. Refined structural parameters for $PbBaFeMnO_5$
SG: *Pnma*(62), *a*=5.7992(1), *b*=3.9099(1), *c*=21.4070(4), Z=4

Atom	Wyck.	x/a	y/b	z/c	SOF	B_{iso}(Å^2)
Pb1	4c	0.0461(3)	1/4	0.5702(1)	1.00	0.72(4)
Ba1	4c	0.5594(3)	1/4	0.6854(1)	1.00	0.46(5)
Fe1	4c	0.459(1)	1/4	0.4484(2)	0.50	0.26(6)
Mn1	4c				0.50	0.26(6)
Fe2	4c	0.9328(9)	1/4	0.3152(2)	0.50	0.26(6)
Mn2	4c				0.50	0.26(6)
O1	4c	0.937(3)	3/4	0.3218(7)	1.00	1.1(2)
O2	4c	0.676(3)	1/4	0.2512(9)	1.00	1.1(2)
O3	4c	0.194(3)	1/4	0.3928(8)	1.00	1.1(2)
O4	4c	0.696(3)	1/4	0.3847(8)	1.00	1.1(2)
O5	4c	0.441(3)	3/4	0.4578(7)	1.00	1.1(2)

R_B = 1.59, R_{wp} = 4.95, R_{exp} = 1.95, GOF = 2.53

Table 3. Refined structural parameters for $PbBaFe_{0.5}Mn_{1.5}O_5$
SG: *Pnma*(62), *a*= 5.8172(1), *b*= 3.8808(1), *c*= 21.5068(2), Z=4

Atom	Wyck.	x/a	y/b	z/c	SOF	B_{iso}(Å^2)
Pb1	4c	0.0608(2)	1/4	0.5709(1)	1.00	0.83(3)
Ba1	4c	0.5769(3)	1/4	0.6851(1)	1.00	0.43(4)
Fe1	4c	0.4409(8)	1/4	0.4492(1)	0.25	0.28(5)
Mn1	4c				0.75	0.28(5)
Fe2	4c	0.9150(7)	1/4	0.3146(2)	0.25	0.28(5)
Mn2	4c				0.75	0.28(5)
O1	4c	0.921(2)	3/4	0.3217(5)	1.00	0.8(1)
O2	4c	0.654(2)	1/4	0.2499(6)	1.00	0.8(1)
O3	4c	0.190(2)	1/4	0.3971(6)	1.00	0.8(1)
O4	4c	0.677(2)	1/4	0.3868(6)	1.00	0.8(1)
O5	4c	0.424(3)	3/4	0.4631(5)	1.00	0.8(1)

R_B = 1.76, R_{wp} = 4.86, R_{exp} = 1.90, GOF = 2.56

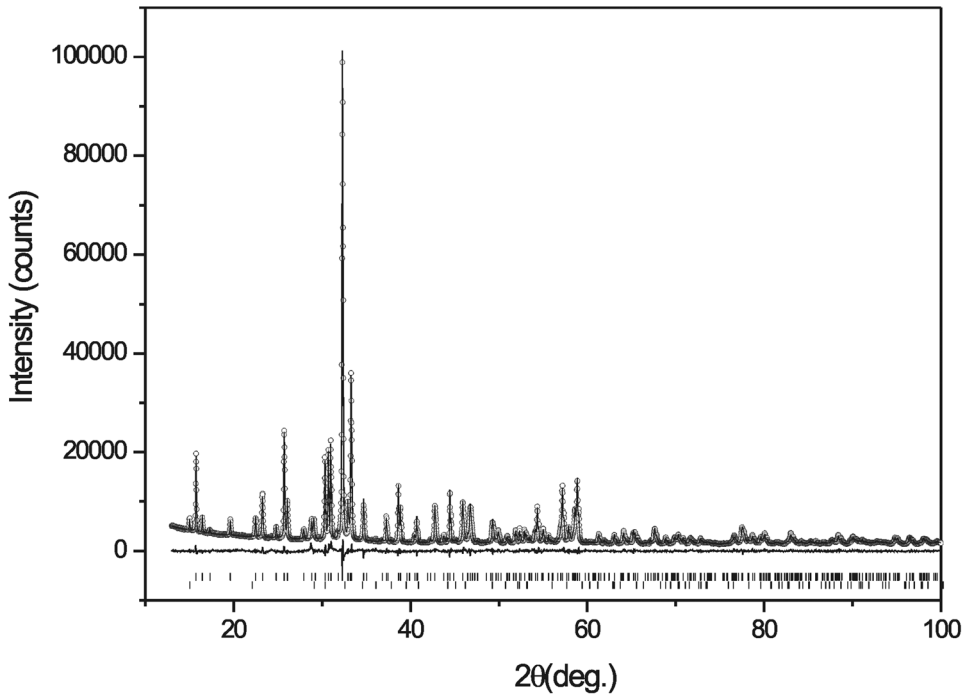

Fig. 2. Experimental (circles), calculated (line) and difference (bottom line) powder XRD patterns for $PbBaFe_{0.5}Mn_{1.5}O_5$. Lower tick bars represent peak positions for $PbBaFe_{0.5}Mn_{1.5}O_5$ and the impurity phase PbO (Massicot)

tion. The Pb1 columns of atoms are ordered in a straight line along the *c* – axis in the structure of $Pb_{1.2}Ba_{0.8}Fe_2O_5$ with coordinate $x = 0.0032(8)$ [9]. According to the refined data for $PbBaFeMnO_5$ and $PbBaFe_{0.5}Mn_{1.5}O_5$, lead atoms are considerably shifted along the *a* – axis having coordinates $x = 0.0461(3)$ and $0.0608(2)$, respectively (Fig. 3). The average distances in $Fe1(Mn)O_5$ pyramids does not change notably. The shortest ones are observed in $PbBaFe_{0.5}Mn_{1.5}O_5$, mainly because of the significant

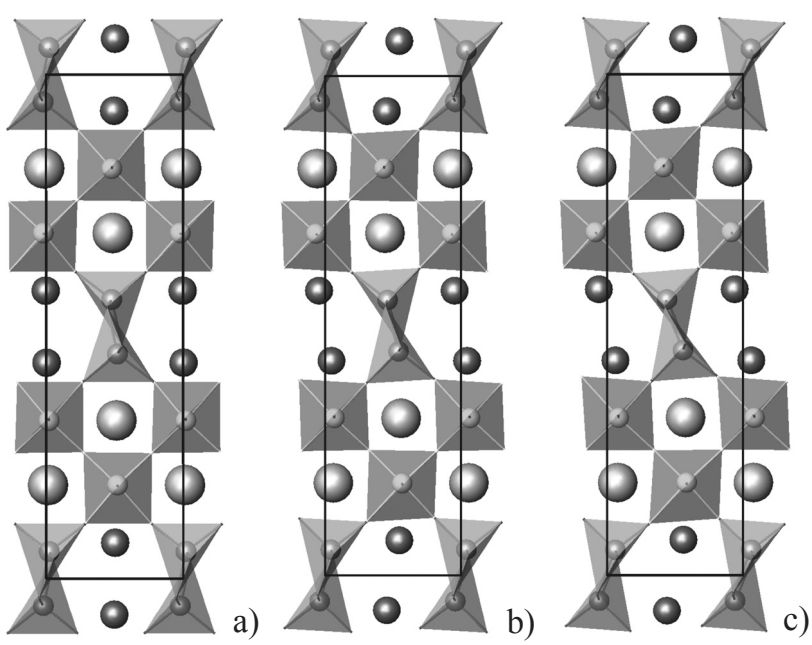

Fig. 3. Polyhedral representation of a) $Pb_{1.2}Ba_{0.8}Fe_2O_5$ [9], b) $PbBaFeMnO_5$, and c) $PbBaFe_{0.5}Mn_{1.5}O_5$ along [010] direction. Pyramids – $Fe(Mn)O_5$, octahedra – $Fe(Mn)O_6$, small dark spheres – Pb atoms, large light spheres – Ba atoms

Table 4. The calculated metal-oxygen distances and bond-valence sums for $Pb_{1.2}Ba_{0.8}Fe_2O_5$, $PbBaFeMnO_5$ and $PbBaFe_{0.5}Mn_{1.5}O_5$

Metal-oxygen distances		Composition		
		$Pb_{1.2}Ba_{0.8}Fe_2O_5$*	$PbBaFeMnO_5$	$PbBaFe_{0.5}Mn_{1.5}O_5$
Pb1	O(1)	2.287(9)	2.314(15)	2.312(11)
	O(3)x2	2.478(6)	2.528(11)	2.523(8)
	O(4)x2	2.631(6)	2.644(12)	2.630(8)
	O(5)	2.673(9)	2.888(17)	2.913(12)
	O(5)	3.241(9)	3.034(17)	3.085(12)
	Average	2.631(3)	2.654(5)	2.660(4)
	Valence	2.04(1)	1.88(2)	1.89(2)
Ba1	O(1)	2.873(11)	2.883(18)	2.900(12)
	O(1)	2.884(11)	2.924(18)	2.924(12)
	O(1)	2.840(12)	2.921(15)	2.939(11)
	O(2)x2	2.771(10)	2.747(13)	2.743(10)
	O(2)x2	2.836(10)	2.854(13)	2.857(10)
	O(3)x2	3.009(9)	2.943(13)	2.954(11)
	O(4)x2	2.925(9)	2.875(13)	2.887(10)
	O(5)	3.113(11)	3.064(15)	3.186(11)
	Average	2.899(3)	2.886(4)	2.903(3)
	Valence	2.36(2)	2.43(3)	2.35(2)
Fe, Mn1	O(3)	1.928(10)	1.947(18)	1.840(14)
	O(4)	1.867(10)	1.933(18)	1.921(13)
	O(5)x2	2.023(2)	1.968(2)	1.966(2)
	O(5)	2.012(8)	2.090(16)	2.043(11)
	Average	1.971(3)	1.981(4)	1.947(4)
	Valence	2.87(3)	2.77(5)	3.06(4)
Fe, Mn2	O(1)x2	1.9944(7)	1.960(1)	1.947(1)
	O(2)	1.963(12)	2.019(19)	2.059(14)
	O(2)	1.979(12)	2.006(19)	1.963(14)
	O(3)	2.106(10)	2.246(18)	2.390(14)
	O(4)	2.159(10)	2.025(18)	2.081(13)
	Average	2.033(4)	2.036(6)	2.064(5)
	Valence	2.92(3)	2.92(5)	2.82(3)

* – The data for $Pb_{1.2}Ba_{0.8}Fe_2O_5$ are taken from Nikolaev et al. [9].

decrease in Fe1(Mn) – O3 bond distance, which is partially compensated with the increase of Fe1(Mn) – O4 bonds. The average metal-oxygen distances in $Fe2(Mn)O_6$ octahedra monotonically increase with the substitution. The oxygen atoms O3 and O4 are common for $Fe1(Mn)O_5$ pyramids and $Fe2(Mn)O_6$ octahedra in the perovskite blocks. With increase of Mn substitution level the Fe2(Mn) – O3 bond distance increases to almost non bonding 2.390(14) Å in $PbBaFe_{0.5}Mn_{1.5}O_5$. The distance Fe2(Mn) – O4 is less changed and decreases to 2.081(13) Å. The twelve-fold oxygen coordination around the Ba atoms does not undergo notable changes. Recently, a comprehensive study of $Pb_2Mn_2O_5$ employing transmission electron microscopy methods was reported [10]. This compound is synthesized under high pressure conditions as a mixture with two other phases. The proposed structural model by Hadermann et al. was found to share many common features with the Rietveld refinement results of the present samples. They report Jahn-Teller distortion of MnO_6 octahedra in the *a-c* plane with two long and two short Mn–O distances (see Fig. 8c, Ref. 10). The Jahn-Teller deformation of octahedral oxygen coordina-

Table 5. ^{57}Fe Mössbauer spectral parameters of hyperfine interaction for $PbBaFe_{1.5}Mn_{0.5}O_5$ at 300K and 77K

Site	T [K]	IS [mm/s]	QS [mm/s]	FWHM± 0.05 [mm/s]	H [kOe]	Rel area [%]
Oct(1)	300	0.35 ± 0.03	0.58 ± 0.04	0.21		20 ± 3
Pyr(2)		0.30 ± 0.03	1.01 ± 0.04	0.75		19 ± 3
Oct(1)	77	0.53 ± 0.04	-0.13 ± 0.04	0.87 0.74 0.46	513 ± 1	48 ± 3
Pyr(2)		0.47 ± 0.04	0.1 ± 0.04	1.12 0.67 0.45	482 ± 1	52 ± 3

tion around the Mn^{3+} ions is well known in many compounds and was found to be crucial for the stabilization of $Pb_2Mn_2O_5$ structure. Similar deformation of the octahedra is observed in the crystal structure of $PbBaFeMnO_5$ and $PbBaFe_{0.5}Mn_{1.5}O_5$. The degree of deformation increases with the increase of the manganese content. Most likely this is the main reason for the observed change of the unit cell parameters with the increase of manganese content (Table 1). The bond distance Fe2(Mn) – O1 contracts with the increase of manganese and can be determined straight form the *b*-parameter. The average Fe1(Mn) – O distances also decrease with manganese substitution. Thereby, the observed increase in unit cell parameters along the *a*- and *c*-axis is mainly due to the Jahn-Teller distortion of MnO_6 octahedra within the (010) plane.

The Mössbauer spectra taken at room temperature and at 77 K are presented in Fig. 4a and Fig. 4b, respectively. The parameters of the fitted spectra corresponding to an isomer shift (IS), a quadrupole splitting/shift (QS), a full width at half maximum (FWHM) of the resonance lines, a magnetic hyperfine field at the site of the Fe nucleus (H), and the relative spectral area are summarized in Table 5. The spectrum measured at room temperature was fitted by superposition of two quadrupole doublets: (1) and (2) and a continuous distribution of magnetic Zeeman sextets. The doublets (1) and (2) correspond to two iron sites in $PbBaFe_{1.5}Mn_{0.5}O_5$ – octahedral (1) and pyramidal (2) ones, respectively. The distribution of the magnetic sextets at room temperature shows an intermediate magnetic state with the presence of a paramagnetic state (two quadrupole doublets with approximately 40% of relative spectral area), and 60% of magnetic ordering.

The Mössbauer spectrum taken at 77 K was fitted by superposition of two magnetic sextets corresponding to the two positions of magnetically ordered iron in $PbBaFe_{1.5}Mn_{0.5}O_5$ (Fig. 4b). The broadening of magnetic components as compared to the corresponding resonance lines at 77 K for $PbBaFe_2O_5$ [9] could be explained by random distribution of magnetic cations, Fe and Mn, at octahedral and pyramidal positions leading to different exchange interaction for the Fe–Fe and Fe–Mn cations. Actually we have two magnetic sextet distributions for the two iron sites, but for the fitting procedure an approximation was used with three different line-widths for the magnetic components of the spectra (1^{st} – 6^{th}), (2^{nd} – 5^{th}) and (3^{rd} – 4^{th}), as it is shown in Table 5.

Comparing with the data for $PbBaFe_2O_5$ at 77 K [9], a diminution of the magnetic hyperfine field at the site of the Fe nucleus (H) is observed in $PbBaFe_{1.5}Mn_{0.5}O_5$ due to the presence of manganese. Finally, our measurements show that the Mn cations replace the Fe cations for the octahedral (1) and the pyramidal (2) sites in equal proportions (within the statistical error). This result is very different from the data previously reported by us on Mössbauer spec-

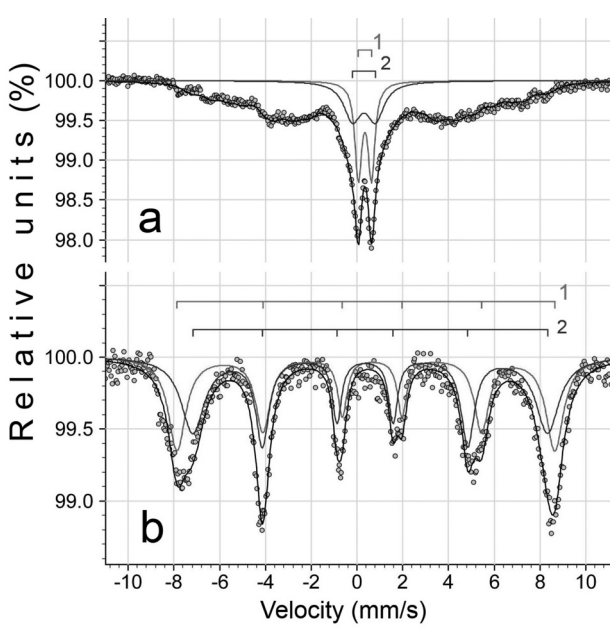

Fig. 4. Mössbauer spectrum of $PbBaFe_{1.5}Mn_{0.5}O_5$ taken at a) 300K and b) 77K

troscopy of $PbBaFe_{1.5}Co_{0.5}O_5$ [11]. The latter compound was found to have magnetic ordering at room temperature and the Co atoms were found to preferably occupy the pyramidal positions, as opposed to the new compound $PbBaFe_{1.5}Mn_{0.5}O_5$ described in this paper.

CONCLUSION

New solid-solution series $PbBaFe_{2-x}Mn_xO_5$ was successfully synthesized. The members of the series are part of the homologous series $A_nB_nO_{3n-2}$ (n = 4). The homogeneity range was determined for *x* up to 1.5. The crystal structures of $PbBaFeMnO_5$ and $PbBaFe_{0.5}Mn_{1.5}O_5$ were refined by Rietveld method. The degree of structural deformation increases with the increase of the manganese content. This fact should be considered as the main reason for the observed changes of the unit cell parameters with the increase of manganese content. The experimental and calculated selected area electron diffraction (SAED) patterns are in very good agreement with the obtained structural data. The Mössbauer spectroscopy reveals a transition from magnetic ordering in $PbBaFe_2O_5$ to paramagnetic state in $PbBaFe_{1.5}Mn_{0.5}O_5$ at room temperature. The measurements at 77 K show that the Mn cations replace the Fe cations for the octahedral (1) and the pyramidal (2) sites in equal proportions.

Acknowledgements: *We thank Ivan Spirov for his help for the Mössbauer measurements and fitting of the spectra. We thank also the National Science Fund of Bulgaria for the financial support under contract DTK-02/77 – 2009 and DO-02-224/17.12.2008.*

REFERENCES

1. M. Anderson, J. Vaughey, K. Poeppelmeier, *Chem. Mater.*, **5**, 151 (1993).
2. J. Vaughey, K. Poeppelmeier, *NIST Special Publication*, **804**, 419 (1991).
3. V. Raynova-Schwarten, W. Massa, D. Babel, *Z. Anorg. Allg. Chem.*, **623**, 1048 (1997).
4. A. Abakumov, J. Hadermann, S. Bals, I. Nikolaev, E. Antipov, G. Van Tendeloo, *Angew. Chem. Int. Ed.*, **45**, 6697 (2006).
5. J. Hadermann, A. Abakumov, I. Nikolaev, E. Antipov, G. Van Tendeloo, *Solid State Sci.*, **10**, 382 (2008).
6. D. Batuk, J. Hadermann, A. Abakumov, T. Vranken, A. Hardy, M. Van Bael, G. Van Tendeloo, *Inorg. Chem.*, **50**, 4978 (2011).
7. A. Abakumov, J. Hadermann, M. Batuk, H. D'Hondt, O. Tyablikov, M. Rozova, K. Pokholok, D. Filimonov, D. Sheptyakov, A. Tsirlin, D. Niermann, J. Hemberger, G. Van Tendeloo, E. Antipov, *Inorg. Chem.*, **49**, 9508 (2010).
8. P. Tzvetkov, N. Petrova, D. Kovacheva, *J. Alloy. Compd.*, **485**, 862 (2009).
9. I. Nikolaev, H. D'Hondt, A. Abakumov, J. Hadermann, A. Balagurov, I. Bobrikov, D. Sheptyakov, V. Pomjakushin, K. Pokholok, D. Filimonov, G. Van Tendeloo, E. Antipov, *Phys. Rev. B*, **78**, 024426 (2008).
10. J. Hadermann, A. Abakumov, T. Perkisas, H. D'Hondt, H. Tan, J. Verbeeck, V. Filonenko, E. Antipov, G. Van Tendeloo, *J. Solid State Chem.*, **183**, 2190 (2010).
11. P. Tzvetkov, D. Kovacheva, D. Nihtianova, T. Ruskov, *Z. Kristallogr. Proc. 1*, 397 (2011).
12. A. Abakumov, J. Hadermann, M. Batuk, H. D'Hondt, O. Tyablikov, M. Rozova, K. Pokholok, D. Filimonov, D. Sheptyakov, A. Tsirlin, D. Niermann, J. Hemberger, G. Van Tendeloo, E. Antipov, *Inorg. Chem.*, **49**, 9508 (2010).
13. O. Korneychik, M. Batuk, A. Abakumov, J. Hadermann, M. Rozova, D. Sheptyakov, K. Pokholok, D. Filimonov, E. Antipov, *J. Solid State Chem.*, **184**, 3150 (2011).
14. TOPAS V4: General profile and structure analysis software for powder diffraction data, User's Manual, Bruker AXS, Karlsruhe, Germany Bruker AXS (2008).
15. G. Shenoy, J. Friedt, H. Maleta, S. Ruby, *Mössbauer Effect Methodology*, **9**, 277 (1974).
16. T. Cranshaw, *J. Phys. E*, **7**, 122 (1974).
17. M. Järvinen, J. Appl. Cryst., **26**, 525 (1993).
18. R. D. Shannon, *Acta Cryst. A*, **32**, 751 (1976).

СИНТЕЗ НА НОВИ $PbBaFe_{2-x}Mn_xO_5$ СЪЕДИНЕНИЯ С ПЕРОВСКИТОВ ТИП СТРУКТУРА

П. Цветков[1]*, Д. Ковачева[1], Д. Нихтянова[1,2], Н. Величкова, Т. Русков[3]

[1] Институт по Обща и Неорганична Химия, Българска Академия на Науките, 1113 София, бул. „Акад. Георги Бончев“, бл. 11
[2] Институт по Минералогия и Кристалография, Българска Академия на Науките, 1113 София, бул. „Акад. Георги Бончев“, бл. 107
[3] Институт за Ядрени изследвания и Ядрена енергия, Българска Академия на Науките, 1784 София „Цариградско шосе“, бл. 72

Постъпила на 22.03.2012 г.; приета на 27.04. 2012 г.

(Резюме)

Нови съединения с перовскитов тип структура и обща формула $PbBaFe_{2-x}Mn_xO_5$ ($0 \le x \le 1.5$) бяха синтезирани чрез твърдофазен синтез в атмосфера от аргон. Получените съединения бяха характеризирани с прахова рентгенова дифракция (XRD), TEM (SAED) и ^{57}Fe Мьосбауерова спектроскопия. Кристалната структура на $PbBaFeMnO_5$ и $PbBaFe_{0.5}Mn_{1.5}O_5$ членове на серията е определена по метода на Ритвелд. Дифракционните картини по направления [100] и [010] са получени чрез SAED. Резултатите от структурната рафинация по метода на Ритвелд са в добро съгласие с данните от електронната дифракция. Съединенията кристализират в орторомбична пространствена група *Pnma* и параметри на елементарната клетка $a \approx \sqrt{2}a_p$, $b \approx a_p$, и $c \approx 4\sqrt{2}a_p$ (a_p – параметър на перовскитовата подклетка). Кристалната структура на изучените фази се състои от перовскитови блокове отделени от $\frac{1}{2}[110]_p(\bar{1}01)_p$ кристалографски равнини на сръзване. В блоковете октаедричната B-позиция е заета от Fe^{3+} и Mn^{3+} йони и дванадесет координираната A-позиция е изцяло заета от Ba^{2+} йони. Перовскитовите блокове са свързани помежду си с двойни вериги от изкривени $(Fe, Mn)O_5$ тетрагонални пирамиди, които споделят общи ръбове. Веригите са по протежение на *b*-оста и ограничават шестоъгълни тунели запълнени изцяло от Pb^{2+} катиони. Пирамидалните вериги имат две огледално свързани конфигурации („лява“ – L и „дясна“ – R), като слоеве изградени само от една от двете конфигурации се редуват по протежение на *c*–оста в –L–R–L–R– последователност. Мьосбауеровата спектроскопия на $PbBaFe_{1.5}Mn_{0.5}O_5$ показва, че с увеличаване на заместването на Fe^{3+} от Mn^{3+} катиони температурата на прехода от магнитно подредено в парамагнитно състояние се понижава. Направените измервания при 77 K показват, че Mn^{3+} замества Fe^{3+} в октаедричната и пирамидална позиции в еднаква степен.

Bulgarian Chemical Communications, Volume 44, Proceedings of the III[rd] National Crystallographic Symposium (pp. 146–150) 2012

A preparation of high-molecular poly(ethylene-oxide)-urea complexes from a solution and their structural changes on heating

S. Uzova[1]*, B. Bogdanov[2], V. Velev[2], T. Angelov[3], A. Popov[4]

[1] *"Prof. Assen Zlatarov" PGT–Burgas, 8000 Burgas, Bulgaria*
[2] *"Konstantin Preslavski" University-Shumen, 9712 Shumen, Bulgaria*
[3] *Lukoil Neftohim Burgas AD, Burgas, Bulgaria*
[4] *"Prof. Assen Zlatarov" University-Burgas, 8010 Burgas, Bulgaria*

Received February 27, 2012; Revised April 18, 2012

The preparation of high-molecular poly(ethylene oxide)-urea molecular complex by mixing their benzene and methanol solutions had been studied. The composition of the soluble and insoluble solid dispersed phase in benzene-methanol mixture had been investigated by means of X-ray and calorimetric analyses. It is shown that at molar ratio between poly(ethylene oxide) and urea of 1:2, which corresponds to the molecular complex composition, the yield of solid dispersed phase increases in a non-linear mode with an extension of the interaction time to 50 hours and after that it doesn't change any more.

The structural changes of poly(ethylene oxide)-urea molecular complex on heating from room temperature up to 147.5 °C had been studied using high-temperature X-ray analyses. It was shown that improvement processes of the molecular complex crystal structure were carried out in the temperature range before melting.

Key words: poly(ethylene-oxide), urea, complexes, preparation, structure.

INTRODUCTION

It is known that poly(ethylene oxide) (PEO) and urea form crystal molecular complex (MC) by mixing [1–5]. The molar ratio of PEO and urea in the molecular complex is 1:2. It has been established that the MC crystal structure is different from the crystal structure of the initial components [4, 5]. Its melting temperature (T_m=144.5 °C) is higher than the melting temperature of PEO (65 °C) and urea (132 °C).

Till now there are no references available concerning investigation of the structural changes in PEO-urea MC on heating and cooling. Wide-angle X-ray is an useful method for this purpose. The structure and the structural transformations of high-molecular PEO-urea molecular complex on heating and its mixtures with the initial components have been studied by means of this method. The results obtained are the subject discussed in the present paper.

EXPERIMENTAL

High-molecular PEO "Badimol", produced industrially by "Chemist plant" at Dimitrovgrad with a molecular weight, determined viscosimetrically M_v=2.7×10^6 was used for the preparation of PEO-urea molecular complex and their binary mixtures with the initial components. The urea is chem. pure for analysis, supplied by "Riedel de Hoen-Germany. The PEO content in its urea mixtures was changed from 15 to 90 wt.%, which corresponds to the change of PEO-urea molar ratio from 1:3.5 to 1:0.1.

PEO-urea binary mixtures were prepared by mixing a 1% solution of PEO in benzene with methanol solutions of urea (10 wt.%) at 20 °C and benzene: methanol ratio of 1:0.27 volume parts. After some time in the range from 1 to 200 hours, the resulting insoluble precipitate was separated by a decantation and it was washed out with benzene. The decanted solution was evaporated under vacuum at 50 °C. The resulting solid residuum and the washed precipitate were dried at 50 °C under vacuum to a constant weight.

The X-ray investigations were carried out at room and elevated temperature by an apparatus "Dron-3" – Russia and "Tur-M 611" – Germany with Ni-filtered CuKα radiation under a reflection

* To whom all correspondence should be sent:
E-mail: pgt_director@abv.bg

condition in the angular range (2θ) from 8 to 44°. A differential scanning calorimeter "DSC-111", a product of Setaram, France, was also used.

RESULTS AND DISCUSSION

A heterophase system of a solid dispersed phase and a liquid continuous phase is obtained by mixing monophased PEO solutions in benzene and a methanol solution of urea at a temperature of 20 °C. The content and the composition of the insoluble solid dispersed phase depend on the initial ratio of the components PEO and urea and on the interaction period. At PEO-urea ratio of 1:2 molar fractions, corresponding to the molecular complex composition, the solid dispersed phase yield, which is insoluble in a benzene-methanol mixture increases in a non-linear mode with an extension of the interaction period 50 hours, it reaches 75–80 wt.% towards PEO-urea mixture and it doesn't change any more (Fig. 1, curve 1).

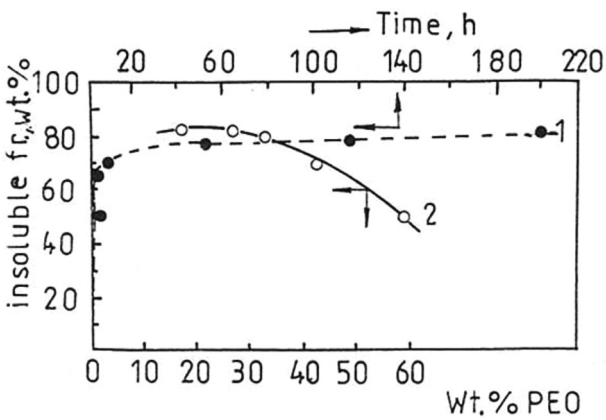

Fig. 1. Dependence of production of insoluble fraction in PEO-urea mixtures on the PEO content in the initial mixture (curve 2) and on the interaction period at PEO-urea ratio of 1:2 molar fractions (curve 1)

It has been established by means of X-ray and calorimetry, that the liquid phase and the solid fraction, dissolved in it and separated after the evaporation of a benzene-methanol mixture, represents PEO-urea molecular complex (Fig. 2, curve 4; Fig. 3, curve 2; Fig. 4, curve 3, 4).

The PEO-urea interaction at a ratio of 1:2 molar fractions and the formation of a molecular complex are carried out relatively quickly at the conditions investigated. Almost a complete (100%) association in a molecular complex has been observed. After 50 hours equilibrium between the soluble and insolu-

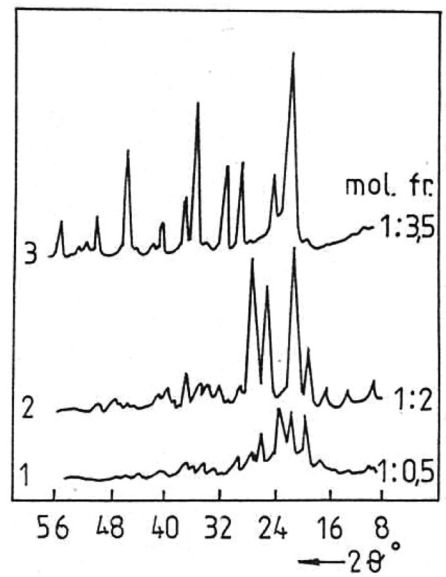

Fig. 2. Wide-angle X-ray diffractograms of PEO-urea mixtures, prepared from a solution (insoluble fraction). PEO – urea ratio, molar fractions: curve 1 – 0:1; curve 2 – 1:0; curve 3 – 1:0.5; curve 4 – 1:2; curve 5 – 1:3.5

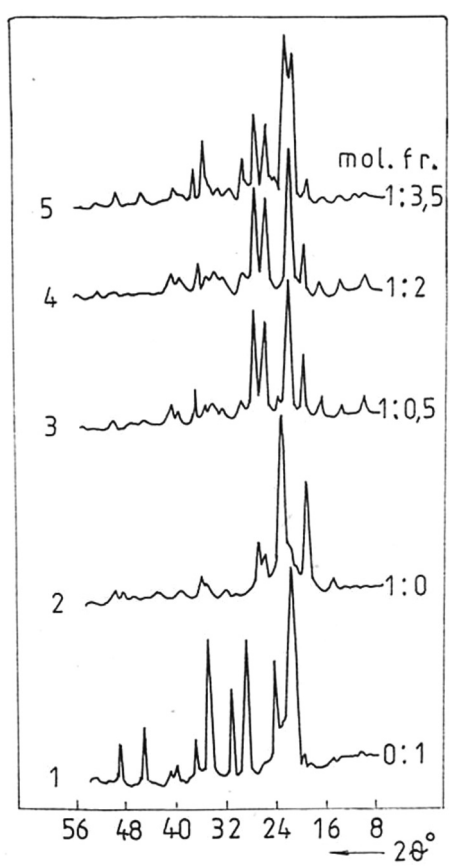

Fig. 3. Wide-angle X-ray diffractograms of PEO-urea mixtures, prepared from a solution (soluble fraction). PEO-urea ratio, molar fractions: curve 1 – 1:0.5; curve 2 – 1:2; curve 3 – 1:3.5.

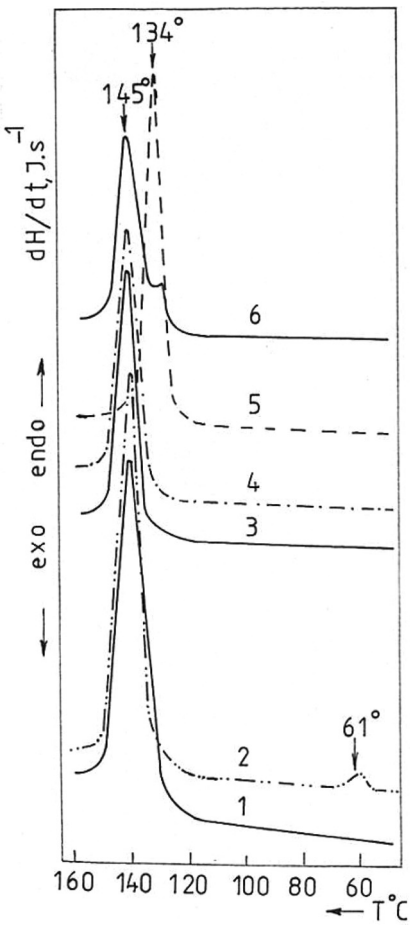

Fig. 4. DSC curves on heating of insoluble (1, 3, 6) and soluble (2, 4, 5) fractions in a benzene-methanol mixture of PEO-urea binary system. Molar fractions of PEO and urea: curves 1, 2 – 1:0; curves 3, 4 – 1:2 and curves 5, 6 – 1:3.5

ble fraction of the molecular complex in a benzene-methanol mixtures is established (Fig. 1, curve 1).

PEO-urea mixtures with a content of the first component from 17.3 to 59.5 wt.% in a benzene-methanol solution at an interaction period of 50 hours and at identical other conditions are prepared. The dependence of the insoluble fraction yield on the proportion between the two components is presented in Fig. 1, curve 2. It has been established by means of X-ray and calorimetry, that the insoluble fraction represents PEO-urea molecular complex at an urea content in the initial mixture from 0.5 to 2 molar fractions per ethylene oxide unit (Fig. 2, curves 3, 4; Fig. 4, curves 1, 3). The insoluble fraction represents PEO-urea molecular complex and traces of free urea at an urea content higher than 2 molar fractions per ethylene oxide unit (Fig. 2, curve 5; Fig. 4, curve 6).

It has been established as it was expected from the results obtained that the soluble fraction in a benzene-methanol mixture differ in a composition from the insoluble solid dispersed phase, when the initial PEO-urea ratio is different from the complex composition. At a PEO content higher then 26.8 wt.% towards its urea mixture (less then 2 moles of urea per one monomeric unit), the soluble fraction in solid state represents molecular complex and free PE mixture, which form separate crystal phases (Fig. 3, curve 1; Fig. 4, curve 2). When the urea content in the initial mixture is above 73.2 wt.% towards its PEO mixture (above 2 moles of urea per ethylene oxide unit), the soluble fraction in solid state contains mainly free urea (Fig. 3, curve 3; Fig. 4, curve 5).

The structural changes on heating of PEO-urea molecular complex fro room temperature to 147.5 °C have been investigated using high-temperature X-ray (Fig. 5).

It has been established that on first heating in the range about 120 to 135 °C, a slight but measurable increase of the integral intensity of the reflexes is observed, due to MC, 002 (2θ = 19.42°), 202 (2θ = 27.35°) and 102 (2θ = 21.64°) and also decrease of their half-width is observed (Fig. 6, 7).

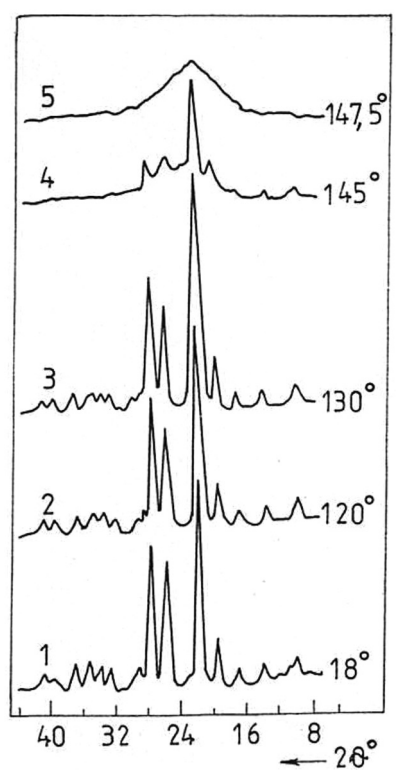

Fig. 5. Wide-angle X-ray diffractograms of PEO-urea MC, prepared from a solution (1:2 molar fractions) at different temperatures. First heating temperature, °C: curve 1–18; curve 2–120; curve 3–130; curve 4–145; curve 5–147.5

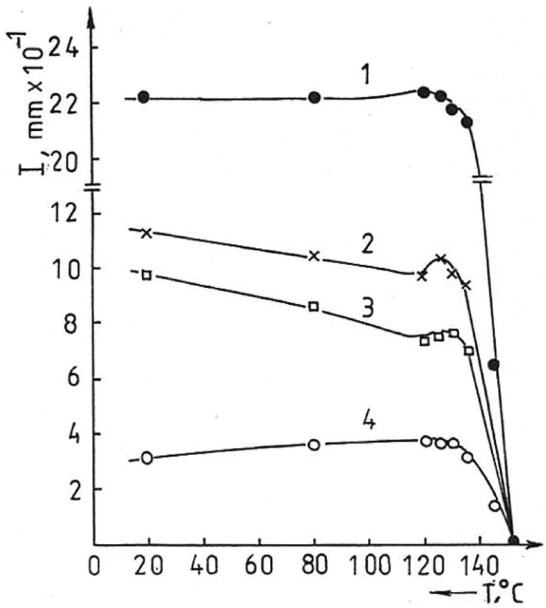

Fig. 6. Dependence of intensity of crystal reflexes in the wide-angle X-ray diffractograms of PEO-urea MC (1:2 molar fractions)(prepared from a solution), on the heating temperature, 2θ: 1–25.5°; 2–21.64°; 3–27.35°; 4–19.42°

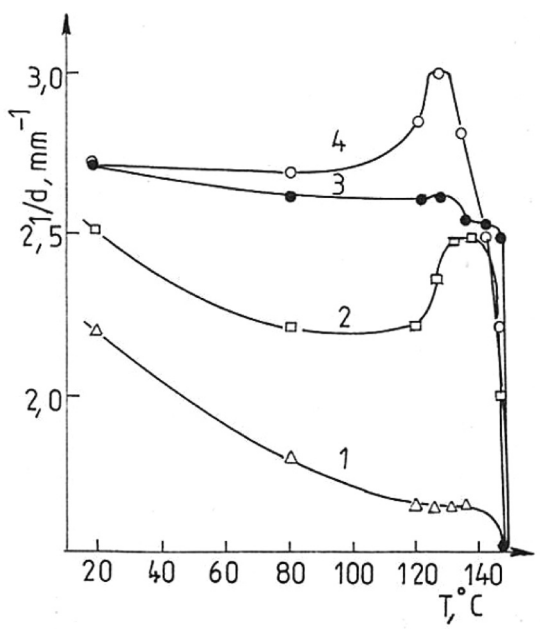

Fig. 7. Dependence of integral half-width of crystal reflexes in the wide-angle X-ray diffractograms of PEO-urea MC (1:2 molar fractions), prepared from a solution, on the heating temperature, 2θ: 1–25.5°; 2-27.35°; 3–21.64°; 4–19.42°

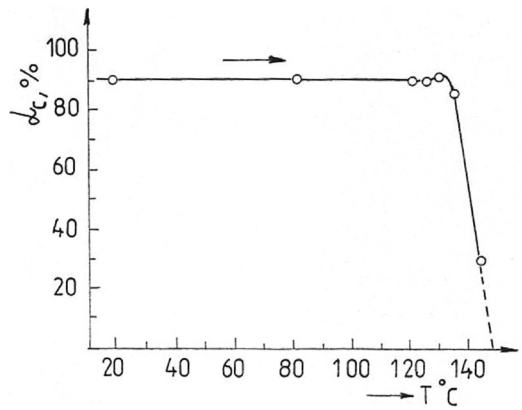

Fig. 8. Dependence of X-ray degree of crystallinity (α_c) of PEO-urea MC (1:2 molar fractions), prepared from a solution, on the temperature

Above 135 °C the intensity of the diffraction maximums of the molecular complex crystal phase (Fig. 6) and the degree of crystallinity (Fig. 8) abruptly decrease.

This temperature coincides with the initial melting temperature of the molecular complex determined calorimetrically. Consequently, improvement processes of the molecular complex crystal structure are carried out on heating in the temperature range before melting. Similar effects have been observed earlier (Fig. 6, 7) for high-molecular PEO and they are explained with the structural changes of the crystal phase into plastic state.

Acnowledgement: *The financial support of the Bulgarian Ministry of Education and Sciences (National Science Fund), contract DO–02–61/2008 and NIH-244, is gratefully acnowledged.*

REFERENCES

1. Е. А. Бектуров, Р. Е Легкунец, Ассоциация полимеров с малыми молекулами, Алма – Ата, Наука, 208, 1983.
2. М. М. Тарноруцкий, Л. С. Школьникова, А. К. Лорей, В. И. Диндойн, Л. И. Зыкова, *Высокомолекулярные соединения*, **Б 17**, 817 (1975).
3. F. E. Bailey, H. G. France, *J. Polym. Sci*., **49**, 397 (1961).
4. G. Hild, *Rev. gen. et plast*., **46**, 771 (1969).
5. G. Hild, *Bull. Soc. Chim. France*, **8**, 2840 (1969).
6. M. Hresteva, E. Nedkov, M. Michailov, *Bulg. J. Phys*., **7**, 63 (1980).
7. M. Michailov, *Makromol. Chem. Suppl*., 7, 87 (1984).

ПОЛУЧАВАНЕ НА КОМПЛЕКСИ НА ВИСОКОМОЛЕКУЛЕН ПОЛИЕТИЛЕНОКСИД И КАРБАМИД ОТ РАЗТВОР И СТРУКТУРНИТЕ ИМ ПРОМЕНИ ПРИ НАГРЯВАНЕ

С. Узова[1]*, Б. Богданов[2], В. Велев[2], Т. Ангелов[3], А. Попов[4]

[1] ПГТ „Проф. д-р Ас. Златаров“ – Бургас, 8000 Бургас, България
[2] Университет „Еп. К. Преславски“ – Шумен, 9712 Шумен, България
[3] Лукойл Нефтохим Бургас АД, Бургас, България
[4] Университет „Проф. д-р Ас. Златаров“ – Бургас, 8010 Бургас, България

Постъпила на 27.02.2012 г.; приета на 18.04. 2012 г.

(Резюме)

Получен бе молекулен комплекс от високомолекулен полиетиленоксид и карбамид чрез смесване на техни бензенови и метанолни разтвори. Композицията на разтворимата и неразтворимата твърда дисперсна фаза в бензен–метанолната смес беше изследвана рентгеноструктурно и калориметрично. Беше показано, че при молно съотношение между полиетиленоксида и карбамида 1:2, съответстващо на молекулния комплекс, количеството на твърдата дисперсна фаза нараства нелинейно с увеличаване на реакционното време до 50 часа и след това не се изменя повече.

Структурните изменения на молекулния комплекс между полиетиленоксида и карбамида при нагряване от стайна температура до 147.5 °C бяха изследвани с помощта високотемпературна прахова рентгенова дифрактометрия. Показано беше, че в температурния интервал преди топене се усъвършенства кристалната структура на молекулния комплекс.

BULGARIAN CHEMICAL COMMUNICATIONS

Instructions about Preparation of Manuscripts

General remarks: Manuscripts are submitted in English by e-mail or by mail (in duplicate). The text must be typed double-spaced, on A4 format paper using Times New Roman font size 12, normal character spacing. The manuscript should not exceed 15 pages (about 3500 words), including photographs, tables, drawings, formulae, etc. Authors are requested to use margins of 3 cm on all sides. For mail submission hard copies, made by a clearly legible duplication process, are requested. Manuscripts should be subdivided into labelled sections, e.g. **Introduction, Experimental, Results and Discussion**, *etc*.

The title page comprises headline, author's names and affiliations, abstract and key words.

Attention is drawn to the following:

a) **The title** of the manuscript should reflect concisely the purpose and findings of the work. Abbreviations, symbols, chemical formulas, references and footnotes should be avoided. If indispensable, abbreviations and formulas should be given in parentheses immediately after the respective full form.

b) **The author**'s first and middle name initials, and family name in full should be given, followed by the address (or addresses) of the contributing laboratory (laboratories). **The affiliation** of the author(s) should be listed in detail (no abbreviations!). The author to whom correspondence and/or inquiries should be sent should be indicated by asterisk (*).

The abstract should be self-explanatory and intelligible without any references to the text and containing not more than 250 words. It should be followed by key words (not more than six).

References should be numbered sequentially in the order, in which they are cited in the text. The numbers in the text should be enclosed in brackets [2], [5, 6], [9−12], etc., set on the text line. References, typed with double spacing, are to be listed in numerical order on a separate sheet. All references are to be given in Latin letters. The names of the authors are given without inversion. Titles of journals must be abbreviated according to Chemical Abstracts and given in italics, the volume is typed in bold, the initial page is given and the year in parentheses. Attention is drawn to the following conventions:

a) The names of all authors of a certain publications should be given. The use of "*et al*." in the list of references is not acceptable.

b) Only the initials of the first and middle names should be given.

In the manuscripts, the reference to author(s) of cited works should be made without giving initials, e.g. "Bush and Smith [7] pioneered...". If the reference carries the names of three or more authors it should be quoted as "Bush *et al*. [7]", if Bush is the first author, or as "Bush and co-workers [7]", if Bush is the senior author.

Footnotes should be reduced to a minimum. Each footnote should be typed double-spaced at the bottom of the page, on which its subject is first mentioned.

Tables are numbered with Arabic numerals on the left-hand top. Each table should be referred to in the text. Column headings should be as short as possible but they must define units unambiguously. The units are to be separated from the preceding symbols by a comma or brackets.

Note: The following format should be used when figures, equations, *etc*. are referred to the text (followed by the respective numbers): Fig., Eqns., Table, Scheme.

Schemes and figures. Each manuscript (hard copy) should contain or be accompanied by the respective illustrative material as well as by the respective figure captions in a separate file (sheet). As far as presentation of units is concerned, SI units are to be used. However, some non-SI units are also acceptable, such as °C, ml, l, etc.

The author(s) name(s), the title of the manuscript, the number of drawings, photographs, diagrams, etc., should be written in black pencil on the back of the illustrative material (hard copies) in accordance with the list enclosed. Avoid using more than 6 (12 for reviews, respectively) figures in the manuscript. Since most of the illustrative materials are to be presented as 8-cm wide pictures, attention should be paid that all axis titles, numerals, legend(s) and texts are legible.

The authors are asked to submit **the final text** (after the manuscript has been accepted for publication) in electronic form either by e-mail or mail on a 3.5"

diskette (CD) using a PC Word-processor. The main text, list of references, tables and figure captions should be saved in separate files (as *.rtf or *.doc) with clearly identifiable file names. It is essential that the name and version of the word-processing program and the format of the text files is clearly indicated. It is recommended that the pictures are presented in *.tif, *.jpg, *.cdr or *.bmp format, the equations are written using "Equation Editor" and chemical reaction schemes are written using ISIS Draw or ChemDraw programme.

The authors are required to submit the final text with a list three individuals and their e-mail addresses that can be considered by the Editors as potential reviewers. Please, note that the reviewers should be outside the authors' own institution or organization. The Editorial Board of the journal is not obliged to accept these proposals

EXAMPLES FOR PRESENTATION OF REFERENCES

REFERENCES

1. D. S. Newsome, *Catal. Rev.–Sci. Eng*., **21**, 275 (1980).
2. C.-H. Lin, C.-Y. Hsu, *J. Chem. Soc. Chem. Commun*., 1479 (1992).
3. R. G. Parr, W. Yang, Density Functional Theory of Atoms and Molecules, Oxford Univ. Press, New York, 1989.
4. V. Ponec, G. C. Bond, Catalysis by Metals and Alloys (Stud. Surf. Sci. Catal., vol. 95), Elsevier, Amsterdam, 1995.
5. G. Kadinov, S. Todorova, A. Palazov, in: New Frontiers in Catalysis (Proc. 10th Int. Congr. Catal., Budapest, 1992), L. Guczi, F. Solymosi, P. Tetenyi (eds.), Akademiai Kiado, Budapest, 1993, Part C, p. 2817.
6. G. L. C. Maire, F. Garin, in: Catalysis. Science and Technology, J. R. Anderson, M. Boudart (eds), vol. 6, Springer-Verlag, Berlin, 1984, p. 161.
7. D. Pocknell, *GB Patent* 2 207 355 (1949).
8. G. Angelov, PhD Thesis, UCTM, Sofia, 2001.
9. JCPDS International Center for Diffraction Data, Power Diffraction File, Swarthmore, PA, 1991.
10. CA **127**, 184 762, (1998).
11. P. Hou, H. Wise, *J. Catal.*, in press.
12. M. Sinev, private communication.
13. http://www.chemweb.com/alchem/articles/1051611477211.html.

CONTENTS

СЪДЪРЖАНИЕ